BIOPHYSICS OF ASYMMETRIC MEMBRANES: PROTOCOLS AND REVELATIONS

A Dissertation

Presented to the Faculty of the Weill Cornell Graduate School

Of Medical Sciences

In Partial Fulfillment of the Requirements for the Degree of

Doctor of Philosophy

by

Milka N. Doktorova

August 2018

BIOPHYSICS OF ASYMMETRIC MEMBRANES: PROTOCOLS AND REVELATIONS

Milka N. Doktorova, Ph.D.

Cornell University 2018

Lipid membranes enclose cells and organelles, and actively participate in cellular processes. Their many functional roles require tight regulation of properties including structure and dynamics. Cells achieve this by producing and dynamically tuning the concentration and organization of hundreds of structurally different types of lipid molecules in the various cellular membranes. The cell-bounding plasma membranes of eukaryotes in particular, exhibit an actively maintained asymmetric lipid distribution across their two leaflets. In addition to exposing certain types of lipids to the extracellular space or intracellular milieu, this specialized transbilayer lipid arrangement also affects the properties of the membrane itself and its interactions with proteins, in ways that are difficult to explore and thus not understood. To address this problem and enable further advancements in the field, we have developed both *in vitro* and *in silico* protocols for building asymmetric model membranes with finely controlled lipid compositions. These protocols allowed us to investigate the dynamics, energetics and structural consequences of interleaflet communication: with small-angle scattering we uncovered asymmetry-mediated changes in the lipid packing of individual leaflets in free-floating liposomes; with electron spin resonance we revealed the ensuing trends in lipid order; and nuclear magnetic resonance helped us bring new appreciation of the interplay between asymmetric bilayers and transmembrane protein inclusions. To interpret and better understand the experimental observations, we developed a new *in silico* protocol for constructing atomistic models of tension-free asymmetric bilayers and used it to simulate the experimentally measured membranes and validate the simulation conditions. By devising a novel computational framework

for calculating the compressibility of individual bilayer leaflets, we analyzed the energetics of protein interaction with the asymmetric membranes and obtained an estimate of the elastic energy of mixing the two leaflets. Together with additional experimental and computational studies of symmetric membrane systems, the results revealed fascinating ways in which cells can mediate the functional diversity of their membranes. The new methods and protocols leading to these insights generate previously unattainable opportunities for dissecting and exploring membrane-mediated cellular processes.

BIOGRAPHICAL SKETCH

Milka Doktorova was born and raised in Varna, the sea capital of Bulgaria, in a family of musicians. She spent most of her childhood being mistaken for a boy due to her short haircut, and inevitably learnt to read music, play the piano, dance Bulgarian and foreign dances, and even attempted singing. Her parents, thinking practically about the future, made sure that she supplemented these activities with extra computer science and English classes. Every summer she went with her family to her grandparents' cottage in the mountains for a month full of hiking, picking up wild herbs and fighting with her younger brother. Back home she kept dreaming about having a dog – one that wouldn't make her grandmother (who was living with them) move out to live in a tent.

Milka's elementary, middle and high schools happened to all be in the same building where her mother worked as a music teacher. Thus, after it became clear that her brother had obtained the privilege of being the mischievous kid in the family, Milka focused on getting good grades in school. During her last year in high school, close friends of her family from the United Sates offered her support to pursue higher education in the US. Milka spent two years in Maryland, from 2006 to 2008, where she attended Montgomery College in Rockville, a local community college offering a variety of classes and opportunities for extracurricular activities. She became familiar with the local culture and slang while tutoring math at school, served as a secretary of the student senate, and built a nice resume which helped her land a scholarship at Mount Holyoke College (MHC) in South Hadley, MA. Milka transferred there and after two years graduated summa cum laude with a double major in math and computer science. Her research experience at MHC introduced her to the field of computational biology and motivated her to apply for graduate programs all

throughout the US. She got a master's degree in computer science at Dartmouth College in Hanover, NH and joined the Tri-I CBM program at Cornell University in July 2012. Her love for research continues to guide her career choices.

To FAH.

ACKNOWLEDGMENTS

I would like to thank my two advisors, Dr. Harel Weinstein and Dr. Gerald Feigenson, for their incredible support and invaluable guidance during my PhD. They both endowed me with their trust – when I decided I wanted to do wet lab experiments without any prior experience; when I left NYC to spend two years in Ithaca while promising I would work remotely and keep in touch; when I was gone for weeks at a time for beamtime experiments; when I got involved in new projects and spent time and resources on exploring new topics. They nourished my curiosity and gave me the freedom to build my own research path. Yet, they were always there to provide advice, troubleshoot problems and discuss various issues. Joining their two labs was one of the best decisions that I made during my PhD.

Doing wet lab experiments focused on membrane asymmetry at Weill Cornell in NYC would not have been possible without the help of Dr. Olaf Andersen and the members of his lab. They openly accepted me as part of the group and let me use all of their resources. Everything I know about gramicidin I owe to them. I want to acknowledge Radda Rusinova, Lea Sanford and Thasin Peyear who helped with the stop-flow measurements and analysis in Chapter 8, and Clay Bracken, thanks to whom I was able to do the NMR flip-flop measurements at Weill Cornell using water suppression and thus, minimal amounts of D_2O.

I want to acknowledge all of my colleagues from the Weinstein and Feigenson labs who, over the years, have created such a stimulating and wonderful work environment. I have learnt a lot from my daily interactions with them. I want to specially thank George Khelashvili who introduced me to the local analysis of bilayer mechanical properties and has been such a pleasure to work with; Mike LeVine who discovered the harmonic relationship between the area compressibility moduli of the two leaflets

in Chapter 3.2 and is the number 1 person I go to with any statistics-related questions; Michel Cuendet who introduced me to the MM-GBSA framework in Chapter 4, helped with the NAMD colvar analysis in Chapter 7 and has been a great listener and mentor; and Niklaus Johner and David Ackerman for lots of insightful discussions on various topics. I also want to thank Sayan Mondal and Lynda Goh who mentored me during my research rotations in NYC and Ithaca and introduced me to MD simulations and GUV preparation and imaging, respectively, and Dr. James Sethna and Dr. David Eliezer who let me rotate in their labs and learn more about Ising models and NMR.

I was fortunate to have the opportunity to meet and work with Robert Dick at Cornell University, who spearheaded the project in Chapter 4 and taught me everything I now know about retroviruses and protein binding experiments. I also want to acknowledge Boris Dzikovski at ACERT for his help with the ESR experiments in Chapter 7.

The studies in Chapters 7 and 8 would not have been possible without the new protocol for preparing aLUVs described in Chapter 5, which I developed together with Fred Heberle, Drew Marquardt and Barbara Eicher. I have been extremely lucky to be able to collaborate with this group of great scientists. I want to acknowledge Peter Heftberger, Benjamin Kollmitzer and Bob Standaert who were also part of the asymmetry initiative; Georg Pabst who has been an avid advocate of the project and has initiated a lot of great interactions with other scientists in Europe; and Erwin London who hosted me and my colleagues for a few days in Stony Brook, showed us the steps of his protocol and has provided useful advice throughout the years.

I would have never discovered my passion for research if it weren't for a very close group of friends of my family who made it possible for me to pursue higher education in the United States. I will be forever grateful to Larry, Margaret, Bob, David, Len, Lisa and Jeanne for what they did for me. I want to specially thank Larry

and Margaret who have treated me like their daughter since I came to the US and have helped me in ways that I cannot even describe.

I owe a lot to my husband who is one of the best scientists I know. He introduced me to the world of small angle scattering techniques, taught me how to do good experimental work and has been an invaluable collaborator and mentor. He was with me through all of the ups and downs during my PhD, providing indispensable moral support and never losing faith in my abilities. I also want to thank all of my family and friends who kept reminding me that there is a side of life that is not work, and were always there to share, distract, listen and comfort.

TABLE OF CONTENTS

BIOGRAPHICAL SKETCH iii
DEDICATION v
ACKNOWLEDGMENTS vi
TABLE OF CONTENTS ix
LIST OF FIGURES xiv
LIST OF TABLES xvii

Chapter 1 Introduction 1
1.1 Importance of biological membranes 1
1.2 Membrane structure and organization – historical overview 4
1.3 Unanswered questions and active areas of research 13
1.3.1 Non-ideal mixing 13
1.3.2 Membrane asymmetry 15
1.4 Thesis overview and organization 17

Chapter 2 Hybrid and non-hybrid lipids exert common effects on membrane raft size and morphology 20
2.1 Abstract 20
2.2 Introduction, results and discussion 20

Chapter 3 Bilayer mechanical properties 30
3.1 Determination of bending rigidity and tilt modulus of lipid membranes from real-space fluctuation analysis of molecular dynamics simulations 30
3.1.1 Abstract 30
3.1.2 Introduction 31
3.1.3 Methods 35
3.1.3.1 Theoretical aspects of the RSF method 35
3.1.3.2 Molecular dynamics simulations 40
3.1.3.3 Application of the RSF method to MD trajectories 43
3.1.4 Results and discussion 45
3.1.4.1 Bending rigidity from the RSF analysis 49
3.1.4.2 Thermodynamic tilt modulus from the RSF analysis 55
3.1.5 Conclusion 62
3.2 A new computational method for membrane compressibility: Bilayer mechanical thickness revisited 62
3.2.1 Abstract 62
3.2.2 Introduction 63
3.2.3 Methods 67
3.2.3.1 Calculation of bilayer compressibility from area fluctuations 68
3.2.3.2 Leaflet compressibility calculated from area fluctuations 69
3.2.3.3 Leaflet compressibility calculated from thickness fluctuations 73
3.2.3.4 Simulation details 81

3.2.3.5 Analysis of simulations and method implementation 81
3.2.3.6 Lateral pressure profile calculation 82
3.2.3.7 Treatment of Chol-containing membranes 83
3.2.4 Results and discussion 84
3.2.4.1 Validation of the new method for quantifying compressibility moduli from local thickness fluctuations (LTF) 84
3.2.4.2 Application of the LTF method to mixed lipid systems 89
3.2.4.3 Compression-bending relationship and the role of chain unsaturation 90
3.2.4.4 The effect of cholesterol on bilayer mechanical thickness 96
3.2.4.5 Revised definition of bilayer mechanical thickness clarifies conflicting reports on PBM's applicability 99
3.2.5 Conclusion and summary 100
3.3 Conclusion 102

Chapter 4 Cholesterol promotes binding of retroviral matrix protein by indirectly affecting membrane electrostatics and solvation properties 106
4.1 Abstract 106
4.2 Introduction 107
4.3 Materials and methods 109
4.3.1 Materials 109
4.3.2 Protein purification and liposome binding 109
4.3.3 SANS sample preparation 110
4.3.4 SANS data collection 111
4.3.5 SANS data analysis 112
4.3.6 High-resolution structure of MA 113
4.3.7 Molecular Dynamics simulations 115
4.4 Results and discussion 116
4.4.1 MA binds to lipid headgroups without perturbing the overall bilayer structure 116
4.4.2 MA binds to POPS clusters 118
4.4.3 Cholesterol enhances MA lysine-membrane contacts 120
4.4.4 Cholesterol increases the membrane surface charge density 122
4.4.5 Nonideal mixing of POPC and POPS lipids has a small effect on surface potential 124
4.4.6 Cholesterol increases the MA/bilayer electrostatic interaction and decreases the penalty for headgroup desolvation 125
4.4.7 The membrane electrostatic potential is a key determinant of MA binding affinity 128
4.4.8 Implications for MA binding at the plasma membrane 131
4.5 Summary and conclusion 133

Chapter 5 Preparation of asymmetric phospholipid vesicles for use as cell membrane models 135
5.1 Abstract 135

5.2 Introduction 136
5.2.1 Preparation of asymmetric vesicles 137
5.2.2 Quantifying leaflet composition 142
5.2.3 Experimental design 145
5.3 Materials 148
5.4 Procedure 151
5.5 Anticipated results 164

Chapter 6 Accurate in silico modeling of asymmetric bilayers based on biophysical principles 167
6.1 Abstract 167
6.2 Introduction 168
6.3 Compatibility criterion 169
6.4 Construction with bilayers with zero leaflet tension 171
6.5 Application of the method to bilayers with diverse properties 172
6.6 Discussion 176
6.7 Conclusion 177

Chapter 7 Effect of membrane asymmetry on bilayer properties 179
7.1 Introduction 179
7.2 Materials and methods 181
7.2.1 Materials 181
7.2.2 Preparation and characterization of symmetric and asymmetric vesicles 182
7.2.3 Small-angle scattering data collection 183
7.2.4 Analysis of the structural properties of individual leaflets from joint refinement of SANS and SAXS data 184
7.2.5 Determination of the phase boundaries of binary mixtures with SAXS 186
7.2.6 Isolation of ESR signal from the inner and outer leaflets of asymmetric liposomes 186
7.2.7 ESR data collection 187
7.2.8 Analysis of ESR data 188
7.2.9 Calculation of spin probe partition coefficients 189
7.2.10 MD simulations 190
7.2.11 Analysis of the properties of coexisting phases in the simulated bilayers 191
7.2.12 Constrained MD simulations of symmetric bilayers 193
7.3 Results 194
7.3.1 Symmetric bilayers provide insight into the mechanisms of interleaflet communication 194
7.3.2 A new experimental strategy enables the examination of individual leaflet properties with ESR 197
7.3.3 Analysis of the spectral profiles of asymmetric bilayers reveals the presence of interleaflet coupling 199

7.3.4 Small-angle scattering data validates MD simulations of asymmetric bilayers 203
7.3.5 In silico exploration of interleaflet coupling reveals the elastic energy of mixing the two leaflets in asymmetric membranes 206
7.4 Discussion 209
7.5 Conclusion 214

Chapter 8 Gramicidin increases lipid flip-flop in symmetric and asymmetric lipid vesicles 216
8.1 Abstract 216
8.2 Introduction 217
8.3 Materials and methods 220
8.3.1 Materials 220
8.3.2 Preparation of liposomes without gramicidin 221
8.3.3 Preparation of liposomes with gramicidin 223
8.3.4 Gas chromatography-mass spectrometry 223
8.3.5 Small-angle X-ray Scattering (SAXS) 224
8.3.6 Circular dichroism (CD) 225
8.3.7 Gramicidin-based fluorescence assay (GBFA) 226
8.3.8 Differential scanning calorimetry (DSC) 226
8.3.9 ^{1}H NMR 227
8.3.10 Analysis of lipid flip-flop kinetics 227
8.3.11 Molecular Dynamics (MD) simulations 228
8.3.12 Quantification of membrane deformation from simulations 230
8.3.13 Quantification of membrane deformation in experiments 230
8.4 Results 231
8.4.1 Gramicidin incorporation, conformation, and function are the same in symmetric and asymmetric liposomes 231
8.4.2 gA scrambles lipids in compositionally asymmetric vesicles 234
8.4.3 gA increases the rate of lipid flip-flop in compositionally asymmetric vesicles 237
8.4.4 Models for gA-mediated lipid flip-flop 238
8.4.5 Membrane deformations are likely to play a role in gA-mediated lipid flip-flop 239
8.5 Discussion 242
8.5.1 Preparation and biophysical characterization of asymmetric proteoliposomes 242
8.5.2 Rates of lipid flip-flop measured with NMR 244
8.5.3 Mechanisms of gA-induced lipid scrambling 245
8.6 Conclusion 246

Chapter 9 Conclusion 248

APPENDIX A Supporting information for Chapter 2 253

APPENDIX B Supporting information for Chapter 3 266

APPENDIX C Supporting information for Chapter 4 284

APPENDIX D Supporting information for Chapter 6 313

APPENDIX E Supporting information for Chapter 7 317

APPENDIX F Supporting information for Chapter 8 332

BIBLIOGRAPHY 340

LIST OF FIGURES

Figure 1.1 Schematic illustration of the major components of an animal cell 3
Figure 1.2 Historical overview of the understanding of cell membrane structure.... 7
Figure 1.3 Some of the major groups of lipids found in nature..... 11
Figure 2.1 Classification of low-melting lipids 21
Figure 2.2 Fluorescence microscopy of GUVs of a non-hybrid lipid mixture..... 23
Figure 2.3 FRET reveals nanodomain formation in a non-hybrid lipid mixture.... 24
Figure 2.4 SANS reveals nanodomain formation in a non-hybrid lipid mixture ... 26
Figure 3.1.1 Structures of all-atom DPPC lipid, cardiolipin and cholesterol..... 36
Figure 3.1.2 Experimentally measured area per lipid vs area per lipid determined from MD simulations..... 44
Figure 3.1.3 Experimentally measured bending rigidities vs bending rigidities determined from RSF analysis of MD simulations..... 48
Figure 3.1.4 Values for K_C and κ_t from RSF analysis vs area per chain..... 53
Figure 3.1.5 Correlation between thermodynamic tilt modulus from RSF analysis and $1/\langle\theta^2\rangle$ and $1/\langle\tan^2\theta\rangle$ 58
Figure 3.1.6 Differences between thermodynamic and theoretical tilt moduli 60
Figure 3.2.1 Identification of relevant thickness for calculation of K_A^L 78
Figure 3.2.2 Calculation of K_A^L from local thickness fluctuations 80
Figure 3.2.3 Bilayer area compressibility for DOPC/Chol mixtures..... 84
Figure 3.2.4 Application of PBM to simulated bilayers..... 92
Figure 4.1 MA binds peripherally to lipid bilayers with minimal structural perturbation 117
Figure 4.2 Cholesterol enhances MA-membrane contacts..... 120
Figure 4.3 Cholesterol influences the membrane surface charge density 123
Figure 4.4 Cholesterol decreases the energetic penalty for lipid desolvation 127
Figure 4.5 RSV MA membrane association is quantitatively explained by membrane surface potential 129
Figure 4.6 Cellular plasma membrane model..... 132
Figure 5.1 Illustration of the different aLUV preparation protocols..... 139
Figure 5.2 GC assay for quantifying vesicle composition..... 144
Figure 5.3 ^{1}H NMR assay for quantifying lipid asymmetry..... 145
Figure 7.1 Lipid packing vs fraction overlap of leaflets' mass density profiles... 195
Figure 7.2 Successful silencing of C5PC on the outer leaflet of extruded vesicles..... 199
Figure 7.3 Model-free analysis of ESR spectra for the DPPC/POPC and DPPC/DEPC bilayers 201
Figure 7.4 Best fits of small-angle scattering data for DMPC/POPC aLUVs..... 205
Figure 8.1 Gramicidin incorporation and conformation remain the same in symmetric and asymmetric liposomes..... 232
Figure 8.2 Gramicidin channel function remains intact in asymmetric liposomes 234
Figure 8.3 Gramicidin scrambles lipids in compositionally asymmetric vesicles 235

Figure 8.4 Gramicidin increases the rate of lipid flip-flop in isotopically and compositionally asymmetric vesicles 236
Figure 8.5 Rate of lipid flip-flop shows a complex relationship with gA mole fraction 238
Figure 8.6 Membrane deformation and gA-mediated lipid flip-flop rate 240

Figure A1 Room temperature phase diagrams for multicomponent lipid bilayer mixtures 255
Figure A2 Fluorescence micrographs of GUVs 256
Figure A3 FRET reveals nanodomain formation in a non-hybrid lipid mixture 257
Figure A4 Comparison of FRET profiles between hybrid and non-hybrid lipid mixtures 258
Figure A5 SANS reveals nanodomain formation in a non-hybrid lipid mixture 259
Figure A6 SANS data used to determine vesicle size and polydispersity 260
Figure B1 Transformation of a leaflet into a set of surfaces 268
Figure B2 Effect of interpolation order on the calculated effective leaflet compressibility moduli 268
Figure B3 Identified relevant leaflet thickness 269
Figure B4 Bilayer area compressibility modulus as a function of the ratio of bilayer thickness and average area per lipid 270
Figure B5 Lateral pressure profiles of bilayers with increasing level of unsaturation 271
Figure B6 Total number of atoms and lateral pressure 272
Figure B7 Heuristic approximation of the double bonds region in unsaturated bilayers 273
Figure B8 PBM applied to unsaturated bilayers with cholesterol 274
Figure B9 Distribution of tilt angles of cholesterol's tail 275
Figure B10 Probability density functions of different changes in relevant thickness 277
Figure B11 K_A^L calculated with Eq. 3.2.12 279
Figure B12 Testing the volume incompressibility condition 281
Figure C1 MA structure 300
Figure C2 Bilayer structure from analysis of SANS data 301
Figure C3 ESR spectra of POPC/POPS and POPC/POPS/Chol with and without MA 302
Figure C4 Adsorption free energy and POPS redistribution in CMF calculations 303
Figure C5 Number density profiles for bilayers with and without MA from MD simulations 304
Figure C6 Analysis of MA conformation and lipid acyl chain order from MD simulations 305
Figure C7 Charge density distribution of individual components in the POPC/POPS and POPC/POPS/Chol bilayers 306
Figure C8 Non-ideal mixing does not induce large changes in membrane surface potential 307

Figure C9 Effect of cholesterol on lipid headgroup desolvation 308
Figure C10 RSV MA membrane association as a function of NaCl concentration 309
Figure C11 Thermodynamic cycle underlying the MM-GBSA method..... 310
Figure C12 Fluctuations of the distance between MA and bilayer surface..... 311
Figure C13 Orientation of MA with respect to the bilayer surface 312
Figure D1 Snapshots of simulation frames of bilayer Examples #1 and #2..... 314
Figure D2 Effect of deviations from the ideal lipid ratio on leaflet tension..... 315
Figure E1 Chemical structures of the lipids examined in Chapter 7..... 323
Figure E2 SAXS data for binary mixtures of DPPC and a low-melting lipid..... 324
Figure E3 Comparison of SAXS form factors for mixtures of DPPC/POPC at 22°C and 45°C 325
Figure E4 Interaction of ascorbate with C5PC 326
Figure E5 Subtraction of ascorbate signal from ESR spectra..... 327
Figure E6 Best fits of ESR data with NLSL software..... 328
Figure E7 Distribution of phosphorus z-positions in uniform and phase separated bilayers 329
Figure E8 Effect of structural perturbation to one leaflet on the order parameter profiles of the lipids..... 330
Figure E9 Model-free analysis of the ESR spectra for the DPPC/DOPC and DPPC/SOPC bilayers 331
Figure F1 Schematic illustration of the protocol for preparation of asymmetric proteoliposomes 334
Figure F2 DSC thermograms for POPC LUVs, DMPC-d54 LUVs and a 1:1 mixture of POPC LUVs and DMPC-d54 LUVs 335
Figure F3 DSC thermograms for DMPCd54 LUVs with and without gramicidin 336

LIST OF TABLES

Table 3.1.1 Lipid bilayer systems studied in Chapter 3.1 41
Table 3.1.2 Bending rigidity values calculated from the RSF analysis 46
Table 3.1.3 Thermodynamic tilt modulus values calculated from the RSF analysis 47
Table 3.1.4 Experimentally determined bilayer bending moduli 50
Table 3.2.1 Area compressibility of compositionally symmetric single component bilayers..... 86
Table 3.2.2 Area compressibility of compositionally symmetric multicomponent bilayers..... 87
Table 5.1 Two-component aLUVs prepared using the heavy donor strategy 146
Table 6.1 Structural leaflet parameters in asymmetric and corresponding symmetric bilayers 175
Table 7.1 Effect of structural perturbation to one leaflet on the bending rigidity and order parameter of the two bilayer leaflets..... 196
Table 7.2 Structural parameters obtained from ESR..... 202
Table 7.3 Comparison of structural parameters of an asymmetric bilayer obtained with SANS/SAXS and MD simulations..... 204
Table 7.4 Structural parameters of asymmetric bilayers and their symmetric counterparts obtained from MD simulations 207
Table 7.5 Elastic energy of mixing the two leaflets in asymmetric bilayers..... 208
Table 8.1 List of abbreviations 221
Table 8.2 Translocation kinetics in the examined systems 237
Table A1 Sample compositions examined in Chapter 2 253
Table A2 Microscopy data obtained in Chapter 2 254
Table A3 SANS data obtained in Chapter 2..... 254
Table A4 Comparison of results for hybrid and non-hybrid mixtures..... 254
Table B1 Bilayer information for all simulated systems in Chapter 3.2..... 266
Table B2 Information for all NPγT simulations 267
Table B3 Bilayers used for comparison with PBM 267
Table C1 Protein crystallization conditions, and statistics associated with the X-ray diffraction data and atomic models 296
Table C2 Bilayer structural parameters obtained from the refinement of SANS data 297
Table C3 Molecular volume, neutron scattering length and neutron scattering length density of different species..... 298
Table C4 Estimated composition and surface charge density of the mammalian plasma membrane inner leaflet 298
Table C5 Decomposition of the interaction energy of MA and the lipids calculated with the MM-GBSA method..... 299
Table D1 Information and results for different simulations run for the asymmetric bilayer Examples #1 and #2..... 313
Table E1 aLUVs examined in Chapter 7..... 319

Table E2 Symmetric and asymmetric LUVs examined with small-angle scattering in Chapter 7 319
Table E3 Partition coefficients of C5PC in the binary mixtures examined in Chapter 7 320
Table E4 Best-fit NLSL parameters for uniform mixtures 320
Table E5 Best-fit NLSL parameters for phase separated mixtures 321
Table E6 Information for the simulated bilayers in Chapter 7 322
Table F1 Asymmetric samples examined in each experiment in Chapter 8 332
Table F2 Information for the simulated bilayers without gramicidin in Chapter 8 333

CHAPTER 1
INTRODUCTION

1.1 Importance of biological lipid membranes

Lipid membranes are an indispensable part of life. Every living cell is enclosed by a membrane (the *plasma* membrane) which defines the cell boundaries and serves as a barrier between the extracellular space and the intracellular milieu. While in prokaryotic organisms the cell interior comprises a single compartment where all cellular needs are fulfilled (e.g. the cell's genetic material is stored, energy is produced and molecules are synthesized and degraded), eukaryotic cells have evolved to compartmentalize different functions into specialized inner organelles. Similar to the cell itself, each organelle has its own bounding membrane which separates the organelle's interior from the cell's cytosol. In a large liver hepatocyte cell, for example, the plasma membrane is only 2% of the total cell membrane; the majority of the membrane area comes from the endoplasmic reticulum (ER) and the mitochondria, which comprise 51% and 39% of the total cell membrane, respectively [6].

The bounding membranes of both cells and their organelles have been optimized through evolution to possess a combination of properties that best serve the function of the enclosed entity (Fig. 1.1). One of their defining characteristics is **selective permeability,** which is needed to protect the cell from harmful pathogens, control the intake of nutrients and other small molecules, and maintain specific concentration gradients of ions and solutes. Cell homeostasis for instance, requires large concentration gradients of Ca^{2+}: the divalent cation is present in the extracellular medium and stored in the ER inside the cell, and its carefully regulated release in the cytosol controls many biological processes. The asymmetric compartmentalization of hydrogen ions on the other hand, helps sustain a high pH in the mitochondria to drive the production of adenosine triphosphate (ATP), the primary energy currency of the

cell, and a low pH in lysosomes, which creates the acidic environment needed for molecular degradation by specialized enzymes.

In addition to their dynamically regulated permeability, membranes also have to possess **sufficient flexibility** to accommodate the myriad of shapes that cells and their organelles need to adopt in order to carry on their function both alone and in larger multicellular assemblies. For example: (1) the outer mitochondrial membrane is relatively smooth while the inner mitochondrial membrane has a complex topology required for the synthesis of ATP; (2) the peculiar morphology of the membrane stacks in rod cells enables the efficient detection and processing of light which ultimately results in our ability to see; (3) red blood cells have discoid shapes that must deform reversibly whenever they squeeze through narrow capillaries in order to enter the blood stream and deliver oxygen to different parts of the body; (4) nerve cells have both highly branched (dendrites) and elongated (axon) parts that facilitate the sensing of a stimulus and the rapid emission of an action potential to neighboring neurons, and; (5) the plasma membrane of epithelial cells in the intestines has distinct membrane domains with heterogeneous and well defined morphologies that serve various functions such as sorting of membrane components and increasing the membrane surface area to absorb more nutrients. Closely related to its flexibility is the membrane's ability to undergo **fusion and fission,** which are two processes essential for cell replication and for the encapsulation and transport of vesicles carrying proteins and small molecules in and out of the cell or between different compartments in the cell interior.

Given the importance of membranes, it is not surprising that changes in their properties can have serious consequences. Increased permeability of the outer mitochondrial membrane and subsequent release of various mitochondrial proteins into the cytosol is a key step in the intrinsic signaling pathway during cell apoptosis

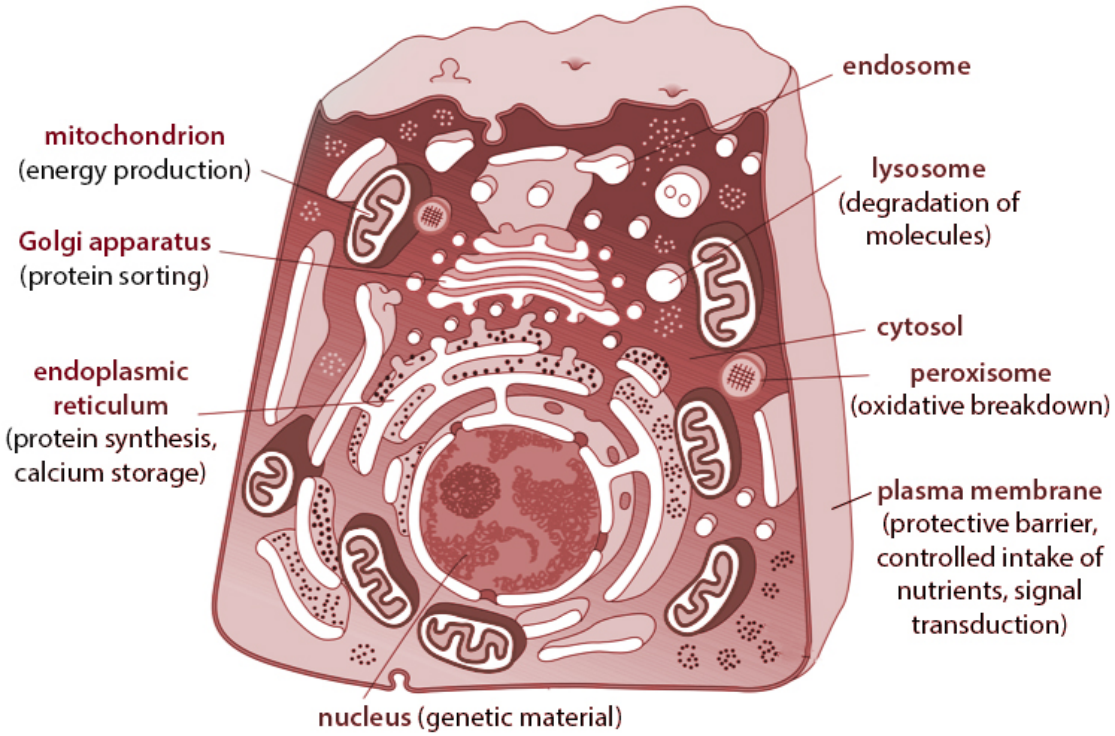

Figure 1.1. Schematic illustration of the major compartments of an animal cell. Shown are: mitochondria, the main sites for energy production in the cell; ER where proteins and lipids are synthesized; Golgi apparatus where proteins and lipids are modified and forwarded to other organelles; the nucleus that stores the cell's genetic material; lysosomes where molecules are degraded by specialized enzymes; endosomes through which molecules have to pass on their way to lysosomes; peroxisomes which store enzymes that catalyze the oxidative breakdown of long chain fatty acids; cytosol which provides the aqueous environment around all organelles; and the plasma membrane which separates the cytoplasm from the external medium. The figure was adapted from Ref. [6].

[13]. At the same time, decreased plasma membrane permeability has been associated with multidrug resistance in cells, including a poorer response to chemotherapy in some cancer cell lines [16]. Changes in membrane stiffness can also have pathological implications. For example, reduced deformability of red blood cells causes disruptions in blood flow and leads to diseases such as sickle cell anemia [17-22], while altered amounts of poly-unsaturated dietary fats—which can remodel the PM lipidome and increase membrane flexibility—have been linked to various conditions such as obesity, diabetes and mental illness [23].

How do cells maintain such a fine balance between the properties of their different membranes? How can they dynamically regulate the permeability and flexibility of individual membrane barriers while preserving their integrity? While many details surrounding these questions are still under active investigation, the basic principles enabling their realization are now generally appreciated. Membranes are composed of two layers of lipid molecules, and cells can produce and regulate the concentration of hundreds of structurally different types of lipids, and thereby selectively tune membrane biophysical properties. Membranes are also fluid, which enables them to solvate, interact with and facilitate the function of a large variety of proteins. Thus, by mediating the composition and structural organization of the membranes' building blocks and their interactions with proteins, cells achieve a functional diversity of their varied membranes that is required for the proper execution of all cellular processes.

1.2 Membrane structure and organization – historical overview

The current understanding about the complexity of cell membrane organization has slowly evolved throughout the years (Fig. 1.2). The presence of a barrier separating the inside and outside of cells was first reported in the second half of the nineteenth century when researches noted that plant protoplasts were selectively permeable to water and solutes (de Vries, 1871; [24]) (Fig. 1.2a). In 1877 Wilhelm Pfeffer, a German botanist and plant physiologist, proposed that this barrier is a thin layer that serves the general purpose of separating aqueous environments of different composition, and called it the *plasma membrane* [25]. 18 years later, Charles Ernest Overton, who was studying the osmotic properties of cells, observed that the ability of molecules (in particular, general anesthetics) to permeate through the plasma membrane depended on their solubility in oil. This led to the hypothesis that the

membrane has a lipophilic nature [26] (Fig. 1.2b) – a speculation also raised earlier by Quincke based on considerations of surface tension, semi-permeability and the relative properties of oil [24]. Overton further went on to suggest that the thin membrane film was made of lecithin and cholesterol [27]. Thus, by the turn of the twentieth century it was established that cells were surrounded by a thin plasma membrane which seemed to have the general properties of a fatty substance.

In 1925 Gorter and Grendel performed a simple experiment to determine the relative thickness of the plasma membrane of red blood cells [28]. They took blood samples from human, sheep, rabbit, dog, goat and guinea pig, and estimated the surface area of the cells (i.e. of their cell plasma membranes) from microscopy images and total cell counts. Then, they extracted all lipids from the cells and used the then recently developed Langmuir trough method [29] to form a monolayer film and measure its surface area. For all samples, without exception, the monolayer area was within error twice that of the whole membrane surface of the cells, from which they concluded that cell membranes are composed of two layers of lipids such that their polar headgroups are oriented towards the aqueous environment (Fig. 1.2c). Even though the authors performed two mistakes in their calculations [30], fortunately the errors cancelled each other, and the study is generally recognized as the first experimental evidence that membranes are indeed, lipid bilayers.

Using the accumulated knowledge about the chemical nature of the cell constituents, Danielli and Davson developed the first biomembrane model with both proteins and lipids, in order to explain the permeability properties of the thin films surrounding the cells [9] (Fig. 1.2d). In their model, globular proteins with “dense impenetrable areas, interspaced by heavily hydrated areas of molecular dimension” are adsorbed on the membrane surface, forming a coating with selective permeability based on molecular size. The lipids in the membrane film possess both acidic and

basic groups and are well hydrated. Thus, charged solutes can permeate through the hydration layers of the proteins and lipids, form complexes with them and reduce their interaction with water, while hydrophobic molecules can easily diffuse through the lipophilic part of the membrane. The authors concluded that membrane permeability does not involve any chemical reactions with the solutes but instead can be explained by the chemical composition of the protein-coated lipid film. This model was generally consistent with the lower resolution protein structural data that came out within the next 20-30 years, and researchers were mostly building on it to explain the growing understanding of the functional diversity of cell membranes.

In the late 1950s and early 1960s, the advent of electron microscopy allowed for the first direct observations of the structure of cellular membranes. Thus, J. David Robertson imaged and described the membrane structures of both the plasma membrane and individual organelles and concluded that all biological membranes follow the same construction principle [11]. Based on his observations, he introduced the fundamental unit common to all membranes which he called the "unit membrane model" (Fig. 1.2e). Robertson's unit membrane was similar to that of Danielli and Davson with three exceptions: 1) it firmly assumed that the lipoid membrane is made of exactly two lipid layers; 2) the proteins coating the membrane surface were not loosely interspaced globular particles but instead formed a fully spread protein monolayer, as evidenced from X-ray studies of myelin and electron microscopy images; and 3) the protein monolayers on the two sides of the lipid film were asymmetric. Thus, being refined by new experimental data, the working picture of the biomembrane was slowly becoming more complex while the notion that all cell membranes share the same basic structural principles established a common ground for the study of their properties.

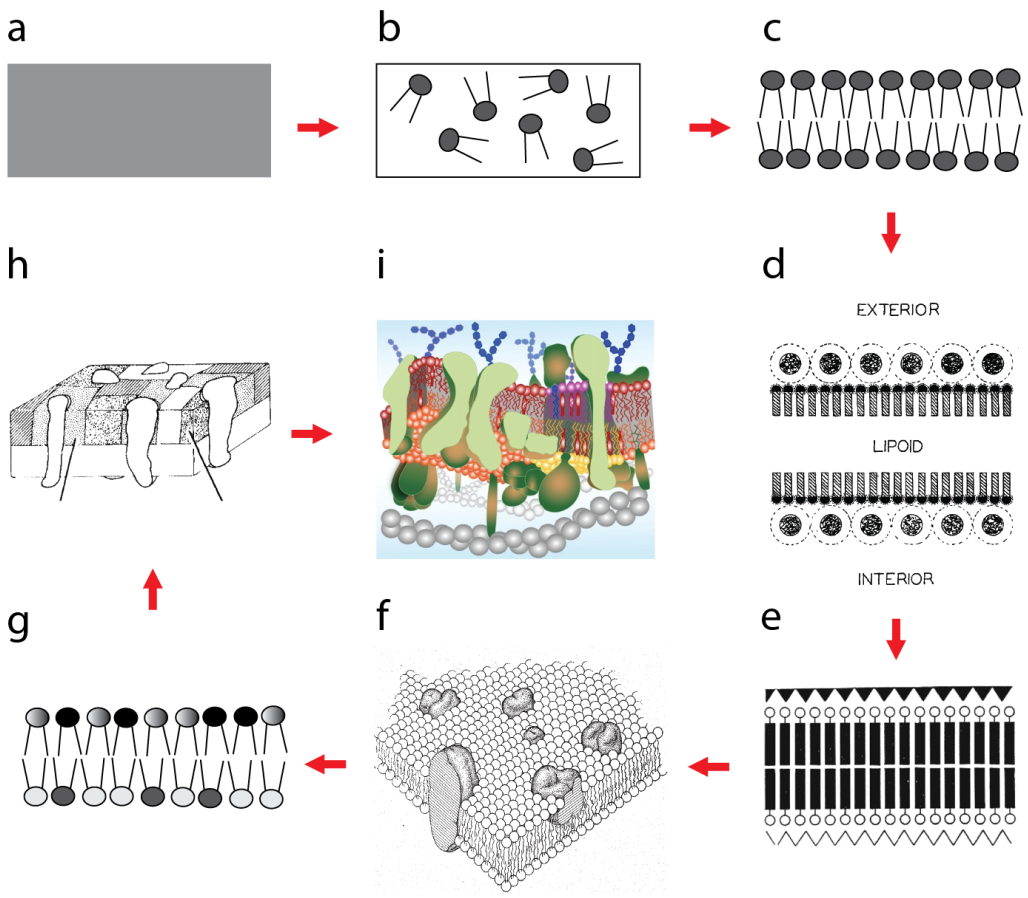

Figure 1.2. Historical overview of the understanding of cell membrane structure. a) The existence of a membrane barrier with selective permeability was first noted in the 1870s. b) Speculation about its lipophilic nature appeared in Overton's report in 1895. c) Gorter and Grendel presented evidence that the membrane is composed of two layers of lipids in 1925. d) The first model of a biomembrane that included proteins was developed by Danielli and Davson in 1935. e) The model was later refined by Robertson in the late 1950s. f) Singer and Nicolson proposed the fluid-mosaic model in 1972. g) The same year Bretscher hypothesized about the asymmetric lipid distribution in the plasma membrane of mammalian cells. h) The biomembrane model evolved further after the discovery of lipid domains in the membrane in the 1980s. i) This led to the development of the raft hypothesis and the current model of plasma membrane organization. The schematic illustration in d) is from Ref. [9]; e) and i) are reprinted from Refs. [11] and [12], with permission from Elsevier; f) and h) are reprinted from Refs. [14] and [15], with permission from AAAS.

It was not until 1970 that the fluid nature of the plasma membrane became apparent. In a seminal study, Frye and Edidin demonstrated that the plasma membrane is not rigid as previously speculated, but rather "'fluid' enough to allow free 'diffusion' of surface antigens" [31]. This discovery, together with further advancements in protein and lipid characterization led to two other seminal developments at the beginning of 1972 – the formalization of the idea for the fluid mosaic structure of the cell membrane [14] and Mark Bretscher's astute proposition that the lipids in the plasma membrane are asymmetrically distributed between the two leaflets [32]. Each of these ideas formed the foundation of the current view of cell membrane structure by emphasizing a different aspect of the three-dimensional biomembrane organization: the lateral arrangement of lipids and proteins, and the transverse heterogeneous distribution of the bilayer lipids.

By 1972 researchers in the biophysics community already knew that the unit membrane model of a lipid bilayer sandwiched between two continuous protein layers was unlikely due to its thermodynamic instability. Singer and Nicolson formalized this notion by integrating a wide range of experimental observations with core thermodynamic principles to paint a protein-centric picture of the interplay between proteins and lipids. The new fluid mosaic model took into account the hydrophobic and hydrophilic interactions between the membrane components and the aqueous environment, and its premise was that the free energy of the system must be minimized (Fig. 1.2f). In their model, the membrane has a dynamic mosaic structure in which globular proteins are either embedded in (fully or partially), or peripherally bound to, a uniform (or featureless) lipid bilayer matrix. The integral (embedded) proteins are amphipathic in nature like the lipids, form the majority of the membrane-associated proteins, give the membrane its functionality, and are generally randomly distributed within the plane of the membrane with no long-range order. In their study,

the authors showed that this model was supported by existing experimental data, could explain disparate results pertaining to membrane organization, protein-membrane interactions and protein function, and suggested new avenues for exploration of membrane functions. Even though the heterogeneous composition and mixing of the protein-solvating lipid bilayer and their role in the discussed effects were largely ignored, the authors noted that the two surfaces of the fluid membrane are likely asymmetric as evidenced by the selective localization of oligosaccharides on the outside of cells.

Less than two weeks after Singer and Nicolson's paper in Science, Mark Bretscher's postulation about the asymmetric nature of biological membranes appeared in Nature [32] (Fig. 1.2g). At that time it was known that erythrocyte membranes were composed of four major types of lipids: phosphatidylcholine (PC), phosphatidylethanolamine (PE), phosphatidylserine (PS) and sphingomyelin (SM). Recent experiments with externally added membrane-impermeable chemical reagents showed that in erythrocytes, few aminolipids (PE and PS) were reactive, implying confinement of these lipids to the inner leaflet. At the same time, studies with phospholipases suggested that SM and PC were localized predominantly on the outer leaflet. Thus, Bretscher hypothesized that the outer leaflet was composed entirely of SM and PC while the inner leaflet contained all the PE and PS in the plasma membranes of both erythrocytes and other mammalian cells.

A year later Verkleij and colleagues published the first complete quantitative estimate of the asymmetric distribution of the major phospholipids in human erythrocytes [33]. In the proposed distribution small fractions of SM/PC and PE were present on the inner and outer leaflets, respectively, while PS was entirely confined to the cytosolic side. While both approaches used for quantifying the phospholipid interleaflet distribution (i.e. chemical modification and enzyme degradation) have

been scrutinized over the years and shown to have certain limitations [34], the red blood cell lipid composition estimated in that 1973 report remains more or less the same today. Later studies have attempted to characterize the lipid composition of the membranes of other cells and their organelles, but the added practical challenges due to the presence of multiple membrane-enclosed compartments have resulted in conflicting results [34].

While the fluid mosaic model provided a protein-centric view of the biomembrane complexity, there was emerging evidence that the lipid bilayer matrix itself was laterally heterogeneous and could influence protein organization and function. Studies on model systems revealed that different types of lipids can mix non-ideally and form temperature-dependent clusters [35] and co-existing liquid-liquid phases [36]. Considerations of the lipids' thermodynamic behavior led to a revised model of the plasma membrane organization which contained compositionally different lipid environments (Fig. 1.2h) – lipid domains were detected in both lipid-only model bilayers and isolated plasma membranes from cells [15, 37]. Thus, Karnovsky and colleagues ended their report in 1982 by posing a number of important questions which, as it turns out, formed the basis of many lines of future research efforts.

Shortly after the discussion of membrane domains was initiated, proteins were shown to exhibit selective partitioning between domains in model membranes [38, 39]. This was followed by an experimental investigation of the functional consequences of nonideal lipid mixing in cells. The separation of sphingolipids and glycerolipids, and the formation of microdomains with specific lipid composition, were proposed to explain the Golgi-mediated sorting of proteins in the apical membrane of epithelial cells [40, 41]. The concept of such microdomains was then formalized as the *raft hypothesis* which postulated that domains enriched in sphingomyelin and cholesterol serve as platforms for the attachment of proteins and

thus actively participate in cellular functions such as trafficking and signal transduction [42]. This idea led to a new model for the plasma membrane (Fig. 1.2i) in which the outer leaflet contained diffusing platforms, or rafts, which attracted specific proteins and could coalesce or disassemble in response to various stimuli [42, 43]. The

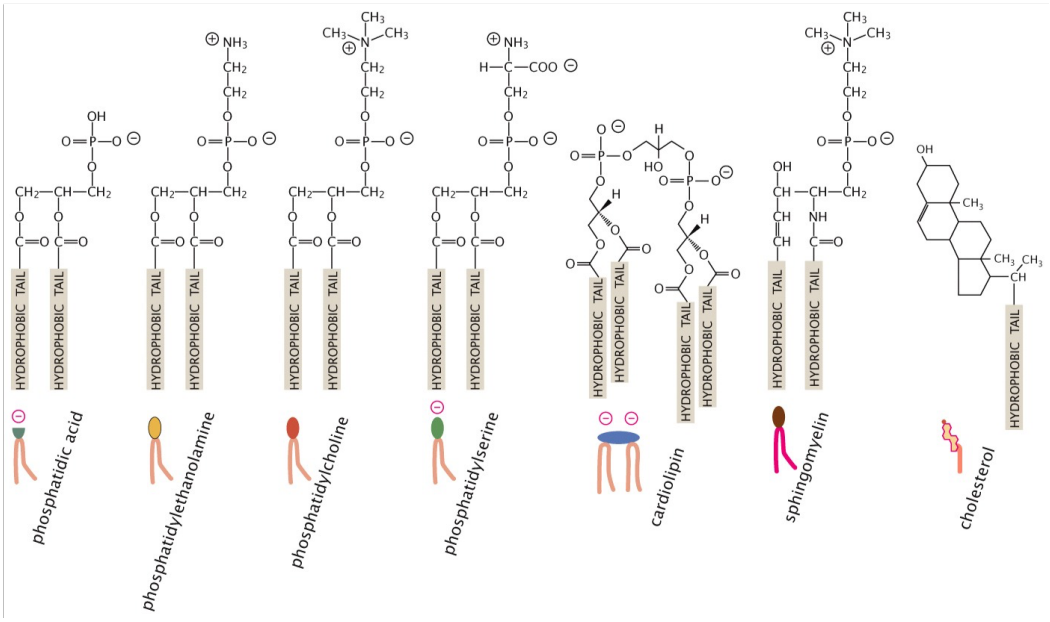

Figure 1.3. Some of the major groups of lipids found in nature. Shown are phosphatidic acid (PA), phosphatidylethanolamine (PE), phosphatidylcholine (PC), phosphatidylserine (PS), cardiolipin (CL), sphingomyelin (SM) and cholesterol (Chol). The figure is reprinted from Ref. [5], with permission from Taylor and Francis; permission conveyed through Copyright Clearance Center, Inc.

formulation of the raft hypothesis was a revolutionary step in both the biology and biophysics fields as it put forward the importance of lipid mixing for the proper functioning of the cell machinery and renewed the interest in, and appreciation for, the properties of the bilayer matrix. Thus, at the beginning of the 21st century, as Simons and Toomre put it "After long neglect, the dynamic organization of lipid bilayers is finally back at center stage." [43].

While the general picture of membrane organization painted by the raft hypothesis has remained more or less the same over the last 20 years, our understanding about the

complexity of cellular membranes has continued to evolve. Technological advances have enabled the characterization of the large diversity of lipids [44], as well as their metabolism and transport between different membrane compartments [45]. Simplifying this diversity, lipids have been conveniently grouped in a few general classes based mostly on the types of their headgroups and glycerol backbones (Fig. 1.3). This classification has made it easier to examine and describe their distribution across cellular organelles and the plasma membrane, including the maintenance of their interleaflet organization [45]. For example, the membrane of the ER, the primary site of lipid synthesis, is symmetric owing to the presence of scramblases that facilitate rapid bi-directional movement of lipids between the two leaflets. At the same time, the asymmetry of the plasma membrane is tightly regulated with the help of enzymes such as P4-ATPases which catalyze the uni-directional translocation of aminophospholipids from the exoplasmic to the cytoplasmic leaflet.

The accumulating body of knowledge about the biophysical properties of the various lipids and lipid mixtures, including their non-ideal mixing tendencies and rich thermodynamic phase behavior, has been instrumental in the study of protein-membrane interactions. Bilayer thickness has been shown to regulate the function of large transmembrane proteins by altering their conformational dynamics [46, 47]; The charge density of the two leaflet surfaces serves as a determinant of protein orientation and topology, as well as a modulator of the binding of charged proteins [48, 49]; The mechanical properties of the thin membrane sheet, including its surface tension, bending rigidity and area compressibility, quantify the energy required to deform the bilayer and are thus directly related to membrane fusion, endo- and exocytosis, and the adaptation of the bilayer to any transmembrane inclusion whose bilayer incorporation results in unfavorable interactions between hydrophilic and hydrophobic moieties [47]. Local variations in lipid composition such as the ones arising from phase

separation or other non-ideal lipid-lipid interactions, lead to spatial variations in the above properties (thickness, charge density, tension and elasticity) and the mediated by them cellular machinery. In addition, the boundary regions between coexisting membrane domains provide yet another distinct environment with unique composition and properties that could serve as a platform for different cellular processes.

1.3 Unanswered questions and active areas of research

Despite the progress over the last 150 years, many questions about cell membranes remain elusive and a subject of active research. Below some of these questions are summarized in two major groups related to non-ideal mixing and membrane asymmetry.

1.3.1 Non-ideal mixing

Lipids have different structures and thermodynamic properties [50]. Thus, when mixed together under given external conditions such as fixed temperature and pressure, different pairs of lipids may exhibit different interaction energies. The magnitude of these energy differences determines the degree of non-ideal mixing, i.e. how strongly the lipid molecules segregate from or else prefer each other. Below a certain threshold they can form clusters (usually small and transient) enriched in a particular lipid type, while above the threshold phase separation occurs and stable domains of well-defined composition emerge [51]. Knowledge of the fundamental principles that determine and influence the lipid-lipid interaction energies is key in identifying the type of micro-environments present in a heterogenous lipid mixture such as the plasma membrane. The phase behavior of some 2 [52], 3 [53] and even 4-component mixtures [54] has been studied and catalogued, as well as the quantitative interaction energies of some lipid types [55]. Yet, a number of questions are left

unanswered. What properties of a lipid determine how well it mixes with other lipids? Models such as the umbrella [56] and condensed complexes [57] models exist to explain the preferential interaction of cholesterol with saturated lipids, but more mechanistic insights are needed to reason about the mixing properties of multi-component membranes. What external factors affect the lipids' interaction preferences? For example: 1) Cell membranes can experience tension arising from large local gradients of solutes or binding of small molecules. Since different lipids and lipid patches can respond differently to tension, it is not clear how such tension would change their mixing behavior; 2) Multivalent ions, which are ubiquitous in nature, have been shown to bind lipids and affect their properties [58]. How would such ion-induced changes alter the propensity for certain lipid-lipid interactions? 3) The lateral movement of phospholipids in the plasma membrane has been shown to exhibit the characteristics of hop diffusion, likely due to the presence of the actin cytoskeleton [59]. How does an imposed compartmentalization of the membrane components affect the inter- and intra-compartment lipid segregation? 4) Transmembrane proteins can induce lipid redistribution as a way to minimize the energy of bilayer deformation around them. Water soluble proteins may also sequester certain lipids upon binding. How would such protein-lipid interactions affect lipid-lipid mixing?

Furthermore, proteins can not only affect but also be affected by the non-ideal mixing behavior of the lipids. The clearest example comes from the differential partitioning of some proteins between the different phases in a phase-separated mixture, or between the detergent-soluble and insoluble fractions extracted from cellular membranes. While significant progress has been made in this research area, much remains unknown. Some key structural properties determining the partitioning of single-span transmembrane proteins have been identified [60], but an analogous

description for multi-helical proteins is missing. A general understanding exists about the free energy of interaction of transmembrane inclusions with their lipid environment and its relationship to protein oligimerization and domain partitioning [47, 61], but the limited data on the conformation and dynamics of many proteins, as well as the precise composition and biophysical properties of the coexisting lipid environments in a complex mixture, makes predictions of protein partitioning challenging. Similarly, the effect of external factors (e.g. temperature, tension) on protein-membrane interactions, including the binding of peripheral proteins to the bilayer surface, remain largely unexplored.

1.3.2 Membrane asymmetry

The discovery of the asymmetric lipid distribution across the two leaflets of the plasma membrane in the early 1970s was an important revelation. It established the existence of another dimension of bilayer organization that was far from chemical equilibrium yet was apparently essential for maintaining cellular homeostasis. Evidence for the functional role of membrane asymmetry began to emerge with the studies of blood coagulation [62] and erythrocyte recognition by macrophages [63]. In particular, thrombosis and phagocytosis were directly linked to the exposure of PS on the outer leaflet of the plasma membrane [64, 65]. Besides the importance of the regulated exposure of a certain type of lipid on either side of the bilayer, the physiological roles of the biophysical properties of the asymmetric membrane have been much less studied. Importantly, the fundamental principles governing the influence of one leaflet on the other remain elusive. As a result, it is not clear how knowledge obtained from symmetric membranes can be extended to asymmetric bilayers. How would the phase behavior (or more generally, the non-ideal mixing) of a lipid mixture change when a leaflet composed of that lipid mixture opposes a leaflet

with a different composition? Would the same models describing the mutual adaptation of a transmembrane protein and its surrounding symmetric bilayer hold in an asymmetric membrane? How would the basic structural and dynamic properties of the lipids such as packing, acyl chain order and diffusion be affected by interleaflet coupling?

The difficulty in studying these questions stems from: 1) the challenges in creating robust models of asymmetric membranes in vitro, and 2) the inability to measure the local variations in tension in a cellular plasma membrane. The biophysical properties of symmetric bilayers and their interaction with proteins are generally obtained from systematic experiments on model systems with easily adjustable parameters. Since membrane asymmetry represents a non-equilibrium state which in cells is maintained by enzymes, the preparation of enzyme-free asymmetric model membranes with easily tunable parameters has been a major challenge. In addition, the development of assays to accurately quantify the lipid composition of individual leaflets, as well as probe the properties of each leaflet separately is still an active area of research.

Another factor hindering progress in the field is the unknown physiological role of tension in the regulation of membrane properties in vivo. Tension in an asymmetric membrane can arise not only from the imbalance of solutes across the membrane but also from an imbalance of the packing densities in the two leaflets. The latter can be caused by the delivery of lipids to only one of the leaflets; binding and partial insertion of small molecules and proteins to one side of the membrane; the uni-directional translocation of lipids between the leaflets; membrane fusion and vesicle budding; and blockage of lateral lipid diffusion by proteins or the cytoskeleton, to name a few. As demonstrated by both in vitro and in silico experiments, tension arising from some of these factors can have profound implications for the properties of the two leaflets [66] and the morphology of the membrane [67, 68]. Unfortunately, measurements of the

tension in a cell membrane are notoriously difficult, which is a big hurdle in examining its role in cellular processes.

Overcoming the obstacles above and unraveling the roots of interleaflet coupling can help address a number of pertinent biological questions. How can molecules interacting solely with one leaflet communicate with molecules interacting solely with the opposite leaflet? What is the role of membrane asymmetry in the conformational transitions (and consequently, function) of transmembrane proteins? Why is palmitoylation used as a means to localize proteins to specific locations in the inner leaflet of the plasma membrane? While basic and scientifically fascinating, such questions can provide new and important insights into human physiology.

1.4 Thesis overview and organization

Here we address some of the unexplored questions and existing hurdles to progress discussed in the previous section. In particular, the goal of this thesis is to explore the following problems:

- How does membrane composition regulate domain size and morphology?
- How do cholesterol and weak non-ideal lipid mixing promote the interaction of peripheral proteins with membranes?
- How do the two leaflets in a membrane communicate with each other, and how does membrane asymmetry impact the biophysical properties of a bilayer?
- How do proteins affect and get affected by the transverse asymmetric lipid distribution?

Our studies utilize model membranes of different types (large and giant unilamellar vesicles, multilamellar liposomes and flat bilayer patches) due to their

amenability to a wide range of biophysical techniques. In Chapter 2 we demonstrate that the hybrid nature of the lipid acyl chains, previously hypothesized to be a key determinant of domain size in symmetric phase separated bilayers, does not constitute a viable mechanism for controlling domain morphology. An extensive quantification of the bending rigidity (Chapter 3.1) and area compressibility (Chapter 3.2) moduli of simulated symmetric bilayers suggests that differences in the mechanical properties of the two phases may instead be responsible for the compositional effects on domain size. The novel computational framework for calculating the compressibility of individual bilayer leaflets from molecular dynamics (MD) simulations in Chapter 3 further reveals important insights into the membranes 'mechanical thickness' which acts as a conduit between the bending rigidity and area compressibility moduli of the bilayer.

In Chapter 4 we identify the mechanisms by which cholesterol promotes the electrostatic interaction of retroviral proteins with membranes by utilizing MD simulations, theoretical modeling and a suite of experiments in vitro. The effects of weak non-ideal mixing of phospholipids on protein binding are also investigated.

In Chapter 5 we present a new protocol and tools for the preparation of asymmetric large unilamellar vesicles in vitro and the robust characterization of the lipid composition of their two leaflets with gas chromatography and nuclear magnetic resonance. Correspondingly, in Chapter 6 we develop a computational methodology for constructing tension-free asymmetric bilayers for MD simulations that adheres to strict biophysical principles ensures compatibility with other symmetric and asymmetric model membranes and is capable of producing realistic changes in the leaflet properties.

Using the protocols from Chapters 3, 5 and 6, in Chapter 7 we investigate the mechanisms of interleaflet coupling and the effects of membrane asymmetry on

bilayer properties by experimentally validating the in-silico approach with small-angle scattering data and integrating new findings from electron spin resonance spectroscopy with MD simulations.

In Chapter 8 we examine the interplay between the ion channel gramicidin and symmetric and asymmetric membranes by measuring lipid flip-flop kinetics with NMR in the presence and absence of the channel and analyzing the free energy of gramicidin-induced membrane deformations with MD simulations.

Finally, in Chapter 9 we conclude by discussing the contribution of the results from this thesis to the development of the membrane research field and the importance of combining experimental and computational approaches in the study of complex biological phenomena. Having scratched only the surface of the open questions in the field, we end by giving an outlook for the necessary next steps toward understanding membrane asymmetry and its role in cellular processes.

CHAPTER 2
HYBRID AND NON-HYBRID LIPIDS EXERT COMMON EFFECTS ON MEMBRANE RAFT SIZE AND MORPHOLOGY*

2.1 Abstract

Nanometer-scale domains in cholesterol-rich model membranes emulate lipid rafts in cell plasma membranes (PMs). The physicochemical mechanisms that maintain a finite, small domain size are, however, not well understood. A special role has been postulated for chain-asymmetric or hybrid lipids, having a saturated *sn*-1 chain and an unsaturated *sn*-2 chain. Hybrid lipids generate nanodomains in some model membranes, and are also abundant in the PM. It was proposed that they align in a preferred orientation at the boundary of ordered and disordered phases, lowering the interfacial energy and thus reducing domain size. We used small-angle neutron scattering and fluorescence techniques to detect nanoscopic and modulated liquid phase domains in a mixture composed entirely of non-hybrid lipids and cholesterol. Our results are indistinguishable from those obtained previously for mixtures containing hybrid lipids, conclusively showing that hybrid lipids are not required for the formation of nanoscopic liquid domains, and strongly implying a common mechanism for the overall control of raft size and morphology. We discuss implications of these findings for theoretical descriptions of nanodomains.

2.2 Introduction, results and discussion

Cell membranes perform multiple functions that may be facilitated by the lateral organization of lipids and proteins into nanoscale compartments, termed membrane

* The following chapter and its supporting information (Appendix A) are reprinted with permission from: Heberle, F. A., Doktorova, M., Goh, S. L., Standaert, R. F., Katsaras, J., & Feigenson, G. W. 2013. *Journal of the American Chemical Society*, *135*(40), 14932-14935. Copyright 2013 American Chemical Society. They have been modified to fit the format of the thesis. FAH, MD and GSL contributed equally to the work. MD collected and analyzed the GUV data.

rafts [69-71]. Because of their small size and dynamic nature [72, 73], and the chemical complexity of biological membranes, rafts have proven difficult to characterize in cells [74]. Three-component mixtures containing a high-melting (high-T_M) lipid, a low-melting (low-T_M) lipid and cholesterol ("HLC" mixtures) are valuable models because they reproduce key properties associated with rafts in animal cell plasma membranes [75, 76]. Specifically, some HLC mixtures separate into liquid phase domains, reminiscent of the distinct chemical and physical environments central to the raft hypothesis. The study of HLC mixtures offers the possibility of elucidating raft formation at the molecular level by identifying structural aspects of mixture components that influence raft properties, including size and lifetime [74].

HLC mixtures yield either nanoscopic or microscopic liquid phase domains, which we previously classified as Type I or Type II behavior, respectively (Fig. A1) [75, 76]. Fig. 2.1 shows three low-T_M lipids that generate either Type I or Type II phase diagrams. Mixtures containing the non-hybrid (*i.e.*, symmetric, having identical acyl chains) lipid 1,2-dioleoyl-*sn*-glycero-3-phosphocholine (DOPC) show liquid-disordered/liquid-ordered (Ld+Lo) phase coexistence of micron-sized domains, visible

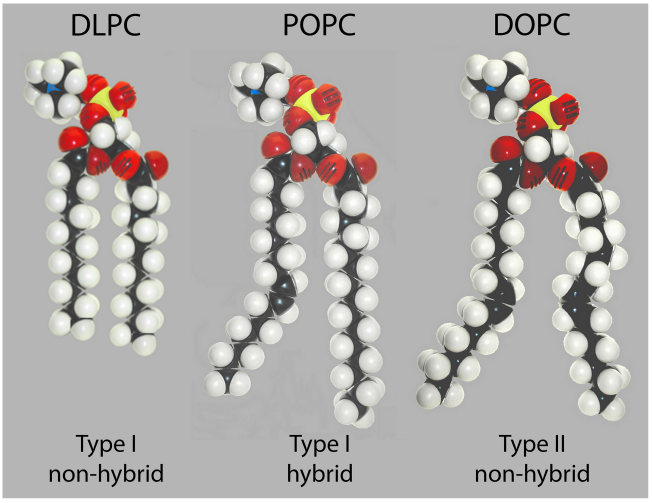

Figure 2.1. Classification of low-melting lipids.

with fluorescence microscopy over a range of composition and temperature (Type II behavior) [77, 78]. In contrast, where the low-T_M component is the hybrid lipid 1-palmitoyl-2-oleoyl-*sn*-glycero-3-phosphocholine (POPC) or 1-stearoyl-2-oleoyl-*sn*-glycero-3-phosphocholine (SOPC), visible domains are absent (Type I behavior) [79]. However, a variety of evidence in POPC- or SOPC-containing HLC mixtures points toward the existence of liquid domains that are smaller than the optical resolution limit of ~200 nm [80-84]. These observations have inspired a body of theoretical work connecting chain asymmetry to nanodomain formation [85-90]. In this model, the more- and less-ordered chains of hybrid lipids located near domain boundaries partition into the ordered and disordered phases, respectively. This preferential alignment is postulated to alleviate interfacial packing frustration, thereby lowering the energetic cost of domain perimeter. A unique "line-active" role for hybrid lipids is an appealing explanation for nanoscopic rafts, as animal cell membranes contain few symmetric low-T_M lipids, but an abundance of hybrid lipids.

HLC mixtures containing the non-hybrid, low-T_M lipid 1,2-dilauroyl-*sn*-glycero-3-phosphocholine (DLPC) exhibit Type I behavior [79, 91]. The existence of nanodomains in DLPC-containing mixtures cannot however be explained by the hybrid linactant hypothesis [91], raising the intriguing possibility that multiple independent mechanisms control raft size. Such mechanisms can be explored with titration experiments that incrementally replace Type I lipids with Type II lipids, revealing additional details of domain size and morphology transitions that can inform theory [92]. Previously, we found that progressive substitution of the hybrid Type I lipid POPC with the Type II lipid DOPC first increases nanodomain size (as revealed by small-angle neutron scattering, SANS), before inducing modulated phase patterns in a particular range of compositions, and ultimately the large, round domains characteristic of Type II behavior [8, 93, 94]. Spatially modulated phases have special

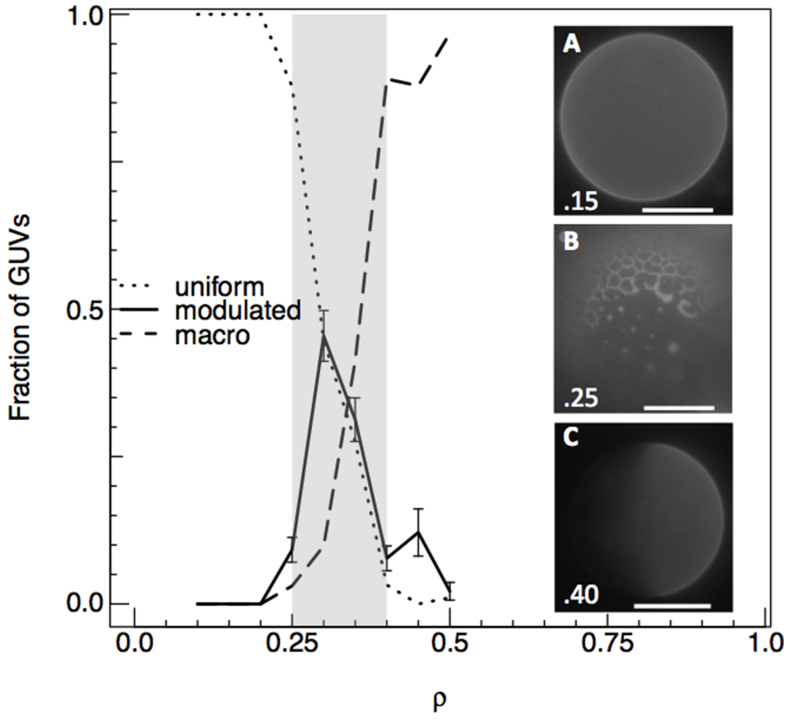

Figure 2.2. Fluorescence microscopy of GUVs shows a transition from nanoscopic to microscopic domains in a non-hybrid lipid mixture. GUVs exhibited either uniform appearance (*A*), modulated phase patterns (*B*), or round domains (*C*) that depended on the fraction of DOPC [$\rho \equiv \chi$DOPC/(χDLPC+χDOPC), values shown on images]. The fraction of all GUVs exhibiting these features is plotted *vs.* ρ for the composition DSPC/(DLPC+DOPC)/Chol = 0.35/0.40/0.25. Total GUV counts are enumerated in Table A1. Temperature 23 °C, scale bar 15 μm.

significance: they occur when line tension is balanced by competing interactions, for example curvature and/or dipole repulsion [95-97]. Here, we demonstrate an identical domain size and morphology transition for the non-hybrid lipid DLPC. Our observations strongly suggest a common mechanism by which hybrid and non-hybrid lipids reduce line tension.

We examined an HLC mixture containing 1,2-distearoyl-*sn*-glycero-3-phosphocholine (DSPC) as the high-T_M lipid. We generalize our previous notation [8, 93, 94] and define $\rho \equiv \chi$Type II/(χType I + χType II) to indicate the fractional replacement of DLPC by DOPC in the mixture. Fig. 2.2 shows representative

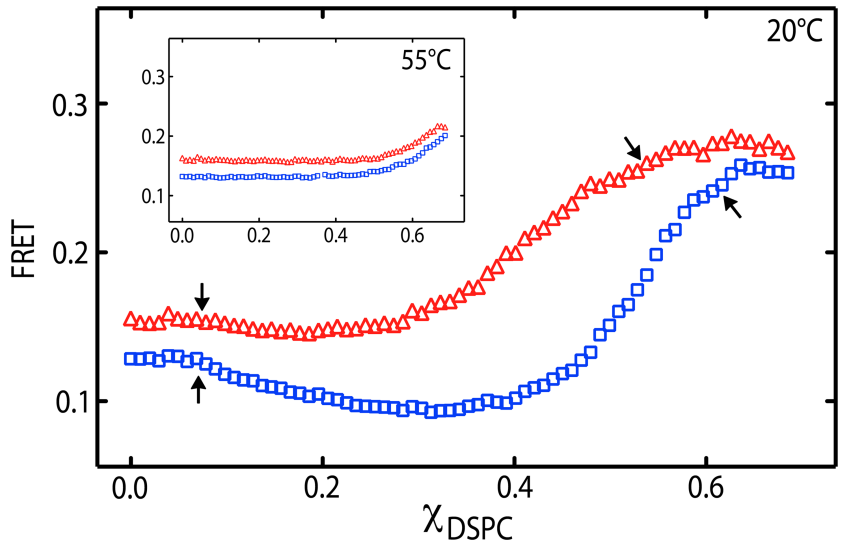

Figure 2.3. FRET reveals nanodomain formation in a non-hybrid lipid mixture. Sensitized acceptor emission is plotted *vs.* DSPC mole fraction for a sample trajectory (shown in Fig. A1) composed of DSPC/(DLPC+DOPC)/Chol, at ρ=0 (red triangles) and 0.25 (blue squares). Plots are offset by 0.02 y-units for clarity. Arrows mark phase boundaries where the trajectory crosses the Ld+Lo coexistence region (see Appendix A for details of boundary determination). Samples between the arrows show reduced FRET efficiency due to partition of DHE donor and BoDIPY-PC acceptor into Lo and Ld phases, respectively. *Inset*: the same samples measured at 55 °C, revealing gradual changes consistent with uniform mixing.

fluorescence micrographs of giant unilamellar vesicles (GUVs) with composition DSPC/(DLPC+DOPC)/Chol = 0.35/0.40/0.25. Three morphological categories were observed: (1) uniform appearance; (2) spatially modulated phase patterns; and (3) large, round domains. The fraction of vesicles exhibiting these morphologies is plotted *vs.* ρ in Fig. 2.2, revealing three distinct compositional regimes: (1) apparently uniform vesicles at $\rho < 0.25$; (2) modulated phases at $0.25 \leq \rho \leq 0.4$; and (3) round domains at $\rho > 0.4$. Similar results were obtained for other compositions within the Ld+Lo coexistence region (Table A2, Fig. A2). The domain size and morphology transition is consistent with an increase in line tension as DOPC replaces DLPC. Significantly, the results obtained for this non-hybrid mixture are essentially

indistinguishable from previous observations in the hybrid lipid mixture DSPC/(POPC+DOPC)/Chol at similar compositions (Table A4) [93, 94].

Next, we investigated compositions where GUVs appeared uniform (*i.e.*, $\rho < 0.25$), using techniques sensitive to nanometer length scales. We used Förster resonance energy transfer (FRET) to interrogate domain formation in paucilamellar vesicles (PLVs, vesicles with one to a few lamellae), as previously described [83]. Briefly, a sample trajectory that crosses a phase coexistence region (see Fig. A1) will exhibit a characteristic pattern of reduced FRET efficiency when fluorescent donor and acceptor lipids partition into different phases. In contrast, a sample trajectory that does not cross a phase boundary (*i.e.*, that remains in a single phase) will exhibit more gradual variation in FRET efficiency due to continuous changes in phase properties (*e.g.*, average molecular area). Fig. 2.3 shows FRET for the non-hybrid mixture DSPC/(DLPC+DOPC)/Chol at $\rho = 0$ and 0.25, for fluorescent donor and acceptor lipids that partition into ordered and disordered phases, respectively. A region of reduced FRET efficiency (RRE) is consistent with coexisting Lo and Ld phases, and the resulting segregation of donor and acceptor lipids. The smaller magnitude of the RRE for $\rho = 0$ indicates smaller domains for these compositions [83]. We also examined sample trajectories using a disorder-preferring donor and acceptor, which resulted in a characteristic region of enhanced FRET efficiency due to probe colocalization in Ld domains (Fig. A3). In both cases, FRET patterns in non-hybrid mixtures are remarkably similar to those observed in hybrid mixtures of DSPC/(POPC+DOPC)/Chol (Fig. A4) [83].

Finally, we used small-angle neutron scattering (SANS) to investigate nanoscopic domain formation in 60-nm diameter large unilamellar vesicles (LUVs), using methods described previously [8, 98]. Briefly, the average scattering length density (SLD) of the aqueous medium and vesicle were matched by adjusting their deuterium

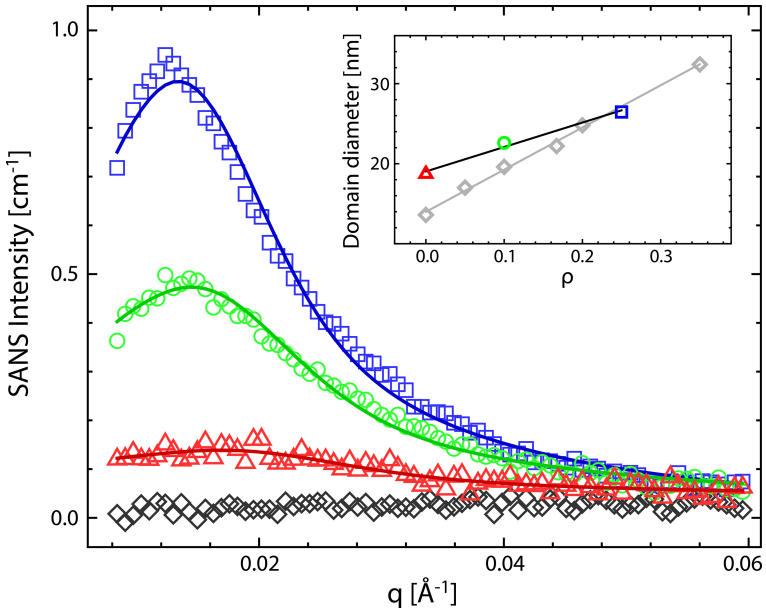

Figure 2.4. SANS reveals nanodomains in a non-hybrid lipid mixture. SANS intensity *vs.* momentum transfer vector *q* for LUVs composed of DSPC/(DLPC+DOPC)/Chol = 0.39/0.39/0.22 at 20 °C, for ρ=0 (red triangles), 0.1 (green circles), and 0.25 (blue squares), and a single-phase control sample composed of DSPC/DLPC/Chol = 0.325/0.325/0.35 (black diamonds). *Inset*: domain size *vs.* ρ determined from Monte Carlo modeling as described in the Appendix A (symbols as before). Also shown are domain sizes for DSPC/(POPC+DOPC)/Chol = 0.39/0.39/0.22 at 20 °C (gray diamonds) [8].

content using D2O and chain-perdeuterated DSPC, respectively (Appendix A). At the match point, the vesicle and surrounding water have no SLD contrast when lipids are randomly mixed, resulting in no coherent scattering. However, separation of high-melting and low-melting lipids generates in-plane contrast, which produces a scattering signal at length scales corresponding to the domain size. Fig. 2.4 shows scattering intensity *vs.* momentum transfer vector *q* for Ld+Lo compositions at ρ = 0, 0.1, and 0.25, as well as a single-phase control sample. At 20 °C, no scattering is observed in the control sample, whereas increased scattering is observed at $q < 0.06$ Å^{-1} for the Ld+Lo compositions. Raising the temperature to 55 °C eliminated the scattering in these samples (Fig. A5), indicating complete lipid mixing. Domain size was determined using a Monte Carlo analysis (Appendix A), and was found to

increase from 18 to 26 nm diameter as ρ increased from 0 to 0.25 at 20 °C (Fig. 2.4 inset, Table A4). The SANS results in these non-hybrid mixtures are qualitatively and quantitatively similar to observations in hybrid mixtures of DSPC/(POPC+DOPC)/ Chol [8].

Our results raise questions regarding mechanisms that control the formation and properties of liquid nanodomains in Type I mixtures. Several theories have been advanced to explain nanodomains, including: (1) competing interactions (CI), whereby coexisting liquid (Ld+Lo) phases below the mixture's critical temperature T_C possess a finite domain size determined by a balance between line tension favoring large domains, and an interaction favoring small domains [96, 97]; (2) Ising-like critical fluctuations (CF) above T_C [99-102]; (3) a curvature-induced microemulsion (CM), whereby a structured single phase above T_C arises from coupling between bilayer composition and curvature [103]; and (4) a hybrid-induced microemulsion (HM) above T_C, arising from special behavior of hybrid lipids located near domain interfaces [85-90]. Each theory predicts a different mechanism by which Type I lipids reduce liquid domain size. In the case of CI, the contribution of the Type I lipid to mechanical properties of the coexisting phases (*e.g.*, bilayer thickness, bending rigidity, spontaneous curvature, *etc.*) acts to reduce line tension and/or enhance the competing interaction [96, 97]. For CF, domains above T_C are described by a correlation length that scales with reduced temperature; the Type I lipid therefore contributes to domain size primarily through its effect on T_C [99-102]. For CM theory, the important property is the difference in spontaneous curvature between the high-T_M and Type I lipids [103]. Finally, in the case of HM theory, the crucial property is the asymmetric structure of the hybrid lipid's acyl chains [85-90].

The observation of composition-dependent nanodomains and modulated phases in both hybrid and non-hybrid mixtures presents new challenges for these theories.

Modulated phases are not accounted for by the simple two-dimensional Ising model of CF theory, and are predicted by CM theory to have anticorrelated composition across the bilayer midplane [103], contrary to fluorescence microscopy observations. CI and HM theories each predict correlated modulated phases and nanoscopic domains, yet CI-based simulations might require unphysically large bending moduli to produce modulated phases [97], and HM cannot account for the macroscopic size of modulated phases [90]. Furthermore, in HM theory, stripe-like composition fluctuations are a direct consequence of chain asymmetry, specifically the nearest-neighbor interactions of orientationally aligned hybrid lipids located at domain interfaces [90]. Given the striking similarities observed here for hybrid and non-hybrid mixtures, we conclude that chain asymmetry is not a unique agent for reducing line tension. However, we cannot exclude the possibility that symmetric lipids located near domain boundaries act *via* a "hybrid-like" mechanism, whereby nominally identical chains interact differently with adjacent phases to alleviate packing frustration or thickness mismatch. Such interfacial phenomena, as well as contrasts in phase material properties, are likely to play a role in the stabilization of nanoscopic and modulated phases. A unified treatment of the full domain morphology transition observed in four-component mixtures may shed new light on the relative contributions of these or other, as yet unidentified interactions.

We have presented three types of experimental data demonstrating changes in domain size and morphology in HLC mixtures containing only non-hybrid lipids. Comparing our present results with previous results using the hybrid lipid POPC [8, 83, 93, 94], we find nanoscopic domains of similar size in both mixtures. Replacing the Type I lipid (DLPC or POPC) with DOPC increases the size of these domains. In both hybrid and non-hybrid four-component mixtures, modulated phase patterns form within a similar composition range, and then transition to large, round domains. These

results suggest a common mechanism by which hybrid and non-hybrid Type I lipids reduce line tension. It is therefore reasonable to place DLPC in the category of Type I lipids that includes POPC and SOPC: for these lipids, line tension is sufficiently low that the additional boundary energy associated with multiple small domains is balanced by a competing, repulsive interaction between domains.

CHAPTER 3
BILAYER MECHANICAL PROPERTIES

3.1 Determination of bending rigidity and tilt modulus of lipid membranes from real-space fluctuation analysis of molecular dynamics simulations*

3.1.1 Abstract

We have recently developed a novel computational methodology (termed RSF for Real-Space Fluctuations) to quantify the bending rigidity and tilt modulus of lipid membranes from real-space analysis of fluctuations in the tilt and splay degrees of freedom as sampled in molecular dynamics (MD) simulations. In this article, we present a comprehensive study that combines results from the application of the RSF method to a wide range of lipid bilayer systems that encompass membranes of different fluidities and sizes, including lipids with saturated and unsaturated lipid tails, single and multi-component lipid systems, as well as non-standard lipids such as the four-tailed cardiolipin. By comparing the material properties calculated with the RSF method to those obtained from experimental data and from other computational methodologies, we rigorously demonstrate the validity of our approach and show its robustness. This should allow for future applications of even more complex lipidic assemblies, whose material properties are not tractable by other computational techniques. In addition, we discuss the relationship between different definitions of the tilt modulus appearing in current literature to address some important unresolved discrepancies in the field.

* The following subsection is reproduced from: Doktorova, M., Harries, D., & Khelashvili, G. 2017. *Physical Chemistry Chemical Physics*, *19*(25), 16806-16818 with permission from the PCCP Owner Societies. It has been modified to fit the format of the thesis. MD performed and analyzed all simulations.

3.1.2 Introduction

Among the various ways that the lipid environment can regulate the function and organization of membrane proteins, the material (elastic) properties of lipid membranes and their modulation have justifiably taken center stage [104, 105]. Dependent sensitively on lipid composition, these properties determine the extent of membrane resistance to different modes of deformation, including membrane curvature and lipid tilt. As such, lipid material properties can directly influence the energetics of membrane reshaping during many cellular processes that require partitioning of proteins in specialized functional lipid domains (e.g., fusion and endocytosis [104]). Once proteins enter these domains, their conformational dynamics can be further affected by the energetic cost associated with deformations of the local lipid environment, as the membrane responds to protein conformational transitions [61, 106].

Given the importance of the bilayer material properties to its biological function, several methodologies have been implemented to probe and follow them *in vitro* and *in silico*. The quantitative framework for these methodologies is most often based on the Helfrich-Canham-Evans theory of elasticity [107], which treats a lipid bilayer as a two-dimensional incompressible, continuum, elastic medium. Under these conditions, and assuming small deformations, the free energy contributions of various modes of membrane elasticity can be approximated by a quadratic function of the relevant deformation.

Membrane bending rigidity, in particular, has generated considerable interest due to the direct implications of bilayer curvature to protein-membrane interactions [61]. The two most common experimental techniques for measuring the bilayer's rigidity, flicker spectroscopy [108-111] and micropipette aspiration [112-115], require the use of giant unilamellar vesicles (GUVs). Less frequently used are electrodeformation of

GUVs [116, 117] and scattering techniques including low angle diffuse X-ray scattering from multibilayer stacks [118, 119] and neutron spin-echo (NSE) analysis of large unilamellar vesicles (LUVs) [120, 121]. Flicker spectroscopy involves analysis of Fourier modes of the fluctuation spectra measured at the GUV equator using video microscopy, and generally produces bending rigidity values that are higher in magnitude compared with other methods [7, 122, 123]. Micropipette aspiration and electrodeformation, on the other hand, quantify bending rigidity from the linear relationship between tension and area expansion of the GUVs in the low tension regime, where thermal undulations are smoothed by increasing tension [112, 122]. The difference between the two techniques is that in the former tension is applied to the GUV surface through suction pressure, while in the latter it is applied through electrostatic stresses induced by an external electric field. Information on bilayer thermal fluctuations is also encoded in the static scattering signature, or form factor, of oriented bilayer stacks measured with X-ray diffraction [118]. The corresponding analysis is model-based and produces bending rigidities similar to those obtained from GUV pipette aspiration [124]. An alternative dynamic technique, NSE, is characterized by correlation times and length scales that are very similar to those of membrane thermal fluctuations, and measures bending rigidity from neutron scattering as a function of Fourier time [125]. A detailed description of these experimental methods can be found in Ref. [126].

These experimental approaches have been recently complemented by computational methods, based on both mean-field level theory [2], and on atomistic (or coarse-grained) molecular dynamics (MD) simulations [127-133]. The quantitative framework for these computational methodologies is based on the generalized "Helfrich Hamiltonian" in which contributions associated with the free energy of bending (splay distortion) and Gaussian curvature from the original Helfrich

formulation are supplemented by additional deformation modes, such as area compression/expansion, lipid tilt, and lipid twist. In the context of this work, we focus our discussion on two major contributions to the bilayer deformation free energy related to the tilt and bending deformations, and express them as:

$$f_t = \frac{1}{2}\kappa_t\langle\vec{t}\rangle^2 = \frac{1}{2}\kappa_t\langle\frac{\vec{n}}{\vec{n}\cdot\vec{N}} - \vec{N}\rangle^2. \quad (3.1.1)$$

$$f_b = \frac{1}{2}\mathrm{K}_C\langle S\rangle^2 = \frac{1}{2}K_C\langle\Delta\vec{n} - \nabla\vec{N}\rangle^2. \quad (3.1.2)$$

In the above, f_t and f_b are the quadratic approximations for the free energies associated with monolayer tilt and bending, respectively. We represent the lipid tilt vector as $\vec{t}$, lipid splay is S, and $\vec{n}$ and $\vec{N}$ unit vectors denote, respectively, the local lipid director and the local normal to the lipid-water interface. In these relations, κ_t and K_C are coefficients representing the thermodynamic tilt modulus and the bending rigidity, correspondingly, per unit area, the $\langle\rangle$ brackets denote a thermodynamic ensemble average, and $\langle\cdot\rangle^2$ in Eq. 3.1.1 represents the dot product. The full derivation of Eqs. 3.1.1-3.1.2 from the Hamiltonian of a monolayer under deformations can be found in Ref [134].

Using Eq. (1), κ_t was previously obtained based on mean field theory of lipid chain packing [2] by computing the mean-square fluctuations in lipid tilt. The approach suggested a range of values ~ 0.1–0.2 $k_BT/Å^2$ for a typical lipid monolayer (k_B represents the Boltzmann constant, and T is temperature), equivalent to ~ 4.0–8.0 $\times 10^{-20}$ J/nm^2 per monolayer at room temperature.

The extraction of the elastic moduli from atomistic MD simulations in recent decades has relied on sampling thermally excited fluctuations in the bilayer shape during the course of the MD trajectory (reviewed in [132]). These undulations are then Fourier transformed into reciprocal space using the two-dimensional reciprocal space vector, $\vec{q}$. Thus, the bending rigidity, for example, can be obtained from the spectral

analysis in the limit of small-q modes. However, dependence on robust sampling of global bilayer undulations has restricted the spectral analysis method to relatively large membrane systems (~1000 lipids or larger). Yet, recent modifications of this approach to sample in reciprocal space the fluctuations in lipid tilt vectors instead of undulations of membrane shape have allowed the application of the method to rather small membrane patches (~400 lipids) [130]. In addition, the spectral analysis technique enabled determination of the so called theoretical tilt modulus, κ_t^0, which is related, yet not identical, to the thermodynamic tilt modulus κ_t in Eq. 1 (see more below).

Importantly, thus far, results from the reciprocal space method have only been reported for single component fluid lipid bilayers where the method yields bending moduli values that are in good agreement with experiments [132]. However, the method is yet to be validated for mixtures of lipids, as well as for lipidic assemblies of different curvatures and different levels of fluidity and stiffness, such as cholesterol-enriched liquid ordered phases.

We have developed an alternative computational approach that is also based on analysis of MD simulations but which calculates the thermodynamic tilt modulus and bending rigidity by analyzing the fluctuations in the tilt and splay degrees of freedom as sampled in the MD trajectories in *real* space. As described in depth elsewhere [135-137] and highlighted below, this real-space fluctuation (RSF) analysis is local in nature, and therefore overcomes several limitations inherent in the Fourier space methodology. Thus, the RSF method typically only requires as input an MD trajectory of a rather small size lipid system (~100 lipids in the case of single-component bilayers), and has been extended to complex multi-component lipid bilayers, including liquid ordered membrane systems consisting of cholesterol in complex with several types of lipids (saturated or unsaturated). Importantly, a recent generalization of the

methodology [135] (see below) not only enabled extensions to lipid assemblies with high curvatures (e.g. hexagonal phases), but also allowed a more accurate determination of the bending and tilt moduli for lamellar membrane systems.

In this article, we present a comprehensive study that combines results from the application of this generalized RSF method to a range of lipid bilayer systems, such as single-component membranes (containing saturated or unsaturated lipids, as well as hybrid lipids with combinations of saturated and unsaturated tails), mixtures of several lipids, including cholesterol-containing systems, and various size lipid membranes (from 128 to 1600 lipid-size patches). Where available, the material properties calculated with our method are compared to those obtained from experimental data and other computational methodologies. This comparison further allowed us to address some unresolved discrepancies related to the different definitions of the tilt modulus that appear in current literature. In the following, we first briefly summarize the theoretical aspects of the RSF method highlighting the recent enhancements to the approach (the full mathematical formulation of the RSF methodology can be found in [135]), and then describe recent results that emerge from implementing this methodology.

3.1.3 Methods

3.1.3.1 Theoretical aspects of the RSF method

In the RSF analysis, the field of vectors normal to the membrane plane, $\vec{N}$, is first derived from the time-averaged shape of the lipid-water interface obtained from a well-equilibrated MD trajectory [135, 138, 139]. Then, fluctuations of tilt and splay degrees of freedom are sampled around this average shape. The director vector $\vec{n}$ for a lipid is defined as the vector pointing from the tail of the lipid to its head (the specific choice of the atoms for constructing $\vec{n}$ is dictated by the type of force-field used in the

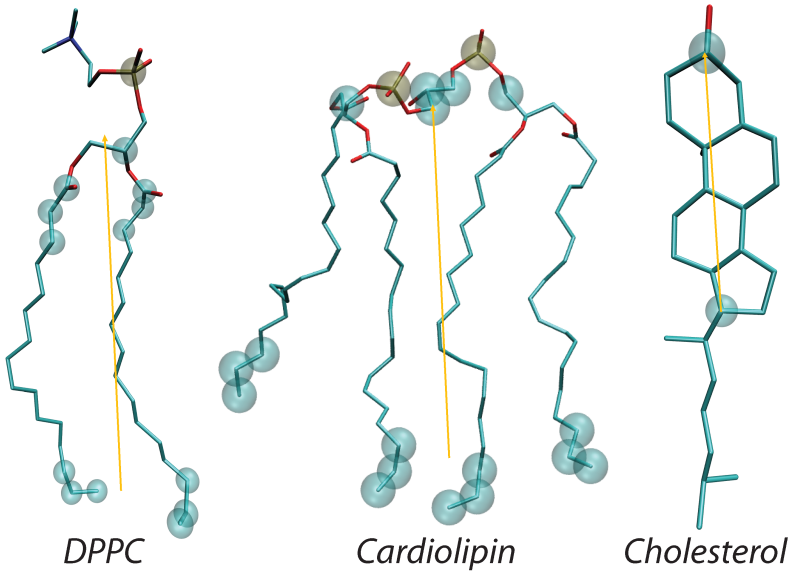

Figure 3.1.1. Structures of all-atom DPPC lipid (*left*), cardiolipin (*middle*), and cholesterol (*right*) molecules highlighting positions of the atoms (in transparent spheres) used for definition of local director vector (yellow). For all-atom systems, the following set of atoms (in CHARMM36 force-field notations) are used: for standard two-tail phospholipids, the director vector connects the center of mass (COM) of the head-group region (defined by P, C2, C21, C22, C23, C31, C32, C33 atoms) to the COM of the last three terminal carbons in each lipid tail. For cardiolipin, the director vector joins the COM of the two phosphates (P1 and P3 atoms), the two carbon atoms attached to each of the PO4 moieties (C1, C3, C11, C31 atoms) and the central carbon atom connecting them (C2 atom), and the center of mass of the last three carbon atoms of all four chain. For cholesterol, the director vector connects C3 and C17 atoms on the ring.

MD simulations to represent the lipid species, i.e. all-atom vs. coarse-grained, and the type of lipid, see Fig. 3.1.1; also see Fig. 1B in Ref. [138, 139] and Fig. S2 in Ref. [135] for a visualization of the vector fields).

Assuming independence of lipid tilt and splay degrees of freedom, we express the probabilities of lipid tilts and splays as Boltzmann distributions:

$$P(\vec{t}) = C_t \exp\left(-\frac{\kappa_t \vec{t}^2 A_l}{2k_B T}\right) = C_t \exp\left(-\frac{1}{2k_B T}\kappa_t \left(\frac{\vec{n}}{\vec{n}\cdot\vec{N}} - \vec{N}\right)^2 A_l\right) \quad (3.1.3)$$

$$P(S) = C_s \exp\left(-\frac{K_C S^2 A_l}{2k_B T}\right) = C_s \exp\left(-\frac{1}{2k_B T} K_C \left(\Delta\vec{n} - \overline{\nabla\vec{N}}\right)^2 A_l\right). \quad (3.1.4)$$

In the above, A_l represents the area per lipid, and C_t and C_s are normalization constants. Eqs. (3.1.3-3.1.4) can be re-written as:

$$-\frac{2k_BT}{A_l}\ln P(\vec{t}) = \kappa_t\left(\frac{\vec{n}}{\vec{n}\cdot\vec{N}} - \vec{N}\right)^2 + C_t' \tag{3.1.5}$$

$$-\frac{2k_BT}{A_l}\ln P(S) = K_C\left(\Delta\vec{n} - \overrightarrow{\nabla N}\right)^2 + C_s'. \tag{3.1.6}$$

From the above, the thermodynamic tilt modulus κ_t and bending rigidity K_C can be obtained by constructing the distributions of tilts and splays in the simulations and fitting a quadratic function to the left-hand side of Eqs. (5-6) in the regime of small splay and tilt angles. Thus, κ_t and K_C will emerge as the coefficients of the quadratic term of the best fit [135].

To proceed with the tilt modulus calculation, it is convenient, for numerical purposes, to assume the limit of small angle θ between the $\vec{n}$ and $\vec{N}$ unit vectors, so that (see also Eq. 3.1.1) [2, 140]:

$$\vec{t}^2 = \left(\frac{\vec{n}}{\vec{n}\cdot\vec{N}} - \vec{N}\right)^2 = \frac{1}{\cos^2\theta} - 1 = \tan^2\theta \approx \theta^2.$$

Note that this limit is equivalent to the small-deformation limit, which is also the assumption that allows the neglect of higher order terms in Eq.3.1.1. Then, from Eq. 3.1.5 we can use $P(\theta)$ to write the probability of finding a lipid with its director vector at an angle θ with the local normal vector, as:

$$-\frac{4k_BT}{A_l}\ln\left(\frac{P(\theta)}{\sin\theta}\right) = \kappa_t\theta^2 + B. \tag{3.1.7}$$

In the above, the $\sin\theta$ factor accounts for the degeneracy of microstates for a particular value of θ (i.e. the number of states accessible to a vector undergoing precession around an axis while maintaining constant polar angle θ with respect to this axis is equal to $\sin\theta$) [140], and B is the normalization constant. Using Eq. 3.1.7, κ_t can be obtained from the $P(\theta)$ distribution by fitting the left-hand-side expression to a quadratic function. Note that this expression in Eq. 3.1.7 contains an additional factor of 2 in comparison to Eq. 3.1.5. This follows from the fact that for laterally isotropic systems (such as lipid monolayers in the liquid state) the tilt modulus is strictly a two-dimensional diagonal tensor with κ_t representing the diagonal contributions (along the *x or y* axes of the lateral plane) of this tensor, $\kappa_t = \kappa_t^{xx} = \kappa_t^{yy}$ [2]. Noting that the sum of two random variables each with Gaussian distribution of variance σ^2 is a random variable with a Gaussian distribution with variance $2\sigma^2$ [135], the change in variables from $\vec{t}^2$ to the scalar θ, therefore, leads to the additional factor that appears in Eq. 3.1.7.

Following a procedure similar to that described above for calculating the tilt modulus, one can obtain the bending rigidity K_C from Eq. 3.1.6 by first approximating S by $(\nabla \cdot \alpha)^2$, where α is the angle formed by the directors of neighboring lipids, and then constructing probability distributions $P(\alpha)$ for all possible pairs of lipids in the system. As we discussed earlier [135], this formulation is only strictly valid in the regime of small tilt and splay angles, in the absence of lipid twist, and assuming, on average, the same distance between neighboring lipids. To overcome these restrictions, we have recently generalized the formulation to include a direct numerical calculation of the $\nabla(\vec{n} - \vec{N})$ divergence that appears in Eq. 3.1.6. To this end, we follow a procedure described in detail in Ref. [135] and introduce S_i – the covariant derivative of the vector field $(\vec{n} - \vec{N})$ at point $\vec{p}$ on the membrane surface and along one direction on the membrane interface:

$$S_i(\vec{p}) = \lim_{h \to 0} \frac{n_i(\vec{p} + h\vec{e}) - n_i(\vec{p}) + N_i(\vec{p} + h\vec{e}) - N_i(\vec{p})}{h}. \tag{3.1.8}$$

In the above, $\vec{e}$ is a unit vector tangent to the membrane, h is the distance between the lipids, and $n_i(\vec{p})$ and $N_i(\vec{p})$ are the components of the lipid director and membrane normal vector fields, respectively, along $\vec{e}$.

It can then be shown [135] that the S_i-s are independent variables, so that we can write their probability distributions as

$$P(S_i) = C \exp\left(-\frac{K_C S^2 A_l}{2k_B T}\right) \tag{3.1.9}$$

from which we obtain

$$-\frac{2k_B T}{A_l} \ln P(S_i) = K_C (S_i)^2 + C'. \tag{3.1.10}$$

Therefore, the bending rigidity K_C can be obtained from $P(S_i)$ by fitting a quadratic function to the left-hand-side of Eq. 3.1.10.

It must be noted that, according to Eqs. 3.1.1 and 3.1.2, κ_t and K_C represent the monolayer tilt modulus and bending rigidity, respectively, for single-component lipid membranes where only one type of lipid can contribute to the tilt and splay degrees of freedom. For mixtures of lipids, the above formulation allows calculation of a tilt modulus for each lipid species and splay moduli for all possible pairs of lipids. Then, κ_t and K_C for the entire membrane can be obtained using the following empirical phenomenological expressions (see details in Ref. [137]):

$$\frac{1}{\kappa_t^l} = \frac{1}{N_{tot}} \sum_i \frac{N_i}{\kappa_t^{li}}. \quad (3.1.11)$$

$$\frac{1}{K_C} = \frac{1}{\phi_{tot}} \sum_{i,j} \frac{\phi_{ij}}{K_C^{ij}} \quad (3.1.12)$$

where $\kappa_t^l = \kappa_t A_l$ denotes tilt modulus per lipid, κ_t^{li} is tilt modulus for i^{th} lipid species, K_C^{ij} represents splay modulus for lipid pair (i, j), N_i denotes the number of lipids of type i, N_{tot} is the total number of lipids, ϕ_{ij} represents the number of near neighbor (i, j) lipid pairs sampled in the MD trajectory (within the cutoff distance), and ϕ_{tot} is the number of all the lipid pairs sampled. The area per molecule, A_l, for lipid mixtures is taken as the area of the unit simulation cell in the membrane plane divided by the total number of lipids per leaflet. Additional details of the RSF method and full derivations are presented in Ref. [135].

3.1.3.2 Molecular dynamics simulations

All-atomistic molecular dynamics (MD) simulations were carried out on a number of single and multi-component lipid membranes, as listed in Table 3.1.1. All systems were built with the CHARMM-GUI web server [141-144] (see details in Table 3.1.1) and the majority of them were equilibrated using the standard multi-step equilibration protocol provided by CHARMM-GUI. The only exceptions were POPC/POPS, POPC/POPS/Chol, the large POPC, POPE/POPS and POPC/PSM bilayers (see Table 3.1.1 caption for lipid definitions) which, after the initial bilayer construction were energy minimized up to 10,000 steps, then simulated with a 1 fs time step for 500 ps. After these initial equilibration phases, all systems were subjected to long MD simulations (for simulation times see Table 3.1.1).

Table 3.1.1. Lipid bilayer systems studied with atomistic MD simulations. Given are: composition of the membranes; temperature (T), total number of lipids in each system, number of water molecules per lipid, concentration of ionic solution; simulation times (total and analyzed trajectories per each system); area per lipid resulting from the simulations with corresponding standard errors calculated from consecutive 20 ns blocks; references for the corresponding experimentally determined areas per lipid compared to the simulation values in Fig. 3.1.2. For several lipid compositions two independent simulations were carried out with different system sizes (denoted by superscripts "*a*" and "*b*"). Lipid name abbreviations used are as follows: *POPC* – 1-palmitoyl-2-oleoyl-*sn*-glycero-3-phosphocholine; *POPE* – 1-palmitoyl-2-oleoyl-*sn*-glycero-3-phosphoethanolamine; *DLPC* – 1,2-dilauroyl-*sn*-glycero-3-phosphocholine; *DPPC* – 1,2-dipalmitoyl-*sn*-glycero-3-phosphocholine; *SOPC* – 1-stearoyl-2-oleoyl-*sn*-glycero-3-phosphocholine; *DOPC* – 1,2-dioleoyl-*sn*-glycero-3-phosphocholine; *DEPC* – 1,2-dielaidoyl-*sn*-glycero-3-phosphocholine; *TOCL* – 1′,3′-bis[1,2-dioleoyl-*sn*-glycero-3-phospho]-*sn*-glycerol (or tetraoleoyl cardiolipin); *DMPC* – 1,2-dimyristoyl-*sn*-glycero-3-phosphocholine; *DLiPC* – 1,2-dilinoleoyl-*sn*-glycero-3-phosphocholine; *POPG* – 1-palmitoyl-2-oleoyl-*sn*-glycero-3-phospho-(1'-*rac*-glycerol); *POPS* – 1-palmitoyl-2-oleoyl-*sn*-glycero-3-phospho-L-serine; *Chol* – cholesterol; *PSM* – N-palmitoyl-D-*erythro*-sphingosyl-phosphorylcholine (or palmitoyl sphingomyelin).

Bilayer	T (°C)	# of lip.	waters per lipid	salt (mM)	simulation time (ns)		A_{lip}^{sim} (Å^2)	A_{lip}^{sim} Ref.
					total	analysis		
POPC [a]	25	416	45	-	520	120	64.6 ± 0.2	[145, 146]
POPC [b]	25	200	70	140	226	123	64.4 ± 0.4	
POPE	55	200	45	-	190	102	60.9 ± 0.2	[147]
DLPC	30	128	45	-	278	120	62.8 ± 0.1	[145, 148]
DPPC	50	200	45	-	335	142	61.2 ± 0.3	[145, 149]
SOPC	25	200	45	-	490	124	63.8 ± 0.3	[145, 150]
DOPC	25	200	45	-	523	126	68 ± 0.1	[149, 151, 152]
DEPC	25	200	45	-	680	92	64.4 ± 0.2	
TOCL	30	100	60	140	310	150	130.3 ± 0.3	[153]
DMPC	30	128	50	140	200	100	60.3 ± 0.1	[145, 148]
DLiPC	25	200	45	-	278	140	70.3 ± 0.1	
DOPG	25	200	60	140	246	122	71.4 ± 0.2	[154]
DPPC/Chol 80:20	25	200	45	-	384	90	40.7 ± 0.1	
POPE/POPG 70:30 [a]	37	1600	60	-	150	80	60.6 ± 0.1	
POPE/POPG 70:30 [b]	37	200	60	-	280	117	61.1 ± 0.3	
POPC/POPS 70:30	20	140	45	50	191	100	60.9 ± 0.1	
POPC/POPS/ Chol 34:30:36	20	200	45	50	270	180	43.5 ± 0.2	
POPE/POPS 70:30 [a]	25	420	82	-	690	140	55.5 ± 0.1	
POPE/POPS 70:30 [b]	25	200	70	140	208	129	55.6 ± 0.3	
POPC/PSM 70:30 [a]	25	400	45	-	517	103	59.9 ± 0.1	
POPC/PSM 70:30 [b]	25	200	70	140	229	126	59.6 ± 0.1	

All simulations were carried out with NAMD versions 2.7-2.10 [155] and using the CHARMM36 force field for lipids and ions [156]. The simulations implemented the *rigidbonds all* option allowing for 2 fs time step, *vdwForceSwitching* option, PME for electrostatic interactions, and were carried out in the NPT ensemble under semi-isotropic pressure coupling conditions, at temperatures listed in Table 3.1.1. The Nose-

Hoover Langevin piston algorithm was used to control the target P = 1 atm pressure. For the POPE/POPG and DMPC bilayers, the *LangevinPistonPeriod* was set to 50 fs and *LangevinPistonDecay* was set to 25 fs. For all other bilayers *LangevinPistonPeriod* was set to 200 fs and *LangevinPistonDecay* was set to 50 fs. The van der Waals interactions were calculated by applying a cutoff distance of 12 Å and switching the potential from 10 Å. All simulations were performed on local computational resources as well as on the resources provided by XSEDE [157].

To build the DEPC bilayer, we first constructed a DOPC bilayer with CHARMM-GUI, then applied a home source tcl script to flip all double bonds between the C9 and C10 atoms on both chains of the lipids from *cis* to *trans* isomerization. The standard equilibration protocol provided from CHARMM-GUI was subsequently used by changing the constraint of the dihedral angle between the C8-C9-C10-C11 atoms to be 180 degrees (corresponding to *trans* isomerization), instead of 0 degrees (corresponding to *cis* isomerization).

3.1.3.3 Application of the RSF method to MD trajectories

For the RSF analysis we used a set of computational modules documented in detail in Refs. [138, 139] and freely available online at https://github.com/njohner/ost_pymodules/. This utility extracts $P(\theta)$ and $P(S)$ distributions from MD simulations by first aligning the analyzed trajectories, and then generating normal $\vec{N}$ and director $\vec{n}$ vector fields using molecular definitions described earlier ([138, 139]). In particular, for all standard two-tail lipids, the director vector joins the center of mass of the last three carbon atoms of each chain to the center of mass of the phosphate and backbone carbon atoms (see Fig. 3.1.1). For cardiolipin, which possesses four hydrocarbon lipid chains, the director vector joins the center of mass of the two phosphates, the two carbon atoms attached to each of the PO4

moieties and the central carbon atom connecting them, and the center of mass of the last three carbon atoms of all four chains. The director vector for cholesterol (Chol) connects C3 and C17 atoms (see Fig. 3.1.1).

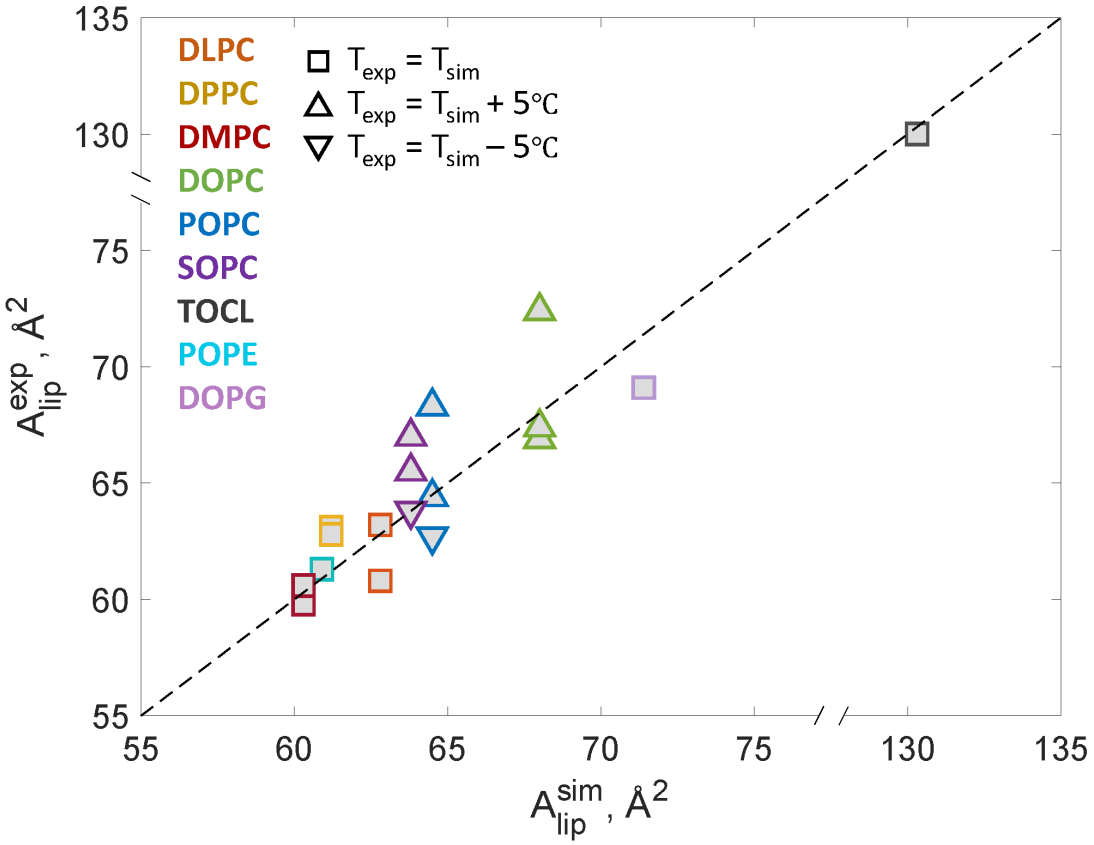

Figure 3.1.2. Experimentally measured area per lipid (A_{lip}^{sim}) is plotted vs. area per lipid determined from the atomistic MD simulations (A_{lip}^{sim}) for various single-component lipid membranes from Table 3.1.1. The data points follow near linear $f(x)=x$ relationship (dashed line) indicating that the MD simulations are well-converged. For lipid abbreviations please see Table 3.1.1 caption and for literature references see Table 3.1.1.

As described previously [135, 137], we restrict the calculation of splays to pairs of lipids that are near-neighbors, to maintain the validity of the numerical calculation of the lipid splay (Eq. 3.1.8) and to ensure that splays are independent. As before, we

used h<10Å for the distance cut-off of all systems except for the cardiolipin membrane. Since this lipid is about twice as large as a typical phospholipid, we reasoned that 10Å cut-off would likely be too short for numerical accuracy of splay calculations. Thus, we evaluated the organization of cardiolipin molecules in the bilayer and compared it to that of DOPC lipids by means of their radial distribution functions (RDFs). The coordination number of DOPC calculated from the integral of the RDF at the default cut-off distance of 10Å was 3.6. The same coordination number for TOCL was reached at 14Å which was therefore set as the respective distance cut-off for the analysis of the cardiolipin bilayer.

Once $P(\theta)$ and $P(S)$ distributions were constructed, fitting of the quadratic functions was performed and κ_t and K_C were obtained according to Eqs. 3.1.7 and 3.1.10. Note that, for the tilt modulus the software outputs $2\kappa_t A_l$ or what could be described as the tilt modulus per bilayer, in units of k_BT. K_C is outputted per monolayer and has units of k_BT.

3.1.4 Results and discussion

The all-atom lipid membrane systems for which bending rigidity and tilt modulus were calculated in the current work encompass membranes of different fluidities and sizes, include lipids with saturated and unsaturated lipid tails, single and multi-component lipid mixtures, as well as non-standard lipids such as cardiolipin which contains four hydrocarbon lipid tails. The wide range of physico-chemical properties represented in these membrane systems allows us to rigorously demonstrate the general applicability of the RSF method.

Since the RSF analysis requires well-equilibrated MD trajectories, we first confirmed that our simulations protocol, simulations times, and force-fields used produced well-behaved membranes by calculating the area per lipid (A_{lip}^{sim} in Table

3.1.1) for each system and comparing the values to experimentally determined A_{lip}^{sim} reported in the literature. All experimental values come from scattering experiments and the variability among these can be attributed to differences in the underlying models used for data analysis (e.g. independent or joint analysis of neutron and X-ray scattering datasets [149]). As shown in Fig. 3.1.2, experimentally and computationally derived areas are in excellent agreement, confirming that the lipid packing in the simulations was well converged.

Table 3.1.2. Bending rigidity (K_C) values calculated from the RSF analysis of the MD simulations. The data are shown for each leaflet and for the bilayer. Error bars were calculated as described previously [135, 138, 139], by obtaining PMFs using four different fitting ranges and calculating the standard deviation. For lipid abbreviations please see Table 3.1.1 caption.

Bilayer	$\boldsymbol{K_C}$ (k_BT)		
	top leaflet	bottom leaflet	bilayer
POPC [a]	12.3 ± 0.5	12 ± 0.4	24.3
POPC [b]	12.9 ± 0.5	12.4 ± 0.6	25.3
POPE	14.5 ± 0.4	14.9 ± 0.6	29.4
DLPC	13.4 ± 0.6	12.4 ± 0.5	25.8
DPPC	17.4 ± 0.9	16.7 ± 0.7	34.1
SOPC	13.2 ± 0.5	13.2 ± 0.5	26.4
DOPC	9.5 ± 0.3	8.8 ± 0.1	18.3
DEPC	12.1 ± 0.4	12.1 ± 0.4	24.2
TOCL	16.2 ± 0.6	15.9 ± 0.3	32.1
DMPC	17.4 ± 0.9	17.3 ± 0.8	34.7
DLiPC	7.9 ± 0.1	8.4 ± 0.3	16.3
DOPG	7.9 ± 0.2	7.5 ± 0.2	15.4
DPPC/Chol 80:20	66.1 ± 2.1	63.9 ± 1	130.0
POPE/POPG 70:30 [a]	14.1 ± 0.3	14.5 ± 0.4	28.6
POPE/POPG 70:30 [b]	14.7 ± 0.4	14.2 ± 0.3	28.9
POPC/POPS 70:30	16.7 ± 0.7	14 ± 0.4	30.7
POPC/POPS/Chol 34:30:36	28.6 ± 0.4	33.5 ± 0.5	62.1
POPE/POPS 70:30 [a]	20.8 ± 0.5	19.7 ± 0.4	40.5
POPE/POPS 70:30 [b]	20.2 ± 0.5	20.6 ± 0.5	40.8
POPC/PSM 70:30 [a]	15.7 ± 0.3	16.8 ± 0.5	32.5
POPC/PSM 70:30 [b]	17.3 ± 0.6	16.9 ± 0.5	34.2

Table 3.1.3. Thermodynamic tilt modulus (κ_t) values calculated from the RSF analysis of the MD simulations. The data are shown for each leaflet and for the bilayer. Error bars were calculated as described previously [135, 138, 139], by obtaining PMFs using four different fitting ranges and calculating the standard deviation. For lipid abbreviations please see Table 3.1.1 caption.

Bilayer	κ_t ($\times 10^{-20}$ J/nm^2)		
	top leaflet	bottom leaflet	bilayer
POPC [a]	4.07 ± 0.032	4.07 ± 0.032	8.15
POPC [b]	4.15 ± 0.013	4.09 ± 0.032	8.24
POPE	5.80 ± 0.074	5.91 ± 0.074	11.71
DLPC	4.13 ± 0.067	4.13 ± 0.067	8.26
DPPC	5.43 ± 0.073	5.43 ± 0.036	10.85
SOPC	4.35 ± 0.064	4.29 ± 0.032	8.64
DOPC	3.33 ± 0.030	3.30 ± 0.001	6.62
DEPC	4.05 ± 0.032	4.02 ± 0.032	8.08
TOCL	3.75 ± 0.032	3.63 ± 0.002	7.38
DMPC	4.85 ± 0.035	4.85 ± 0.001	9.71
DLiPC	3.04 ± 0.003	3.13 ± 0.029	6.17
DOPG	3.00 ± 0.029	2.71 ± 0.058	5.70
DPPC/Chol 80:20	13.79 ± 0.202	11.17 ± 0.606	24.96
POPE/POPG 70:30 [a]	5.22 ± 0.035	5.19 ± 0.035	10.41
POPE/POPG 70:30 [b]	5.36 ± 0.070	5.29 ± 0.035	10.64
POPC/POPS 70:30	5.51 ± 0.100	4.78 ± 0.033	10.29
POPC/POPS/Chol 34:30:36	12.41 ± 0.139	13.20 ± 0.139	25.61
POPE/POPS 70:30 [a]	7.26 ± 0.074	7.19 ± 0.037	14.45
POPE/POPS 70:30 [b]	7.58 ± 0.111	7.66 ± 0.074	15.24
POPC/PSM 70:30 [a]	5.53 ± 0.069	5.36 ± 0.103	10.88
POPC/PSM 70:30 [b]	5.66 ± 0.069	5.76 ± 0.104	11.42

In Tables 3.1.2 and 3.1.3 we report bending rigidity (K_C) and thermodynamic tilt modulus (κ_t) values, respectively, from the RSF analysis obtained separately for each leaflet in all simulated membranes. The data shows that the bending rigidity and tilt modulus values are insensitive to the system size (e.g., K_C and κ_t are the same, within uncertainty, for 200-lipid and 1600-lipid patches of 70:30 POPE/POPG membranes). Also, in general, the values obtained for the two bilayer leaflets are found to be within

error bars. The only exceptions are several lipid mixtures, 70:30 binary POPC/POPS and POPC/PSM systems as well as 34:30:36 ternary mixture of POPC/POPS/Chol, for which we observe small, yet outside the statistical error, variations between the two leaflets. These differences are likely due to insufficient simulation times to allow for proper lipid mixing in these systems.

Importantly, as we describe in the following, the material properties calculated with the RSF method are in close agreement with those obtained from experimental studies as well as from other computational approaches. We first discuss in depth the bending rigidity data followed by presentation of the tilt modulus results.

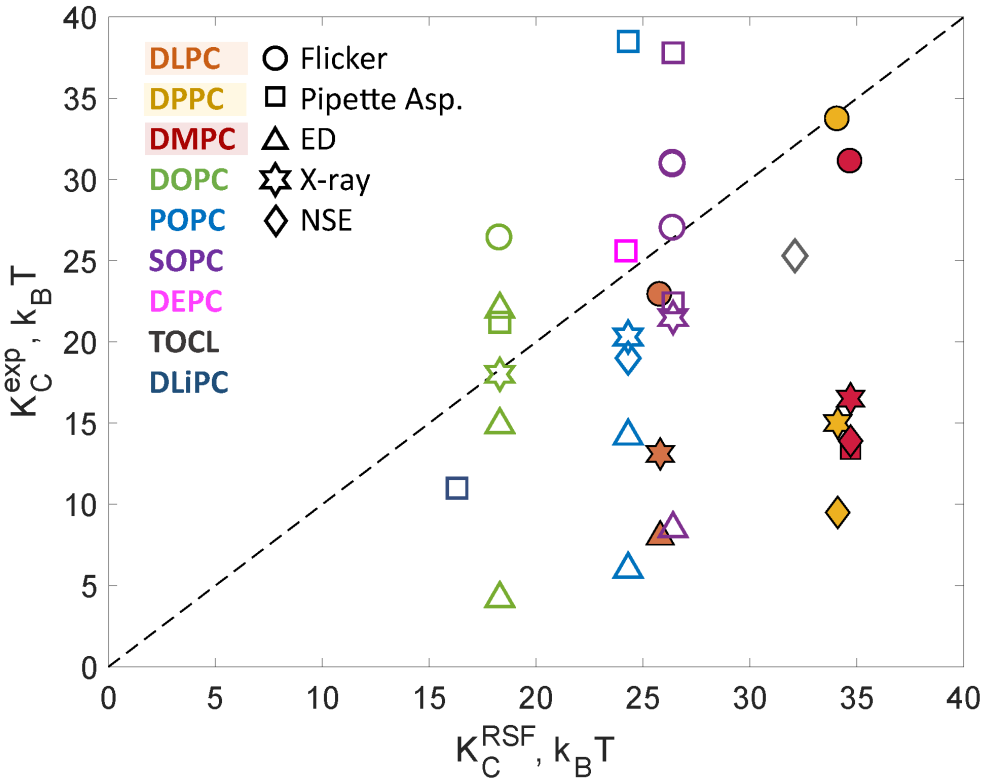

Figure 3.1.3. Bending rigidities *per bilayer* for selected systems from Table 3.1.2 determined from the atomistic MD simulations using the RSF analysis (K_C^{RSF}) are plotted against corresponding values determined experimentally (K_C^{exp}). Dashed line represents $f(x)=x$ function. Colors denote different lipids and symbols denote different experimental techniques used for measuring K_C^{exp}. Filled symbols denote all fully saturated lipids. For lipid abbreviations please see Table 3.1.1 caption and for literature references see Table 3.1.4.

3.1.4.1 Bending rigidity from the RSF analysis

Fig. 3.1.3 compares K_C values calculated from the RSF method to literature values obtained from various experimental techniques (see also Table 3.1.4). The best agreement for all simulated bilayers is with the flicker spectroscopy technique that measures rigidities by analysis of GUV shape fluctuations (denoted as circles in Fig. 3.1.3). The values obtained by electrodeformation are generally much lower and consequently deviate significantly from both the flicker and simulation results (triangles localized mostly at the bottom right of the 1-to-1 correlation line in Fig. 3.1.3). The K_C values from micropipette aspiration (square symbols in Fig. 3.1.3) also correlate reasonably well with the simulation rigidities, with the exception of POPC and DMPC. It should be noted that the value for POPC was obtained by Henriksen et al. [114] after applying a modified algorithm for analyzing the micropipette aspiration data, which generally produced higher values than the ones initially reported by Rawicz et al. [113]. Indeed, the K_C of SOPC reported by Henriksen et al. [115] is higher than those obtained by both Rawicz et al. and the RSF method (compare the two purple squares in Fig. 3.1.3). Regarding DMPC, Rawicz et al. measured a lower K_C compared to the value obtained by the RSF analysis; yet note that micropipette aspiration measurements of K_C are best performed at lower temperatures (e.g. 18˚C) that minimize evaporative loss from the sample chamber. Due to DMPC's higher melting temperature (T_M = 24˚C) the measurement had to be performed at 29˚C, subjecting the sample to potential hyperosmotic conditions and changes in the entrapped GUV volume.

It is interesting that the two scattering techniques, X-ray and NSE (denoted in Fig. 3.1.3 by stars and diamonds respectively), show general agreement with the simulation and flicker values for lipids possessing one or two unsaturated chains (i.e., DOPC, POPC, SOPC), but give smaller K_C values for all lipids with fully saturated chains

Table 3.1.4. Experimentally determined bilayer bending moduli from Fig. 3.1.3 expressed as a percent difference from the simulation values, $K_C^{\%} = 100 \times \left(K_C^{\exp} - K_C^{\mathrm{sim}}\right)/K_C^{\mathrm{sim}}$, and the corresponding literature references. Shown also are the respective temperatures (T) of the experimental measurements in units of Celsius. Note that in the calculation all experimental values have been rounded from those reported in the original publications. The different techniques are designated as follows: *Flicker* – flicker spectroscopy; *Pipette Asp.* – pipette aspiration; *ED* – electrodeformation; *X-ray* – low angle diffuse X-ray scattering; *NSE* – neutron spin-echo.

Bilayer	**Flicker**			**Pipette Asp.**			**ED**		
	$K_C^{\%}$	**T**	**Ref.**	$K_C^{\%}$	**T**	**Ref.**	$K_C^{\%}$	**T**	**Ref.**
POPC				57	25	[114]	-76 -44	22 24	[116] [158]
DLPC	-34	24	[159]				-77	22	[116]
DPPC	0	50	[159]						
SOPC	17 17 2	24 24 24	[111] [160] [160]	17 44	18 25	[113] [115]	-70	21	[158]
DOPC	42	23	[117]	15	18	[113]	20 -18 -78	23 23 21	[117] [158] [158]
DEPC				7	18	[113]			
TOCL									
DMPC	-11	30	[159]	-63	29	[113]			
DLiPC				-33	18	[113]			
	X-ray			**NSE**					
POPC	-19	30	[146]	-23	22	[121]			
DLPC	-63	30	[148]						
DPPC	-56	50	[161]	-71	60	[120]			
SOPC	-17	30	[150]						
DOPC	2	30	[152]						
DEPC									
TOCL				25	30	[153]			
DMPC	-51	30	[148]	-60	28	[120]			
DLiPC									

(i.e., DLPC, DMPC, DPPC). In contrast to the GUV experiments, scattering data is determined only by fluctuations at shorter (10-100Å) length scales. In this respect, it is

informative to note recent work by Nagle and co-workers [162, 163] that brings into light the importance of considering lipid tilt-dependent corrections to the K_C values in this dynamics regime. The importance of lipid tilt in this regime has been previously shown *in silico* [164] which has prompted current computational approaches based on Fourier space analysis to include this deformation mode in the derivation of the bending rigidity modulus (reviewed in [132]). Indeed, our results for κ_t (see below) indicate that fully saturated lipids have larger tilt moduli than the unsaturated ones, which could help explain the observed trends in the K_C values determined from scattering experiments.

We also compared K_C values for single-component systems obtained from the RSF analysis to bending rigidities reported from the alternative and most commonly used computational methodology based on sampling in the Fourier space of thermally excited fluctuations in the bilayer shape [132]. We found the two methods yielding consistent results for DPPC, POPE, and DMPC lipids (within 4%, 6%, and 15%, respectively). For the DOPC and POPC bilayers the discrepancies between the two approaches are larger, with the K_C values obtained from the RSF method being 35% and 21% lower, respectively.

It is instructive to examine the complete dataset of bending rigidities presented in Table 3.1.2 in view of the chemical structure and thermodynamic behavior of the respective lipids. First, increasing the degree of unsaturation (e.g. SOPC < DOPC < DLiPC) increases the area per lipid (63.8 < 68 < 70.3 Å^2) and consequently decreases the bending rigidity (26.4 > 18.3 > 16.3 k_BT) as expected. Changing the isomerization of the double bonds from *cis* to *trans*, e.g. DOPC vs. DEPC, increases K_C from 18.3 to 24.2 k_BT, consistent with the corresponding increase in the melting temperature from -17˚C to 12˚C and the subsequent decrease in area per lipid, from 68 to 64.4 Å^2 at 25˚C. Both DMPC and DPPC have similar bending rigidities (34.7 vs. 34.1 k_BT) at 30 and

50˚C, respectively, consistent with their similar *reduced* temperatures, $\tau = (T - T_M)/T_M$, in the simulations (T_M being the melting temperature). Indeed, τ for DMPC and DPPC systems were 0.22 and 0.25, respectively.

The detailed structure of tetraoleoyl cardiolipin (TOCL), a less commonly studied lipid present in the mitochondrial membrane, was recently reported from scattering experiments [153]. The area per lipid from our simulations performed under the same conditions as the experiments (i.e. at 30˚C and at 140 mM NaCl), was 130.3 Å^2, in excellent agreement with the experimental result of 129.8 Å^2. The bending rigidity obtained with the RSF method was 32.1 k_BT, about 27% higher than the K_C measured with the NSE technique, which we found generally to underestimate K_C for the other lipids as well when compared to the RSF values (see Fig. 3.1.3). Since TOCL has four oleoyl chains (i.e. 18 carbon long with one double bond), and two phosphate moieties connected by a single glycerol headgroup (see Fig. 3.1.1), it chemically resembles two linked DOPG lipids. Indeed, we found that while DOPG area per lipid was a little over half that of TOCL (71.4 vs 130.3 Å^2), its K_C was 15.4 k_BT, exactly half the K_C of TOCL.

In addition to illustrating the relationship between experimental and simulation bending moduli, Fig. 3.1.3 also shows an interesting clustering of the RSF-based K_C values in 3 groups with increasing average K_C: 1) DOPC and DLiPC, 2) DLPC, DEPC, POPC and SOPC, and 3) DMPC and DPPC. While there are no apparent structural features (chain length, saturation) that connect the lipids within each of these groups, we reasoned that the observed clustering could be based on area per lipid. Indeed, as shown in Fig. 3.1.4 (*left panel*), the grouping is very apparent when the K_C values are plotted against area per lipid chain, A_C (the area per lipid divided by the number of lipid chains). Importantly, when the data was fitted using a power law relation $K_C \sim c_1 A_C^{-\alpha} + c_2$, the simulation values were best fit by the curve with an $\alpha \approx$

7 exponent, the exact scaling predicted between K_C and A_C by Szleifer et al. from theoretical mean field calculations (Fig. 13c in Ref. [3]). This analysis indicates that the bilayer bending rigidity is influenced mostly by the packing of the lipid chains (or similarly, the area per lipid) and not by other generic lipid properties such as chain length and unsaturation.

Our simulations also allow us to examine the effect of charged lipids on K_C. Theoretical considerations predict an increase in bending rigidity in the presence of charged lipids due to stronger repulsion between the lipid headgroups [165-167] while

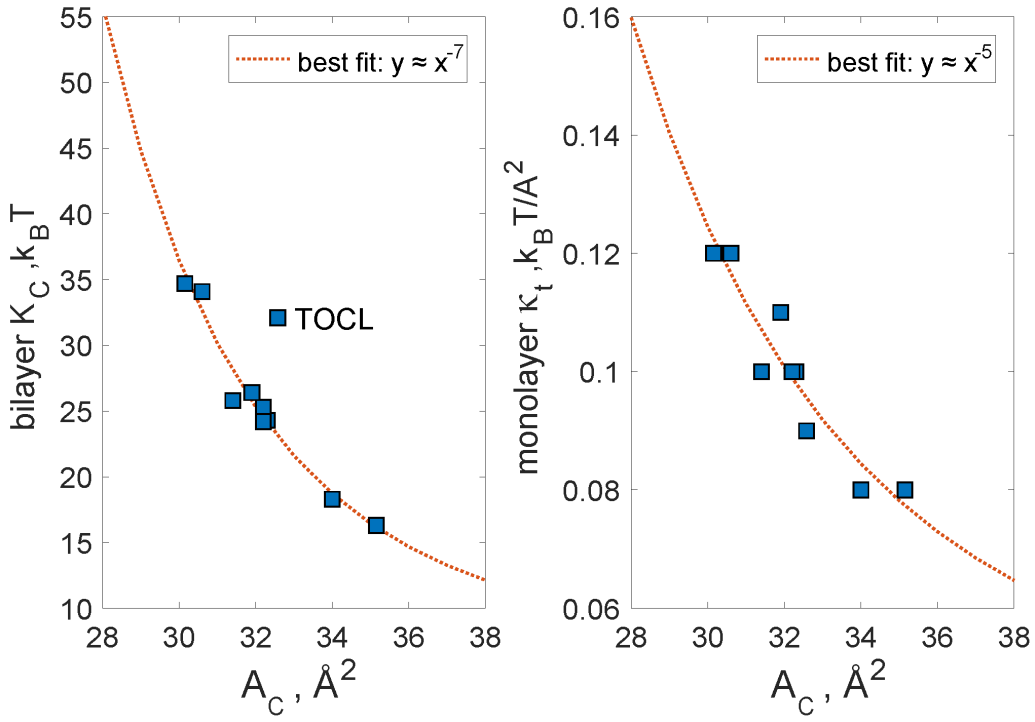

Figure 3.1.4. Values for K_C (*left panel*) and κ_t (*right panel*) calculated from the RSF analysis plotted against the respective areas per chain (A_C) for all lipid bilayers from Fig. 3. The data was fit using a power law form $c_1 A_C^{-\alpha} + c_2$ and the best fit is shown as a dotted line. For K_C, the best-fit parameters were: c_1=1.972e+12, c_2=6.904, and α=7.328; For κ_t we found the best fit with: c_1=1.903e+06, c_2=0.03802, and α=4.971. The apparent outlier, TOCL (that has a different headgroup) was excluded from the fitting procedure on the left panel. The optimal scaling parameters reported in the legends of the two panels match earlier predictions from computational mean field theory for the respective relationships [2, 3]. See text for details.

experimental measurements are scarce and report conflicting trends [122, 168-171]. From our simulations, we find that DOPG in 140 mM NaCl has lower bending rigidity than DOPC (15.4 vs 18.3 k_BT, respectively). While this observation does not correspond to the theoretically expected membrane stiffening, it does correlate well with the larger area per lipid of DOPG versus DOPC, suggesting that possibly membrane thinning could be a decisive consequence of headgroup charging that leads to the apparent softening of the charged membrane. At the same time, while POPE has a K_C of 29.4 k_BT at 55˚C and is expected to have higher rigidity at lower temperatures, addition of 30 mol% POPG at 37˚C slightly lowers the bilayer K_C to 28.8 k_BT. We must note however, that POPG has a lower melting temperature than POPE (-2˚C vs 25˚C, respectively) and the addition of a lower melting temperature lipid to a bilayer would naturally act to decrease K_C. On the other hand, adding PS (which bears the same negative charge as PG) appears to increase somewhat the bending rigidity of the bilayer (compare POPC with POPC/POPS and POPE with POPE/POPS). In contrast to PG lipids, which have similar melting temperatures as their corresponding PC lipids with the same chains (e.g. DOPG and DOPC), PS lipids are characterized by melting temperatures that are higher from their PC counterparts (e.g. 14˚C and -2˚C for POPS and POPC, respectively). As a result, the lipid packing and consequently the surface charge density in PS-containing bilayer mixtures can be higher from those in PG-containing bilayers. Thus, the effect of charged lipids on bilayer K_C is expected to depend not only on the amount of charge carried by the lipid headgroup (in addition to the salt concentration of the solvent) but also on the general chemical structure of the lipid, and can hardly be generalized to different lipid types.

The RSF method further quantifies the increase of K_C upon addition of cholesterol and high melting lipids. Replacing 36 mol% of POPC in a POPC/POPS 0.7/0.3 bilayer with Chol increased the membrane rigidity two-fold, from 30.7 to 62.1 k_BT. For

comparison, a POPC bilayer with similar amounts of Chol was found to have K_C in the range 27 – 86.8 k_BT with different experimental techniques [114, 121]. Addition of 30 mol% of palmitoyl sphingomyelin (PSM) to a POPC bilayer also increased K_C by 34%, as expected from the higher melting temperature of PSM relative to POPC (42 vs -2˚C).

Due to the local nature of the lipid splays calculations, the RSF method can also be applied to simulation trajectories of highly ordered lipid bilayers, whose global thermal fluctuations are suppressed on the time scale of the simulation, and thus are not tractable by the computational methods that seek to determine membrane elastic properties from Fourier-space analysis. Indeed, we have previously shown that the bending rigidity of liquid ordered bilayers calculated from the RSF method was in good agreement with the experimentally determined K_C values [137]. Here, we report the bending modulus of a very ordered gel-like DPPC bilayer with 20 mol% Chol at 25˚C. The resulting K_C of 130 k_BT, is much higher than the K_C of any of the other examined bilayers and is comparable to the experimentally determined rigidities of SM:Chol mixtures [117] and liquid ordered phases [172, 173].

Collectively, these results demonstrate the direct applicability of the RSF method to a wide range of lipids and lipid mixtures as the calculated bending rigidities are in good agreement with experiments and successfully reproduce expected trends in bilayer mechanical properties based on considerations of the known physical and chemical characteristics of the lipids.

3.1.4.2 Thermodynamic tilt modulus form the RSF analysis

The thermodynamic tilt modulus κ_t was first introduced into the Helfrich-Evans-Canham theory of elasticity by Kozlov and Hamm as a parameter that describes the extent of the resistance of a lipid monolayer to lipid tilt deformations [174] (see Eq. 1).

In subsequent work ([2]), May et al. derived a simple relationship between the tilt modulus κ_t, and the tilt vector fluctuations:

$$\kappa_t = \frac{k_B T}{A_l \langle \vec{t}^2 \rangle}. \tag{3.1.13}$$

Accordingly, κ_t was estimated using a molecular-level chain-packing mean field theory, from the probability distribution function of chain conformations in the monolayer. In the RSF analysis, we follow a somewhat similar methodology in that we determine κ_t from the probability distribution function of the lipid tilt degree of freedom sampled in MD simulations. The resulting values, presented in Table 3.1.3, are in general agreement with the 4.0–8.0 × 10^{-20} J/nm^2 range of the thermodynamic tilt modulus per monolayer predicted from the chain-packing theory [2], and exhibit high correlation with the bending rigidity values from Table 3.1.2 (with Pearson correlation coefficient 0.86). Indeed, similar to the trends observed in bending rigidity, κ_t values are smallest for lipids with unsaturated tails, such as DOPC, DLiPC, and DOPG and increase in magnitude with increasing lipid tail saturation. Interestingly, for TOCL, which contains 4 unsaturated lipid tails, we find a relatively low κ_t, whereas the bending rigidity for TOCL was comparable to that of other saturated lipids, such as DPPC and DMPC.

To better evaluate the observed trends in κ_t, we plotted the thermodynamic tilt modulus against A_C (area per lipid chain). Similar to the bending rigidity, we found a clear relation between the tilt modulus and A_C (Fig. 3.1.4, *right panel*). Importantly, the data could be fitted by $\kappa_t \sim c_1 A_C^{-\alpha} + c_2$ functional form with $\alpha \approx 5$ – a relationship very similar to that predicted by May et al. from theoretical mean field calculations (Fig. 6 in Ref. [2]).

In order to further validate the κ_t values as obtained from the RSF analysis, we computed the thermodynamic tilt modulus in an alternative way, by directly using the equality in Eq. 3.1.13. To this end, we calculated the right-hand-side of Eq. 3.1.13 by first expressing $\vec{t}^2$ either by $\tan^2\theta$ or by approximating it as θ^2 (i.e., taking the small angle approximation), and then computed $1/\langle\tan^2\theta\rangle$ and $1/\langle\theta^2\rangle$ quantities from the $P(\theta)$ probability distributions using:

$$\langle\theta^2\rangle = \int_0^{\pi/2} \theta^2 P(\theta) d\theta \tag{3.1.14}$$

$$\langle\tan^2\theta\rangle = \int_0^{\pi/2} (\tan^2\theta) P(\theta) d\theta \tag{3.1.15}$$

The results (converted to $k_B T/A_l$ units using Eq. 3.1.13) were then plotted against κ_t values from Table 3.1.3. As illustrated in Fig. 3.1.5*A*, the κ_t values are nearly identical to $1/\langle\theta^2\rangle$ for all membrane systems tested. On the other hand, as shown in Fig. 3.1.5*B*, $1/\langle\tan^2\theta\rangle$ values are systematically lower than the tilt moduli values calculated from Eq. 3.1.7 (or compared to $1/\langle\theta^2\rangle$). This result is not surprising given the fundamental assumption of the underlying theory, which approximates free energy contribution of the lipid tilt as a quadratic function (see Eq. (3.1.1)), an assumption that is strictly valid only in the limit of small tilt angles where $\tan\theta$ and θ are equivalent. Indeed, including sampling outside the small tilt regime, where $\tan\theta$ function deviates strongly from θ, leads to inconsistent values for the tilt modulus. Altogether, the data in Fig. 3.1.5 provide additional support for the low-angle fitting procedure implemented in the RSF analysis for obtaining κ_t.

Next, we sought to compare κ_t values from the RSF method to the tilt moduli reported from computational studies based on the spectral analysis (SA) of MD

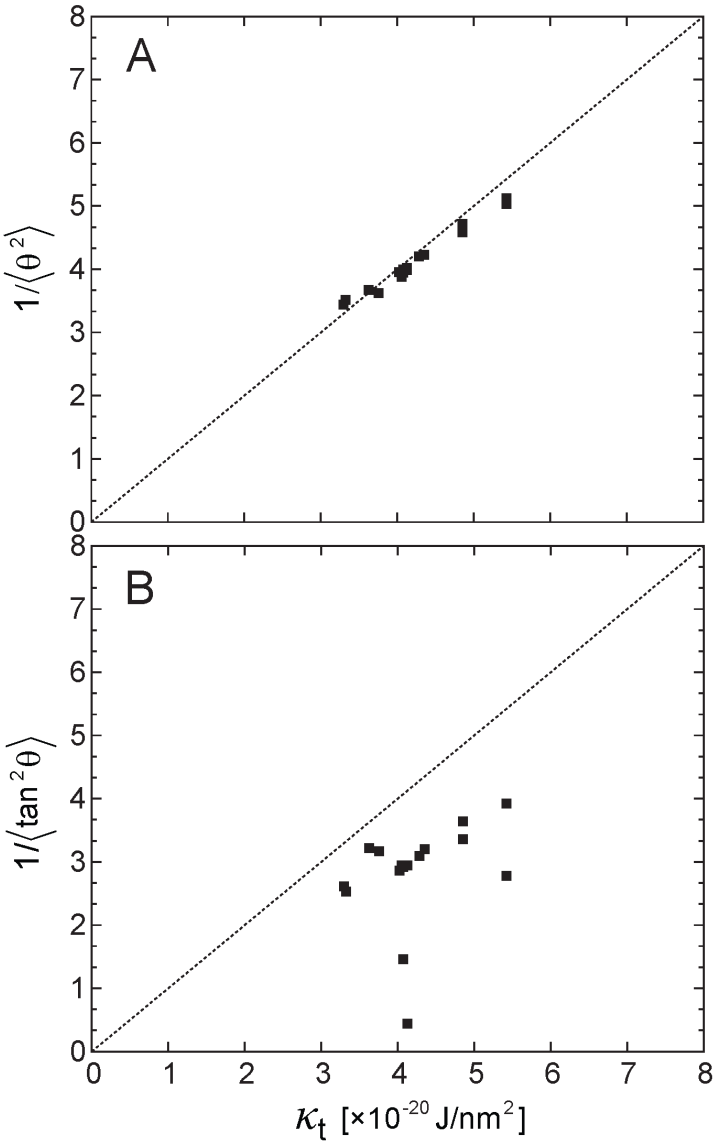

Figure 3.1.5. Correlation between the thermodynamic tilt modulus (κ_t) determined from the RFS analysis and $1/\langle\theta^2\rangle$ (*A*) and $1/\langle\tan^2\theta\rangle$ (*B*). All measures are per monolayer and given in the units of [×10^{-20} J/nm^2]. Symbols represent data per each leaflet for all single component systems from Table 3. $\langle\theta^2\rangle$ and $\langle\tan^2\theta\rangle$ were obtained from the respective $P(\theta)$ distributions, see text. Dashed line represents $f(x) = x$ function.

simulations performed in the reciprocal space [132]. In this context, it is important to note that the SA approach derives a somewhat different tilt modulus parameter, sometimes termed the *theoretical tilt modulus* [7] (also referred to as the elastic

contribution to the tilt modulus [2]), which we denote here by κ_t^0 (following the notation in Ref. [2]). As described in Ref. [2] and extensively reviewed in Ref. [7], the two moduli κ_t and κ_t^0 are inequivalent. According to Ref. [2], κ_t^0 was interpreted as a contribution to the thermodynamic tilt modulus that arises from stretching of lipid chains when lipids are tilted and the following phenomenological expression was suggested to relate the two moduli:

$$\kappa_t = \kappa_t^0 + \kappa_{OE} \tag{3.1.16}$$

where the second term on the right-hand side of Eq. 3.1.16 quantifies contributions from losses in the orientational entropy (*OE*) experienced by a tilted lipid chain. Using molecular level chain packing theory, May et al. predicted [2] that for typical lipids (i.e. with area per lipid in the range of 60-70 Å^2) the two contributions to the thermodynamic tilt modulus would be approximately equal, suggesting that κ_t^0 is roughly half of κ_t since it was calculated in the model to be ~2×10^{-20} J/nm^2 (assuming 60Å^2 area per lipid in the expression $\kappa_{OE} = 3k_BT/A_l$ as proposed in Ref. [2]). An alternative model was proposed by Nagle et al. [7], which argued that the difference between the two moduli should depend on the value of κ_t^0 (or κ_t). Indeed, according to this model, the difference between the κ_t and κ_t^0 moduli grows as the magnitude of the tilt modulus itself increases. This trend is illustrated in Fig. 3.1.6 as a dashed line within the typical range of 3.0 – 6.0 $\times10^{-20}$ J/nm^2 of κ_t.

In order to compare the values of κ_t from Table 3.1.3 to published κ_t^0 values obtained from the SA method (Ref. [132]), we calculated the differences between the two moduli, $\Delta\kappa = \kappa_t - \kappa_t^0$, as a function of the thermodynamic tilt modulus. It must be noted that the force fields as well as simulation protocol used in Ref. [132] and in the current work are practically identical, thereby allowing for direct comparison of the two sets of data (i.e. from the RSF and SA analyses). As shown in Fig. 3.1.6

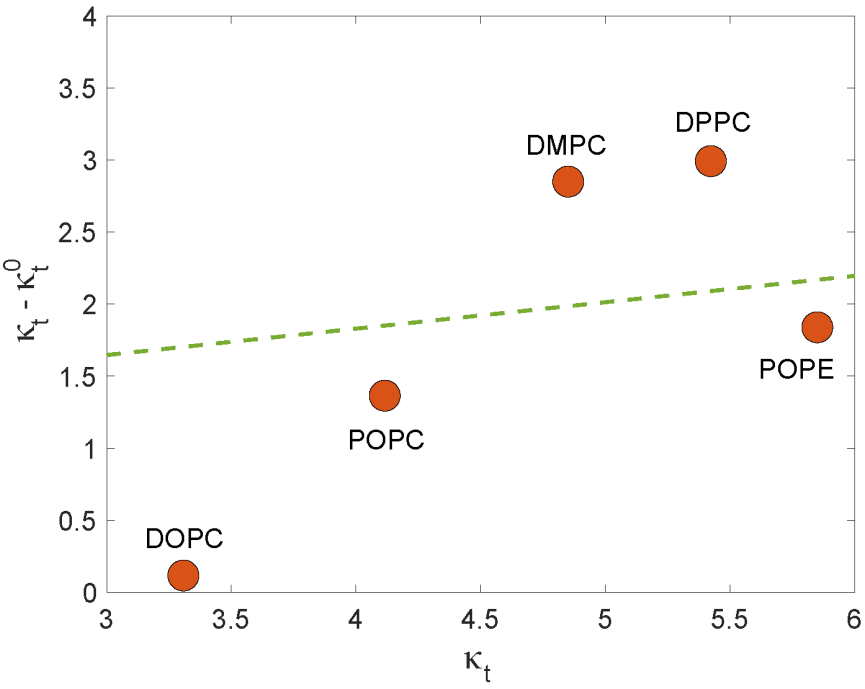

Figure 3.1.6. Differences between the thermodynamic tilt modulus calculated from the RSF analysis (κ_t) and the theoretical tilt modulus obtained from the spectral analysis (κ_t^0) as a function of κ_t for selected single component membrane systems. The dashed line corresponds to the model prediction by Nagle et al. (Ref. [7]). All reported values are per monolayer and given in units of [$\times 10^{-20}$ J/nm^2].

(symbols) we find that $\Delta\kappa$ strongly depends on the level of lipid saturation. Thus, $\Delta\kappa$ decreases with the extent of chain saturation such that $\Delta\kappa_{DPPC,DMPC} > \Delta\kappa_{POPC,POPE} > \Delta\kappa_{DOPC}$. This progression is interesting considering Eq. 3.1.16 which suggests that $\Delta\kappa$ differences presented in Fig. 3.1.6 should be closely related to the entropic losses of the orientational degrees of freedom as lipids are tilted. Indeed, a lipid directed on average along the normal to the surface has 2π to explore. A chain that is tilted is necessarily constrained because the average tilt angle is nonzero, so states with specific tilt should get more weight. Stated differently, any deviation of the average from zero means a departure from the totally random configuration – so it necessarily entails entropic loss.

Thus, the data in Fig. 3.1.6 suggests that the loss in orientational entropy upon lipid tilt is largest for lipids with saturated tails and decreases with the degree of unsaturation. This trend can be rationalized by the fact that the orientational entropy of unsaturated lipid tails is larger than that of the saturated lipids even in the conformations where lipid director vector on average remains aligned with the membrane normal. Therefore, a tilt of a saturated lipid molecule away from the normal will bring about larger losses in the orientational entropy than a tilt of an unsaturated lipid. Stated differently, the orientational entropic cost of tilting is lower for lipids with unsaturated chains than for lipids with saturated chains, potentially because for saturated lipids this entropy was lower already in the untilted state due to the larger conformational constraints. A more quantitative exploration of this point would require additional computational analysis.

From Fig. 3.1.6, it is also apparent that for pairs of lipids with similar extent of chain saturation, such as DPPC and DMPC, or POPC and POPE, $\Delta\kappa$ increases moderately with increasing κ_t. This observation is in general agreement with the trend in $\Delta\kappa$ suggested by the model of Nagle et al. (see dashed line in Fig. 3.1.6), however from Fig. 3.1.6 it also follows that the ratio between the two moduli can take a wide range of values $\kappa_t/\kappa_t^0 \in [1; 2.4]$ that depends sensitively on the lipid properties, most notably the degree of saturation. While it is yet unclear what is the exact link between the κ_t and κ_t^0, from the above analysis as well as from the works by May et al. [2] and Nagle et al. [7], it is now apparent that not only is the relationship between κ_t and κ_t^0 strongly dependent on the underlying model, but that the various methodologies report on distinctly different tilt moduli. While addressing this issue in depth goes beyond the scope of the current work, the analyses presented here provide an important framework to connect the tilt modulus obtained from the RSF approach to the tilt

modulus calculated from alternative methodologies, as well as to the different free energy terms that contribute to it directly.

3.1.5 Conclusions

In conclusion, we have applied the RSF method to MD trajectories from a large set of lipid membranes encompassing a wide range of lipid types and biophysical properties. Moreover, we have rigorously demonstrated the applicability of the RSF approach to quantify elastic properties of lipid bilayers, such as the tilt modulus and bending rigidity, and discussed how different definitions of the tilt modulus appearing in the current literature could be related to each other. Due to the local nature of the analysis, the RSF method has already proven to be a unique computational tool to treat lipid mixtures or curved lipid assemblies. The method is now perfectly set to tackle future applications of even more complex systems that could include asymmetric membranes, phase-separated lipid mixtures [175], as well as protein-decorated membranes.

3.2 A new computational method for membrane compressibility: Bilayer mechanical thickness revisited

3.2.1 Abstract

Because lipid bilayers can bend and stretch in ways similar to thin elastic sheets, physical models of bilayer deformation have utilized mechanical constants such as the moduli for bending rigidity (κ_C) and area compressibility (K_A). However, the use of these models to quantify the energetics of membrane deformation associated with protein-membrane interactions and the membrane response to stress is often hampered by the shortage of experimental data suitable for the estimation of the mechanical

constants of various lipid mixtures. While computational tools such as Molecular Dynamics (MD) simulations can provide alternative means to estimate K_A values, current approaches suffer significant technical limitations. Here, we present a novel computational framework that allows for a direct estimation of K_A values for individual bilayer leaflets. The theory is based on the concept of elasticity and derives K_A from real-space analysis of local thickness fluctuations sampled in MD simulations. We explore and validate the model on a large set of single and multicomponent bilayers of different lipid composition and sizes, simulated at different temperatures. The calculated bilayer compressibility moduli agree with values estimated previously from experiments and those obtained from a standard computational method based on a series of constrained tension simulations. We further validate our framework in a comparison with an existing polymer brush model (PBM) and confirm the PBM's predicted linear relationship with proportionality coefficient of 24 using elastic parameters calculated from the simulation trajectories. The robustness of the results that emerge from the new method allows us to revisit the origins of the bilayer mechanical (compressible) thickness and in particular, its dependence on acyl chain unsaturation and the presence of cholesterol.

3.2.2 Introduction

Cells exhibit a wide variety of morphologies ranging from discoid or spherical shapes (e.g. erythrocytes and staphylococcus bacteria, respectively), to branched formations with multiple highly curved and flat elongated segments (e.g. nerve axons in the brain, microvilli in the intestines and rod cells in the retina of the eye). A cell's ability to take on distinct shapes is directly dependent on the flexibility of its bounding plasma membrane (PM), and thus maintaining a certain level of flexibility of the PM is essential to both cell and human physiology. A prominent example of the

consequences of deficits in PM flexibility is sickle cell anemia, a disease characterized by a drastic change in the shape and stiffness of red blood cells that leads to their accumulation on vessel walls and blockage of blood flow [17-22].

The PM is composed of two layers, or leaflets, composed of a mixture of various types of amphiphilic lipid molecules, each type with its own set of structural and thermodynamic properties. Despite this complexity, the PM's flexibility has been successfully modeled quantitatively as a simple elastic sheet with characteristic bending and compressibility constants [176]. While measurements of PM's elastic properties have been performed directly on live cells, the interpretation of such measurements is still challenging due to the complexity and non-uniformity of the cellular membrane environment [177, 178]. Instead, experiments on less complex, compositionally symmetric model membranes have been utilized to characterize the bilayer's bending rigidity (κ_C) and area compressibility (K_A) moduli as a function of lipid composition. These mechanical constants quantify, respectively, the energetic cost associated with bending the membrane and stretching/compressing its area, and have thus been used to make successful predictions about biological phenomena, e.g., of the changes in shape of closed lipid vesicles under stress [68, 179, 180]. Since the proper function and organization of transmembrane proteins are often regulated by membrane deformations near the protein (e.g. local bilayer bending and thinning or thickening), K_A and κ_C also appear as important parameters in theoretical models quantifying the energetics of protein-membrane interaction [47, 61, 181]. All these approaches directly link the elastic properties of membranes to bilayer shape and the sorting of both lipids (e.g., into distinct lipid domains) and proteins (e.g., into local clusters or oligomers) on the surface of a heterogeneous membrane such as the PM.

Various methods exist for measuring κ_C both *in vitro* and *in silico* [7, 132] (see also Section 3.1), but the equally important compressibility modulus K_A is less well

studied. It quantifies the response of membrane area to tension, which under physiological conditions may arise from various perturbations, such as changes in osmolarity across the membrane or the addition of lipids or other molecules to only one of the membrane's leaflets. Several experimental approaches have been developed to measure K_A in model membranes, and these methods rely on extracting the compressibility modulus from a relationship between systematically varied tension and the resulting bilayer area expansion. Perhaps the most commonly used technique utilizing this approach is the micropipette aspiration of giant unilamellar vesicles (GUVs), which has supplied the largest set of bilayer K_A data available currently [113, 182, 183]. The procedure involves imaging a single GUV while applying incremental amounts of suction pressure to it with a micropipette. The tension exerted on the bilayer is calculated directly from the applied pressure while the resulting changes in the bilayer area are inferred from geometrical considerations of the corresponding changes in GUV shape. In an alternative approach, pressure is applied to extruded unilamellar vesicles through osmotic imbalance between the vesicles' interior and exterior due to solutes such as salt or sugar [184-186]. The ensuing trends in the bilayer structure are monitored from the vesicle diameter measured with techniques such as light scattering or electron microscopy. NMR alone [187] or in combination with X-ray diffraction [188] have also been used to measure K_A of bilayers at low hydration by relating changes in bilayer area to changes in the osmotic pressure of a polymer (e.g. polyethylene glycol) solution. Unfortunately, experimental data on the behavior of many lipids, including lipid mixtures, is still scarce and the availability of the resources needed to make the measurements is often limited. In that respect, a combination of rigorous physics-based simulation and well-calibrated computational tools holds great promise for enabling an otherwise impossible elasticity-based analysis of membrane systems that remain elusive to experimental methods.

With the feasibility of more extensive molecular dynamics (MD) simulations, the area compressibility modulus has been estimated from trajectories of (on average) flat lipid bilayer patches. The classical computational approach is based on the same principle as the experimental methods, i.e., that for small changes in area per lipid (A_{lip}), tension is linear with direct area expansion. To calculate the bilayer K_A, a series of constrained-area (or tension) simulations is performed and the value emerges from the slope of the best-fit line through the data of ln (A_{lip}) vs surface tension. While the estimated moduli are typically in good agreement with experimental estimates, the analysis of one lipid composition requires multiple simulations, which makes this approach very expensive computationally. An alternative computational strategy that circumvents this requirement uses the equilibrium thermal fluctuations of the bilayer at constant zero tension instead. In this spirit, K_A is estimated from a single simulation trajectory utilizing the equilibrium expression $K_A = \langle A_{box} \rangle / \langle \delta {A_{box}}^2 \rangle k_B T$, where A_{box} represents the lateral area of the simulation box, k_B is the Boltzmann constant, T is temperature and $\langle \cdot \rangle$ denotes ensemble average (see Methods section below). Since the analysis is directly related to the fluctuations in the simulation box, the modulus exhibits a strong dependency on the thermodynamic phase behavior of the bilayer (which is directly related to the relaxation rate of its lateral area), system size, and the corresponding length of the simulation trajectory. Importantly, no existing computational or experimental methods allow for calculation of K_A of individual bilayer leaflets, which is a prerequisite for the quantification of the energy of local leaflet distortions in an asymmetric bilayer.

Here, we report a novel computational methodology that overcomes the aforementioned shortcomings in the calculation of area compressibility, and obtains the K_A moduli of a bilayer and of each of its leaflets from a single MD trajectory. Like the existing methods, we take advantage of thermal fluctuations, but express the

compressibility modulus as a function of leaflet thickness instead of bilayer area. Following our recent success in calculating each leaflet's bending rigidity from real-space analysis of local splay fluctuations (Section 3.1), we base our method for K_A estimation on sampling the leaflet thickness locally, and estimate the corresponding probability distribution and potential of mean force (PMF) profile as a function of changes in thickness. Finally, the K_A is extracted from a quadratic fit of a small region of the PMF around the global minimum, according to the elastic energy of stretching (see Methods). We show that for a large set of single and multicomponent bilayers, the compressibility moduli we calculate with the new method are in excellent agreement with the ones reported from experiments *in vitro*, or calculated with alternative computational approaches. We find that the K_A values obtained with our framework are less sensitive to bilayer size and simulation length due to the local nature of the analysis. We further validate our approach by reproducing the linear relationship between bilayer thickness, K_A and κ_C in the polymer brush model (PBM) [113], using mechanical constants calculated from the simulation trajectories. This analysis lets us revisit the definition of the bilayer mechanical thickness and clarify observed discrepancies reported in the literature with respect to PBM's predictions [132, 152, 189].

3.2.3 Methods

Here, we present the theoretical framework and details of the new method for the calculation of the area compressibility moduli of a bilayer and each of its leaflets, based on the analysis of trajectories from molecular dynamics simulations. We begin by reviewing the calculation of bilayer compressibility from area fluctuations, and then expand the formulation to the calculation of individual local leaflet moduli. Since the use of area in the latter presents certain practical challenges as outlined below, we

then re-express the theory in terms of local leaflet thicknesses and provide a detailed methodological description of our new computational framework.

3.2.3.1 *Calculation of bilayer compressibility from area fluctuations*

Following Helfrich's formalism [190], we treat the bilayer as a two-dimensional elastic sheet with mechanical constants describing its modes of deformation. For small equilibrium fluctuations around the free energy minimum, each deformation mode is associated with an elastic energy that is approximated by a quadratic function of the relevant deformation. For changes in area, the elastic energy E of stretching/compressing a bilayer patch with equilibrium area a_0 is given as:

$$E = \frac{1}{2} K_A a_0 \left(\frac{a - a_0}{a_0} \right)^2, \tag{3.2.1}$$

where a is the deformed area and K_A is the bilayer area compressibility modulus. Assuming that bilayer area stretching/compression are independent degrees of freedom in the context of the full energy functional describing bilayer mechanics (cf. bending or tilt), K_A can be obtained from the bilayer's thermally excited area fluctuations [191]. Specifically, from the equipartition theorem, $\langle E \rangle = (1/2) k_B T$ where k_B is Boltzmann constant and T is temperature, it follows that:

$$K_A = \frac{a_0}{\langle (a - a_0)^2 \rangle} k_B T. \tag{3.2.2}$$

This is the expression commonly used to obtain K_A from MD simulations of a bilayer by sampling fluctuations in the lateral area of the simulation box A_{box} [132, 191, 192]. Since E is the energy of a deformed state described by $\Delta a/a_0 = (a - a_0)/a_0$, from statistical mechanics it also follows that the probability of this state can be written as:

$$p(\Delta a/a_0) = Ce^{-\frac{E}{k_B T}} \tag{3.2.3}$$

where C is a constant. Rearrangement of Eq. 3.2.3 leads to an alternative equality from which K_A can be calculated provided the probability distribution of the deformed states is known:

$$\ln p\left(\frac{\Delta a}{a_0}\right) = -\frac{1}{2k_B T} K_A a_0 \left(\frac{\Delta a}{a_0}\right)^2 + \ln C, \tag{3.2.4}$$

which can be written as:

$$-\frac{2k_B T}{a_0} \ln p\left(\frac{\Delta a}{a_0}\right) = K_A \left(\frac{\Delta a}{a_0}\right)^2 + C'. \tag{3.2.5}$$

While both Eqs. 3.2.2 and 3.2.5 are equivalent upon sufficient sampling of area fluctuations, Eq. 3.2.2 in which K_A is inversely proportional to the mean square area fluctuations, is more sensitive to outliers and deviations from the elastic regime (see Eqs. 3.2.12-3.2.13 and discussion afterwards) when used for K_A estimation. In contrast, Eq. 3.2.5 relies on the distribution of deformations around the mean and can thus provide a more robust approximation of the area compressibility modulus.

3.2.3.2 Leaflet compressibility calculated from area fluctuations

The area compressibility modulus of a bilayer quantifies the total energy of membrane deformation and can be used to infer the energetics of deforming individual bilayer leaflets in *symmetric* bilayers whose two leaflets are assumed to behave in the same way. However, in an *asymmetric* membrane, the two leaflets can have very different lipid compositions with potentially different energetic costs for stretching/compression that cannot be simply inferred from the elastic properties of the

bilayer. To enable the analysis of these more general (and physiologically relevant) systems, we sought a formulation that would yield the area compressibility modulus of each leaflet of the membrane independently. Specifically, the goal was to obtain leaflet compressibility from area fluctuations in the spirit of the above-described theory (Eqs. 3.2.2-3.2.5).

Globally (e.g. considering the entire simulated bilayer patch), the area fluctuations of the two leaflets are identical and equal to the area fluctuations of the whole bilayer. Therefore, the apparent leaflet compressibility moduli calculated from area fluctuations at that scale would always appear the same, masking any potential differences in the inherent mechanical properties of the leaflets. In order to extract these differences and find the effective local leaflet moduli, we perform the analysis on a length scale much smaller than the global bilayer area. In particular, we view each leaflet as a collection of more than one parallel elastic blocks that are made of the same material (i.e. have the same compressibility modulus). Within a leaflet, it is assumed that all blocks have the same average area (e.g. the average area of a lipid) but can have different instantaneous areas and their area fluctuations are weakly coupled. Due to its elastic nature, the deformation energy of a block has the same form as Eq. 3.2.1 and its compressibility modulus (which is the effective local leaflet modulus) can be obtained accordingly from its area fluctuations through Eq. 3.2.2 or Eq. 3.2.5.

In order to relate the effective local leaflet moduli to the bilayer's compressibility, we express the energy of bilayer stretching/compression as a function of the stretching/compression of the individual leaflet blocks. If we denote the instantaneous global areas of the two leaflets with A_x and A_y and the instantaneous and average local areas of their elastic blocks with a_{xi}, a_{yi} and a_{xo}, a_{yo} respectively (i being the

identity of the block), the second order approximation of the bilayer energy can be written as:

$$E = \sum_i K_A^x a_{x0} \left(\frac{a_{xi} - a_{x0}}{a_{x0}}\right)^2 + \sum_i K_A^y a_{y0} \left(\frac{a_{yi} - a_{y0}}{a_{y0}}\right)^2 + \sum_{i,j} K_{xx} a_{x0} \left(\frac{a_{xi} - a_{x0}}{a_{x0}}\right)\left(\frac{a_{xj} - a_{x0}}{a_{x0}}\right) + \sum_{i,j} K_{yy} a_{y0} \left(\frac{a_{yi} - a_{y0}}{a_{y0}}\right)\left(\frac{a_{yj} - a_{y0}}{a_{y0}}\right) + \sum_{i,j} K_{xy} \sqrt{a_{x0} a_{y0}} \left(\frac{a_{xi} - a_{x0}}{a_{x0}}\right)\left(\frac{a_{yj} - a_{y0}}{a_{y0}}\right). \quad (3.2.6)$$

The first two terms in Eq. 3.2.6 represent summations over the deformation energies of the individual elastic blocks in the two leaflets, the next two terms are the corresponding inter-block correlations within each leaflet, and the last term quantifies the correlations between blocks from different leaflets. Each term has its characteristic modulus, and K_A^x and K_A^y in particular are the effective local leaflet compressibility moduli.

Since the bilayer area A is $A = A_x = A_y = (A_x + A_y)/2$, $A_x = \sum_i a_{xi}$ and $A_y = \sum_i a_{yi}$, we can express the variance of A as a sum over variances and covariances of the local areas:

$$\sigma^2(A) = \frac{\sum_i \sigma^2(a_{xi}) + \sum_i \sigma^2(a_{yi}) + \sum_{ij} \sigma^2(a_{xi}, a_{xj}) + \sum_{ij} \sigma^2(a_{yi}, a_{yj}) + W}{2}, \quad (3.2.7)$$

where $W = \sum_{ij} \sigma^2(a_{xi}, a_{yj})$. Since the global areas of the two leaflets are constrained to be the same, their variances are the same and consequently, the sum of the interleaflet correlations is 0, i.e. $W = 0$.

In addition, $\sigma^2(a_{xi}) = a_{x0}\sigma^2\left(\frac{a_{xi}-a_{x0}}{a_{x0}}\right)$ and at the same time $\sigma^2(a_{xi}) = 1/K_A^x$ (as in the second order approximation of the energy the multivariate Boltzmann distribution becomes the multivariate normal distribution). If n denotes the number of blocks, Eq. 3.2.7 then simplifies to:

$$\frac{1}{K_A} = \frac{1}{2}\left(\frac{1}{K_A^x} + \frac{1}{K_A^y}\right) + Q, \tag{3.2.8}$$

where Q is the average sum of the inter-block correlations within each leaflet:

$$Q = \frac{\sum_{ij} \sigma^2(a_{xi}, a_{xj}) + \sum_{ij} \sigma^2(a_{yi}, a_{yj})}{2n}. \tag{3.2.9}$$

While these inter-block correlations within a leaflet can generally deviate from 0, when the local areas (elastic blocks) are small the correlations can be both positive and negative (representing the fact that the blocks can undergo stretching/compression deformations in two dimensions) and we find that they cancel each other out in the respective sums (see Section B.1 in Appendix B). As a result, we assume $Q \approx 0$ and arrive at the final relationship between the bilayer K_A and the local compressibility moduli, K_A^x and K_A^y, of the two leaflets:

$$\frac{1}{K_A} = \frac{1}{2}\left(\frac{1}{K_A^x} + \frac{1}{K_A^y}\right). \tag{3.2.10}$$

Note that the derivation above assumes that the two leaflets have the same number of elastic blocks, however Eq. 3.2.10 holds even in the general case when these

numbers are different (as for membranes with asymmetric lipid composition; see Section B.1 in Appendix B for the extended derivation).

It is important to note that in our formulation a local leaflet K_A in a symmetric bilayer has the same magnitude as the bilayer K_A and therefore should be treated differently from the *global* leaflet compressibility moduli often referred to in the literature as 1/2 the bilayer K_A [123]. The latter are based on a model in which the global area changes in the two leaflets are the same due to the constraints on the bilayer geometry, but are uncoupled, and thus the elastic energy (and consequently, the K_A) of deforming each leaflet is half the energy (K_A) of deforming the bilayer. In contrast, K_A^x and K_A^y capture the *local* properties of the leaflets, which are affected by the global constraint on area only indirectly and thus reveal features that are more specific of the leaflets themselves. From Eqs. 3.2.6-3.2.10 it further follows that the harmonic mean of the local leaflet moduli gives the bilayer K_A, which as we show in Results quantitatively matches experimentally measured bilayer moduli for various membrane systems.

3.2.3.3 Leaflet compressibility calculated from thickness fluctuations

The theoretical formulation presented in the previous section allows the calculation of an effective local leaflet compressibility modulus from area fluctuations. To capture the individual leaflet properties when calculating K_A^L (where L can be x or y), given the outlined considerations (e.g. the cancelation of the Q term in Eq. 3.2.8), we chose to analyze the fluctuations of the smallest local unit area that is characteristic for leaflet L, that is the average area per lipid in the leaflet. In this way, the two leaflets in a symmetric bilayer will have the same local unit area, as expected, while in an asymmetric bilayer they may be different. We thus seek a local description of

instantaneous leaflet area that would allow for ample sampling of area fluctuations, while treating each leaflet independently from the other leaflet.

Since the definition and calculation of local leaflet areas is rather challenging [191, 193], we assume volume conservation to relate deformations in local area to deformations in local thickness, and then estimate the coefficients from thickness fluctuations. Specifically, let a^L and t^L be the instantaneous local area and thickness of a leaflet, and a_0^L and t_0^L are their corresponding equilibrium values. Assuming that $a_0^L t_0^L = a^L t^L = V$ where V is a constant, we can express the energy of stretching/compressing leaflet L, E^L, as a function of *characteristic* changes in thickness instead of *relative* changes in area:

$$E^L = \frac{1}{2} K_A^L a_0^L \left(\frac{a^L - a_0^L}{a_0^L} \right)^2 = \frac{1}{2} K_A^L a_0^L \left(\frac{V/t^L - V/t_0^L}{V/t_0^L} \right)^2$$

$$= \frac{1}{2} K_A^L a_0^L \left(\frac{t_0^L - t^L}{t^L} \right)^2. \tag{3.2.11}$$

Consequently, Eqs. 3.2.2 and 3.2.5 become:

$$K_A^L = \frac{1}{a_0^L \langle (t^L - t_0^L)^2 / (t^L)^2 \rangle} k_B T \tag{3.2.12}$$

$$-\frac{2 k_B T}{a_0^L} \ln p \left(\frac{t_0^L - t^L}{t^L} \right) = K_a^L \left(\frac{t_0^L - t^L}{t^L} \right)^2 + C'. \tag{3.2.13}$$

While both Eqs. 3.2.12 and 3.2.13 can be used to obtain K_A^L in theory, practical (numerical) considerations render Eq. 3.2.13 more suitable (see Section B.2 in Appendix B for comparison between the two approaches). Our formal framework is therefore centered on extracting K_A^L from Eq. 3.2.13 through the following steps:

1. Calculate local leaflet thicknesses at different chain depths within the bilayer.

2. From all possible definitions of leaflet thickness, identify the one that is suitable for the calculation of K_A^L.

3. Use Eq. 3.2.13 to obtain K_A^L.

In the following, we present details of the above three stages in our algorithm.

1. Calculating local leaflet thicknesses from simulations. Over the course of a simulation trajectory, the thickness of each bilayer leaflet is laterally inhomogeneous and fluctuates around its equilibrium value t_0^L as a result of thermal motions. To construct the probability distribution of thickness changes in Eq. 3.2.13, $p(\Delta t/t^L)$, by sampling local fluctuations, we take a grid-based approach and calculate the leaflet thickness at different grid points on the leaflet surface. In a continuum representation, a leaflet can be viewed as a stack of layers with each layer being a surface made of a particular lipid atom (ς), e.g. a phosphate surface ($\varsigma = P$), a first glycerol carbon surface ($\varsigma = C1$ using CHARMM36 atom naming scheme), a first sn-1 carbon surface ($\varsigma = C21$), a first sn-2 carbon surface ($\varsigma = C31$) and so on (see Fig. B1). To calculate the leaflet thickness at a grid point (x, y) we first find the height of each of these surfaces at this grid point by performing interpolation on the corresponding atomic z-coordinates as follows:

$$h_{\varsigma,(x,y)} = \frac{\sum_i \frac{z_{\varsigma,i}}{d_{i,(x,y)}^n}}{\sum_i \frac{1}{d_{i,(x,y)}^n}}, \tag{3.2.14}$$

where $h_{\varsigma,(x,y)}$ is the height of the ς-surface (i.e. the surface made of atom type ς at grid point (x, y)), $z_{\varsigma,i}$ is the z-coordinate of atom i, $d_{i,(x,y)}$ is the 2D distance between atom i and (x, y), n is interpolation order, and the summations are done over all leaflet atoms i of type ς (note that the atoms on individual lipid chains have unique atom

names, thus each lipid has at most one atom of type ς). Since a lipid can have multiple chains and the heights in Eq. 3.2.14 are calculated separately for each carbon atom on each chain, we simplify the analysis by averaging the corresponding surface heights across all lipid chains:

$$h_{\varsigma,(x,y)} = \frac{1}{N_{sn}} \sum_{ch=1}^{N_{sn}} h_{\varsigma(ch),(x,y)} \tag{3.2.15}$$

where $h_{\varsigma(ch),(x,y)}$ is the height of the surface calculated from the ς carbon on the ch chain, and N_{sn} is the number of lipid chains. Eq. 3.2.15 can also be extended to lipids whose chains have different lengths (see Section B.3 in Appendix B). While this approach works well for most bilayers, we found that for lipids like SAPE (see Simulation details below for lipid name abbreviations) which has one fully saturated and one highly-unsaturated chain, this averaging can become problematic for the subsequent analysis that is based on correlations of the resulting heights (described in the next section). Empirically, we found that the problem is alleviated when prior to the averaging in Eq. 3.2.15, each double bond and its preceding carbon are represented by a single data point with an instantaneous height equal to the average interpolated height across the 3 carbons. Thus, each double bond effectively reduces the unsaturated chain length (or the number of surfaces defining the unsaturated chain) by 2 carbons. As this procedure is more general and at the same time does not affect the results for the bilayers for which Eq. 3.2.15 can be applied, it was integrated in the methodological framework.

The leaflet thickness at the level of the ς-surface, denoted τ_{ς}, is defined as the difference between the height of the ς-surface and the height of the lowest-situated surface at the grid point (usually, the surface of the terminal methyl carbons):

$$\tau_{\varsigma,(x,y)} = h_{\varsigma,(x,y)} - \min h_{(x,y)}. \tag{3.2.16}$$

The interpolation order n in Eq. 3.2.14 determines the contribution to $h_{\varsigma,(x,y)}$ of the atoms closest to (x, y) relative to those that are further apart, i.e., the higher the n, the larger the effect from nearby atoms, and the lower the n, the larger the effect from all atoms. Hence, n is related to the effective number of atoms (lipids) that are being averaged, and consequently to the equilibrium area a_0^L in Eq. 3.2.13 (i.e. the area whose thickness fluctuations are effectively being analyzed).

Since atoms are weighted differently in the interpolation, we estimate a_0^L by first using the denominator in Eq. 3.2.14 to approximate the *effective* number of lipids being averaged, and then multiplying this number by the average area per lipid in the leaflet, A_{lip}^L. When $n = 2$ the denominator in Eq. 3.2.14 is approximately 1, conveniently setting $a_0^L \sim A_{lip}^L$, and we therefore use $n = 2$ and $a_0^L = A_{lip}^L$ in the subsequent analysis (see Section B.4 in the Appendix B for the derivation, and Fig. B2 for a demonstration of the invariability of the results with n). As described in the Appendix B (Section B.5), the interpolated thicknesses (Eq. 3.2.16) preserve the product of local area and thickness (i.e. the assumption underlying Eq. 3.2.11), which further establishes their suitability for the calculation of K_A^L.

2. Identifying the relevant thickness for fluctuations analysis. The first step of the method described above allows us to calculate local thicknesses at different surfaces (i.e. different depths) within the leaflet. Naturally, surfaces at heights near the water/hydrocarbon interface fluctuate less due to interfacial tension, while those further down into the leaflet fluctuate more, due to the increased fluidity of the lipid chains around the bilayer midplane. The height (and consequently thickness) fluctuations in a leaflet therefore fall roughly into two categories: ones that are relatively suppressed, and ones that are dominated by relatively unconstrained motion

of the lipid chains. The former would tend to overestimate K_A^L while the latter would tend to underestimate it. The fluctuations of the surface lying at the intersection of these two regimes will thus be the most suitable from the elasticity considerations to obtain a reliable estimate of K_A^L. We term the thickness at the level of this surface the *relevant thickness for* K_A^L and proceed to identify its location within a bilayer leaflet.

The location of the atomic surface corresponding to the relevant thickness may differ in different membranes due to various degrees of bilayer fluidity. We have therefore developed a general algorithm for identifying the surface relevant for K_A^L calculations for an arbitrary lipid membrane. Specifically, we examine the correlation between the height fluctuations of a particular surface ς and those of a reference surface (RS) close to the water-hydrocarbon interface (in our case, the RS is the surface of the first acyl chain carbon atom that is not connected to oxygen). Fig. 3.2.1 shows a typical behavior of this correlation, $r(\varsigma) = r(h_{RS}, h_\varsigma)$, (here, for the top

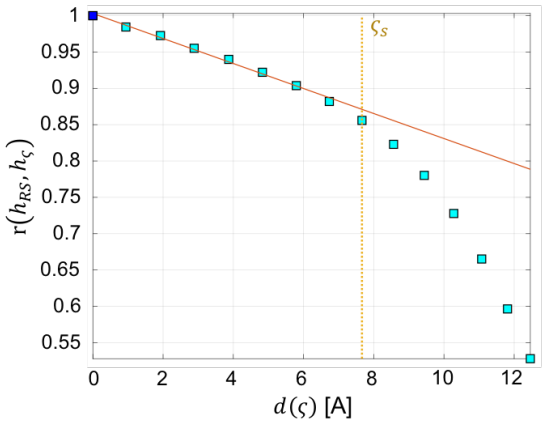

Algorithm for identification of relevant thickness

Start from the reference surface (surface 1).
Skip the two surfaces below the RS (surfaces 2-3).
For each subsequent surface i:

- calculate slope of best-fit line through surfaces 1,2, … , i
- calculate average of all slopes up to surface i: $\frac{1}{i-2}\sum_{j=3}^{j=i} \text{slope}(1,2,\dots,j)$
- if slope at surface i deviates from average slope by more than 10%, stop. This is the relevant surface ς_s.

Figure 3.2.1. Identification of relevant thickness for calculation of K_A^L. Left, the correlation of the height fluctuations of a surface ς with the height fluctuations of a *reference surface* RS (first acyl chain carbon atom not attached to oxygen, shown in blue here and in Fig. B1) is plotted as a function of distance from RS for the top leaflet of a DPPC membrane. Right, outline of the algorithm used to identify the relevant surface ς_s from the data (denoted by a yellow dotted line on the plot). The solid red line shows the corresponding best-fit line through all points preceding ς_s. A sample representation of the relevant surface can be seen in yellow in Fig. B1.

leaflet of a DPPC bilayer) as the distance, $d(\varsigma)$, between a surface ς and the reference surface increases ($d(\varsigma) = \left|\widetilde{h_{RS}} - \widetilde{h_{\varsigma}}\right|$; where $\breve{h}$ denotes median of the distribution of local heights). At small $d(\varsigma)$, the correlation drops slowly and linearly with distance (Fig. 3.2.1, red solid line), implying a regime of suppressed thickness fluctuations (i.e. fluctuations of the atoms in this segment of the chain are strongly coupled to one another). At larger $d(\varsigma)$ distances, the $r(\varsigma)$ vs. $d(\varsigma)$ profile strongly deviates from the initial linear behavior as $d(\varsigma)$ increases more slowly while $r(\varsigma)$ decreases more rapidly, characteristic of the more fluid region of the bilayer in which the lipid chains exhibit greater flexibility and intercalate with the chains of the opposing leaflet. Given the two well-defined regimes, we choose the first point outside of the linear regime (Fig. 3.2.1, yellow dashed line) to represent the leaflet whose thickness fluctuations can be used to extract K_A^L. We identify this surface ς_s following the algorithm outlined on the right hand side box in Fig. 3.2.1. For DPPC the surface ς_s is at the 10$^{\text{th}}$ carbon (shown in yellow in Figs. 1 and S1). Interestingly, for this and all other bilayers that we examined, ς_s appears to be located right around the region within the leaflet where the density of the opposing leaflet vanishes (i.e. just outside the interleaflet interdigitation zone, see Fig. B3).

3. Calculating K_A^L from local thickness fluctuations. Having identified ς_s, we calculate the local thickness τ_{ς_s} at every grid point in every frame of the trajectory and estimate its probability distribution using kernel density estimation (Fig. 3.2.2A). From this distribution, we estimate t_0 (defined here and throughout as the most probable thickness, i.e. at the peak of the distribution), and the left hand side of Eq. 3.2.13, i.e. the Potential of Mean Force (PMF), as shown on Fig. 3.2.2B. The characteristic asymmetric shape of the PMF is consistent with the free energy vs. area per molecule profile predicted by Ben-Shaul from theoretical considerations of lipid

chain packing [194] and arises from the relative ease of deforming the membrane upon thickness contraction (area expansion, increase in entropy) compared to thickness expansion (area contraction, decrease in entropy). To find the leaflet compressibility, we identify a small region around t_0 (typically ≤7% of t_0) where the PMF is closest to a normal distribution. We then fit a quadratic function to the PMF in this region and obtain K_A^L from the quadratic coefficient in the best fit (see Section B.6 in Appendix B for a step-by-step outline of the procedure). Errors are calculated with a two-dimensional bootstrapping approach over both time and space as described in Section B.7 in Appendix B.

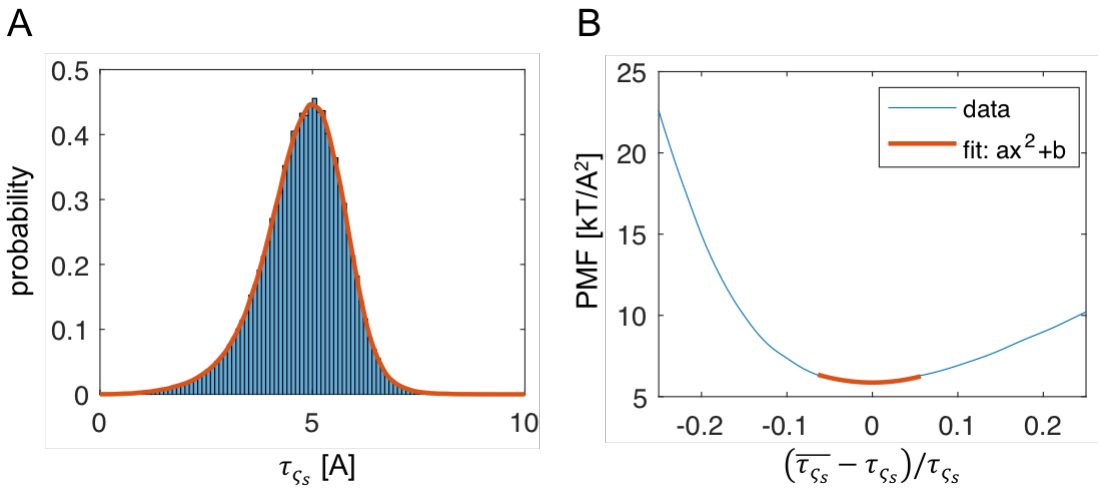

Figure 3.2.2. Calculation of K_A^L from local thickness fluctuations. A, Probability distribution of the relevant thickness, τ_{ς_s}, constructed from the time evolution of the local interpolated thicknesses for the top leaflet of a DPPC bilayer (blue). The distribution is smoothed for subsequent analysis by using a kernel density (red). B, The left-hand side of Eq. 3.2.16 is plotted as a function of characteristic changes in the local thickness. The PMF in the region of thicknesses within 6% of the mean thickness is fit to a function of the form $y \sim ax^2 + b$ (see text for details). K_A^L is obtained from the quadratic coefficient $a = 238$ mN/m of the best fit (shown in red).

3.2.3.4 Simulation details

Table B1 lists information for all simulated bilayers. The following lipid names are abbreviated as shown in the parenthesis: 1,2-dilauroyl-*sn*-glycero-3-phosphocholine (DLPC, di12:0), 1,2-dimyristoyl-*sn*-glycero-3-phosphocholine (DMPC, di14:0), 1,2-palmitoyl-*sn*-glycero-3-phosphocholine (DPPC, di16:0), 1,2-dilinoleoyl-*sn*-glycero-3-phosphocholine (DLiPC, di18:2), 1,2-dioleoyl-*sn*-glycero-3-phosphocholine (DOPC, di18:1(cis)), 1-stearoyl-2-oleoyl-*sn*-glycero-3-phosphocholine (SOPC, 18:0,18:1), 1,2-dielaidoyl-*sn*-glycero-3-phosphocholine (DEPC, di18:1(trans)), 1-palmitoyl-2-oleoyl-*sn*-glycero-3-phosphocholine (POPC, 16:0,18:1), 1-palmitoyl-2-oleoyl-*sn*-glycero-3-phosphoethanolamine (POPE, 16:0,18:1), 1-stearoyl-2-diarachidonoyl-*sn*-glycero-3-phosphoethanolamine (SAPE, 18:0,20:4), 1,2-dioleoyl-*sn*-glycero-3-phospho-(1'-rac-glycerol) (DOPG, di18:1(cis)), 1',3'-bis[1,2-dioleoyl-*sn*-glycero-3-phospho]-*sn*-glycerol (TOCL, tetra18:1), N-palmitoyl-D-*erythro*-sphingosylphosphorylcholine (PSM), cholesterol (Chol). As indicated in Table B1, some of the bilayers were taken from Section 3.1. All remaining bilayers were constructed with CHARMM-GUI [141, 142, 144] and simulated with NAMD [155] using the CHARMM36 force field [156, 195]. Initial equilibration was carried out with CHARMM-GUI's protocols. Following equilibration, the simulations were performed with a 10-12 Å cutoff for non-bonded and short-range electrostatic interactions, and Particle Mesh Ewald with grid spacing of 1 Å for long-range electrostatics. Vdw force switching was turned on. Temperature was controlled with a Langevin thermostat while constant pressure was maintained with NAMD's Langevin piston Nose-Hoover method with a 200 fs period and 50 fs decay. All simulations were run with a time step of 2 fs, *rigidbonds* set to all, and both atomic coordinates and velocities were output every 20 ps.

3.2.3.5 Analysis of simulations and method implementation

All bilayer properties were estimated from the last segments of the trajectories over which the lateral area of the simulation box was considered converged, as determined with a method based on maximizing the number of effectively uncorrelated data points [196]. Table B1 lists the total simulation time for each system and the length of the trajectory segments used for the analysis. All trajectories were centered prior to analysis, such that the mean z position of the terminal methyl carbons on all lipids was set to 0.

The interpolated heights, as described in Step 1 of the calculation of leaflet compressibility from thickness fluctuations, were calculated for each leaflet with a modified version of VMD's MEMBPLUGIN [197] and sampled on an 8x8 $Å^2$ square grid. All subsequent analysis (outlined in Section B.6 in Appendix B) was performed with MATLAB. Number density profiles were calculated with the Density Profile tool in VMD [198] and acyl chain order parameter profiles were obtained with in-house Tcl and MATLAB scripts. All code for calculation of the area compressibility moduli is available upon request.

3.2.3.6 Lateral pressure profile calculation

Lateral pressure profiles were calculated from the last ~100 ns of the centered simulation trajectories. The calculation was done with NAMD using stored instantaneous atomic coordinates and velocities. Each system was divided into slabs of approximately 0.8 Å thickness. The total lateral pressure was the sum of the independently obtained Ewald and non-Ewald pressure contributions. The x, y and z dimensions of the grid size used for calculating the Ewald contribution were all equal and less than half the z dimension of the simulation box. Due to the known limitations of the Harasima algorithm with PME electrostatics implemented in NAMD for the discretized pressure calculation, the normal component of the pressure tensor in each

slab, p_N, was set to $p_N = L_N^{-1} \int \mathrm{d}z\, p_L(z)$ where L_N is the length of the simulation box in the direction of the bilayer normal, and $p_L(z)$ is the lateral (or tangential) pressure in slab z [199, 200]. The total pressure in slab z was then calculated as $p(z) = p_L(z) - p_N$.

3.2.3.7 Treatment of Chol-containing membranes

At relatively small mole fractions (up to 0.3-0.35) of cholesterol (Chol) in the bilayers, the expected effect of Chol on the bilayer structural properties (average area and volume per lipid) is mainly a *condensing* effect on the non-Chol lipids [193, 201]. It is reasonable, therefore, to assume that Chol's effect on the area compressibility modulus at such small Chol mole fractions will be indirect and captured in the K_A calculated from the non-Chol components only, as detailed in Section B.3 in the Appendix B. However, as shown (see, for example, Ref. [201]), at higher mole fractions (above 0.35) the distribution of Chol's tilt angles becomes narrower and moves closer to zero, indicating that its motion is more restricted and the molecule is more parallel to the bilayer normal. In this regime Chol is likely to contribute directly to the leaflet compressibility (i.e. compression of the bilayer would involve compression of the Chol molecules themselves), and its effect needs to be considered explicitly. This is achieved by assuming that the ratio of the area compressibility calculated by considering only the non-Chol components ($K_a^{L(nonCh)}$) and all components (K_a^L) is the same as the fraction (s_f) of the surface area occupied by the non-Chol lipids, i.e. $K_a^{L(nonCh)}/K_a^L = s_f$ (where $s_f = \chi_{nonCh} a_{0(nonCh)}^L / a_0^L$). From here $K_a^L = K_a^{L(nonCh)}/s_f$. This correction to K_a^L is used only for bilayers with Chol mole fractions > 0.35, and is found to produce a gradual increase in the bilayer compressibility modulus, consistent with experimental measurements (see Fig. 3.2.3 and discussion below).

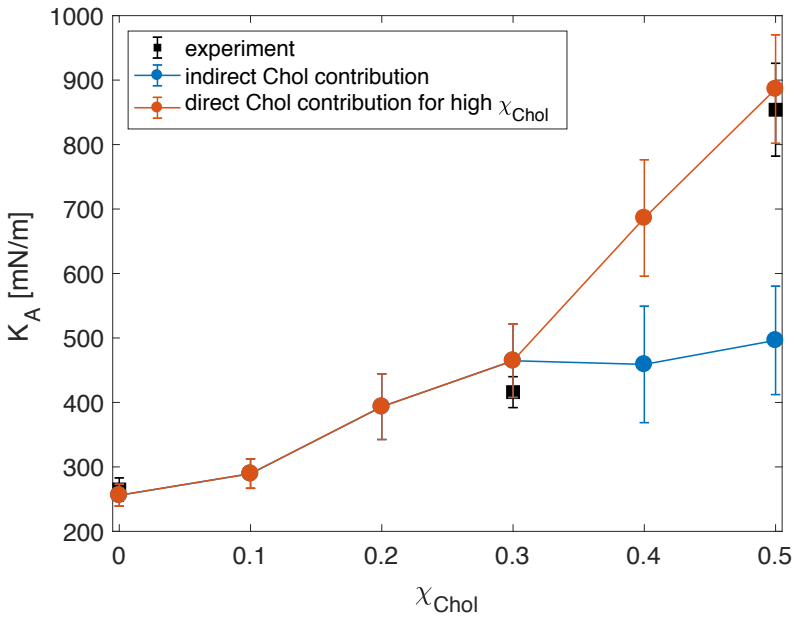

Figure 3.2.3. Bilayer area compressibility for DOPC/Chol mixtures with increasing amount of cholesterol. The bilayer K_A was calculated either by considering only the non-Chol lipids for all Chol mole fractions χ_{Chol} (blue symbols) or the non-Chol lipids for $\chi_{Chol} \leq 0.3$ and the direct contribution of Chol to the bilayer compressibility for $\chi_{Chol} > 0.3$ (red symbols, see Simulations analysis and method implementation section for details). Experimentally determined compressibility moduli are shown in black. The red and blue lines are guides to the eye to the respective data points.

3.2.4 Results and discussion

3.2.4.1 Validation of the new method for quantifying compressibility moduli from local thickness fluctuations (LTF)

The canonical method for calculating bilayer area compressibility from MD simulations involves performing a series of NPγT simulations (e.g., [191]). In each simulation a non-zero tension γ is applied in the x-y plane and the bilayer K_A is obtained by analyzing the linear relationship between the applied tension and the resulting area expansion [191]. Since this methodology directly mimics the micropipette aspiration technique [202], it is expected to reproduce closely the

experimental results provided that the properties of the simulated bilayers are correctly captured by the underlying force field. Table 3.2.1 shows the calculated moduli from NPγT simulations of several single-component lipid membranes and the corresponding experimental measurements (see also Table B2). There is indeed a very good agreement between the two, verifying that the simulations are well-converged and able to reproduce the known values of K_A using standard techniques. Therefore, these and other single and multicomponent symmetric bilayers served as controls for the validation of our new LTF method.

Tables 3.2.1 and 3.2.2 list the compressibility moduli for each leaflet and for the bilayer obtained from LTF analysis of the equilibrated trajectories (see Table B1 for a detailed description of all simulated bilayers). The bilayer K_A's obtained from the LTF method are in excellent agreement with those measured experimentally or obtained from NPγT simulations (Table 3.2.1), indicating that our new approach reproduces the accuracy of existing methods when applied to symmetric bilayers. We note, however, that while the confidence intervals associated with the linear fits from the NPγT simulations are large, the LTF errors calculated with a 2D bootstrapping algorithm (as described in Section B.7 in Appendix B) are much smaller and comparable to the experimental uncertainties. (The experimental uncertainty for POPC is notably larger than the rest because the measurement was obtained with a different infrared (IR) linear dichroism-based method [203].)

Table 3.2.1 also lists the corresponding compressibility moduli calculated from the same equilibrated portions of the trajectories, but from lateral bilayer area fluctuations using Eq. 3.2.2. While these values are also in reasonable agreement with published results from the same method [132, 142], there is a large variability among the resulting K_A's. For example, for PSM simulated at 48-55ºC, Lee et al. [142] calculated a value of 456 ± 65 mN/m, which is similar to the one we obtained from the bilayer

Table 3.2.1. Area compressibility of compositionally symmetric single component bilayers calculated with different methods: local thickness fluctuations (LTF), constrained tension (NPγT) simulations and box (i.e. bilayer) area fluctuations. Where available, experimentally measured moduli are shown (Exp) with references to the respective literature sources. All moduli are given in units of mN/m. The LTF bilayer K_A was calculated with Eq. 3.2.10. LTF errors for the leaflets were calculated with a 2-dimensional bootstrap method as described in Section B.7 in Appendix B and propagated to obtain the error on the bilayer K_A. The 95% confidence interval for the values obtained from a linear fit of tension versus area expansion in NPγT simulations (Table B2) are shown in brackets. For lipid name abbreviations see Simulation details section in the text.

Bilayer	LTF			Exp	NPγT simulations	Box Area Fluctuations
	top	bottom	bilayer			
DLPC	258 ± 28	214 ± 22	234 ± 17			213 ± 20
DMPC	236 ± 20	236 ± 22	236 ± 15	234[a] ± 23	235 [172, 297]	263 ± 23
DPPC	238 ± 34	274 ± 34	255 ± 24	231[b] ± 20	223 [188, 257]	183 ± 20
DLiPC	200 ± 26	202 ± 22	201 ± 17	247[a] ± 21	237 [189, 285]	261 ± 23
DOPC [full]	240 ± 20	274 ± 28	256 ± 17	265[a] ± 18 310[c] ± 20	253 [211, 295]	246 ± 20
DOPC [part]	266 ± 32	260 ± 26	263 ± 21			313 ± 33
DOPC rep 1	246 ± 24	256 ± 26	251 ± 18			223 ± 31
DOPC rep 2	272 ± 28	272 ± 68	272 ± 37			274 ± 26
SOPC	260 ± 24	232 ± 32	245 ± 21	235[a] ± 14 290[c] ± 6		236 ± 21
DEPC [full]	212 ± 24	214 ± 22	213 ± 16	229[a] ± 12		204 ± 18
DEPC [part]	240 ± 38	186 ± 42	210 ± 30			321 ± 53
POPC 1	206 ± 32	168 ± 20	185 ± 18	255[d] ± 75	214 [134, 293]	220 ± 17
POPC 2	236 ± 26	186 ± 28	208 ± 20			172 ± 30
POPC 3	258 ± 28	234 ± 32	245 ± 22			250 ± 23
POPC 4	214 ± 38	198 ± 36	206 ± 26			236 ± 22
POPE	242 ± 28	218 ± 15	229 ± 30	233[e]	285 [260, 310]	291 ± 26
SAPE	230 ± 12	208 ± 20	218 ± 25			265 ± 14
DOPG	236 ± 13	230 ± 14	233 ± 19			220 ± 26
TOCL	224 ± 8	238 ± 7	231 ± 11			254 ± 20
PSM	344 ± 20	286 ± 20	312 ± 29		324 [251, 396]	499 ± 42

[a] Ref. [113], [b] Ref. [204], [c] Ref. [183], [d] Ref. [203], [e] Ref. [205]

Table 3.2.2. Area compressibility of compositionally symmetric multicomponent bilayers calculated with the three different methods described in the caption of Table 3.2.1. For lipid name abbreviations see Simulation details section in the text.

Bilayer	LTF method			Exp	Box Area Fluctuations
	top	bottom	bilayer		
POPC/Chol 70/30	862 ± 92	676 ± 126	757 ± 87	673[a]	562 ± 87
DOPC/Chol 90/10	276 ± 36	306 ± 24	290 ± 23		260 ± 27
DOPC/Chol 80/20	466 ± 62	340 ± 68	393 ± 51		338 ± 34
DOPC/Chol 70/30	544 ± 74	406 ± 76	465 ± 57	416[a] ± 24	532 ± 75
DOPC/Chol 60/40	804 ± 118	598 ± 120	686 ± 90		829 ± 76
DOPC/Chol 50/50	956 ± 140	826 ± 102	886 ± 84	854[a] ± 72	1011 ± 99
DPPC/Chol 80/20	2916 ± 364	3368 ± 436	3126 ± 281		1968 ± 208
POPE/POPG 70/30	194 ± 22	228 ± 28	210 ± 17		193 ± 19
POPC/POPS 70/30	350 ± 40	318 ± 34	333 ± 26		360 ± 43
POPE/POPS 70/30	366 ± 40	332 ± 50	348 ± 33		322 ± 69
DMPC/POPC 10/90	238 ± 22	188 ± 32	210 ± 22		258 ± 19
DMPC/POPC 43/57	264 ± 26	230 ± 32	246 ± 21		224 ± 19
DMPC/POPC 75/25	282 ± 24	244 ± 38	262 ± 24		250 ± 19

[a] Ref [182]

area fluctuation analysis (499 ± 42 mN/m), but Venable et al. [132] reported 310-350 mN/m, which is very similar to the moduli we obtained from NPγT simulations and with the LTF method. This variability seems more likely for high-melting lipids (PSM, DMPC, DPPC) whose dynamics 5-10ºC above their melting temperatures are generally slower compared to low-melting temperature lipids, suggesting that the

underlying reason for the divergent results is likely an insufficient sampling of the lateral area fluctuations. Indeed, in the analysis of box fluctuations each frame of the simulation trajectory represents a single data point, which makes proper sampling highly dependent on the length of the simulation and the size of the bilayer patch (the latter is closely related to the amplitude of the fluctuations [206]). To illustrate this point, we compare in Table 3.2.1 the K_A's for DOPC and DEPC (two fluid bilayers of the same size) calculated from either the full equilibrated trajectories of 517 and 680 ns respectively, or only from the last 100 ns of the simulation runs. The K_A moduli obtained with bilayer area fluctuation analysis vary from 246 ± 20 mN/m to 313 ± 33 mN/m for DOPC and from 204 ± 18 mN/m to 321 ± 53 mN/m for DEPC, whereas those calculated with the LTF method do not show such variability. The reproducibility of the LTF moduli can also be seen from the analysis of replica simulations of DOPC, i.e. systems with identical size and lipid composition that were constructed and simulated independently from one another (Table 3.2.1).

For bilayers with up to 200 lipids, the results from our method are only weakly dependent on bilayer size: For POPC membranes with 128 and 200 lipids, we calculated K_A's of 245 ± 22 and 208 ± 20 mN/m respectively (Table 3.2.1). For a larger POPC bilayer with 416 lipids, the K_A was 185 ± 18 mN/m, which may indicate a potential challenge for the analysis of larger systems, although the result is within the error of one of the smaller bilayers. Notably, since larger size of the simulated systems generally leads to larger undulations [206], the results might be affected by the assumption inherent in our method that the bilayer normal is the same throughout the bilayer surface (along the z axis of the simulation box). Because thicknesses are calculated by interpolation on the z positions of all atoms in the leaflet (see Methods), using the LTF method with the single bilayer normal assumption would tend to underestimate the apparent K_A when large-scale undulations are present in the system.

It is feasible to introduce local normals in the LTF formulation, but this would result in more complex numerical calculations. Instead, we sought to circumvent the problem by constraining the radius of interpolation, R_{int}. We reasoned that because large-scale bilayer undulations are known to appear on length scales larger than the bilayer thickness (t_{pp}), setting R_{int} to a length slightly larger than t_{pp} could help alleviate the size dependence of K_A. Indeed, using R_{int} that is 10% larger than t_{pp} produced a bilayer K_A of 241 ± 23 mN/m for the larger POPC bilayer with 416 lipids, the same as calculated for the smaller systems.

Table 3.2.1 shows that the bilayer K_A varied between 230 and 260 mN/m for most single-component bilayers we studied. One exception is PSM, which is characterized by a somewhat higher compressibility of 312 ± 29 mN/m. Interestingly, we found tetra-oleloyl cardiolipin (TOCL) to have a compressibility modulus of 231 ± 11 mN/m, in contrast to a previously reported modulus of 342 mN/m obtained from a rather poor linear fit of tension versus area expansion in a set of constrained tension simulations (Fig. 4 in Ref. [153]). The similarity of TOCL's compressibility to that of a DOPG membrane (233 ± 19 mN/m) is particularly interesting because TOCL's bending rigidity modulus was found to be twice that of DOPG (Section 3.1). (Note that chemically, TOCL resembles 2 DOPG lipids with linked headgroups).

3.2.4.2 Application of the LTF method to mixed lipid systems

Interestingly, we found that binary mixtures of 30 mol% POPS with 70 mol% POPC or POPE at 20 and 25ºC (respectively) have higher K_A's compared to most single-component bilayers. This is consistent with the combination of their large phosphate-to-phosphate thicknesses (40.1 and 42.8 Å) and small areas per lipid (60.9 and 55 Å^2). Similarly, when increasing amounts of DMPC are added to POPC at 25ºC, the bilayer K_A increases gradually: from 210 ± 22 for 10 mol% DMPC to 262 ± 24 for

75 mol% DMPC, which is accompanied by a systematic decrease in the average bilayer thickness (from 38.6 to 36.6 Å) and area per lipid (from 63.8 to 61.4 Å^2). Indeed, as shown in Fig. B4, we found a strong correlation (0.965) between the bilayer K_A and the ratio of bilayer thickness to area per lipid for all fluid multi-component bilayers we studied, with the exception of the 8:2 DPPC/Chol membrane which is under gel-like conditions (see Table 3.2.2).

Chol has a large effect on membrane compressibility (see Refs. in Table 3.2.2) and this is captured successfully by the LTF analysis as shown by the good agreement with experimental data (see Table 3.2.2 and Fig. 3.2.3). Indeed, the addition of Chol to DOPC at low concentrations (10 mol%) has a negligible effect on K_A, but from approximately 20 mol% and higher, the K_A value starts to increase gradually (see Fig. 3.2.3 and the discussion on the effect of Chol on bilayer mechanical thickness below). In agreement with results from experiments, we also find that Chol has a larger effect on the compressibility of POPC compared to DOPC: at 30 mol% Chol, POPC/Chol has a K_A of 757 ± 87 mN/m while DOPC/Chol has a K_A of 465 ± 57 mN/m. Interestingly, the large K_A of the highly ordered 8:2 DPPC/Chol bilayer at 25ºC (3126 ± 281 mN/m) is similar to the one reported for a 1:1 SM/Chol bilayer at 15ºC (3327 ± 276 mN/m) [183].

3.2.4.3 Compression-bending relationship and the role of chain unsaturation

Another aspect of the validation of our method relates to the reproducibility of known relationships among the mechanical properties of the membrane. One basic principle of the mechanical properties of elastic sheets is that the compression (K_A) and bending (κ_C) moduli are related to one another through the sheet's thickness t_{el} up to some constant C, i.e., $K_A = C\kappa_C/t_{el}^2$. Since the elastic moduli of a lipid bilayer are calculated by assuming that the bilayer behaves as an elastic sheet, we tested whether

the same compression-bending relationship holds for our systems. Using experimentally measured K_A, κ_C and phosphate-to-phosphate thickness of a number of phosphatidylcholine bilayers, this relation was initially demonstrated using *in vitro* data by treating each leaflet as a collection of freely jointed polymer chains [113]. The proposed simple model is referred to as the *polymer brush model* (PBM), which derives a proportionality constant C of 24 and thus gives:

$$K_A \approx \frac{24\kappa_C}{t_m^2} \quad \rightarrow \quad \sqrt{\frac{\kappa_C}{K_A}} \approx t_m \sqrt{\frac{1}{24}} \tag{3.2.17}$$

where t_m is the *mechanical* thickness of the bilayer (i.e. the "deformable" thickness corresponding to t_{el} in the above elastic sheet analogy). Since bilayer thickness is often measured as the average distance between the phosphate atoms of the two leaflets (t_{pp}), t_m can be expressed as $t_{pp} - t_{inc}$ where t_{inc} is some incompressible part within the length of the membrane. Notably, if t_{pp} is the true mechanical thickness of the bilayer, then $t_{inc} = 0$ and in a plot of t_{pp} vs $\sqrt{\kappa_C/K_A}$, according to Eq. 3.2.17 above, all data points would lie on a line with slope $\sqrt{1/24}$ and *x*-intercept 0. However, t_{inc} was found to be non-zero [113] and equal to 10 Å, implying that t_m was 10 Å shorter than t_{pp}. This difference was proposed to reflect the fact that the deformable thickness of a bilayer is limited to its hydrocarbon thickness, and since 5 Å represents the approximate vertical separation between the phosphorus atoms from the hydrocarbon acyl chains on either side of the bilayer, t_m is 10 Å shorter than t_{pp}, explaining the non-zero t_{inc}. The only bilayers described as deviating from this behavior were polyunsaturated membranes [113], which appeared to have shorter mechanical thicknesses than expected.

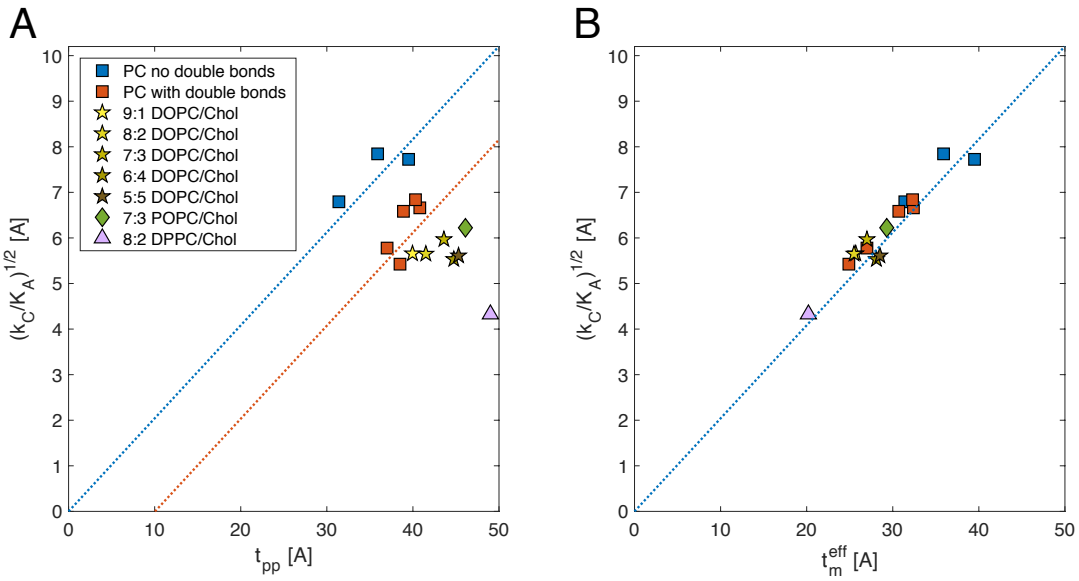

Figure 3.2.4. Application of the polymer brush model (PBM) to simulated bilayers suggests a new definition of bilayer mechanical thickness. A, The ratio of the bilayer bending rigidity (calculated from real-space analysis of splay fluctuations, see Section 3.1) and area compressibility (calculated with the LTF method) from Eq. 3.2.17 is shown as a function of phosphate-to-phosphate distance, t_{pp} for all single-component fully saturated (blue) and unsaturated (red) PC bilayers (Table 3.2.1) and binary mixtures of PC and Chol (yellow, Table 3.2.2). All dotted lines have been drawn with PBM's slope of $\sqrt{1/24}$, and different *x*-intercepts. A non-zero *x*-intercept indicates a deviation of the bilayer mechanical thickness, t_m, from t_{pp} as explained in the text. B, The ratio of the mechanical constants of the same bilayers in (A) are plotted against the *effective* mechanical thickness of the bilayers t_m^{eff}, which is assumed to equal to: 1) t_{pp} for all fully saturated PCs, 2) the difference between t_{pp} and the length of the region around the double bonds for single-component unsaturated PCs and 9:1 DOPC/Chol, 3) the difference between t_{pp} and the length of cholesterol's ring body for all remaining binary mixtures of DOPC and Chol, and POPC and Chol, and 4) the difference between t_{pp} and the full length of cholesterol for DPPC/Chol (Table B3). See text for more details.

We were able to test the relation between compression and bending and the applicability of PBM to the membrane systems we studied by taking advantage of the ability to calculate all three bilayer properties: bending rigidity (Section 3.1), area compressibility and phosphate-to-phosphate thickness (Table B3) from our

trajectories. Fig. 3.2.4A shows the results for all single-component PC bilayers together with the data for the binary mixtures of PC and Chol. Notably, the relationship between bending, compression and thickness could be explained with the PBM model (each dotted line has a slope of $\sqrt{1/24}$) for all single-component bilayers. However, based on the results in Fig. 3.2.4A the membranes can be roughly divided into 2 categories with different mechanical thicknesses (*x*-intercepts): PC lipids with fully saturated acyl chains for which $t_m \approx t_{pp}$ (DLPC, DMPC, DPPC shown in blue) and lipids with 1 or more double bonds for which $t_m \approx t_{pp} - 10\text{Å}$ (POPC, SOPC, DEPC, DOPC, DLiPC shown in red in Fig. 3.2.4). We find that the data in Fig. 3.2.4A cannot be explained by the rationale for t_{inc} given in Ref. [113], because the distance between the phosphates and the hydrocarbon chains on either side of the bilayer, proposed to be the origin of t_{inc}, is independent of the saturation of the lipid chains (e.g. the average distance between the phosphates and the first carbons on the acyl chains is 4.7 Å for DPPC, 5.0 Å for POPC, 4.6 Å for DOPC and 4.6 Å for DLiPC). Instead, our result suggests an alternative model in which the double bonds are the ones responsible for reducing the deformable thickness.

To evaluate this alternative model, we tested if double bonds lead to relatively incompressible regions in the bilayer and decrease t_m by increasing t_{inc}. We first examined how pressure was distributed in tension-free bilayers with varying degrees of saturation (Fig. B5) and analyzed the pressure profile as a function of the average number of atoms in equal volume segments along the membrane normal. If the segments of the membrane each behaved like non-interacting ideal gasses, the pressure P can be expressed as a linear function of the number of atoms n, where the slope is proportional to the usual state variables:

$$P = \left(\frac{RT}{V}\right) n. \tag{3.2.18}$$

However, when pressure is plotted as a function of n for the saturated lipid bilayer DPPC, we find that P is inversely proportional to n (Fig. B6, row 1). This result can be rationalized by utilizing the van der Waals equation of state,

$$\left(P + \frac{n^2 a}{V^2}\right)(V - nb) = nRT, \tag{3.2.19}$$

where a describes attractive interactions between atoms in the gas and b describes the *excluded volume* (i.e. the volume occupied by the atoms that is excluded from the total volume) [207]. Eq. 3.2.19 can thus be rewritten as:

$$P = \left(\frac{RT}{V - nb}\right) n - \frac{n^2 a}{V^2}, \tag{3.2.20}$$

which reveals a strictly negative component that is a function of n and of the strength of the attractive interactions a. Thus, the negative relationship between P and n that is seen for DPPC can be explained by the inter- and intra- molecular bonds present in the bilayer. However, when analyzing membranes with varying degrees of unsaturation, we find that upon adding double bonds, a regime of positive slope occurs (Fig. B6, rows 2-4). This observation can be explained by the dominance of the first term in Eq. 3.2.20 due to the increase in excluded volume caused by the presence of double bonds, which limit the space that can be sampled by the lipid chains. Indeed, a comparison between the van der Waal's constants for ethylene (C_2H_4 $b = 0.05821$ L/mol), ethane (C_2H_6 $b = 0.06499$ L/mol) and hydrogen (H_2 $b = 0.02651$ L/mol) [207, 208] clearly shows that a double bond increases the b term (i.e. $b_{C_2H_4} > b_{C_2H_6} - b_{H_2}$). Further comparison of the corresponding a terms (C_2H_4 $a = 4.612$ bar L^2/mol^2, C_2H_6 $a =$

5.570 bar L^2/mol^2, H_2 $a = 0.2453$ bar L^2/mol^2) suggests that a double bond also decreases the attractive interactions between atoms (i.e. $a_{C_2H_4} < a_{C_2H_6} - a_{H_2}$), which would further contribute to the dominance of the first term in Eq. 3.2.20.

To investigate the expected change in compressibility due to the additional double bonds we interpreted the data in Fig. B5 in the context of the compressibility factor which is defined as:

$$Z = \frac{PV}{nRT}. \tag{3.2.21}$$

When $Z > 1$, the volume is greater than expected for a given pressure due to its incompressibility. When combined with Eq. 3.2.20, the compressibility factor becomes a function of the excluded volume and the interaction between atoms,

$$Z = \frac{V}{V - nb} - \frac{an}{RTV}. \tag{3.2.22}$$

In the regime in which the excluded volume term dominates (i.e. when there are double bonds present), Z becomes large and positive, indicating the membrane is less compressible. This analysis thus confirms that the addition of double bonds to lipid chains leads to relatively incompressible regions that decrease t_m by increasing t_{inc}.

Motivated by the effect of the double bonds on the chain order parameter profile of the lipids, we used a simple heuristic approach to approximate the length of the perturbed region around the double bonds, t_{DB}, for the unsaturated PC bilayers from Fig. 3.2.4A: namely, the perturbed region extends 4 carbons above and below the midpoint of all double bonds for DOPC and DLiPC, and 2 carbons above and below the midpoint of the double bonds for POPC, SOPC and DEPC (see Fig. B7 and Table B3). Remarkably, after subtracting t_{DB} from t_{pp} and replotting the data in Fig. 3.2.4B, all data points moved to the line with *x*-intercept at 0, confirming our hypothesis

regarding the nature and source of the incompressibility, and suggesting that the bilayer mechanical thickness for unsaturated lipids can be defined as the phosphate-to-phosphate thickness *excluding* the regions around the double bonds. We note that this result explains as well the observation in Ref. [113] that polyunsaturated bilayers have shorter mechanical thicknesses, since the perturbed region around their double bonds would be larger and consequently, t_m would be smaller.

Although DLiPC (di18:2 PC) has two more double bonds per molecule than DOPC (di18:1 PC), we find that both DLiPC and DOPC bilayers have similar mechanical thicknesses. This result is consistent with the nearly identical chain stress distributions in monolayers of these two lipids, predicted by Cantor [209]. As illustrated by the analysis in Ref. [209], the effect of the double bonds on monolayer properties (and very likely, bilayer properties) depends on both the number and the location of the double bonds.

Note that in the validation of the PBM described in Ref. [113], the mechanical thickness of DMPC was found to be 10 Å shorter than t_{pp}, like the rest of the examined bilayers. However, the reported DMPC's bending rigidity modulus measured by micropipette aspiration (13.2 kT) was much lower than the one obtained with flicker spectroscopy (31.1 kT, [210]) and also with our computational method (34.7 kT, Section 3.1). The low value of κ_C reported in Ref. [113] is most likely due to the difficulties of applying the micropipette aspiration technique to higher melting temperature lipids as discussed in Section 3.1. If a higher κ_C had been used instead in the PBM analysis, DMPC's mechanical thickness would likely have been predicted to be much closer to t_{pp}, consistent with the data in Fig. 3.2.4.

3.2.4.4 The effect of cholesterol on bilayer mechanical thickness

As illustrated by the analysis above, the effective mechanical thickness of a bilayer, t_m^{eff}, can be expressed as the phosphate-to-phosphate distance excluding the length of any region that resists compression. In this respect, it is interesting to investigate the behavior of lipid bilayers containing cholesterol, as the sterol contains a rigid and relatively incompressible set of rings [201]. Fig. 3.2.4A shows the mechanical properties of various lipid mixtures with cholesterol, including a set of DOPC/Chol bilayers with varying amounts of Chol tested against PBM. Most of these bilayers exhibit a larger deviation from either of the dotted lines, indicating a larger t_{inc} than the non-Chol membranes. To determine t_{inc} for the DOPC/Chol and POPC/Chol membranes, we first used the same heuristic approach as for the unsaturated lipids described above and calculated $t_m^{DB} = t_{pp} - 2t_{DB}$. With this definition, all DOPC/Chol data points from Fig. 3.2.4A shifted to the line with an x-intercept at 0, but for the POPC/Chol bilayer t_m^{eff} was shorter than t_m^{DB} (Fig. B8A). Given the larger effect of Chol on POPC compared to DOPC and the relatively incompressible and rigid nature of the sterol ring structure as discussed above, we reasoned that in the POPC/Chol membrane t_{inc} would be better approximated by the length of cholesterol's ring region, t_{Chol}. To test this hypothesis, we calculated t_{Chol} as the average distance between the C3 and C17 atoms of Chol (using CHARMM36 notation) projected onto the *z*-axis, and found it to be 8.4 Å (Table B3). Remarkably, plotted as a function of $t_m^{Ch} = (t_{pp} - 2t_{Chol})$, the PBM data-point for POPC/Chol fell on the line with x-intercept at 0 (Fig. B8B), indicating that $t_m^{Ch} \approx t_m^{\text{eff}}$.

We then tested how well t_m^{Ch} approximates t_m^{eff} in the DOPC/Chol mixtures. In light of the results in Fig. 3.2.3 showing that Chol has an effect on the bilayer K_A only at 20 mol% or higher, we expected that $t_{inc} \approx 2t_{Chol}$ for these Chol bilayers but not for the 9:1 DOPC/Chol membrane. Indeed, as shown in Fig. B8B, $t_m^{\text{eff}} \approx t_m^{Ch}$ for the 20-50% DOPC/Chol mixtures, and $t_m^{\text{eff}} > t_m^{Ch}$ for the 10% DOPC/Chol bilayer.

Three different regimes are required to describe the effect of Chol on the structural properties of bilayers, corresponding to low, intermediate, and high cholesterol mole fractions [201, 211]. The results presented above and summarized in Figs. 3 and 4 suggest that this is also the case for the Chol effects on bilayer mechanical thickness and compressibility. Thus, our analysis shows that at 10 mol%, Chol does not have an effect on either t_m^{eff} or K_A; at 20 and 30 mol% Chol affects t_m^{eff} and increases K_A *indirectly* through its condensing effect on DOPC; and at 40 and 50 mol% Chol affects t_m^{eff} and increases K_A directly, i.e. its contribution to K_A must be considered explicitly (Fig. 3.2.3). These regimes are consistent with the reduction in the translational and rotational entropy for Chol with increasing concentration: at low mole fractions Chol adopts relatively large tilt angles with respect to the bilayer normal, and thus relatively random orientations (large tilt angles result in larger degeneracy of rotational states [212]). This increased orientational freedom can alleviate any potential stress from compressing the bilayer's thickness. At higher concentrations, Chol's conformational freedom gradually decreases, as Chol molecules tend to align parallel to the bilayer normal [212]. Bilayer compression under such conditions likely involves compression of the Chol molecules.

We also investigated the applicability of the PBM to a fully saturated DPPC/Chol bilayer with 20 mol% Chol. The bilayer was simulated at 25ºC and is in a very ordered gel-like state as indicated by its small area per lipid and large elastic moduli (Tables 3.2.2, B1, B3). The PBM comparison for this system, shown in Fig. 3.2.4A, indicates that the mechanical thickness of the membrane is significantly smaller than t_{pp}. Interestingly, we found that for this bilayer the Chol tail was more rigid than in the other membranes (Fig. B9A), and comparable in its tilt distribution to the ring body of Chol in the 7:3 DOPC/Chol bilayer (Fig. B9B), suggesting that it was harder to compress, and that the mechanical thickness of the membrane could exclude the sterol

tail as well due to the high order in the system. Indeed, considering in the calculations the full length of Chol, including its ring and tail regions, we were able to successfully recover t_m^{eff} of the DPPC/Chol bilayer (Fig. 3.2.4B). Both Chol concentration and the temperature determine the thermodynamic phase behavior of the bilayer and thereby the degree of Chol's conformational freedom. Therefore, it remains to be investigated whether Chol affects the mechanical properties of other fully saturated lipids in a similar way, and how the observed relationships vary with temperature.

3.2.4.5 Revised definition of bilayer mechanical thickness clarifies conflicting reports on PBM's applicability

As illustrated by our analysis, the effect of double bonds and cholesterol on bilayer's mechanical thickness has not been systematically characterized before. Therefore, we sought to examine the relation of our findings to published observations from both *in vitro* and *in silico* work. We found that our results resolve some contradictory reports in the literature regarding the validity of PBM for different bilayers. Indeed, since PBM was first introduced, the model has been experimentally tested in a number of studies by assuming that $t_m = t_{pp} - 10$ Å, yielding conflicting results [132, 152, 189]. In 2008 Pan et al. found a good agreement between their results and PBM's predictions for DOPC [152] but in 2009 they reported that the theory was incapable of describing the relationship between the mechanical constants in cholesterol-containing bilayers [189]. In a comprehensive review of bilayer mechanical properties from MD simulations published more recently, Venable et al. found a relatively good agreement between the simulation results and PBM for POPC and DOPC but there was a bigger deviation for DMPC and DPPC (see Fig. 11 in Ref. [132]). These conflicting observations can be consolidated in light of our finding that the presence of cholesterol and/or acyl chain unsaturation can affect the mechanical

thickness of the bilayers. Not surprisingly, PBM was successfully applied to lipids with 1 or 2 double bonded tails such as DOPC and POPC both in the experimental and computational studies, since for those lipids t_m can indeed be approximated by $t_{pp} - 10$ Å. However, according to our analysis, the incompressible body of cholesterol has length of about 8.3 Å, effectively decreasing t_m by an additional 6 Å (3 Å from each leaflet), i.e. $t_m \approx t_{pp} - 16$ Å. Thus, if the hydrocarbon thickness $2D_C$ (used as a proxy to $t_{pp} - 10$ Å) in Eq. 3.2.6 in Ref. [189] is substituted with $(2D_C - 6$ Å), the ratio between predicted and actual κ_C for SOPC and DOPC in the presence of 30 mol% cholesterol becomes 1.0 and 1.36, respectively, indicating a good agreement with the theory contrary to the stated conclusion in Ref. [50]. Similarly, since DMPC and DPPC are fully saturated and hence $t_m \approx t_{pp}$, the use of $t_{pp} - 10$ Å for their mechanical thickness in Ref. [132] explains the larger deviation of their calculated bending moduli from PBM's predictions.

Together, all these results are consistent with the notion that bilayer mechanical thickness depends on lipid composition and cannot be simply taken as the bilayer hydrocarbon thickness. Our analysis illustrates a simple but general principle of bilayer mechanics whereas the assumption for elastic material behavior holds only for the regions within the membrane that are equally compressible. In particular, the presence of both acyl chain unsaturation and cholesterol produce non-uniform compressibility in the membrane hydrocarbon core that needs to be taken into account when quantifying the deformable membrane thickness.

3.2.5 Conclusion and summary

We have presented a new computational framework for calculating area compressibility moduli of lipid bilayers and their individual leaflets from all-atom MD simulations that is based on sampling local thickness fluctuations from one sufficiently

converged MD simulation. The method alleviates a number of limitations of existing computational approaches, and yields elastic moduli that are in agreement with available experimental data for both single and multi-component bilayers composed of saturated, unsaturated lipids and cholesterol and simulated at different temperatures. Importantly, because it is free from sampling of global lateral bilayer fluctuations, our method is uniquely capable of analyzing the area compressibility of bilayers under tension (i.e. simulated in an NPAT ensemble). It should also allow, in principle, future applications for the calculation of the spatial variability in leaflet compressibility moduli in the presence of transmembrane inclusions.

Notably, the presented data show that the mechanical properties of the simulated bilayers, and the relation between specific parameters representing their properties, are consistent with an elastic sheet model and consonant with a polymer brush model (PBM). However, we showed that the application of the PBM requires a significant modification of the canonical definition of the membrane mechanical thickness as simply the hydrocarbon region of the bilayer. We demonstrated the specific considerations that are necessary to determine the appropriate mechanical thickness needed to calculate unknown elastic moduli. These include the quantitative accounting for acyl chain unsaturation and cholesterol concentration, both of which introduce relatively incompressible regions within the bilayer that decrease the effective mechanical thickness.

While all of the bilayers we have examined have the same lipid composition and the same number of lipids in their two leaflets, the physical model underlying Eq. 3.2.10 is general enough to allow for analysis of the great variety of compositionally asymmetric bilayers that are physiologically relevant, as their local leaflet K_A-s could be different. This aspect of the method continues to be the subject of our ongoing computational studies. Systematic experimental measurements of the compressibility

moduli of asymmetric bilayers, especially ones whose leaflets are expected to have significantly different mechanical properties, would greatly benefit the validation and/or refinement of the theoretical predictions from the harmonic mean relationship between the bilayer K_A and the local leaflet moduli (Eq. 3.2.10).

3.3 Conclusion

Chapters 3.1 and 3.2 establish the robustness and versatility of two computational methodologies that utilize real-space local fluctuations to obtain the mechanical properties of individual bilayer leaflets from MD simulations. Together with the improvements in the development of lipid force fields [156, 195, 213] and the availability of bilayer construction and equilibration protocols [142], the ability to calculate elastic constants from simulated bilayers makes the otherwise experimentally infeasible analysis of many lipids and lipid mixtures under different external conditions readily accessible. While large discrepancies in the mechanical constants obtained with different techniques in vitro preclude meaningful comparisons between different systems, an added advantage of the presented computational frameworks is that they provide a single tool that can be used to examine the relative properties of various membranes. The protocols can thus reveal the contribution of bilayer elasticity to various experimental observations, as discussed below.

In Chapter 2 we showed that mixtures with hybrid and non-hybrid lipids exhibit very similar phase behavior. In particular, three-component bilayers of DSPC, Chol and one of two low-melting lipids—either the hybrid lipid POPC, or the non-hybrid lipid DLPC—displayed almost identical transitions in domain size and morphology when the low-melting lipid was gradually replaced with DOPC. The ability to induce nanoscopic domains in a system composed only of symmetric lipids suggests that chain asymmetry is not the main driving force behind nanodomain formation, as

previously hypothesized [85-90]. Instead, interfacial tension between domains is likely lowered by some more general mechanism. In 2013 Heberle et al. discovered a direct correlation between domain size and the thickness mismatch between co-existing phases [8], suggesting that larger differences between the bulk structural properties of the two phases are responsible for the small domain size. The results in Sections 3.1 and 3.2 give further insights into the relative contribution of the phases' mechanical properties to the observed phase behavior. In particular, we can use the following observations to reason about the elastic properties of domains:

1) POPC and DLPC have very similar bending rigidity (Table 3.1.2) and tilt moduli (Table 3.1.3), and both are larger than the respective DOPC constants;
2) Saturated higher-melting lipids have generally larger bending rigidity and tilt moduli than lower-melting lipids (see DMPC and DPPC in Tables 3.1.2-3.1.3, and Section 3.1.4);
3) The liquid-ordered (Lo) phase in Type II mixtures (such as DSPC/DOPC/Chol) has more DSPC and Chol than the Lo phase in Type I mixtures (such as DSPC/POPC/Chol) (compare the composition of the tieline endpoints on the Lo side of the Ld+Lo region in the phase diagrams in Ref. [214], see also Ref. [215]);
4) The area compressibility modulus increases with increasing amounts of high-melting lipid (compare the DMPC/POPC bilayers in Table 3.2.2) and cholesterol (Fig. 3.2.3).

From (1) and (2) it follows that there are likely larger differences between the bending rigidity and tilt moduli of the Lo and Ld phases in Type II mixtures compared to Type I mixtures (see also [137]). Similarly, from (3) and (4) it follows that the same trend holds for the area compressibility modulus. Hence, these results suggest that the

mismatch in both the structural and mechanical properties of the two types of phases determines domain size in the three-component mixtures: larger mismatch acts to increase line tension leading to macroscopic phase-separation in Type II mixtures while smaller mismatch makes the two phases more similar, effectively reducing the energy penalty of the Ld/Lo boundary and leading to nanodomain formation in Type I mixtures. This hypothesis is directly confirmed by experimental measurements of the bending rigidity of Ld and Lo phases in three-component DOPC and POPC mixtures at low cholesterol mole fraction (see Table 1 in Ref. [215]). It is also consistent with predictions from the model proposed by Kuzmin et al. which links line tension to the bending rigidity and tilt moduli of the two phases [216]: increasing the bending rigidity (and/or tilt modulus) of the Lo phase while keeping all other constants the same and ignoring the contribution from spontaneous curvature, leads to an increase in line tension (Eq. 17 in Ref. [216]).

Similarly, our results can explain the curvature-dependent domain sorting observed on the surface of giant unilamellar vesicles (GUVs). Baumgart et al. used fluorescence microscopy to examine the relationship between domain composition and local membrane curvature [95] in three-component mixtures of egg sphingomyelin (which is predominantly palmitoyl sphingomyelin, PSM), DOPC and Chol. The authors saw that the DOPC-rich Ld phase favored the high curvature regions on GUVs while the SM/Chol-rich Lo phase segregated into the flat surface segments (see Figures 1f and 2g-h in Ref. [95]). This sorting behavior can be directly related to the mechanical properties of the two phases: relative to DOPC, whose bending rigidity and area compressibility moduli at 25°C are 18.3 ± 0.3 k_BT (Table 3.1.2) and 256 ± 17 mN/m (Table 3.2.1), respectively, and are expected to be even lower at higher temperature, those of PSM at 55°C are much higher: 41.8 ± 1.4 k_BT and 312 ± 29 mN/m. In addition, the presence of Chol in the domains would, if anything, increase

the differences between the two phases: at 15°C we found that the area compressibility of the 1:1 binary mixture of DOPC/Chol is 886 ± 84 mN/m (Table 3.2.2) while that of a 1:1 SM/Chol bilayer at the same temperature was reported to be 3327 ± 276 mN/m [183]. Since the moduli of both mixtures would decrease with increasing temperature and the mole fraction of Chol is expected to be much higher in the Lo phase compared to the Ld phase (see, e.g. [84]), the big difference between the mechanical properties of the two phases is very likely to be preserved. These results indicate that the energy of membrane deformation of the SM/Chol-rich Lo domains is higher than the penalty for deforming the DOPC-rich Ld phase, explaining the respective preferences of the phases for the flat vs. curved regions on the GUV surface.

The presented computational methodologies can thus be used to better understand experimental observations and formulate testable conjectures about the corresponding driving forces. As current biophysical studies continue to address increasingly complex model membranes, the difficulties in measuring membrane mechanical constants in vitro necessitate the application of alternative techniques to characterize their properties. In that respect, MD simulations and the methods discussed in this and later chapters provide convenient tools for the analysis of both symmetric and asymmetric membranes.

CHAPTER 4
CHOLESTEROL PROMOTES BINDING OF RETROVIRAL MATRIX PROTEIN BY INDIRECTLY AFFECTING MEMBRANE ELECTROSTATICS AND SOLVATION PROPERTIES*

4.1 Abstract

Binding of the retroviral structural protein Gag to the cellular plasma membrane (PM) is mediated by the protein's matrix (MA) domain. Prominent among MA-PM interactions is electrostatic attraction between the positively charged MA domain and the negatively charged PM inner leaflet. Previously, we reported that membrane association of HIV-1 Gag, as well as purified Rous sarcoma virus (RSV) MA and Gag, depends strongly on the presence of acidic lipids and is enhanced by cholesterol (Chol). The mechanism underlying this enhancement was unclear. Here, using a broad set of in vitro and in silico techniques we addressed molecular mechanisms of association between RSV MA and model membranes, and investigated how Chol enhances this association. In neutron scattering experiments with liposomes in the presence or absence of Chol, MA preferentially interacted with pre-existing POPS-rich clusters formed by non-ideal lipid mixing, binding peripherally to the lipid headgroups with minimal perturbation to the bilayer structure. Molecular dynamics simulations showed a stronger MA-bilayer interaction in the presence of Chol, and a large Chol-driven increase in lipid packing and membrane surface charge density. Although in vitro MA-liposome association is influenced by disparate variables, including ionic strength and concentrations of Chol and charged lipids, continuum electrostatic theory revealed an underlying dependence on membrane surface potential. Together, these

* The following chapter and its supporting information (Appendix C) are reproduced from: Doktorova, M., Heberle, F. A., Kingston, R. L., Khelashvili, G., Cuendet, M. A., Wen, Y., Katsaras, J., Feigenson, G. W., Vogt, V. M. & Dick, R. A. 2017. *Biophysical journal*, *113*(9), 2004-2015. They have been modified to fit the format of the thesis. MD, FAH and RD designed the research and contributed equally to the work. MD performed the MD simulations and did the MD simulation- and Gouy-Chapman theory-based analysis.

results conclusively show that Chol affects RSV MA-membrane association by making the electrostatic potential at the membrane surface more negative, while decreasing the penalty for lipid headgroup desolvation. The presented approach can be applied to other viral and non-viral proteins.

4.2 Introduction

For HIV and Rous sarcoma virus (RSV), formation of an infectious form of the virus requires interaction of the viral structural protein Gag with the acidic inner leaflet of the plasma membrane (PM). The resulting lateral Gag-Gag interactions lead to the formation of a Gag lattice and subsequently a budding virus particle. The N-terminal matrix (MA) domain of Gag mediates interaction with the PM by responding to multiple signals, including electrostatic and hydrophobic interactions, and in some cases, specific interaction with lipid headgroups [217]. Cholesterol (Chol), an abundant PM lipid, is a critical component of the viral envelope [218]. Compared with the PM, the viral envelope is enriched in sphingomyelin (SM) and anionic lipids, including phosphatidylserine (PS) and phosphatidyl (4,5)-inositol bisphosphate (PI(4,5)P2) [219-221]. Moreover, viral budding sites co-localize with tetraspanin-rich domains [222]. These data suggest that Gag selects or modulates compositionally distinct domains in the PM.

Neutron reflectometry (NR) has shown that for HIV and RSV Gag, the highly basic region of MA is oriented towards the membrane surface [223, 224], and that the Gag conformation changes upon addition of a nucleic acid [225]. One drawback of NR is the requirement of a supported lipid bilayer which can influence lipid diffusion [226] and mixing behavior [227]. Moreover, NR is primarily sensitive to the time-averaged matter distribution in the direction perpendicular to the bilayer plane, while in-plane structural information is much more difficult to access. However, a related

technique, small-angle neutron scattering (SANS), can provide information about both in-plane and out-of-plane bilayer structure. Since neutrons are scattered differently by protium (^{1}H) and hydrogen's stable isotope deuterium (^{2}H), mixtures of protiated and deuterated lipids generate a strong in-plane contrast upon clustering or phase separation, resulting in a distinct SANS signature [8], thus providing a unique tool to probe lipid lateral organization [228]. SANS can also easily be applied to liposomes of the type used in biochemical or NMR analyses of protein-membrane interaction [149, 229].

Complementing the time averaged structural data from SANS, molecular dynamics (MD) simulations provide atomistic detail, allowing a focused examination of different protein binding modes and their dependence on membrane structure. For example, a coarse-grained MD study found that HIV MA can sequester multivalent but not monovalent acidic lipids upon anchoring in membranes without Chol [230]. However, the cellular PM contains approximately 40 mol% Chol [45], and liposome binding of both RSV and HIV Gag is stimulated by physiological Chol concentrations in model membranes [231]. Both in vitro and in silico experiments have shown that the addition of Chol to fluid bilayers causes significant structural changes, including increased bilayer thickness [232, 233], increased headgroup spacing [234] and hydration [235], and reduced water penetration into the membrane hydrocarbon region [235, 236].

Here, using SANS, MD simulations, and liposome binding assays, we investigated the mechanism by which Chol influences RSV MA membrane binding, and whether protein binding changes the structure or lateral organization of lipids in the bilayer. Our results show that in bilayers with a fixed concentration of acidic lipids, Chol promotes binding of RSV MA by making the electrostatic potential above the membrane surface more negative, while at the same time decreasing the energetic

penalty for lipid headgroup desolvation. We also find that MA selectively binds to pre-existing patches of acidic lipids, but does not significantly affect their structure or composition. These findings reveal the intrinsic ability of lipid membranes to modulate the electrostatically-driven binding of charged molecules, and have important implications for interpreting in vitro binding data.

4.3 Materials and methods

4.3.1 Materials

Phospholipids were purchased from Avanti Polar Lipids (Alabaster, AL) as dry powders and dissolved in HPLC-grade chloroform. Lipid stock concentrations were determined by inorganic phosphate assay [237] with an error < 2%. Cholesterol powder was purchased from Nu Chek Prep, Inc. (Elysian, MN) and prepared as chloroform stock solutions at defined concentration using standard gravimetric procedures. Ultrapure H_2O was obtained from a High-Q purification system (Wilmette, IL). D_2O (99.96%), deuterated Tris buffer (Tris-D11, 98%), and deuterated glycerol (glycerol-D8, 99%) were purchased from Cambridge Isotopes (Andover, MA). Deuterium chloride (DCl) and Tris(2-carboxyethyl)phosphine (TCEP) were purchased from Sigma-Aldrich (St. Louis, MO) and AMRESCO (Solon, OH), respectively. Buffer solutions were filtered through a pre-rinsed 0.2 micron filter prior to use.

4.3.2 Protein purification and liposome binding

Protein was purified as previously described [224] and stored at –80°C until use. Preparation of 100 nm extruded liposomes and binding reactions were performed as previously described [238]. Briefly, all binding reactions were performed with 15 μg (4.7 μM) protein and 50 μg (328–431 μM) lipid in 200 μL at 20 mM Tris-HCl pH 8,

and adjusted with buffer to the stated NaCl concentration. Binding reactions were subjected to centrifugation at 90,000 RPM (RCF = 351,955 × g) in a TLA-100 rotor (Beckman Coulter, Brea, CA) for 45 min at 4°C to pellet the liposome-bound protein. Pelleted protein was subjected to SDS-PAGE analysis. Gels were stained with Coomassie blue and then destained, and band intensity was determined by densitometry analysis using ImageQuant 5.2 (Molecular Dynamics, Sunnyvale, CA). Each binding reaction was repeated no less than four times. The binding data reported in Fig. 4.5 is the average, and error bars the standard deviation, of measurements from these independent replicate samples.

4.3.3 SANS sample preparation

Lipid mixtures were prepared by transferring lipid and cholesterol chloroform stocks to a glass vial with a glass syringe. Organic solvent was removed with a nitrogen stream and gentle heating, followed by vacuum drying for > 12 h. Dry lipid films were hydrated to 40 mg/mL total lipid concentration with "liposome storage buffer" (D_2O, 50 mM NaCl, 20 mM Tris-D11-DCl, 2 mM TCEP, pD 8), then vortexed vigorously to generate multilamellar vesicles (MLVs). The MLV suspension was incubated for 1 h with intermittent vortexing, followed by 5 freeze/thaw cycles. LUVs were prepared using a miniextruder (Avanti Polar Lipids, Alabaster, AL) by passing the lipid suspension 31 times through a single 100 nm pore size polycarbonate filter. RSV-MA solution in "protein storage buffer" (D_2O, 375 mM NaCl, 20 mM Tris-D11-DCl, 2 mM TCEP, 5 wt% glycerol-D8, pD 8) at 40 mg/mL was prepared from protein in H_2O buffer by serial dilution and centrifugal filter concentration.

Samples for SANS measurements were prepared by combining and pipet-mixing 57 µL of the protein solution with 150 µL of the liposome solution and 390 µL pure D_2O. By design, a small excess of osmolytes in the vesicle interior (liposome storage

buffer) compared to the extravesicular buffer after mixing (D_2O, 48 mM NaCl, 7 mM Tris-D11-DCl, 0.7 mM TCEP, 0.5 wt% glycerol-D8, pD 8) generated slightly hypotonic conditions that tended to swell the vesicles. This precaution was necessary to avoid distorted or partially collapsed vesicles which result in complex scattering curves that cannot be analyzed with conventional spherical shell form factors. The final protein and lipid concentrations of SANS samples were 3.8 mg/mL (0.227 mM) and 10 mg/mL (13-16 mM, depending on the lipid composition), respectively, with all protein located in the extravesicular fluid. At these concentrations, enough protein was present to cover 70–80% of the vesicle surface area, assuming complete binding and average lipid and protein cross-sectional areas of 48–65 $Å^2$ and 1375 $Å^2$, respectively. The actual surface coverage determined by analysis of the scattering curves was 35–40% (Table C2), indicating that approximately half of the protein was bound to vesicles, with half remaining free in solution.

4.3.4 SANS data collection

Small-angle neutron scattering (SANS) measurements were performed using the BL-6 extended Q-range small-angle neutron scattering (EQ-SANS) instrument of the Spallation Neutron Source (SNS) at Oak Ridge National Laboratory (ORNL). Samples were loaded into 2 mm path-length quartz banjo cells (Hellma USA, Plainview, NY) and mounted in a temperature-controlled cell holder with ~ 1°C accuracy. EQ-SANS data were taken at a 2.5 m sample-to-detector distance with a 2.5–6.0 Å wavelength band for a total scattering vector of $0.01 < q < 0.5$ $Å^{-1}$. Scattered neutrons were collected with a two-dimensional (1 × 1 m) ^3He position-sensitive detector (ORDELA, Inc., Oak Ridge, TN) with 256 × 192 pixels. The 2D data were reduced using the software package Mantid [239]. During reduction, data were corrected for detector pixel sensitivity, dark current, and sample transmission, as well as background

scattering from buffer. The one-dimensional scattering intensity $I(q)$ [$q = 4\pi \sin(\theta)/\lambda$, where λ is the neutron wavelength and 2θ is the scattering angle relative to the incident beam] was obtained by radial averaging of the corrected 2D data.

4.3.5 SANS data analysis

SANS curves were fit with a laterally heterogeneous core-shell (HCS) form factor [240] in order to account for coherent scattering contributions from both transverse (out-of-plane) and lateral (in-plane) neutron scattering length density (NSLD) variation within the vesicle (a detailed description of the model is provided in the SI). As shown schematically in CS2A, transverse NSLD variation arises primarily from the different atomic composition of the lipid headgroup and hydrocarbon layers, while lateral NSLD variation is primarily due to lipid clustering resulting from non-ideal mixing or phase separation, and is pronounced when some lipid species are selectively deuterated. Both the transverse and lateral NSLD variation are further influenced by the presence of surface-bound protein, which has a different NSLD than lipid or water.

The HCS form factor requires as input the transverse NSLD profiles of the domain and continuous phases, as well as the size, surface coverage, and spatial arrangement of the domains (Fig. C2A). Our analysis allowed for the possibility of nonrandom lipid mixing, which we modeled as a PS-rich domain phase surrounded by a continuous phase depleted in PS. The compositions of the two phases were allowed to vary in the fit, but not independently; given a fixed overall vesicle composition, a domain composition, and phase area fractions, the composition of the continuous phase was constrained by material balance. Following Kučerka et al. [241], NSLD profiles for the domain and continuous phases were derived from underlying lipid volume probability distributions, modeled as the sum of separate distributions for the lipid headgroups and hydrocarbon chains. The total unit cell volume was calculated as

a mole-fraction weighted sum of lipid component volumes obtained from literature (Table C3) and constrained in the fit, leaving adjustable parameters for the area per lipid A_L and headgroup thickness D_H. Additional structural parameters, including the total bilayer thickness D_B and the hydrocarbon thickness $2D_C$, were derived from relationships between the adjustable parameters and the lipid headgroup and hydrocarbon volumes as described in the SM. For MA-containing samples, a Gaussian volume probability distribution with adjustable parameters for position (z_P) and width (σ_P) was added to the domain phase. NSLD profiles were then obtained as a sum of the separate headgroup, hydrocarbon, and protein volume probability distributions multiplied by their respective total scattering lengths. Lateral structure was modeled by assuming round domains with a 21 Å radius (corresponding to a cross-sectional area of 1375 Å^2 for an MA monomer) that were randomly arranged on the vesicle surface. The in-plane contributions to the vesicle form factor were calculated to 200 expansion orders and included an adjustable parameter for the fraction of the vesicle surface area occupied by domains, a_P.

For each nominal sample composition (i.e., POPC/POPS 70/30 mol%, and POPC/POPS/Chol 34/30/36 mol%), separate SANS samples with different contrast were prepared using the four permutations of protiated and palmitoyl chain-perdeuterated variants of the two phospholipids (i.e., POPC or POPC-D31, mixed with POPS or POPS-D31, Fig. C2C-F). Fitting was implemented in Mathematica 11.0 (Wolfram Research, Champaign, IL) and MATLAB R2013b (MathWorks, Natick, MA). Each data set was fit independently, and the reported structural parameters represent the mean and standard deviation from the four fits. A complete list of the structural parameters is found in Table C2.

4.3.6 High-resolution structure of MA

To provide the structural models required for the detailed interrogation of molecular interactions, we crystallized full length RSV MA (155 amino acids) and determined an experimentally phased X-ray structure at 2.8 Å resolution. Residues 1−102 were well resolved but there was no interpretable electron density for the remainder of the molecule. We therefore characterized a truncated variant (MA2−102) with the disordered region removed. This variant crystallized in the same form as the full-length molecule (space group $I4_122$), and also in an alternate form (space group $I4_1$). Structures were determined to 3.2 and 1.8 Å resolution, respectively. The three crystallographic models (Table C1) differ in detail from an earlier NMR solution structure for the first 88 amino acids [242]. This likely reflects both the limited restraint set and the methodology used to derive the NMR model [243]. However, consistent with NMR relaxation measurements [242], the basic surface loop (residues 14−22), which is critical for membrane association, is the most mobile element in the crystallographic models. For crystals in the space group $I4_122$, the final helix of the N-terminal domain (helix 6, residues 89−102) interdigitates with the corresponding helix from a neighboring molecule, forming a symmetric dimer (Fig. C1A). In contrast, for space group $I4_1$ crystals, the C-terminal sequence is disordered and neither helix 6 nor the dimer is observed. Since deletions in the C-terminal region of MA (amino acids 87−155) do not abrogate viral budding and infectivity [244], and since there is no evidence that MA dimerizes in solution [224] or when membrane-associated [245], it is likely that the crystallographic dimer is biologically irrelevant. Because the monomer structure was not available when our MD simulations were carried out, one subunit of the dimer was adapted as the working model for the in silico experiments reported here (see below and Fig. C1).

4.3.7 Molecular Dynamics simulations

All MD simulations were performed with the NAMD software [155] and the CHARMM36 force field for lipids and protein [156, 246]. The simulations were run with a 2 fs time-step with all bonds to hydrogens constrained, in NPT ensemble with semi-isotropic (for bilayer simulations) or isotropic (for water box simulation) pressure coupling at 1 bar and 293 K. Temperature and pressure were controlled with a Langevin thermostat and barostat, with a damping parameter set to 5 ps^{-1}, a piston period of 200 fs, and a piston decay of 50 fs. The *vdwForceSwitching* option was used for all membrane simulations [132]. Van der Waals cutoff and switching distances were set to 12 and 10 Å, respectively. Particle Mesh Ewald (PME) was used with a grid spacing of 1.0 Å.

In order to determine a starting conformation for MA in subsequent MA-membrane simulations, we first simulated one monomer from the crystal dimer structure of MA (Fig. C1A) in an aqueous environment consisting of a water box with 13,470 water molecules and 20 mM NaCl. Following the hypothesis that the large angle between the C-terminal helix of MA (residues 91 to 102) and the rest of the protein body was dimer-specific and would not be a stable conformation of the MA monomer, we fixed the C-terminal helix in space and monitored the relaxation dynamics of the rest of the protein. The system was energy minimized for 5400 steps, then run for 500 ps with a 1 fs time step, followed by a production run of 110 ns. In the course of the simulation, the protein body moved closer to the C-terminal helix, adopting a stable compact conformation (Fig. C1B-C). The protein coordinates from the last frame were used as the starting MA conformation for MA-membrane simulations described below.

The two simulated bilayers (POPC/POPS 70/30 mol% and POPC/POPS/Chol 34/30/36 mol%) were taken from [247]. After the production runs (191 and 270 ns

respectively), MA was placed on one or both sides of the bilayer and oriented with respect to the membrane surface in a way that optimized interactions between lysines and the surface as described for HIV MA [223], and for RSV MA [248]. Multiple replica simulations of the bilayer-protein systems in 50 mM NaCl were run for ~ 200 ns each and analyzed jointly as described in the SM.

4.4 Results and discussion

4.4.1 MA binds to lipid headgroups without perturbing the overall bilayer structure

We used SANS to determine the bilayer structure before and after RSV MA binding to 100 nm diameter unilamellar vesicles (LUVs, also referred to as liposomes throughout) at 20°C and 50 mM NaCl. Motivated by previous work showing that cholesterol enhances MA binding [231], we examined two compositions having a fixed amount of the negatively charged lipid POPS, namely POPC/POPS 70/30 mol% and POPC/POPS/Chol 34/30/36 mol%. The POPS concentration was based on estimates of the concentration of charged lipids in the PM inner leaflet (32 mol%, Table C4). These compositions allow for a direct comparison that isolates the effect of cholesterol, and are simple enough to be tractable in a SANS analysis. Scattering data (Fig. C2C-F) were analyzed with a model describing the projected distribution of matter (i.e., lipid headgroups, lipid chains, protein and water) along the bilayer normal, as a function of distance from the bilayer center. In particular, we used volume probability distributions to model the relative locations of the different components, which enabled the determination of bilayer structural parameters including area per lipid, total bilayer thickness and hydrocarbon thickness, as well as the position of the bound protein within the bilayer and the transverse water distribution (Appendix C).

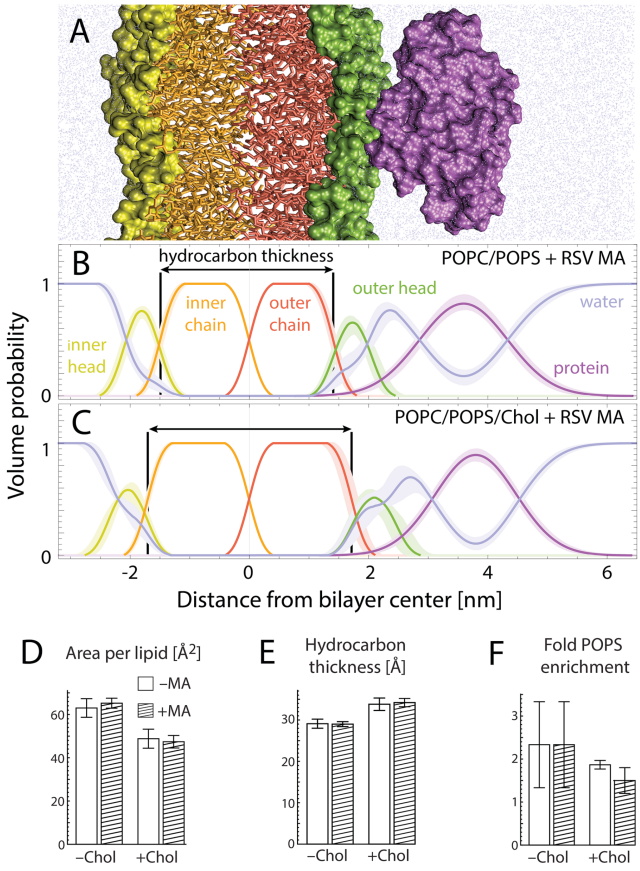

Figure 4.1. MA binds peripherally to lipid bilayers with minimal structural perturbation. (A) An MD simulation snapshot showing the different lipid and protein components modeled in the SANS analysis: inner leaflet headgroups (yellow) and chains (orange), outer leaflet chains (red) and headgroups (green), protein (purple), and water (blue). Below the cross-sectional view, the volume probability profiles obtained from experimental SANS data are displayed (thick lines surrounding the volume probability profiles reflect uncertainties): POPC/POPS 70/30 mol% with bound RSV MA (B); POPC/POPS/Chol 34/30/36 mol% with bound RSV MA (C). (D–F) structural parameters obtained from SANS analysis of POPC/POPS bilayers without and with Chol, in the absence (white bars) or presence (hatched bars) of RSV MA: average area per molecule (D); lipid hydrocarbon thickness (E); and fold-enrichment of POPS over the average composition in PS-rich clusters (F). The reported structural parameters and errors represent the mean and standard deviation from independent fits to four different neutron contrast data sets as described in the text and Appendix C. A complete list of structural parameters is found in Table C2.

Figure 4.1 shows the lipid and protein matter distribution for bilayers without (Fig. 4.1B) and with Chol (Fig. 4.1C) obtained from SANS analysis. The bulk of the protein

density (purple curves) resides above the lipid headgroups (green curves), although a small degree of overlap suggests that some residues are able to intercalate between lipid headgroups. Importantly, practically no protein density overlaps with the lipid hydrocarbon region (red curves), an indication that MA does not penetrate the bilayer's hydrophobic core, and binds in a manner consistent with electrostatic attraction to the negatively charged headgroup region. Structural parameters recovered from our analysis are in agreement with published values for POPC and POPS bilayers [145, 249]. The replacement of 36 mol% of POPC with Chol (mimicking physiological Chol concentrations and charged-to-neutral headgroup ratios) reduced the area per lipid (defined here and throughout to include Chol) by ~ 25%, from 63.0 to 48.8 $Å^2$ (Fig. 4.1D). Hydrocarbon chain thickness increased by nearly 5 Å, from 29.1 to 33.8 Å (Fig. 4.1E), also consistent with published data [250]. Neither the area per lipid nor the hydrocarbon thickness changed significantly in the presence of MA, suggesting that protein binding does not perturb the bilayer structure. This finding was supported by Electron Spin Resonance (ESR) measurements showing that the lipid acyl chain order parameter did not change in the presence of MA (Fig. C3). A complete list of structural parameters obtained from the SANS analysis is found in Table C2.

4.4.2 MA binds to POPS clusters

Neither POPC/POPS nor POPC/POPS/Chol bilayers are phase separated at 20°C (L. Goh personal communication). Such mixtures may nevertheless be heterogeneous on small (< 5 nm) length scales [92]. To a first approximation, non-ideality arises from the different nearest-neighbor interactions of unlike lipids (e.g., POPC and POPS). Interactions between unlike phospholipids can be unfavorable [55], resulting in clustering of like lipids in order to reduce unlike contacts. To account for the

possibility of such non-random lipid mixing, we analyzed our scattering data using a form factor appropriate for laterally heterogeneous vesicles [240]. We analyzed four combinations of protiated and palmitoyl chain-perdeuterated variants of POPC and POPS (Fig. C2B) in order to take full advantage of neutron contrast for detecting possible lateral segregation of these lipids. The scattering model allowed for two distinct bilayer environments whose compositions were varied in the fit while maintaining overall matter balance (Fig. C2A). In the analysis of data from MA-containing samples, the compositions of the protein-bound and protein-free portions of the bilayer were also allowed to vary. Consistent with previous reports [251], the SANS analysis indicated a "patchy" bilayer characterized by lipid clusters that are enriched approximately two-fold in POPS (Fig. 4.1F). In MA-containing samples, we found a similar amount of PS enrichment in the protein-bound bilayer composition (Fig. 4.1F). The addition of Chol did not have a significant effect on the extent of non-ideal mixing of POPC and POPS, either in the presence or absence of MA.

Although the lateral heterogeneity observed in our SANS analysis is statistically significant, the large uncertainties in PS enrichment (Fig. 4.1F) do not allow us to draw any conclusions regarding the ability of MA to sequester charged lipids upon binding. To test this possibility, we applied a previously developed computational method based on continuum mean-field theory [252, 253] to quantify the extent of lipid redistribution in response to protein binding to an ideally mixed bilayer, and to calculate changes in the corresponding adsorption free energy upon the de-mixing process (Fig. C4, Appendix C). Our calculations predict that MA cannot effectively sequester POPS as has been shown previously for other proteins (see [253] and references therein); minimal lipid segregation was achieved, which produced an insignificant change in the adsorption free energy ($< 1\ k_BT$). Taken together with the SANS results, this calculation suggests that MA does not induce lipid redistribution.

Rather, the protein takes advantage of the inherent patchiness of the non-ideally mixed bilayers, binding to the membrane primarily at sites already enriched with anionic lipids.

4.4.3 Cholesterol enhances MA lysine-membrane contacts

To investigate the atomic-level details of MA-membrane interactions, we performed MD simulations mimicking the SANS experimental conditions, i.e. monomeric MA in the presence of a lipid membrane composed of either POPC/POPS at 70/30 mol% (Fig. 4.2A), or POPC/POPS/Chol at 34/30/36 mol% (Fig. 4.2B) in 50 mM NaCl solution at 20°C. The MA structure used as a starting point in these simulations was obtained from the monomer of the dimer crystal after relaxation in

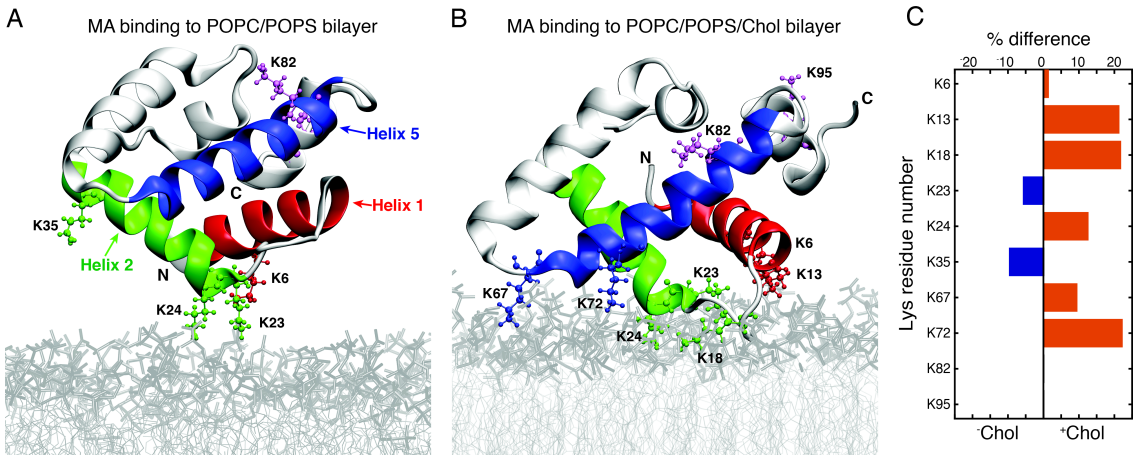

Figure 4.2. Cholesterol enhances MA-membrane contacts. Snapshots of MA interacting with POPC/POPS (A) and POPC/POPS/Chol (B) bilayers after 100 ns of simulation (for corresponding movies, see Movies S1A-B in Ref. [1]). The protein is displayed in silver cartoon representation with specific lysine residues labeled and shown in space-fill representation ("N" and "C" denote the protein termini). Lipid tails and headgroups are shown as light and dark gray lines, respectively, and water and ions are omitted for clarity. (C) Difference in the percent time that MA lysine residues spend in contact with the bilayer in the absence and presence of Chol, where contact is defined as a distance not greater than 3 Å between any residue atom and any lipid atom. K13, K18 and K72 spend a mean 22% more time in contact with the membrane when Chol is present, while K82 and K95 are never in contact with either bilayer.

water (see Methods section), and is similar to the independently determined monomer crystal structure (the backbone RMSD between the two structures is 2.8 Å, Fig. C1D).

The protein's secondary structure remained stable during the simulations (Fig. C6A), and the protein density did not penetrate further than the lipid headgroup region in either system (Fig. C5), consistent with the SANS results (Fig. 4.1B,C). However, in the presence of Chol the helices' tilts changed slightly, facilitating the exposure of K13, K18, K24 and K72 to the membrane (Fig. C6C). Of the protein's 10 lysine residues, two did not interact with either the POPC/POPS or POPC/POPS/Chol bilayer, while six exhibited a greater number of contacts with the +Chol membrane (Fig. 4.2C). The slight conformational changes of the protein were accompanied by a moderate increase in the number of instantaneous lysine-POPS contacts (Fig. C6B). For example, during the last 100 ns of the simulations when the bilayer contained Chol, up to seven lysine residues (as opposed to six in the POPC/POPS bilayer) simultaneously came in contact with PS, and the probability of a single PS lipid interacting with three lysine residues was 25 times greater than in the POPC/POPS bilayer. These results are consistent with a stronger electrostatic interaction between MA and the Chol-containing membrane.

The modes of RSV MA-membrane interaction observed in the simulations have been implicated in functional phenotypes in vivo [254]. In the simulations, the basic residues in the first 35 amino acids of the protein were actively engaged in contacts with the bilayer. The exception was K35, which spent less than 20% of the time close to the membrane, consistent with the unaffected budding of virus particles in the K35Q mutant [254]. In the simulations, neither K82, R61, or R85 (K82, K61 and K85 in the RSV strain studied in reference [254]) came in contact with the lipids, which agrees with the less severe reductions in virus particle release observed in the double mutants of K61Q/K82Q and K61Q/K85Q. Furthermore, in contrast to E25 and E70,

the location of D52 on helix 4 keeps that residue away from the bilayer surface in the simulations, helping clarify the experimental observation of full versus partial rescue of a budding-defective mutant upon lysine substitution of the glutamic or aspartic acids, respectively [254].

4.4.4 Cholesterol increases the membrane surface charge density

Neither SANS nor MD simulations provided evidence for a direct interaction between MA and Chol, although SANS showed a reduction in area per lipid and an increase in hydrocarbon thickness for Chol-containing bilayers (Fig. 4.1D,E). We therefore hypothesized that Chol indirectly influences MA binding by inducing changes in the bilayer structure that promote electrostatic interactions with the protein. To test this hypothesis, we first compared the structural properties of the two simulated bilayers in the absence of protein. It is important to note that because the ratio of negative charge to total lipid was fixed, the PC-to-PS ratio in the –Chol and +Chol bilayers was different (7/3 and 3.4/3, respectively). This choice was made in order to isolate the effects of cholesterol without changing the total negative charge.

Incorporation of Chol increased the lipid acyl chain order parameter by more than 65% (Fig. C6D), consistent with ESR measurements [231]. This change was accompanied by a 28% decrease in the average area per lipid from 60.9 to 43.5 $Å^2$, and a 6 Å increase in bilayer thickness from 40.5 to 46.9 Å, similar to SANS results (Fig. 4.1D,E and Table C2). The reduction of bilayer area led to an increase in the PS surface density: for example, a 6.5 × 6.5 nm membrane patch would contain on average 42 or 60 charged headgroups in the absence or presence of 36 mol% Chol, respectively. The greater PS area density increased the bilayer's negative surface charge density (i.e., charge per unit area), which together with the lower PC:PS headgroup ratio (see Fig. C7 for the individual contributions of PC and PS to the

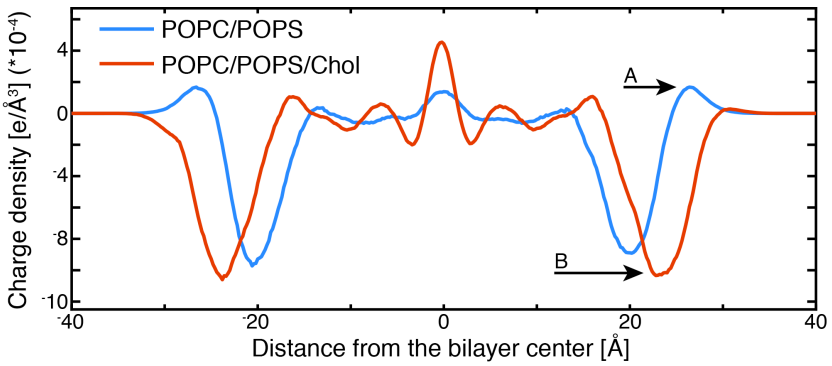

Figure 4.3. Cholesterol influences the membrane surface charge density. Charge distribution along the bilayer normal calculated from the two simulated bilayers in the absence of MA. Addition of Chol increases the negative charge density in the headgroup region (arrow B), eliminating the peak of positive density at the water-lipid interface present in the POPC/POPS bilayer (arrow A). See Fig. C7 for the individual contributions of the membrane components.

charge density) completely eliminated the small peak of positive charge density observed in the –Chol bilayer, thus making electrostatic interactions with the +Chol membrane more favorable (Fig. 4.3, C7).

In order to relate the changes in surface charge density to MA binding, we calculated the bilayer electrostatic potential (defined here and henceforth as 3 Å above the surface) using non-linear Poisson-Boltzmann theory and the Gouy-Chapman model of the electrical double layer [255]. The potential is a function of salt concentration, temperature, and surface charge density, with the latter calculated as the ratio of POPS mole fraction to the average area per lipid and having units of $e^{-}/Å^2$ (the reference potential in the bulk water far from the surface is zero). This formulation assumes that the charges are uniformly distributed on a continuum flat surface and therefore reports an *average* surface potential. Calculations based on conditions used in the MD simulations yielded potentials of –67 and –76 mV for the respective -Chol and +Chol bilayers, suggesting that the preference of MA for Chol-containing

membranes is due to a stronger electrostatic attraction, since MA bears a net +3 charge.

4.4.5 Nonideal mixing of POPC and POPS lipids has a small effect on surface potential

Bilayers for MD simulations were constructed from an initially random lateral arrangement of phospholipids and Chol by using CHARMM-GUI [141]. In light of the SANS finding of POPS clusters (Fig. 4.1F), and because the simulation length of ~ 200 ns did not allow sufficient time for lipids to explore their configuration space through lateral diffusion, it is important to independently examine the effect of non-ideal mixing on the bilayer's electrostatic potential. To this end, we performed Monte Carlo (MC) lattice simulations of a binary mixture of neutral and charged lipids in a 70/30 ratio, in order to obtain their equilibrium lateral distribution (Appendix C). In this simple model, the lipid distribution is a function of a single adjustable parameter, the excess mixing energy ΔE_m of a PC/PS pair, which accounts for all non-ideal interactions between these lipids [55]. To examine different degrees of non-ideal mixing we varied ΔE_m from zero (i.e., random mixing) to + 0.5 k_BT (i.e., Boltzmann constant times T), which is just below the threshold for complete phase separation [51].

Static snapshots of the equilibrium lipid distributions with increasing degree of non-ideal mixing are shown in Fig. C8 (see Appendix C for details). Also shown (Fig. C8 lower panels) are corresponding maps of the electrostatic surface potential relative to that of a uniform bilayer with 30 mol% charged lipids (Appendix C). While some patchiness of the potential is observed with increasing non-ideality, in most cases the local potential varies by less than 10% from the average value, indicating that for low to moderate degrees of non-ideal mixing the average potential calculated with the

uniform Gouy-Chapman model is a reasonable approximation for the potential above the bilayer surface. Taken together with the SANS results showing similar degrees of non-ideal mixing of POPC and POPS in the presence and absence of Chol, as well as the calculated 13% decrease in the average potential in the +Chol membrane, these findings suggest that non-ideal mixing cannot account for the Chol-enhanced MA/bilayer interaction observed both in vitro [231] and in silico (present work).

4.4.6 Cholesterol increases the MA/bilayer electrostatic interaction and decreases the penalty for headgroup desolvation

To examine the specific energetic contributions of the protein and bilayer in the MA-membrane interaction, we used the Molecular Mechanics-Generalized Born Surface Area (MM-GBSA) approach to estimate the binding free energy ΔG_{bind} of MA with the POPC/POPS and POPC/POPS/Chol bilayers, based on conformations sampled in the MD simulations [256, 257]. In the MM-GBSA framework, ΔG_{bind} is approximated as the sum of the interaction energy of the two binding partners (here, MA and bilayer) in vacuum $\Delta E_{\text{int}}^{\text{vac}}$, and the penalty for displacing water molecules upon protein binding. The latter is expressed as a difference in the energetic cost for desolvating the MA-bilayer complex and each partner separately and is referred to as $\Delta\Delta G_{solv}$.

Our analysis showed that in the presence of Chol, the binding free energy was over 4 kcal/mol more favorable than in the absence of Chol (–5.8 ± 0.3 vs. –1.6 ± 0.2 kcal/mol, respectively). Decomposition of ΔG_{bind} into electrostatic and desolvation contributions confirmed the much stronger electrostatic interaction of MA with the Chol-containing bilayer (–1531 vs. –1215 kcal/mol for +Chol and –Chol bilayers, respectively), while also revealing a similar trend in the polar desolvation penalties (1552 vs. 1242 kcal/mol), as shown in Table C5. When the two partners bind, the

favorable electrostatic attraction between them is partially offset by the displacement of water molecules from the binding interface, which incurs an unfavorable desolvation penalty resulting from the high dielectric strength of water and charge screening by the salt.

Further insight was gained by decomposing $\Delta G_{\mathrm{bind}} = \Delta E_{\mathrm{int}}^{\mathrm{vac}} + \Delta\Delta G_{\mathrm{solv}}$ into the separate contributions from each binding partner [257, 258]. While the balance between $\Delta E_{\mathrm{int}}^{\mathrm{vac}}$ and $\Delta\Delta G_{\mathrm{solv}}$ for MA was similar in the two MA-bilayer systems (Fig. 4.4A, blue bars), the energetic cost for desolvating the lipids was lower for the +Chol bilayer, resulting in a more favorable MA-membrane interaction energy (Fig. 4.4A, orange bars). The desolvation penalty is closely related to both the charge density and the solvent accessible surface area (SASA) of the binding partners. Thus, the smaller desolvation penalty of the +Chol bilayer could be due to either a lower charge density, and/or smaller solvent exposed molecular surface to desolvate in the presence of Chol. The area of the MA shadow (defined by the projection of the MA coordinates onto the bilayer plane) in the two bilayers was practically identical (Fig. C9B), and the +Chol bilayer had on average one more POPS lipid than the –Chol bilayer (Fig. C9E), thereby excluding the former possibility.

To test for the latter, we compared the SASA of the top leaflet patch in the MA shadow in the two bilayers. As expected, the +Chol bilayer had a significantly smaller SASA than the –Chol bilayer (Fig. C9A). At first glance, a smaller SASA in the presence of Chol suggests fewer waters per lipid. Interestingly, a count of the number of waters within 3 Å of a POPC or POPS lipid revealed that, consistent with experimental data [235], lipids were in fact *better* hydrated in the +Chol bilayer, having roughly 13.3 waters/headgroup compared to 12.3 in the Chol-free bilayer (Fig. C9C). However, due to the surface area occupied by Chol itself, there were on average four *fewer* lipid headgroups under the protein in the presence of Chol (Fig. C9D). This

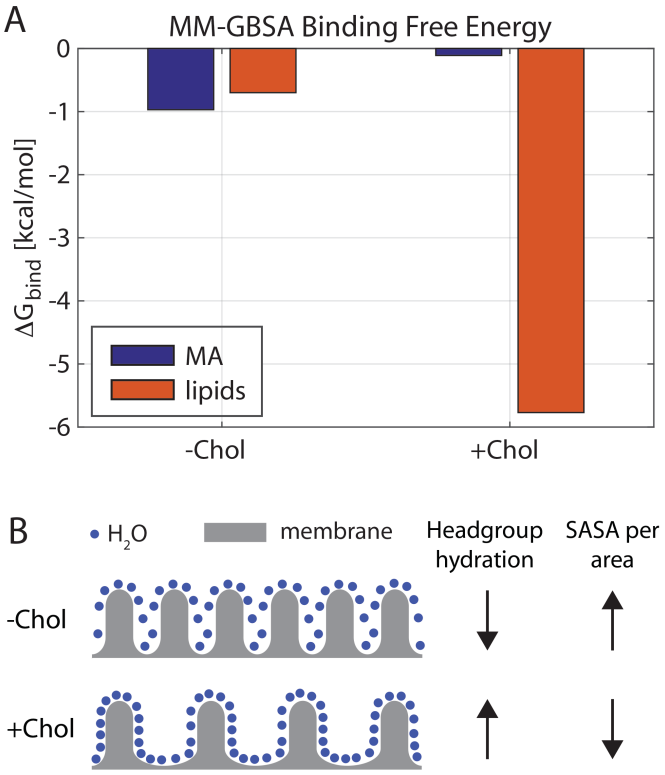

Figure 4.4. Cholesterol decreases the energetic penalty for lipid desolvation. (A) Contributions of MA and lipids to the total binding free energy ΔG_{bind} of the MA-bilayer complex estimated with the MM-GBSA method. Each energetic contribution is the sum of the interaction energy in vacuum for the respective system and the solvation penalty calculated separately for MA and the lipids. The presence of Chol results in a 5 kcal/mol reduction in the solvation penalty of the lipids relative to $\Delta E_{\text{int}}^{\text{vac}}$, resulting in a more favorable bilayer contribution to ΔG_{bind} compared to the PC/PS bilayer. For a detailed break-down of the energy contributions and details of the underlying calculation, see SM. (B) Schematic illustration of the lipid headgroups (grey) on the bilayer surface in the +Chol and –Chol membranes, and the water molecules that solvate them (blue dots). Due to the area occupied by Chol itself, there are fewer lipid (PC or PS) headgroups in a bilayer patch of given size. Thus, even though Chol increases the number of bound waters per headgroup, it decreases the SASA per unit area of the bilayer (see text). Note that the spacing between the lipid headgroups in the +Chol schematic has been exaggerated to emphasize the lower packing density in this region.

resulted in ~ 30 fewer lipid-bound waters in the MA shadow in the +Chol bilayer compared to the –Chol bilayer (226 vs. 258), in agreement with the observed SASA difference. A count of the number of PC, PS and Chol molecules in the MA shadow

further confirmed that this difference was due to the replacement of POPC with Chol (Fig. C9E). Thus, while Chol increases headgroup hydration, it decreases the overall bilayer SASA per unit of planar area in the bilayer, as illustrated schematically in Fig. 4.5B, resulting in a smaller desolvation penalty of the POPC/POPS/Chol membrane upon protein binding. Therefore, our MM-GBSA analysis indicates that Chol both increases the electrostatic attraction between MA and the bilayer, and decreases the cost for headgroup desolvation when the protein binds. These two effects, in concert, result in the energetically more favorable interaction of MA with the +Chol membrane.

4.4.7 The membrane electrostatic potential is a key determinant of MA binding affinity

Although the effects of Chol on membrane thickness and lipid packing are well known (see [189]), the calculations of the previous sections demonstrate that bilayer structural perturbations induced by Chol constitute a general mechanism by which the molecule can indirectly mediate electrostatic interactions with proteins. To further explore retroviral MA-membrane association in the context of these interactions, we used liposome pelleting [238] to measure binding of RSV MA to LUVs with varying POPS and Chol concentrations, and at varying salt concentration. The data were analyzed in terms of calculated electrostatic potential above the membrane surface (Figs. 4.5 and C10).

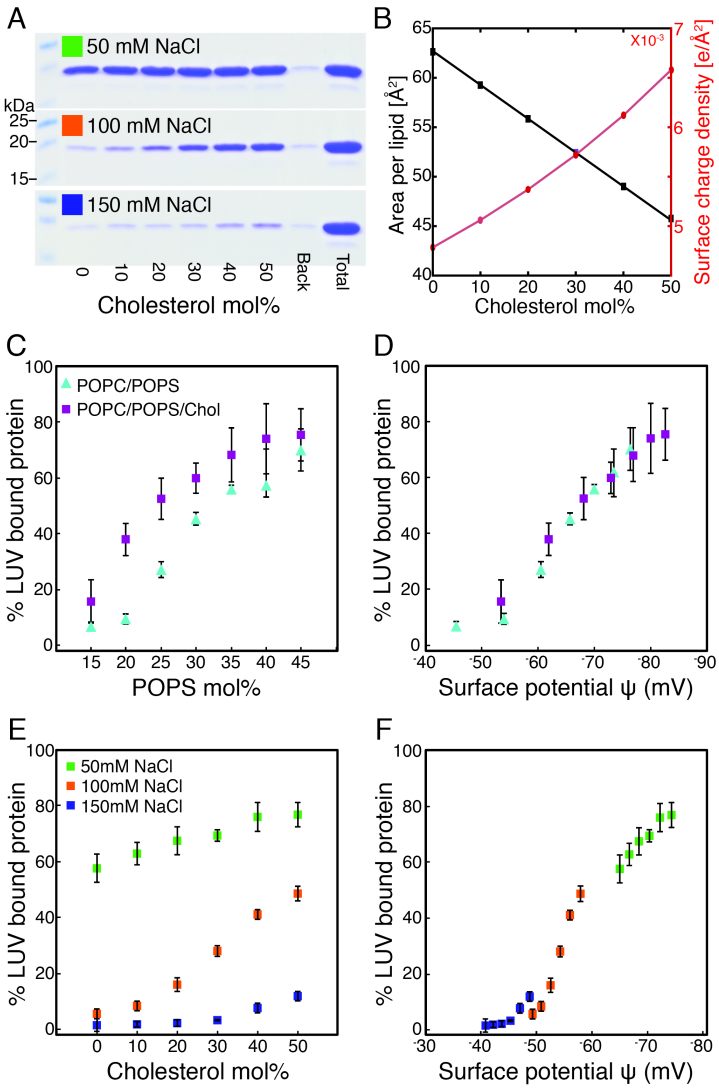

Figure 4.5. RSV MA membrane association is quantitatively explained by membrane surface potential. (A) Coomassie stained gel of pelleted MA associated with LUVs with increasing Chol concentration (0–50 mol%, lanes 2–7). "Back" (lane 8) represents the amount of MA pelleted in the absence of LUVs and "Total" (lane 9) represents the total MA in each binding reaction. (B) Calculated membrane surface charge density (right axis, red) and average area per molecule (left axis, black) for POPC/POPS/Chol bilayers plotted vs. Chol concentration. (C) Percent of LUV-bound MA plotted against POPS concentration for membranes without (light blue triangles) and with (purple squares) 36 mol% Chol. (D) Binding data from C plotted vs. calculated ψ. (E) Percent of MA bound to LUVs at 30 mol% POPS with increasing Chol and decreasing POPC concentration at different NaCl concentrations: 50 mM (green), 100 mM (orange), and 150 mM (blue). (F) Binding data from E plotted vs. calculated ψ. Legend in A corresponds to A, E, and F; legend in C corresponds to C and D. All data points are the average, and error bars are the standard deviation, of no less than four independent replicate samples.

Consistent with previous results for RSV and HIV MA and Gag [224, 238, 248, 259], increasing the POPS concentration from 15 to 45 mol% resulted in increased RSV MA binding to LUVs from ~10% to 70% (Fig. 4.5C, blue triangles). A significant enhancement in binding affinity was observed when 36 mol% POPC was replaced with Chol (Fig. 4.5C, purple squares): for example, at 20 mol% POPS, Chol increased MA association with LUVs from 10% to 40%. We also directly tested the ability of Chol to enhance binding under a range of ionic strengths by incrementally replacing POPC with Chol at a fixed POPS concentration of 30 mol%. This replacement decreases the average area per molecule from 62 to 45 $Å^2$, and increases the surface charge density from 4.8×10^{-3} to 6.6×10^{-3} $e^-/Å^2$ (Fig. 4.5B). At 100 mM NaCl, we observed a significant increase in the amount of RSV MA associated with LUVs upon increasing Chol concentration (Fig. 4.5E, red squares). Reducing the NaCl concentration to 50 mM resulted in increased binding at all Chol concentrations (Fig. 4.5E, green squares), while increasing NaCl concentration to 150 mM practically eliminated binding (Fig. 4.5E, blue squares).

Importantly, the binding trends for all bilayers with and without Chol, and at different ionic strength, collapse onto a single curve when plotted against the electrostatic potential above the membrane surface, ψ, calculated using the Gouy-Chapman model (Fig. 4.5D-F). In all cases, MA shows little membrane affinity at $\psi > -50$ mV, while a dramatic increase in binding occurs as ψ drops to –70 mV. We also observed a similar trend when MA binding was measured as a function of varying NaCl concentration (Fig. C10). Taken together, these results reveal a sigmoidal dependence of binding on membrane surface potential, and demonstrate that the ability of Chol to enhance RSV MA membrane association can be explained by changes in bilayer structure that increase the surface charge density.

4.4.8 Implications for MA binding at the plasma membrane

Fig. 4.6A shows a model of a mammalian PM taken from published estimates of the outer and inner leaflet lipid composition [45, 221, 260]. Using literature values for individual lipid areas, we calculated the average molecular area (48.9 $Å^2$) and charge (0.32 e^-) for the PM inner leaflet composition (Table C4), which results in an average surface charge density of 6.5×10^{-3} $e^-/Å^2$. It is instructive to consider this charge density in the context of our binding results. Fig. 4.6B shows a contour plot of ψ as a function of average molecular area and charge at physiological ionic strength (150 mM NaCl) and temperature (37°C), calculated with the Gouy-Chapman model. Also shown is a contour plot of the percentage of membrane-bound MA protein under the same conditions, obtained by mapping the sigmoidal binding curve of Fig. 4.5F to the calculated surface potential (Fig. C10, Appendix C). While ψ changes gradually as a function of surface charge density, the fraction of bound protein exhibits large changes over a relatively small range of ψ, from about –50 to –60 mV. The average PM composition is located approximately at the –50 mV contour, a point that corresponds to weak binding, but that is near the edge of the binding transition. Compositional perturbations such as non-ideal mixing that increase the local concentration of charged lipid (corresponding to movement in the +y direction), or increase the local concentration of Chol (corresponding to movement in the –x direction) could therefore act as a binding switch. For example, a 10 $Å^2$ reduction in the average lipid area—which corresponds to a 10^{-3} $e^-/Å^2$ increase in charge density, or roughly a 20% increase in the local PS density in a patch of average concentration of 30 mol%—could be sufficient to promote electrostatic binding. Thus, by tuning the local lipid composition in the inner leaflet, cells could create binding platforms enriched in monovalent charged lipids and Chol, which can attract proteins by means of electrostatic interactions.

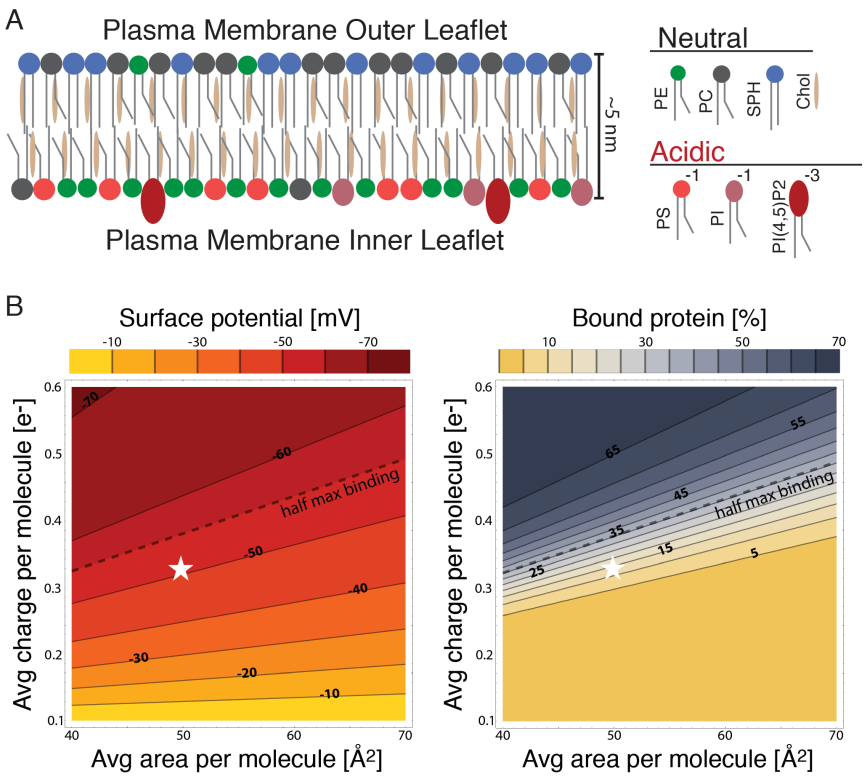

Figure 4.6. Cellular plasma membrane model. (A) Asymmetric distribution of PM lipids between the inner (Chol/PE/PC/PS/PI/PIP 40/28/5/18/8/2 mol%) and outer (Chol/PE/PC/SM 40/7/27/26 mol%) leaflets (see Table C4). (B) Contour plots of electrostatic surface potential (left) and protein binding (right) as a function of average area and charge per molecule. Electrostatic potential was calculated from non-linear Poisson-Boltzmann theory assuming physiological ionic strength (150 mM NaCl) and temperature (37°C). Protein binding was calculated from a sigmoidal function that maps the binding data displayed in Fig 5F to surface potential (Fig. C10, Appendix C). The dashed line traces the corresponding contour of half-max binding, and the white star denotes the approximate molecular area (48.9 $Å^2$) and charge (0.32 e^-) of the PM's inner leaflet estimated from the composition given above.

The mechanistic insights gained from this study also enable predictions for the effect on protein binding of Chol relative to other lipids. Our results indicate that Chol enhances protein binding through two synergistic effects: it both increases the charge density of the bilayer and decreases the energetic cost of displacing water from the

lipid headgroups. As mentioned earlier, the penalty for headgroup desolvation is related to the SASA per unit of planar area. Thus, increasing the membrane's charge density at fixed SASA (for example, by adding PIP2 lipids instead of Chol to a POPC/POPS membrane with a fixed PS mole fraction) should cause a large increase in protein binding. Indeed, this has been shown experimentally for a number of different proteins and model peptides (see Fig. 4.8 in [238]). On the other hand, decreasing the bilayer's desolvation penalty (or SASA/unit area) at a fixed membrane charge density should result in a smaller increase in binding. One such example can be seen directly in the binding data in Fig. 4.5C: namely the –Chol bilayer with 25 mol% PS and the +Chol bilayer with 20 mol% PS have a similar charge density of ~$4x10^{-3}$ e^{-} /$Å^2$, yet the binding to the +Chol bilayer is stronger. This is likely due to Chol's effects on the solvation properties of the membrane. PE lipids, which are abundant in the PM inner leaflet, have smaller headgroups (hence, smaller SASA) and smaller cross-sectional areas than corresponding PC or PS lipids [147]. Due to their small SASA and ability to reduce the bilayer area, PE and Chol should have similar effects on binding. Indeed, while at 25 mol% PS, 27% and 53% MA is bound to POPC/POPS and POPC/POPS/Chol bilayers, respectively (Fig. 4.5C), we find that 58% MA is bound to the corresponding POPE/POPS liposomes under the same conditions.

4.5 Summary and conclusion

We have shown how the interactions crucial for Gag association with the PM can depend on the types of lipids present in the PM inner leaflet. Model membrane studies have previously shown that: (a) electrostatic interactions are critical for MA binding [217, 261]; (b) cholesterol enhances MA and Gag binding [231, 262]; and (c) cholesterol condenses the membrane area [263]. Our work is the first to explain these observations by describing cholesterol's role using Guoy-Chapman electrostatics. For

example, HIV virions are enriched in charged lipids compared to the cellular plasma membrane, and contain 30-40 mol% cholesterol [221], yet many studies of viral protein binding to model membranes do not include cholesterol. Our results suggest that cholesterol enhances MA binding by affecting both the electrostatic and solvation properties of the membrane. Thus, it is an essential component in model membranes, recreating a surface potential and binding conditions representative of the PM inner leaflet. Moreover, we found that the non-ideal mixing behavior of neutral and charged lipids can promote the formation of anionic lipid clusters that act as protein binding sites. We conclude that membranes can mediate non-specific electrostatic interactions with proteins even in the absence of multivalent acidic lipids, and that bilayer mixing behavior and structural properties should be considered when interpreting protein binding data.

CHAPTER 5
PREPARATION OF ASYMMETRIC PHOSPHOLIPID VESICLES FOR USE AS CELL MEMBRANE MODELS*

5.1 Abstract

Freely suspended liposomes are widely used as model membranes for studying lipid-lipid and protein-lipid interactions. Liposomes prepared by conventional methods have chemically identical bilayer leaflets. In contrast, living cells actively maintain a different lipid composition in the two leaflets of the plasma membrane, resulting in asymmetric membrane properties that are crucial for normal cell function. Here, we present a protocol for the preparation of unilamellar asymmetric phospholipid vesicles that better mimic biological membranes. Asymmetry is generated by methyl-β-cyclodextrin catalyzed exchange of the outer leaflet lipids between vesicle pools of differing lipid composition. Lipid destined for the outer leaflet of the asymmetric vesicles is provided by heavy donor multilamellar vesicles containing a dense sucrose core. Donor lipid is exchanged into extruded unilamellar acceptor vesicles that lack the sucrose core, thereby facilitating the post-exchange separation of the donor and acceptor pools by centrifugation due to differences in vesicle size and density. We present two complementary assays for the quantification of each leaflet's lipid composition: the overall lipid composition is determined by GC-MS, while the lipid distribution between the two leaflets is determined by NMR using the lanthanide shift reagent Pr^{3+}. The preparation protocol and the chromatographic assay can be applied to any type of phospholipid bilayer, while the NMR assay is specific to lipids with choline-containing headgroups, such as phosphatidylcholine and sphingomyelin. In approximately 12 hours, the protocol can produce a large yield of asymmetric vesicles

* The following chapter is reproduced from: Doktorova, M., Heberle, F. A., Eicher, B., Standaert, R. F., Katsaras, J., London, E., Pabst, G. & Marquardt, D. *Nature Protocols*, *In press*. It has been modified to fit the format of the thesis. MD, FAH and DM wrote the protocol. MD, FAH, DM and BE conducted the experiments.

(up to 20 mg) suitable for a wide range of biophysical studies.

5.2 Introduction

The plasma membrane is a marvel of evolutionary nanoengineering. The physical properties of this remarkable organelle are optimized for its dual roles as a cellular barrier and gateway. In a sense, these roles are contradictory: the plasma membrane must be sturdy enough to provide protection against an often harsh external environment, yet malleable enough to allow for cell growth, division and motility, and the passage of water and nutrients. Nature solved this problem with a quasi- two-dimensional fluid formed from a complex mixture of lipid, protein, and carbohydrate. Although its basic architecture is well established, there is an emerging consensus that some critical processes occurring at and within the plasma membrane cannot be adequately explained without invoking nanoscopic membrane structure [1, 60, 69], see also Chapter 4. This realization has generated renewed interest in biophysical characterization of membranes at the level of molecular interactions. However, teasing apart these interactions is hardly feasible in a natural plasma membrane that might contain several hundred chemically distinct lipids, and thousands of unique proteins. Instead, uncovering the specific interactions that are responsible for functional phenotypes in vivo requires the study of simplified models in vitro, where their composition can be finely controlled.

Lipid bilayer vesicles are among the most widely used model systems for biophysical studies of lipid-lipid and protein-lipid interactions. Conventional liposome preparations by hydration of a dry lipid film (typically followed by sonication or extrusion to generate unilamellar vesicles) produce bilayers in which the two leaflets have an identical composition. Cellular plasma membranes, on the other hand, actively maintain a different lipid composition in the exofacial (outer) and cytofacial (inner)

leaflets [33, 264]. Phosphatidylserine (PS), for instance, is located exclusively in the inner leaflet of the plasma membrane (PM), and its exposure on the outer leaflet serves as a marker of impending cell death in eukaryotes [65]. Mounting evidence suggests that the lipid compositional *asymmetry* of the PM not only confines certain lipids to their respective leaflets in order to facilitate their direct interaction with other molecules, but also results in unique membrane properties that, although currently poorly understood, are likely to be crucial for normal cellular function [48, 265-267]. It follows that symmetric model membranes lack at least some key structural characteristics of natural cell membranes that may critically affect membrane interactions with proteins and small molecules. There is a widely recognized need to expand the biophysical toolkit with model systems that more closely mimic the asymmetric cell membrane environment, while still allowing for easily controlled variation of the inner and outer leaflet lipid compositions.

5.2.1 Preparation of asymmetric vesicles

Several techniques exist for preparing asymmetric bilayers [268]. The preparation of asymmetric large unilamellar vesicles (LUVs) is particularly useful, because their size is well-defined, and their bilayer properties are not greatly affected by the high curvature found in small unilamellar vesicles (SUVs), or by interactions with a substrate found in supported lipid bilayers (SLBs).

While asymmetric giant unilamellar vesicles (GUVs) are also not affected by curvature and substrate interaction, their size is harder to control precisely. The main method for preparing GUVs of micron size involves passing an inverted emulsion droplet through a lipid lined oil-water interface [269] which has the added limitation that the vesicles contain residual organic solvent that could affect bilayer properties.

The generation of asymmetric LUVs (aLUVs) has been achieved by three different methods: (1) application of a pH differential to vesicles that contain anionic lipids; (2) external addition of enzymes that selectively modify outer leaflet lipid headgroups; and (3) external addition of lipid carrier molecules that catalyze intervesicular exchange of outer leaflet lipids. The pH adjustment method exploits the fact that certain anionic phospholipids (namely, phosphatidylglycerol and phosphatidic acid, PG and PA respectively) can rapidly diffuse between bilayer leaflets in their uncharged, protonated form [270]. Applying a pH differential across the bilayer thus induces a redistribution of these lipids with an accumulation on the more alkaline side [271]. Enzymatic headgroup modification has been used to convert outer leaflet phosphatidylserine (PS) to phosphatidylethanolamine (PE) using PS-decarboxylase [272], or outer leaflet phosphatidylcholine (PC) to either PE or PS using phospholipase D [273]. In contrast to these methods—each of which acts by chemically modifying a single population of initially symmetric vesicles—catalyzed lipid exchange requires mixing together *two* symmetric vesicle populations of different composition in the presence of a lipid carrier such as, phospholipid exchange protein [274], bovine serum albumin [275], or certain classes of cyclodextrins [276].

We have chosen to use the catalyzed lipid exchange approach, due to its greater versatility in comparison to the other methods. The primary disadvantage of catalyzed exchange is that the two vesicle populations must eventually be separated to recover the asymmetric liposomes; below, we describe two different strategies to address this problem. Its primary advantage, however, is its versatility. While pH adjustment and enzymatic modification are each specific for a subset of phospholipids, catalyzed exchange is compatible with a wide variety of phospholipids and can be used to create asymmetric vesicles with diverse inner and outer leaflet compositions.

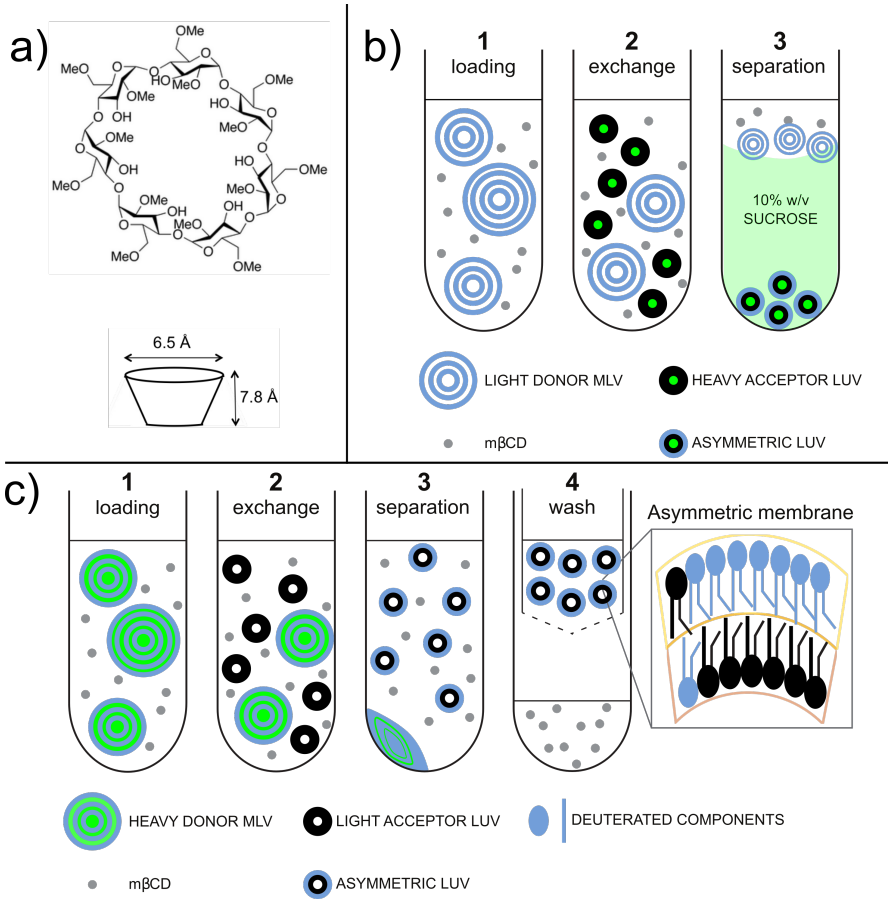

Figure 5.1. Illustration of the different aLUV preparation protocols. (**a**) Chemical structure of methyl-β-cyclodextrin (mβCD), and the size and shape of its hydrophobic pocket. (**b**) Heavy acceptor strategy: (1) mβCD is incubated with donor lipid MLVs suspended in buffer; (2) mβCD facilitates the exchange of the outer leaflet of acceptor LUVs (entrapped with sucrose) with donor lipid; (3) the desired aLUVs are recovered from the pellet after ultracentrifugation through a sucrose cushion. (**c**) Heavy donor strategy: (1) mβCD is incubated with donor lipid MLVs entrapped with sucrose. The donor lipid is composed of the desired outer leaflet lipid; (2) mβCD facilitates the exchange of the outer leaflet of acceptor LUVs with donor lipid; (3) remaining sucrose loaded donor MLVs are removed by centrifugation; (4) the aLUV sample is further purified through the removal of mβCD and mβCD-lipid complexes with a centrifugal concentrator. The desired aLUVs are then recovered from the retentate (figure adapted from Ref. [4]).

Here, we focus on the preparation of aLUVs using catalyzed exchange, with methyl-β-cyclodextrin (mβCD) as the lipid carrier. mβCD is a water-soluble, ring-

shaped oligosaccharide possessing a hydrophilic outer surface and a central hydrophobic cavity that is large enough to accommodate a lipid chain (Fig. 5.1a). The reversible formation of an mβCD/lipid complex effectively displaces water from the cavity, replacing unfavorable interactions with favorable ones [277]. At high concentrations, mβCD will completely dissolve a lipid vesicle suspension, but at lower concentrations, a dynamic equilibrium exists between intact vesicles, mβCD/lipid complexes, and free mβCD [278]. This "exchange-competent" solution of mβCD and excess *donor* lipid is the starting point for preparing aLUVs, as shown in Step 1 of Fig. 5.1b and c. Addition of *acceptor* LUVs to the mβCD/donor solution results in mβCD-catalyzed exchange of the acceptor vesicles' exposed outer leaflet lipids with the donor lipid pool, while leaving the inner leaflet of the acceptor vesicles relatively unperturbed [276], as shown in Step 2.

Two strategies have been used to separate the original acceptor pool (which contains the aLUVs) from the donor/acceptor/mβCD *exchange slurry*; each exploits size and/or density differences between the donor and acceptor vesicle pools. The *heavy acceptor* strategy (Fig. 5.1b) makes use of a dense sucrose solution (typically 25% w/v) trapped in the acceptor vesicle lumen. Donor lipid is typically in the form of multilamellar vesicles (MLVs). MLVs scatter visible light more strongly than LUVs and allow for visual verification that excess donor lipid is present after incubation with mβCD, an important condition for minimizing the loss of acceptor vesicles to dissolution by free cyclodextrin. Following exchange, separation is achieved by layering the exchange slurry onto a sucrose solution of intermediate density (typically 10% w/v, although adjustment may be necessary depending on the density of the donor lipid) followed by ultracentrifugation at 190,000 × g. The lighter solution composed primarily of undissolved donor MLVs and mβCD remains at the top of the centrifuge tube, while the heavy acceptor LUVs sink through the sucrose cushion and

are recovered in the pellet, as shown in Fig. 5.1b Step 3. The *heavy donor* protocol (Fig. 5.1c) essentially reverses this strategy: the donor lipid film is hydrated in a sucrose solution (typically 20% w/w) to create large, dense MLVs, while the acceptor lipid is hydrated in pure water or buffer. Following exchange, the donor MLVs are separated from the lighter, smaller acceptor LUVs by low-speed centrifugation (20,000 × g), with the now-asymmetric acceptors recovered in the supernatant, as shown in Fig. 5.1c Step 3. Residual mβCD is then removed with a centrifugal ultrafiltration device (Fig. 5.1c Step 4).

The choice between the two strategies outlined above depends on details of the specific experiment. The heavy acceptor protocol simplifies purification of asymmetric vesicles and can minimize donor contamination in cases where the donor lipid is less dense than the acceptor lipid. However, the sensitivity of follow-up experiments to the presence of sucrose in the asymmetric vesicle core should also be considered. One potential consequence of entrapped sucrose is the introduction of an osmotic stress that can cause bilayer thinning and lipid area expansion [4]. Extruded vesicles are often non-spherical and can easily accommodate small osmotic gradients without accumulating stress by "rounding up", effectively diluting the internal solution by increasing their volume [279]. Even accounting for such volume changes, typical experimental conditions—for example, vesicles with a 25% (w/v) sucrose core, suspended in PBS buffer—result in a residual osmotic differential of ~ 300 mOsm/kg in aLUVs prepared using the heavy acceptor strategy. For 100 nm diameter vesicles, the corresponding tension calculated from Laplace's law is ~ 20 mN/m, a value that can exceed the rupture tension of some lipid bilayers [280]. In cases where it is desirable to use the heavy acceptor protocol, the tension can be minimized or eliminated by adjusting the buffer osmolality (e.g., with sucrose) to balance the osmotic pressure. Of course, the osmolyte should be carefully chosen to maintain

compatibility with the chosen experimental techniques, as well as to avoid direct interactions with lipids that might alter membrane properties. The heavy donor strategy—described in detail in the PROCEDURE below— circumvents these issues and eliminates the need for ultracentrifugation. A caveat of the heavy donor method is that additional purification steps may be required if the donor lipid is less dense than the acceptor lipid, which may result in reduced yield of the final asymmetric vesicles.

5.2.2 Quantifying leaflet composition

Both the efficiency of outer leaflet exchange and the spontaneous lipid translocation (flip-flop) rate depend on several factors [281]. For example, the exchange efficiency increases with the ratio of donor-to-acceptor lipid used in the preparation, and may by influenced non-trivially by preferential interactions between cyclodextrin and the chosen lipids [278]. Lipid flip-flop, while generally much slower than other diffusive lipid motions [50, 282], depends on the chemical structure of the lipid molecules including the size and charge of the headgroup [283] and the length and degree of unsaturation of the hydrocarbon chains [284, 285]. It is therefore critical to determine the composition of each bilayer leaflet after the asymmetric liposomes are prepared; it is not safe to assume that the outer leaflet contains only donor lipid, or that the inner leaflet contains only acceptor lipid. Quantifying the leaflet composition requires a separate determination of the overall vesicle composition and the asymmetric distribution of each lipid species. The former is generally accomplished with chromatography, for example thin layer chromatography (TLC) [276], gas chromatography (GC) [4], or ultra-high performance liquid chromatography (UHPLC) [286]. Asymmetry assays generally involve the selective modification, extraction, or interaction of outer leaflet lipids with reagents added externally to the aLUV suspension, followed by detection and quantification; these assays are usually specific

for lipid headgroups. Among the methods that have been used to quantify asymmetry are: labeling of exposed aminophospholipids (i.e., PS or PE) with trinitrobenzenesulfonic acid (TNBS), followed by thin layer chromatography [272]; periodate oxidation of exposed PG, followed by detection of oxidation byproducts [270]; selective outer leaflet extraction of radiolabeled lipids with bovine serum albumin or phospholipid exchange protein [270]; binding of a cationic peptide to exposed negatively charged lipids (e.g., PS or PG) [267]; zeta potential measurements of asymmetric bilayers containing charged lipids [287]; and hydrolysis of PC by phospholipase D, followed by detection of free choline [273].

In the PROCEDURE section, we describe a two-part assay for determining leaflet composition that involves GC-MS and NMR. In the first step, GC coupled to mass spectrometry is used to quantify the total mole fraction of each lipid species. This is done after the aLUV preparation to get information about the exchange efficiency (i.e., how much donor lipid was exchanged into the acceptor vesicles). As shown in Fig. 5.2c, GC is extremely sensitive to even small differences in fatty acid composition (i.e., length and degree of unsaturation) or isotopic content (i.e., protiated vs. deuterated chains), making the method ideal for obtaining reliable quantitative information. An alternative technique, UHPLC, can be used instead to determine the overall composition of lipids with the same acyl chains but different headgroups [286].

In the second step, ^{1}H NMR coupled with a shift reagent is used to determine the asymmetric distribution of lipids with protiated choline headgroups (Fig. 5.3). This assay can distinguish choline headgroups located in the inner and outer leaflets because the shift reagent (e.g., a lanthanide ion such as Pr^{3+}) is added externally and selectively interacts with outer leaflet lipids [4]. Compared to the other asymmetry assays mentioned above, NMR is the most straightforward to implement because the signals from the inner and outer leaflet populations are resolved in a single

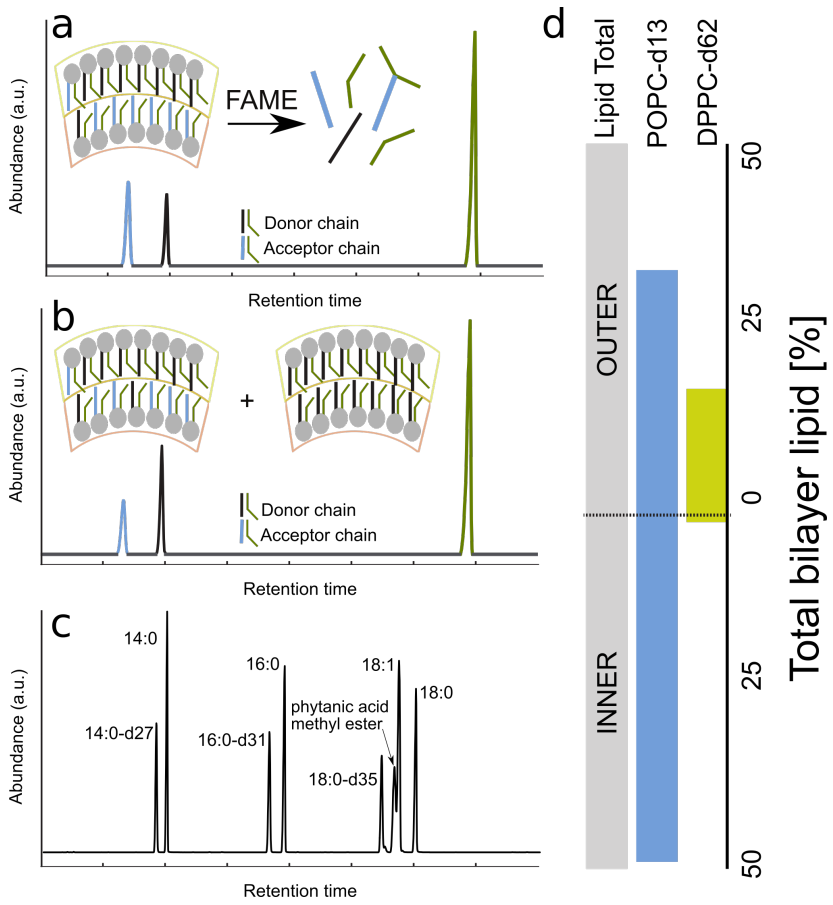

Figure 5.2. Gas chromatography (GC) assay for quantifying vesicle composition. To analyze the lipid composition, the phospholipid must be derivatized into fatty acid methyl esters (FAMEs). (**a**) An illustration of a GC chromatograph from a typical aLUV preparation; (**b**) An illustration of a GC chromatograph where more donor than acceptor is present, an example of donor contamination. (**c**) A GC chromatograph of different fatty acids and their deuterated variants. (**d**) Individual leaflet compositions, determined by combining results from GC and ^{1}H NMR assays, of an aLUV prepared from DPPC-d62 donor exchanged into POPC-d13 acceptor.

measurement. The primary limitations of NMR are: (1) it requires that at least one of the lipid components of the aLUV has a choline headgroup (i.e., PC or sphingomyelin (SM)); and (2) it often fails when aLUVs contain charged lipid in the outer leaflet (in our hands, more than 10 mol% PG, or 2 mol% PS). The latter limitation results from

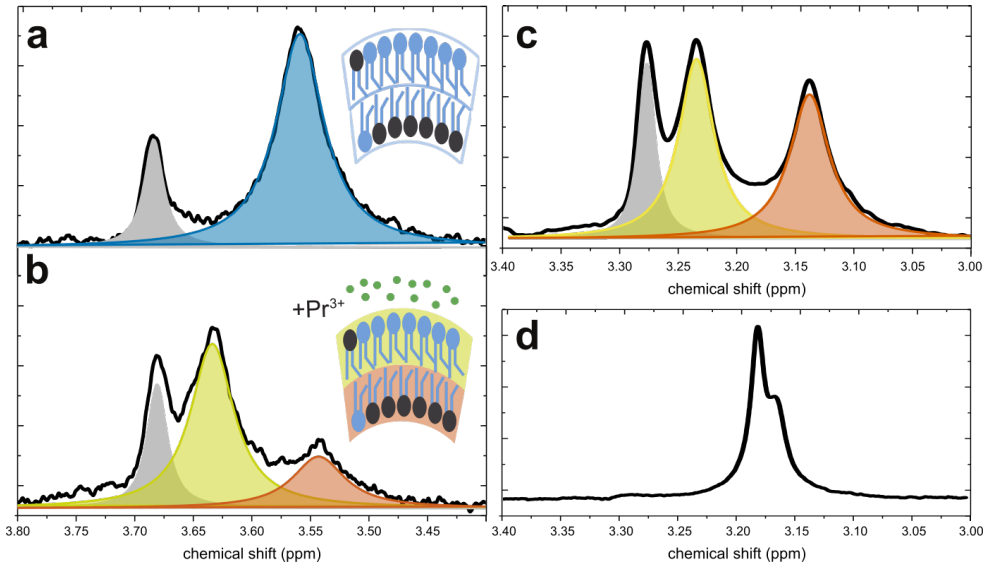

Figure 5.3. ^{1}H NMR assay for quantifying lipid asymmetry. (**a**) ^{1}H NMR of aLUVs using a deuterated-choline acceptor lipid. The blue area represents the signal from the inner and outer leaflet protiated cholines in the sample (the gray peak is residual mβCD). (**b**) After external addition of Pr^{3+}, inner leaflet (red) and outer leaflet (yellow) choline resonances are resolved, and the area under each peak is proportional to the amount of protiated choline present in each leaflet. (**c**) ^{1}H NMR of scrambled aLUVs shows inner and outer leaflet peaks of approximately equal area. (**d**) ^{1}H NMR of SUVs shows distinct inner and outer peaks in the absence of shift reagent. SUVs can be generated by an imbalance in the mβCD:lipid ratio. Figure adapted from refs. [4] and [10].

interactions between Pr^{3+} and exposed anionic lipid, which can cause liposome aggregation that degrades the NMR signal.

5.2.3 Experimental design

In the PROCEDURE section below, we describe the preparation of aLUVs composed of a DPPC-enriched outer leaflet and a POPC-enriched inner leaflet [4, 286]. In principle, the variety of compositions that can be prepared is limited only by the nature of the interaction between mβCD and the different types of lipids. In our own work (summarized in Table 5.1), we have used the protocol to prepare chemically asymmetric vesicles composed of POPC and POPE [288], DPPC and POPE, egg

sphingomyelin and POPE, and DMPC and POPC, as well as isotopically labelled aLUVs composed of deuterated variants of POPC [4, 288] or DPPC [10].

Table 5.1 Two-component aLUVs prepared using the heavy donor strategy described in the PROCEDURE section. Shown are: the donor lipid; the acceptor lipid; the donor:acceptor molar ratio; the temperature during mβCD/donor and mβCD/donor/acceptor incubation (Steps 14 and 15 in the PROCEDURE); the mole fractions of donor lipid in the inner ($\chi_{D,inner}$) and outer ($\chi_{D,outer}$) leaflets of the aLUVs; the observed exchange efficiency (E_{obs}); the fraction of donor lipid in the outer leaflet (D_{asym}); and the respective references.

Donor (D)	Acceptor (A)	D:A ratio	Exchange temp. [°C]	$\chi_{D,inner}$	$\chi_{D,outer}$	E_{obs}	D_{asym}	Ref.
POPC-d44	POPC	2	22	0.1	0.62	0.72	0.86	[4]
POPC	POPC-d44	2	22	0.16	0.6	0.74	0.79	[4]
DMPC-d54	POPC-d13	2	22	0.05	0.51	0.55	0.91	*
DPPC-d62	POPC-d13	3	22	0.02	0.34	0.36	0.95	[4]
POPE	POPC	2	22	0	0.6	0.64	1.00	[286]
POPE	POPC	3	22	0.19	0.76	1.04	0.8	[286]
DPPC-d62	DPPC-d13	3	22	0.3	0.59	0.89	0.66	[10]
POPC	POPE	2	35	0.06	0.54	0.58	0.90	[286]
POPC	POPE	3	35	0.11	0.64	0.72	0.85	[286]
eSM	POPE	3	35	0.09	0.44	0.54	0.83	*
DPPC	POPE	3	35	0.08	0.8	0.88	0.91	*

* this protocol

Some basic sample characterization is an integral part of the protocol. Essential analyses include measuring the vesicle size distribution with dynamic light scattering (DLS) and quantifying the inner and outer leaflet lipid composition (the example described here uses GC and NMR for this purpose, although other assays may be

necessary depending on the choice of lipids). There are a few important considerations when modifying the described protocol for a different lipid composition:

1) Exchange conditions. The mβCD concentration is carefully chosen to be as high as possible without appreciably dissolving the vesicles, in order to maximize exchange and yield. Because different lipids interact differently with mβCD [278], any change in lipid composition should first be examined with DLS to determine the mβCD concentration at which vesicles begin to rapidly dissolve. To ensure that acceptor vesicles are not osmotically stressed during the exchange of lipid between the donors and acceptors, the acceptor LUVs are also prepared in a dilute salt solution (e.g., 20-30 mM NaCl) to balance the osmolarity of the mβCD solution. If it is necessary to prepare aLUVs in a higher molarity buffer, appropriate tests (e.g., DLS) should be performed to ensure vesicle integrity.

2) Overall composition assay. The GC assay for quantifying liposome composition is sensitive to differences in the acyl chains (including isotopic differences) of the acceptor and donor lipids, as shown in Fig. 5.2c. If lipids with identical acyl chains are desired (e.g, POPC and POPE), TLC [276] or UHPLC [286] can be used instead of GC, as these techniques separate lipids based on chemical differences in their headgroups rather than their chains.

3) Asymmetry assay. Asymmetry assays are specific for lipid headgroups, and the ^{1}H NMR assay described below quantifies the inner/outer distribution of lipids with protiated choline headgroups (i.e., PC and SM). If an asymmetric bilayer composed of two different PC lipids is desired, it is possible to determine the transbilayer distribution of the lipids using NMR, provided that one of the lipids has a deuterated choline (as in the example used in the PROCEDURE below). Other assays have been described to quantify the asymmetry of mixtures that do not contain any PC lipids or that have a high concentration of charged lipids, for example TNBS labeling of

aminophospholipids [272], oxidation of exposed PG or radiolabeling [270], binding of a cationic peptide [267], and zeta potential measurements [287].

4) Preparation of asymmetric proteoliposomes. If incorporation of a transmembrane protein into the asymmetric liposomes is desired, the protein should be reconstituted into the acceptor vesicles. Additional control experiments should be performed to ensure that the presence of the protein does not interfere with the composition assays.

5) Preparation of cholesterol-containing aLUVs. If cholesterol-containing aLUVs are desired, the protocol should be modified by either: (1) adding cholesterol to both the donor and acceptor vesicles; (2) introducing cholesterol *after* preparation of phospholipid-only aLUVs, using cholesterol-loaded mβCD [289]; or (3) adding cholesterol only to the acceptor vesicles and optimizing the exchange conditions for the use of either hydroxypropyl-α-cyclodextrin [290] or methyl-α-cyclodextrin [291] (α-CDs can transport phospholipids but not cholesterol due to their smaller hydrophobic cavity). We note that determining the transbilayer distribution of cholesterol is not straightforward as this molecule flip-flops rapidly between the two bilayer leaflets, making its extraction from, or selective labeling in, the outer leaflet inappropriate for quantification.

5.3 Materials

REAGENTS

- 1,2-Dipalmitoyl-d62-*sn*-glycero-3-phosphocholine [di-16:0 PC-d62, DPPC-d62, chain perdeuterated DPPC, 796.4 g/mol] (Avanti Polar Lipids cat. no. 860355)

- 1-Palmitoyl-2-oleoyl-*sn*-glycero-3-phosphocholine-1,1,2,2-d4-N,N,N-trimethyl-d9 [16:0/18:1 PC(d13), POPC-d13, headgroup deuterated POPC, 773.08 g/mol] (Avanti Polar Lipids cat. no. 790433)
- 1-Palmitoyl-2-oleoyl-*sn*-glycero-3-phospho-(1′-*rac*-glycerol) (sodium salt) [16:0/18:1 PG, POPG, 771.0 g/mol] (Avanti Polar Lipids cat. no. 840457)
- Methyl-β-cyclodextrin (mβCD, 1310 g/mol) (Fisher Scientific cat. no. AC377110000)
- Sucrose (342.3 g/mol) (Fisher Scientific cat. no. BP2201)
- HPLC-grade chloroform (Fisher Scientific cat. no. AA43685)
- HPLC-grade methanol (Fisher Scientific cat. no. AA22909)
- CAUTION Hydrochloric acid HCl (Fisher Scientific cat. no. SA48). Harmful if inhaled, ingested, or comes in contact with the skin. Proper goggles and gloves should be worn during handling and manipulation.
- Praseodymium(III) nitrate hexahydrate {$Pr(NO_3)_3$ $6H_2O$} (Pr^{3+}, 435.0 g/mol) (Fisher Scientific cat. no. AA11240)
- Ultrapure H_2O
- 99.9% D_2O (Cambridge Isotopes cat. no. DLM-4)
- 20% w/w sucrose in H_2O (0.632 M, 1.08 g/mL). Store at 4 °C for not more than a week to prevent bacterial growth.
- 25 mM NaCl in H_2O. Store at room temperature.
- 20 mM $Pr(NO_3)_3$ in D_2O. Store at room temperature.

EQUIPMENT

- Avance III 400 MHz spectrometer (Bruker, Billerica, MA) using Bruker TopSpin acquisition software, and analyzed with TopSpin 3.2.
- Wilmad LabGlass 5 mm NMR tubes (Fisher Scientific cat. no. 1680008).

- Agilent 5890A gas chromatograph (Santa Clara, CA) with a 5975C mass-sensitive detector operating in electron-impact mode.
- An HP-5MS capillary column (30 m × 0.25 mm, 0.25 μm film thickness) (Agilent cat. no. 19091S-433E)
- Centrifugal filter devices: Amicon Ultra-15, 100,000 Da molecular weight cutoff (Fisher Scientific cat. no. UFC910024)
- Sorvall LYNX 4000 Superspeed Centrifuge (Thermo Fisher Scientific cat. no. 75006580)
- BI-200SM Research Goniometer and Laser Light Scattering system (Brookhaven Instruments cat. no. BI-200SM).
- Hand-held miniextruder with a 100 nm pore-diameter polycarbonate filter (Avanti Polar Lipids cat. no. 610026)
- 250 μL glass syringe (Hamilton cat. no. 81175)

REAGENT SETUP

Lipid stock solutions: Prepare the following lipid stock solutions in glass vials with Teflon-lined caps: DPPC-d62 (30 mM in $CHCl_3$); POPC-d13 (30 mM in $CHCl_3$); POPG (2 mM in $CHCl_3$). Store at -20 °C for up to one year, or at -80 °C indefinitely. Lipids stored for longer than one year should be checked for impurities by TLC.

Methanolic HCl: In a fume hood, prepare methanolic HCl (1 M) by adding 3.04 mL concentrated HCl to 30 mL methanol in a beaker, then stir to mix. Transfer the solution to a graduated cylinder, then add methanol to a total volume to 37 mL. Store the solution in a glass vial with a Teflon-lined cap at room temperature for up to 2 months [292].

Methyl-β-cyclodextrin (35 mM).

1. Weigh the cyclodextrin powder in a volumetric flask (for 25 mL of solution, 1.1463 g mβCD is needed).
2. Add water until the flask is about half full, then cover the opening with foil and incubate at room temperature for 1-2 hours, or until the powder is fully dissolved. Bring the solution to the appropriate volume with water and mix by inverting the flask 20 times. The density of the solution should be 1.0114 g/cm^3.

<CRITICAL> The solution can be safely kept for a few days on the bench but freezing at -20 °C is recommended for longer term storage to prevent bacterial growth.

3. Allow the frozen solution to warm to room temperature, and gently mix before use.

5.4 Procedure

Preparation of donor and acceptor films

TIMING ~14 h

1. Transfer 647 µL (15.46 mg, 19.4 µmol) of the DPPC-d62 stock solution to a glass scintillation vial ("donor") using a glass syringe.

2. Transfer 205 µL (4.75 mg, 6.15 µmol) of the POPC-d13 stock solution and 162 µL (0.25 mg, 0.324 µmol) of the POPG stock solution to a glass scintillation vial ("acceptor") using a glass syringe.

   CRITICAL STEP Acceptor films are doped with 5 mol % POPG, a negatively

charged lipid that has the same gel-to-fluid transition temperature as POPC, to ensure that all vesicles are unilamellar. Extrusion of lipid dispersions that contain only neutral lipids results in a non-negligible fraction of vesicles with two or more lamellae that are easily observed by small-angle X-ray scattering [293].

3. Remove the organic solvent from the scintillation vials from Steps 1 and 2 with an inert gas stream and gentle heating, followed by overnight drying under high vacuum (~12 h).
   PAUSE POINT Lipid films can be stored frozen for several months prior to hydration.

Preparation of acceptor unilamellar vesicles

TIMING ~2.5 h

4. Preheat the acceptor film from Step 2 to 40 °C and hydrate it with 500 μL of preheated 25 mM NaCl solution to a lipid concentration of 10 mg/mL. Vortex the solution vigorously (i.e., at the highest setting) until the lipid film is completely removed from the walls of the vial.
   CRITICAL STEP The temperature for hydration should always be above the melting temperature of the lipids.

5. Incubate the acceptor MLV suspension at 40 °C for 1 h with occasional vortexing.

6. Transfer the acceptor MLV suspension to a -80 °C freezer for ~ 10 min or until completely frozen. Thaw at 40 °C for 5-10 min and then vortex. Repeat the freeze-thaw cycle five times.

   PAUSE POINT MLV suspensions can be stored frozen for several months. Prior to use a few freeze/thaw cycles should be performed.

7. To obtain unilamellar vesicles, pass the acceptor MLV suspension 31 times through a miniextruder assembled with a 100 nm pore-diameter polycarbonate filter.

   CRITICAL STEP The extrusion should always be carried out at a temperature higher than the melting temperature of the lipids. Use a hot plate if needed and preheat the extruder before loading the lipid suspension. Then incubate for at least 10 min on the hot plate to equilibrate the temperature before extrusion.

   <PAUSE POINT> Use immediately or store at room temperature for up to 1 week.

8. Measure the size distribution of the acceptor LUVs with DLS. Checking the size of the acceptors at this point is useful for diagnosing problems in the final aLUVs.

   ?Troubleshooting

Preparation of donor multilamellar vesicles

TIMING ~3 h

9. Preheat the donor film from Step 1 to 50 °C and hydrate it with 775 μL of preheated 20% (w/w) sucrose to a lipid concentration of 20 mg/mL. Prepare an

MLV suspension by vortexing the solution vigorously (i.e., at the highest setting) until the lipid film is completely removed from the walls of the vial.

CRITICAL STEP The temperature for hydration should always be above the melting temperature of the lipids.

10. Incubate the donor MLV suspension at 50 °C for 1 h with occasional vigorous vortexing.

11. Transfer the donor MLV suspension to a -80 °C freezer for ~ 10 min or until completely frozen. Thaw at 50 °C for 5-10 min and then vortex. Repeat the freeze-thaw cycle five times.

    <PAUSE POINT> MLV suspensions can be stored frozen for several months. Prior to use a few freeze/thaw cycles should be performed.

12. Dilute the donor suspension 20-fold by adding 14.7 mL H_2O, and immediately centrifuge at 20,000 × g for 30 min at 20 °C. Discard the supernatant by tipping the centrifuge tube.

    CRITICAL STEP Perform this step immediately before proceeding to the next step.

    ?Troubleshooting

Incubation of donor vesicles with mβCD

TIMING ~2 h

13. Suspend the donor pellet with 4.43 mL of the 35 mM mβCD solution for a mβCD:lipid molar ratio of ~ 8:1. Transfer the suspension to a 20 mL glass

scintillation vial with a magnetic stir bar.

CRITICAL STEP Calculate the mβCD:lipid ratio assuming that no lipid is lost during centrifugation in Step 12.

CRITICAL STEP To minimize the formation of bubbles and foam, gently pipet the mβCD solution onto the pellet, then slowly pipet mix until the pellet is dissolved.

CRITICAL STEP To ensure efficient mixing during the next step, check that the level of the mβCD/donor solution is not much higher than the level of the stir bar. If the level is much higher, a larger beaker or other flat bottom glass container can be used instead of the scintillation vial.

14. Incubate the mβCD/donor solution at room temperature with gentle stirring (~ 250 rpm) for 2 h.
CRITICAL STEP Vigorous stirring can create foam, which may reduce the exchange efficiency.

CRITICAL STEP For optimal exchange efficiency, the incubation should be performed at a temperature higher than the melting temperature of the acceptor lipids.

CRITICAL STEP Perform this step immediately before proceeding to the next step.

Incubation of acceptor vesicles with mβCD/donor solution

TIMING ~0.5h

15. Add the acceptor LUVs from Step 7 to the mβCD/donor solution, and then incubate at room temperature with gentle stirring (~ 250 rpm) for 30 min.
    CRITICAL STEP We find little gain in exchange efficiency beyond 30 min for this lipid composition (unpublished).

    CRITICAL STEP For optimal exchange efficiency, the incubation should be performed at a temperature higher than the melting temperature of the acceptor lipids.

Purification of aLUVs

TIMING ~4 h

16. Measure the volume of the mβCD/donor/acceptor slurry and dilute it 8-fold by adding ~ 36 mL of ultrapure H_2O. Transfer the mixture to a 50 mL conical tube and centrifuge at 20,000 × g for 30 min at 20 °C.

17. Without disturbing the pellet, carefully remove the supernatant with a glass Pasteur pipet and transfer to a clean 50 mL container. Discard the pellet.
    CRITICAL STEP When a fixed angle centrifuge rotor is used in Step 16, the pellet will form on the side wall of the centrifuge tube. Do not be overly aggressive when removing the supernatant. Keep the centrifuge tube immobilized on the bench and stop when ~ 1 mL of supernatant remains above

the topmost point of the pellet.

18. Transfer the supernatant to two 15 mL centrifugal filter devices. Centrifuge at 5000 × g until the volume has been reduced below 500 μL in each filter (~ 30 min).

    CRITICAL STEP This step proceeds at a faster rate when using a swinging bucket rotor even at a lower speed (e.g., 2500 × g).

    CRITICAL STEP For larger scale preps, use additional centrifugal filters to reduce the time required to concentrate the supernatant.

19. Discard the filtrate (which contains mβCD and mβCD/lipid complexes) from each centrifugal filter device, and then add D_2O to the maximum volume (~ 15 mL). Centrifuge at 5000 × g until the volume has again been reduced below 500 μL in each filter (~ 30 min). Repeat this step three times to remove mβCD, and to replace H_2O with D_2O.

    CRITICAL STEP Washing with D_2O instead of H_2O enables the use of ^1H NMR without the need for solvent suppression, as described in Steps 30-34.

20. Using a mechanical pipet with a 200 μL tip, transfer the retentate into a 1.5 mL snap-top centrifuge tube.

21. To check vesicle integrity and test for the presence of donor MLVs or other contaminants, measure the size distribution of the aLUVs with DLS and compare to the acceptor LUV size measured in Step 8.

    ?Troubleshooting

Assessing exchange efficiency with gas chromatography (GC)

TIMING ~3 h

22. Transfer 5-10 μL of the aLUV suspension (50-100 μg of lipid) into a 13×100 mm screw top glass culture tube for conversion to fatty acid methyl esters (FAMEs) via acid catalyzed methanolysis.

    CRITICAL STEP The DLS count rates measured in Steps 8 and 21 can be used to estimate the aLUV concentration, which is helpful for determining the amount of sample required for the GC assay.

23. Add 1 mL methanolic HCl to the culture tube, vortex, flush with Ar, and seal tightly with a Teflon-lined cap. Incubate in a dry block heater at 85 °C for 1 h, and then allow the tube to cool for 5 min.

24. Add 1 mL H_2O and vortex to mix. Then, add 1 mL hexane and vortex vigorously (i.e., at the highest setting) for 15-30 s to create an emulsion and extract the FAMEs.

    CRITICAL STEP Formation of the emulsion is visible to the eye as a rapid transition to a cloudy appearance of the vortexing solution. It may take several seconds for the emulsion to form.

25. Centrifuge at low speed (~ 400 × g) for 5 min to break the emulsion, then remove 500-800 μL of the upper (hexane) phase and transfer to a GC autosampler vial. Bring the total volume to 1 mL with hexane.

26. Load the autosampler vial into the GC automatic liquid sampler. Using an inlet temperature of 270 °C and helium carrier gas at a 1 mL/min flow rate, initiate the following column temperature program for a 1 μL sample aliquot in splitless injection mode (total run time 25.5 min).

step	Total time [min]	Rate [°C/min]	Start temperature [°C]	End temperature [°C]
1	2	0	60	60
2	5.5	20	60	170
3	14	5	170	240
4	2	30	240	300
5	2	0	300	300

27. GC/MSD ChemStation Enhanced Data Analysis software (Agilent Technologies, Santa Clara, CA) will assign and integrate the total ion chromatogram peaks.

28. Calculate the donor mole fraction χ_D in the aLUV sample:

$$\chi_D = \frac{A_{d16:0}}{A_{d16:0} + A_{16:0} + A_{18:1}},$$

where $A_{d16:0}$, $A_{16:0}$, and $A_{18:1}$ are the integrated areas of the peaks corresponding to methyl palmitate-d31, methyl palmitate, and methyl oleate,

respectively. Estimate the fraction of outer leaflet exchange (i.e., the exchange efficiency):

$$E_{obs} = 2\chi_D.$$

Note that this equation assumes negligible donor flip-flop and equal lipid packing density within the two leaflets.

CRITICAL STEP The accuracy of the determined composition can be increased with the use of a standard curve for the specific lipid mixture as the area fractions may not vary linearly with the component mole fractions.

29. Compare E_{obs} calculated in Step 28 with the maximum theoretical exchange efficiency $E_{max} = \rho/(\rho + 0.5)$ where ρ is the donor-to-acceptor ratio. For the 3:1 ratio used in this protocol, E_{max}= 0.86.

    CRITICAL STEP The equation for E_{max} assumes that all donor lipid is available for exchange with the outer leaflet acceptor lipid, and that mβCD does not preferentially interact with either the donor or acceptor lipid. E_{max} therefore represents an upper limit of the exchange efficiency. Assuming negligible donor flip-flop during the exchange step, $E_{obs} > E_{max}$ may indicate the presence of donor contamination.

    ?Troubleshooting

Assessing donor asymmetry with ^{1}H NMR

TIMING ~1 h

30. In a plastic snap-cap centrifuge tube, bring ~ 50-100 μL of the aLUV suspension to 500 μL with D_2O for a final lipid concentration of ~ 0.5 mg/mL, then transfer to a 5 mm NMR tube.

31. Load the sample into the NMR spectrometer and collect a standard ^{1}H pulse sequence with a 30º flip angle and 2 s delay time at 50 °C. Collect 32-256 transients, depending on signal-to-noise. Locate the singlet resonance at ~ 3.1-3.6 ppm corresponding to the 9 equivalent protons of the donor choline moiety (Fig. 5.3a). Separate resonances may appear at ~ 3.7 ppm corresponding to residual mβCD in the sample. Broad peaks for the hydrocarbon acyl chains should be visible from ~ 0.5-1.5 ppm.

    CRITICAL STEP An asymmetric choline resonance may indicate contamination from small unilamellar vesicles (SUVs), as shown in Fig. 5.3d.

    ?Troubleshooting

32. Dispense 2 μL of the 20 mM Pr^{3+}/D_2O solution directly into the NMR tube. Cap the tube and invert it a minimum of three times to mix the contents. Reload the sample in the NMR and collect 32-256 transients. All or part of the choline resonance will shift downfield (i.e., to higher ppm) and broaden, as in Fig. 5.3b; the shifted portion corresponds to protiated choline lipid (here, the donor lipid) located in the outer leaflet. Repeat this procedure a minimum of 2-3 times, or until a shift of at least 0.05 ppm is achieved.

33. Export the NMR spectrum as an ASCII file, then fit the resonances to Lorentz functions (Fig. 5.3). Two Lorentzians are used to model NMR data in the absence of Pr^{3+}: one for the choline and one for the mβCD (if multiple mβCD peaks are present, each can be fit with a separate Lorentzian). In the presence of Pr^{3+} a third Lorentzian is used to account for the second (outer leaflet) choline resonance. To assist with the fitting routine, the peak area ratio between the choline and mβCD peaks in the absence of Pr^{3+} can be used to constrain the area ratio of the total choline (i.e. the sum of the shifted and unshifted choline peaks) and mβCD in the presence of Pr^{3+} since neither choline nor mβCD are being lost from or added to the system.

34. Find the integrated areas *R* of the Lorentzians representing the shifted and unshifted (if present) choline resonances. Determine the fraction of donor lipid located in the outer leaflet using the following equation:

$$f_D{}^{out} = \frac{R_{shifted}}{R_{shifted} + R_{unshifted}}.$$

Standard errors on $f_D{}^{out}$ can be obtained from additional Pr^{3+} titrations**.** **CRITICAL STEP** Values of $f_D{}^{out}$ close to 0.5 indicate a symmetric donor distribution, as shown in Fig. 5.3c. While a *gradual* loss of asymmetry over several days will occur due to spontaneous lipid flip-flop, this process is slow for the specific sample described here when stored at room temperature (elevated temperatures will accelerate flip-flop [10]). An *initial* absence of asymmetry, though not expected here, may occur for different choices of donor and acceptor lipids. The explanation may be trivial (i.e., an intrinsically fast flip-flop rate for the chosen composition), or it may indicate experimental conditions that are incompatible with aLUV preparation (i.e., an mβCD

concentration that is too high for the chosen donor and acceptor lipids).

Determining the composition of the inner and outer leaflets

TIMING ~ 1 min

35. Using the experimentally determined quantities of f_D^{out} from NMR (Step 34) and χ_D from GC/MS (Step 28), calculate the donor mole fraction in each leaflet:

$$\chi_D^{out} = 2\chi_D f_D^{out}$$

$$\chi_D^{in} = 2\chi_D(1 - f_D^{out})$$

The acceptor mole fraction in the outer and inner leaflets is then equal to $1 - \chi_D^{out}$ and $1 - \chi_D^{in}$, respectively.

?TROUBLESHOOTING

Acceptor LUVs size distribution is too large or too small (Step 8)

Vesicles prepared by extrusion through 100 nm pores typically have size distributions centered at a 100-150 nm hydrodynamic diameter, as measured by DLS. If the acceptor vesicles are larger than 150 nm, repeat Steps 7-8. Diameters much smaller than 100 nm may indicate that the extruder was accidentally assembled with a smaller pore size filter.

Donor pellet appears loose (Step 12)

A loose pellet is an indication that the donor MLVs are markedly heterogeneous in size and/or density, which may result in donor contamination in the final aLUV sample. Remove the diffuse parts of the pellet along with the supernatant and retain only that part of the pellet that adheres firmly to the wall of the centrifuge tube.

Recovered aLUV sample has visible aggregates and/or a large increase in average size (Step 21)

Visible aggregates and/or a considerable increase in the average vesicle size (i.e., more than 10% larger than the acceptor LUVs) is an indication of donor MLV contamination. Dilute the sample 20-fold with H_2O, vortex briefly, and spin at 20,000 × g for 10-20 min. Carefully recover the supernatant with a glass transfer pipet, leaving the last ~ 5 mL even if there is no visible pellet. Repeat Steps 18-21.

Recovered aLUV sample contains more donor lipid than acceptor lipid (Step 29)

More donor than acceptor lipid (as measured by GC) is an indication of donor MLV contamination. Dilute the sample 20-fold with H_2O, vortex briefly, and spin at 20,000 × g for 10-20 min. Carefully recover the supernatant with a glass transfer pipet, leaving the last ~ 5 mL even if there is no visible pellet. Repeat Steps 18-29.

NMR shows an asymmetric choline resonance before the addition of shift reagent (Step 31)

Fig. 5.3d demonstrates how the NMR line shape can reveal the presence of contaminating SUVs that can be generated during incubation of mβCD and lipid. SUVs are diagnosed by an asymmetric choline resonance (often appearing as two distinct peaks) in the absence of a shift reagent. The two peaks are the result of different packing constraints in the outer and inner leaflets. If SUVs are present, it may be necessary to reduce the mβCD concentration.

5.5 Anticipated results

Beginners will need to perform several practice runs to obtain consistent results. Of note, factors that influence mixing of the exchange slurry (e.g., temperature and stirring speed) in Steps 14-15 may influence the exchange efficiency, and careful removal of the supernatant in Step 17 is critical for avoiding contamination. With time and experience, aLUV compositional variation of < 10% and a yield of > 60% of the initial acceptor LUV mass can be achieved. If contamination of donor vesicles is present and additional dilution-concentration-wash steps are needed as outlined in the Troubleshooting section, the yield may be smaller.

For the specific lipid composition described above, the exchange efficiency E_{obs} varies between 0.35 and 0.45 in our hands. If greater outer leaflet replacement is desired, the donor:acceptor ratio can be increased or multiple rounds of exchange can be performed (keeping in mind that additional exchange steps will reduce the yield). Unsurprisingly, we find that exchange efficiency depends on the identity of both the donor and acceptor lipids, with some systems approaching the maximum theoretical efficiency [4, 10, 286]. This is likely due to preferential interactions between mβCD and certain types of lipids that depend on both chain and headgroup structure [278, 294]. We find nearly complete donor asymmetry for this composition, with ~ 95% of DPPC-d62 residing in the outer leaflet, as determined by ^{1}H NMR. For other choices of donor and acceptor lipids, donor asymmetry measured immediately post-preparation ranges from 65-95% [4, 10, 286]. Table 5.1 summarizes the aLUVs prepared in our laboratories.

Much can be learned about the fundamental physical and chemical properties of cell membranes using aLUVs. For example, it is possible to systematically study the nature and mechanisms of interleaflet coupling in vesicles that mimic the asymmetric lipid distribution found in the plasma membrane, including whether phase separation in one leaflet induces demixing of lipid components in the other leaflet. Such basic

insights are necessary for understanding cellular processes including transmembrane signaling. Using the procedure described above, we prepared aLUVs having an outer leaflet composed of DPPC-d62/POPC-d13 in a 34/66 molar ratio, and an inner leaflet composed of POPC-d13 [4]. Using small-angle neutron scattering, we determined structural parameters for the inner and outer leaflets, including thickness and area per lipid. At room temperature, phase coexistence was observed in the outer leaflet of these aLUVs. Interestingly, we found a relatively low packing density for DPPC-d62 located in the outer leaflet compared to the typical tight packing of gel phases, suggesting a disordering effect from interactions with the fluid inner leaflet. This apparent strong interleaflet coupling was abolished at higher temperatures, where both leaflets were in the disordered fluid phase [286].

Without question, asymmetric vesicles are better biological mimetics when compared to their symmetric counterparts that have dominated membrane biophysical studies for nearly 50 years. The tradeoff is ease-of-preparation, although we expect substantial improvements will come with more widespread use of the procedures presented here and elsewhere [276]. Studies using aLUVs are still in their relative infancy, but it is already clear that asymmetry can significantly alter lipid lateral diffusion [295], packing density [4] and phase behavior [296], and the conformation [267], partitioning [265] and topology [48] of transmembrane proteins. Continued investigation will provide a deeper understanding of the properties of asymmetric bilayers and shed new light on the functional significance of membrane asymmetry in living cells.

CHAPTER 6
ACCURATE IN SILICO MODELING OF ASYMMETRIC BILAYERS BASED ON BIOPHYSICAL PRINCIPLES

6.1 Abstract

Technological advances in the last decade have enabled the study of ever more complex and physiologically relevant model membranes to help dispel the mystery surrounding the role of plasma membrane asymmetry in various cellular processes. The slowly accumulating body of experimental data is fueling renewed interest in, and the need for, computational methods to support interpretations and address a wide range of problems that are still not amenable to direct experimental study. The specific appeal of molecular dynamics (MD) simulations lies in their ability to access information at atomic resolution, which is useful for the formulation of testable mechanistic hypotheses. But the appropriate construction and simulation of asymmetric bilayer models determines the range of questions that can be addressed reliably with such simulations. Following rigorous biophysical criteria and principles in these efforts is one essential way to achieve this goal. We show that a robust comparison between the properties of simulated asymmetric and symmetric model membranes requires the tension in each bilayer leaflet to be zero. Because commonly used methods for constructing asymmetric bilayers including matching the average areas of the leaflets from the corresponding symmetric systems does not ensure zero leaflet tension, physically realistic changes in the areas of the two leaflets are precluded. We present a new method for identifying the ideal lipid packing in bilayers with different leaflet compositions that achieves the zero tension goal and discuss the basic principles underlying the biophysically correct computational study of asymmetric membranes.

6.2 Introduction

The cell plasma membrane (PM) is a hub of biological activity. Its involvement in various cellular processes is based on a carefully orchestrated balance between the properties of the lipid bilayer matrix and its interactions with membrane-associated proteins and small molecules. The quest for understanding this balance has made use of a variety of simplified model systems to dissect the biological complexity and probe the biophysical mechanisms underlying observed phenomena [60, 297-299]. The suitability of these models depends on their ability to reproduce membrane properties that are relevant to the specific phenomena. In this context, one of the features of current interest and debate is the asymmetric transverse lipid distribution across the membrane.

That certain types of lipids are found predominantly in the exoplasmic leaflet of the PM in eukaryotic cells, whereas other types are located exclusively in the cytosolic leaflet, is well known [33]. Beyond the consequences of exposure of a certain lipid species on either side of the membrane (e.g. phosphatidylserine exposure triggering a series of events leading to cell death [65]), the biophysical properties of such an asymmetric membrane environment and their role in cellular processes, have attracted special attention. The reasons include: (1) the importance of these properties for proper cell function as demonstrated by the active maintenance of the PM asymmetry through energy-driven protein machines; (2) the inability to predict the behavior of the asymmetric bilayer due to the big differences in the types of lipids and lipid mixtures found in the exoplasmic and cytosolic PM leaflets [76, 300]; and (3) the characteristics of protein-membrane interactions in asymmetric membranes which remain largely unexplored yet have been shown to play key roles in mechanisms of function in symmetric bilayers [46, 48, 301]. To attempt such explorations, many studies have taken advantage of the use of model systems. Significant progress ensued when the

preparation and study of asymmetric model membranes in vitro overcame the need for enzyme-catalyzed generation and maintenance of the non-equilibrium nature of bilayer asymmetry [4, 276, 289, 295]. Computational modeling provides a complementary description of intermolecular interactions and processes, and has added context and interpretation to the experimental results [302-304]. Molecular dynamics (MD) simulations have been especially appealing in this respect, due to their inherently high resolution and ability to access time and length scales that are hard to analyze with alternative techniques. In silico studies have thus examined membrane asymmetry effects on the thickness and acyl chain order parameter profiles of the two leaflets, the membrane electrostatic potential, the adsorption of ions, water permeation, lipid mixing heterogeneities including phase coexistence and domain registration, lipid diffusion, and a few aspects of protein-membrane interactions [304-314].

6.3 Compatibility criterion

In studying the effects of membrane asymmetry on biological phenomena, the properties of asymmetric bilayers are often compared to those of cognate symmetric membranes or to other asymmetric bilayers. The robustness and general applicability of such comparisons, and hence of the resulting predictions and hypotheses, depend on the extent to which the asymmetric bilayers are indeed *comparable* to symmetric bilayers, and even to one another. In fact, the validity of the comparison is not assured just by the use of similar computation conditions (e.g. a flat bilayer patch simulated at constant temperature and pressure) but rather requires adherence to pertinent biophysical principles, as discussed below.

A critical comparability criterion is *tension*, which can affect both the bilayer itself and its interactions with non-lipid molecules. Tension can arise both from factors

intrinsic to the bilayer (such as an imbalance of the areas of the two leaflets constrained to be in a closed geometry), and from external ones such as osmotic imbalance of solutes across the membrane or mechanically applied pressure. In symmetric bilayers for example, a property such as the bilayer's area compressibility modulus emerges from changes in bilayer area (lipid packing) induced by systematically varied tension [113, 191]. Similarly, leaflet tension induced by systematically removing lipids from one of the leaflets in symmetric bilayers was shown to produce differences in the lipid packing densities of the two individual leaflets [66, 315]. As lipid packing is intricately related to virtually all other aspects of bilayer structure, it is not surprising that tension has also been shown to affect a variety of properties including the density and lateral pressure distribution of the lipid matrix, the order parameter, and interdigitation of the lipid acyl chains, as well as the bilayer thickness and electrostatic potential, and lipid diffusion and hydration [66, 315-317]. Therefore, tension-induced changes have clear functional consequences as illustrated by their effects on e.g. mechanosensitive ion channels [105].

Unfortunately, it is still nearly impossible to measure the actual tension in a real (asymmetric) PM which is likely laterally heterogeneous. In the symmetric bilayer models, however, the tension in each leaflet is zero, and the proper comparison with asymmetric bilayer models requires that the tension in each of the asymmetric bilayer leaflets is also 0. Thus, a "0 leaflet tension (0-LT)" condition is a strong requirement for comparability of different bilayer and leaflet properties in model systems.

Failure to satisfy the 0-LT condition will affect the validity of mechanistic insights from comparisons. Notably, simply running an MD simulation of an asymmetric bilayer with the surface tension parameter set to zero (which is the default in many software packages) does *not* guarantee that the tension in each bilayer leaflet is zero [66, 315]. A non-zero leaflet tension may thus go essentially unnoticed, and yet have

significant effects on the structural properties of the leaflets. Indeed, commonly used methods for constructing asymmetric bilayers *in silico* (including ones that rely on information from symmetric bilayers) do not assure zero leaflet tension and, as we show herein, they must fail to reproduce experimentally observed changes in the structural properties of the two bilayer leaflets. Building asymmetric bilayers with 0 leaflet tension requires an explicit calculation of the leaflet tension and appropriate adjustment of the number of lipids. While such adjustment can be executed by trial-and-error, this approach could be computationally expensive and highly inefficient. Here we propose a simple and efficient method to overcome this key difficulty.

6.4 Construction of bilayers with zero leaflet tension

Our method starts with a bilayer constructed from arbitrarily chosen numbers of lipids in the two leaflets (e.g. as estimated from the average areas per lipid of the corresponding symmetric bilayers). The key step in the adjustment protocol is an optimization guided by the relationship between tension and area expansion. Namely, if T_L is the tension in leaflet L (top or bottom), and K_A is the bilayer area compressibility modulus, then:

$$T_L = K_A\left(\frac{a_L'}{a_L} - 1\right), \tag{6.1}$$

where a_L and a_L' are, respectively, the ideal area per lipid in the leaflet (i.e. at 0-LT) and its current (instantaneous) average. Since the sum of T_T and T_B (where subscripts T and B denote 'top' and 'bottom' leaflet respectively) is equal to the bilayer surface tension, it follows that when the tension is 0, $T_T = -T_B$ and hence $|T_T| = |T_B| = T$. In a symmetric bilayer in which the two leaflets have the same composition and number

of lipids, $T = 0$. But if the two leaflets are different, it is possible that $T \neq 0$, in which case the number of lipids needs to be adjusted to make $T = 0$.

The response of the areas of the two leaflets to T depends on the compressibility modulus of the *bilayer*, and not on the compressibility modulus of each *leaflet* alone, because in the simulation protocol the total leaflet areas are constrained to be the same by the imposed periodic boundary conditions. The total area of the leaflet can be written as $a_L' N_L' = a_L N_L$, where N_L and N_L' denote the ideal and current number of lipids in the leaflet. It follows that $N_L = N_L'(a_L'/a_L)$ and using Eq. 6.1 the ideal number of lipids in a leaflet can be expressed as a function of known (i.e. easily calculable) properties, i.e. the leaflet tension, the bilayer K_A and the number of lipids in the leaflet:

$$N_T = \frac{N_T'(T_T + K_A)}{K_A} \quad \text{and} \quad N_B = \frac{N_B'(T_B + K_A)}{K_A}. \tag{6.2}$$

Importantly, the number of lipids in *both* leaflets needs to be adjusted to satisfy the 0-LT condition because both $T_T \neq 0$ and $T_B \neq 0$ when $T \neq 0$. Consequently, the ratio N_T/N_B:

$$\frac{N_T}{N_B} = \frac{N_T'(T_T + K_A)}{N_B'(T_B + K_A)}, \tag{6.3}$$

serves to determine how to adjust the number of lipids in the bilayer. This adjustment can be achieved, for example, by keeping the number of lipids in one leaflet fixed and calculating how many lipids to add or remove from the opposing leaflet, or by building a new bilayer with the same composition but different size.

6.5 Application of the method to bilayers with diverse properties

We illustrate the new method with two examples of asymmetric bilayers with diverse properties. Example #1: An asymmetric bilayer with two single-component leaflets composed of the low-melting lipids SOPC and DOPC (see the caption of Table 6.1 for lipid abbreviations). Example #2: An asymmetric bilayer whose two leaflet compositions have very different thermodynamic properties in symmetric bilayers: one consisting of the low-melting lipid SOPC and the other one of a mixture of DPPC and 20 mol% cholesterol (Chol). For the all-atom simulations performed at 25°C with NAMD, each bilayer was constructed with CHARMM-GUI by specifying the number of lipids in the two leaflets. Bilayer area compressibility was calculated with a recently developed method (Chapter 3.2), and leaflet tension was obtained by integrating the lateral pressure profile of the bilayers (see Appendix D for software references and more details on the simulations and analysis).

In Example #1, the average *areas per lipid* (*apl*) for the two leaflets obtained from the cognate symmetric bilayers are 63.8 $Å^2$ for SOPC, and 68.2 $Å^2$ for DOPC [318]. An asymmetric bilayer that preserves this area ratio would be expected to have 100 SOPC lipids in one leaflet and 94 DOPC lipids in the opposing leaflet. A simulation of this bilayer indicated a bilayer area compressibility modulus of 228 ± 20 mN/m and a tension of -1.2 mN/m in the SOPC leaflet, and 1.2 mN/m in the DOPC leaflet. According to Eq. 6.3 the ideal lipid ratio was 1.05 and if the number of SOPC lipids is kept fixed, 95 DOPC lipids would be needed to satisfy the 0-LT condition. Indeed, a subsequent simulation of the asymmetric bilayer with 95 DOPC and 100 SOPC lipids resulted in a tensionless bilayer ($T = 0.5$ mN/m) and no further adjustment was needed. A smaller asymmetric bilayer that preserves the same ratio by containing 64 SOPC lipids and 61 DOPC lipids was then constructed, and found to meet the 0-LT condition without adjustment. Thus, simulations of smaller bilayers can be used to

initially identify the ideal interleaflet lipid ratio and save computational resources in the construction of larger tension-free asymmetric bilayers.

For the construction of Example #2, the average *apl* in a symmetric DPPC/Chol bilayer of 40.8 Å^2 suggested that 86 SOPC lipids are needed to match the initial area of a DPPC/Chol leaflet with 135 lipids. A simulation started with 100 SOPC lipids as in Example #1 yielded a bilayer K_A of 1080 $\pm$ 129 mN/m, and the tension in the SOPC and DPPC/Chol leaflets was -5.7 mN/m and 5.7 mN/m, respectively. From Eq. 6.3 the calculated ideal ratio was 1.36 so that keeping the 135 lipids in the DPPC/Chol leaflet yielded an ideal number of 99 SOPC lipids. In a subsequent simulation with 99 SOPC lipids, the tension in the two leaflets decreased to -2.2 and 2.2 mN/m, indicating that the ideal ratio is 1.37 and the ideal number of lipids in the bottom leaflet is indeed between 99 and 98 (98.5). Notably, due to the requirement for an integer number of lipids in a leaflet the ideal leaflet tension may be non-zero, yet represent the minimal tension achievable in a bilayer of this composition.

Table 6.1 shows the average *apl* in each leaflet of the two examples above, both in the asymmetric and the corresponding symmetric bilayers. In both examples, the areas of the two leaflets change to different extents and in opposite directions compared to the symmetric systems: when SOPC is coupled to the more loosely packed DOPC leaflet, the SOPC *apl* goes up slightly, and the DOPC *apl* goes down slightly. When SOPC is opposite the much more ordered DPPC/Chol leaflet, the direction is reversed and the SOPC *apl* goes down by 8% (4.9 Å^2) whereas the DPPC/Chol *apl* increases only slightly, by 6% (2.4 Å^2). These trends are consistent with results from *in vitro* measurements reporting fluidization of DPPC-rich domains as a result of coupling to a fluid POPC inner leaflet [4], and increase in the order of a DOPC/DOPS leaflet as a result of coupling to a sphingomyelin (SM)-rich leaflet; the effect on the order of the SM leaflet is smaller [276]. The contrast with the results of asymmetric bilayer

construction following the common protocol of matching the leaflet areas from the cognate symmetric bilayers is dramatic as in the latter approach the structural properties of the leaflets remain largely unchanged (Table 6.1). This can be explained by 1) the two leaflet areas being constrained to change in the same way due to the periodic boundary conditions, and 2) the ratio of their *apl*-s being fixed during the simulation due to the much longer time scales needed for lipid translocation between leaflets. Depending on how far this symmetric *apl* ratio is from the ideal one, the resulting leaflet tension may or may not produce a distinct phenotype (Fig. D1) and interfere with the estimation of the ideal ratio (Table D1). Asymmetric bilayers made of two leaflets with very different structural and thermodynamic properties are particularly challenging in that respect as they may undergo larger changes due to interleaflet coupling as illustrated by Example #2.

Table 6.1. Structural leaflet parameters in asymmetric and corresponding symmetric bilayers. Lipid names are abbreviated as follows: 1,2-dioleoyl-*sn*-glycero-3-phosphocholine (DOPC), 1-stearoyl-2-oleoyl-*sn*-glycero-3-phosphocholine (SOPC), 1,2-palmitoyl-*sn*-glycero-3-phosphocholine (DPPC) and cholesterol (Chol). Shown is the average area per lipid, calculated by dividing the box area by the number of lipids in the leaflet. For each leaflet (L), the displayed structural properties are calculated either from a symmetric bilayer of that composition (Sym), an asymmetric bilayer constructed by matching the areas of the cognate symmetric bilayers (Asym [sArea]) or an asymmetric bilayer constructed with the ideal number of lipids in the leaflets, i.e. ensuring minimal leaflet tension as explained in the text (Asym [0-LT]). The reported uncertainties are shown in parentheses and represent standard errors calculated from consecutive blocks of length determined by the effective number of samples following the algorithm in Ref. [196].

	L	Lipids	APL [Å^2]		
			Sym.	Asym [sArea]	Asym [0-LT]
#1	top	DOPC	68.2 (0.1)	68.1 (0.2)	67.5 (0.1)
	bot	SOPC	63.8 (0.1)	64.0 (0.2)	64.1 (0.1)
#2	top	DPPC/Chol	40.8 (0.0)	40.7 (0.0)	43.2 (0.1)
	bot	SOPC	63.8 (0.1)	63.9 (0.1)	58.9 (0.1)

6.6 Discussion

The formalism we described helps to identify bilayers that are more susceptible to artifacts from inappropriate bilayer construction by examining the key factors contributing to the leaflet tension caused by deviations from the ideal lipid ratio $R = N_T/N_B$. Suppose that $N_B' = N_B$ and $N_T' = N_T + c$ where $c \neq 0$ can be a positive or negative integer and denotes the number of *mismatch* lipids in the top leaflet. Then the current ratio will be $R' = N_T'/N_B' = R + c/N_B$. Fig. D2A shows how R' varies with c for bilayers with ideal ratio $R = 1.35$ and different number of lipids in the bottom leaflet: As the bilayer size grows each mismatch lipid represents a smaller percentage of N_B and consequently, has a smaller effect on R'. Thus, larger bilayers are more tolerant to deviations from the ideal number of lipids and would be generally less prone to inaccurate estimates of bilayer properties.

From Eq. 6.3 we can also express the tension $T_T = -T_B$ as a function of R':

$$T_T = K_A \frac{R - R'}{R + R'}. \tag{6.4}$$

Fig. D2B shows how T_T varies with R' and K_A. The tension is negative when the top leaflet has more lipids than N_T (i.e. when $c > 0$ and $R' > R$), and positive when the top leaflet has less lipids than N_T (i.e. when $c < 0$ and $R' < R$). Importantly, T_T scales with the bilayer K_A. This dependence is particularly relevant for bilayers containing high melting lipids and cholesterol: Chol increases the packing and area compressibility of symmetric bilayers [183, 189, 319] and we see a similar effect in asymmetric bilayers (Table 6.1). Thus, the naturally higher K_A of the Chol containing bilayers results in higher tension making them more sensitive to deviations from the

ideal ratio and hence more vulnerable to artifacts caused by inappropriate bilayer construction (Fig. D2). This means that in asymmetric bilayer models of the PM in which one leaflet is enriched in Chol and high melting lipids, special care must be taken to ensure that the bilayer satisfies the 0-LT condition for a meaningful comparison with other model systems.

Building an asymmetric bilayer by matching leaflet areas using information from symmetric bilayers [304-308, 311, 312] can have profound consequences for the observable effects of interleaflet coupling (Table 6.1). Indeed, the idea of matching leaflet areas from symmetric bilayers to avoid tension in a simulated asymmetric bilayer is inherently flawed – regardless of how many lipids the two leaflets have – because their areas are always constrained to be the same by the imposed periodic boundary conditions, thus hiding any non-zero leaflet tension. Randomly choosing the number of lipids in the two leaflets [320] or making the total number of lipids in the two leaflets the same [309, 310] does not guarantee a 0-LT condition. A recently described method for self-assembly of coarse-grained asymmetric bilayers which ensures 0-LT [313] is intriguing, but it uses a spontaneous self-assembly process in which control over the exact compositions of the two leaflets is limited. This makes it challenging to study bilayers with specific experimentally determined, or systematically varied, leaflet compositions.

6.7 Conclusion

The method presented here provides a simple solution to an important problem in the computational analysis of asymmetric bilayers, because only bilayers satisfying the 0-LT criterion can be used to gain relevant insights about the effects of interleaflet coupling and be on a par with the emerging body of experimental data. The approach follows specific biophysical principles required for valid simulation of asymmetric

bilayers and enables robust comparisons of asymmetric model bilayers to other model membranes under zero leaflet tension conditions by directing the adjustment of the number of lipids in the leaflet.

CHAPTER 7
EFFECT OF MEMBRANE ASYMMETRY ON BILAYER PROPERTIES

7.1 Introduction

Membrane asymmetry is an important component of the complexity of biological membranes. Since the discovery of the asymmetric lipid distribution in the erythrocyte membrane in the early 1970s, it has been established that plasma membrane asymmetry is ubiquitous in eukaryotic cells. While its precise characterization in most cell types is hindered by the presence of membrane-bound inner organelles, its importance for cellular homeostasis has been widely acknowledged. The constitutive appearance of the negatively charged lipid phosphatidylserine (PS) on the outer leaflet of the plasma membrane, for example, serves as a universal marker for phagocytosis and cell death [65], while the transient exposure of PS has been shown to accompany certain events such as the activation of platelets (i.e. thrombosis) [64] and mast cells (i.e. IgE-mediated release of histamines and cytokines) [321]. Furthermore, the existence and ubiquitous expression across cell types of proteins that regulate the asymmetric phospholipid distribution in the plasma membrane, and the corresponding physiological consequences associated with their malfunction (e.g., Scott syndrome) provide yet another piece of evidence for the biological importance of this peculiar transverse membrane organization.

The asymmetric phospholipid distribution found in cellular membranes invites many questions about the biophysical properties of the membrane environment. Some effects are more obvious from the respective lipid leaflet compositions, like an asymmetric charge density due to the asymmetric distribution of charged lipids. But others, such as the mechanical properties of the bilayer or the packing and order of the lipids in each leaflet, are harder to predict. Studies on symmetric bilayers have demonstrated that the properties of lipid mixtures representative of the exoplasmic PM

leaflet (i.e., high melting lipids and cholesterol) [76] are very different from those of mixtures mimicking the cytosolic PM leaflet (i.e., lower melting lipids and cholesterol) [300]. This observation, together with the generally unknown extent to which the membrane leaflets can alter each other's physical properties, have prompted the investigation of interleaflet coupling with model systems.

Given the importance of rafts for cellular organization and function, many efforts have focused on studying the effects of asymmetry on the leaflets' ability to phase separate [12, 296, 322-326]. However, the complexity of these multi-component mixtures and the inability to probe the composition of the co-existing environments have made it difficult to hypothesize about the molecular mechanisms responsible for the observed effects. Since biological membranes have diverse compositions that are harder to precisely reconstitute and study in vitro, mechanistic knowledge is essential for reasoning about their properties. Thus, theoretical models have considered the roles of cholesterol, which can flip rapidly between leaflets, and lipids with long acyl chains that can penetrate deep into the opposing leaflet as possible mechanisms of interleaflet communication [327, 328]. However, changes in leaflet properties have been observed even in asymmetric bilayers that do not contain cholesterol or such long acyl chain lipids [4, 276, 295, 329], suggesting the existence of alternative ways by which the two leaflets can affect each other.

Molecular dynamics (MD) simulations with their atomic resolution have been instrumental in identifying mechanisms of function in many molecular systems; however, their utility relies on validation against experiments. While existing lipid force fields have been calibrated using in vitro data for symmetric bilayers, the construction and simulation of asymmetric membranes present additional challenges and require further validation (see Chapter 6). Unfortunately, existing structural data for asymmetric bilayers, consisting mostly of indirect measurements of lipid diffusion

and ill-defined leaflet packing, lacks the robustness and precision needed to corroborate simulation results.

Here we address these problems by applying a suite of different techniques both in vitro and in silico to investigate some of the fundamental mechanisms of interleaflet communication in asymmetric bilayers. We focus on simple mixtures with one or at most two non-cholesterol components, having a chain length not greater than 18 carbons in each leaflet. We define interleaflet coupling and formulate a hypothesis about its underlying mechanisms based on results from symmetric bilayers. To test this hypothesis in vitro, we perform a comparative study of the order parameter and rotational diffusion of the individual bilayer leaflets of asymmetric vesicles with Electron Spin Resonance (ESR) spectroscopy. Using small-angle neutron (SANS) and X-ray (SAXS) scattering data, we validate the protocol for construction of asymmetric bilayers for MD simulations described in Chapter 6, and through analysis of MD simulations of the ESR systems, estimate the elastic energy of mixing the two leaflets in the asymmetric bilayers. Our results indicate that when the two leaflets in the membrane are more ordered, the coupling between them is stronger, i.e. they are better able to change each other's properties. This study illustrates the power of combining experimental and computational approaches to uncover some of the core principles behind leaflet-leaflet interaction and the organization of the cellular PM.

7.2 Materials and methods

7.2.1 Materials

All lipids (POPC, POPG, DMPC, DPPC, DEPC, DOPC, SOPC, POPC-d31, POPC-d13, DMPC-d54) were purchased from Avanti Polar Lipids (Alabaster, AL) either as dry powders or dissolved in chloroform (see Fig. E1 for the chemical structures and abbreviations of most lipids; the corresponding information for the deuterated lipid

variants can be found in the SI of Ref. [4]). The dry powders were dissolved in HPLC-grade chloroform (assuming 2 water molecules are bound to each lipid headgroup) to a particular stock concentration, while the concentration of the already dissolved lipids was determined by inorganic phosphate assay [237]. 1-palmitoyl-2-stearoyl-(5-doxyl)-*sn*-glycero-3-phocphocholine (5 Doxyl PC, C5PC) was a gift from Boris Dzikovski and was stored in ethanol. Methyl-β-cyclodextrin (MβCD), sucrose and NaCl were purchased from Fisher Scientific. Ascorbic acid (purity > 99.5%) was purchased from Sigma Aldrich. D_2O was purchased from Cambridge Isotopes (Andover, MA).

7.2.2 Preparation and characterization of symmetric and asymmetric vesicles

Symmetric liposomes were prepared as described in Chapter 5. Briefly, lipids (with or without 0.9 mol% of the spin probe C5PC) were mixed in organic solvent, dried to a film with an Ar or N_2 stream and incubated under high vacuum overnight. Hydration of the dry lipid film was performed at 50°C for 1 h with intermittent vortexing. The sample was frozen (using either a -80°C freezer or liquid N_2) and thawed at 50°C at least 5 times. To make large unilamellar vesicles (LUVs), the resulting multilamellar vesicle (MLV) suspension was extruded with a mini-extruder (Avanti Polar Lipids) by passing it through a 100 nm pore-diameter polycarbonate filter 31 times. If the sample contained high melting lipids like DPPC, the extrusion was performed at 50°C. All LUVs were doped with 5 mol% POPG to prevent the formation of vesicles with more than one bilayer [293].

Asymmetric LUVs (aLUVs) were prepared using the protocol described in Chapter 5 with slight modifications for the ESR samples, namely, the donor-to-acceptor ratio was 4:1 and the MβCD-to-donor ratio was 6:1 (see Table E1). For those samples, after the acceptor LUVs were added to the donor/MβCD solution, the mixture was incubated for 1 h at room temperature with gentle stirring. Following

pelleting of the donor vesicles and concentration of the supernatant in a centrifugal filter device (100K MWCO), the sample was washed three times with 30 mM NaCl. Half of the sample (RT) was incubated at ambient temperature while the other half (HT) was heated to 50°C for 30 min, then slowly cooled down over 3-4 h to ensure equilibration of the spin probe between coexisting phases. The HT sample was used only for the ESR measurements of the DPPC/POPC aLUVs. All other aLUV measurements were performed with the RT samples.

The overall composition of the aLUVs (Table E1) and vesicle size (data not shown) were determined with gas chromatography mass spectrometry (GC-MS) and dynamic light scattering (DLS), respectively, as described in Chapter 5. For the scattering experiments, the degree of asymmetry in the aLUVs was measured with ^{1}H NMR for the sample with POPC-d13 acceptors (see Chapter 5) and assumed to be the same for the samples with POPC-d31 acceptors. For the aLUVs measured with ESR, the degree of DPPC asymmetry in all samples was assumed to be either 100% (for all ESR samples) or 95% as reported in [4] (for the respective MD simulations, see below).

7.2.3 Small-angle scattering data collection

Small-angle neutron (SANS) and X-ray (SAXS) scattering experiments were conducted at Oak Ridge National Laboratory. SANS measurements were performed on the CG-3 BioSANS instrument of the High Flux Isotope Reactor (HFIR) using 6 Å wavelength neutrons (FWHM 15%) and a 14.5 m sample-to-detector distance (SDD) for a total scattering vector of $0.005 < q < 0.06$ Å^{-1} [$q = 4\pi \sin(\theta)/\lambda$, where λ is the neutron wavelength and θ is the scattering angle relative to the incident beam]. LUV samples were loaded into 1 mm path-length quartz banjo cells (Hellma USA, Plainview, NY) and mounted in a temperature-controlled cell holder. The scattered

neutrons were collected with a two-dimensional (1×1 m) ^{3}He position-sensitive detector (ORDELA, Inc., Oak Ridge, TN) with 192×192 pixels. Reduction of the 2D data was performed with the software package Mantid [239] by correcting the data for the background scattering of water, the detector pixel sensitivity, dark current and sample transmission. The one-dimensional scattering intensity $I(q)$ was obtained by radial averaging of the corrected 2D image data.

SAXS experiments were performed on a Rigaku BioSAXS-2000 home source system as described in Chapter 8. For determining phase boundaries, MLV suspensions were prepared at 30 mg/mL and scattering data was collected for 30 min.

7.2.4 Analysis of the structural properties of individual leaflets from joint refinement of SANS and SAXS data

Obtaining information about bilayer structure from small-angle scattering data requires a model of the bilayer organization. The raw data are fit to the model and the structural parameters emerge from the refinement. Consequently, accurate results about bilayer structure rely both on the relevance of the model and the quality of the experimental data. The distinctive scattering patterns of neutrons (which interact with the atomic nucleus and therefore "see" hydrogen and deuterium differently) compared to X-rays (which interact with the atomic electron cloud) allow for generating multiple differently contrasted datasets for a given nominal sample composition, by selectively deuterating parts of the sample and performing both SANS and SAXS measurements on it. Thus, while being unique, each dataset provides complementary information about the inherent structure and spatial organization of the sample, and a robust determination of the bilayer structure when all datasets are analyzed together in a global analysis. For all samples analyzed with scattering techniques, multiple contrast

conditions were generated (see Tables E1-E2) and refined jointly to ensure a robust parameter estimation.

The model used to analyze the data, as well as a software package that implements the fitting routine in Mathematica, were developed and provided by Fred Heberle. A description of a more general version of the model (including lateral heterogeneity and an explicit Gaussian to model the volume distribution of a peripherally bound protein) can be found in Appendix C. Briefly, the asymmetric bilayer is represented by 6 slabs of uniform volume probability projected onto the bilayer normal; the slabs correspond to the headgroup and hydrocarbon regions of the two bilayer leaflets, with separate slabs for their terminal methyl distributions at the center of the bilayer. The compositions of the two leaflets determined by a combination of GC and NMR as described above are provided as fixed input parameters, as are the molecular volumes of individual lipid species obtained from the literature [145, 154]. Using mathematical relationships between the volume, thickness, and average area of the lipids, an analytical expression is obtained in which the remaining unknown (i.e., adjustable) parameters are the areas per lipid and headgroup slab thicknesses of the two leaflets. A particular choice of model parameters corresponds to a bilayer structure expressed in terms of volume probability profiles of each slab which, when scaled by the total neutron or X-ray scattering length of the atoms (as specified by the sample composition) and summed, generates a scattering length density profile for each differently contrasted sample. The 1D Fourier transform of the scattering length density profile is a prediction for the scattering intensity that is compared to the experimental scattering data in reciprocal space. Parameter refinement is performed with a standard chi-square minimization procedure and the Levenberg-Marquardt algorithm for nonlinear least squares optimization.

7.2.5 Determination of the phase boundaries of binary mixtures with SAXS

The phase boundaries of four binary mixtures of DPPC combined with either POPC, DEPC, DOPC or SOPC (see Fig. E1 for lipid name abbreviations) were determined from MLV suspensions using SAXS [263]. For each binary mixture a series of samples at 5 mol% increments of DPPC were prepared in H_2O as described above. The compositional range for the left- (LHS) and right-hand-side (RHS) boundaries was chosen to encompass the range of respective values in published phase diagrams determined with different techniques (Table E3). SAXS data for each sample were collected at 20-22°C and the one-dimensional scattering intensities for all samples in the series were overlaid and compared (Fig. E2). The form factor of an MLV suspension in which the lipids are uniformly mixed within the bilayer (i.e., a single phase) results in a scattering pattern characterized by regularly spaced Bragg peaks whose position in reciprocal space corresponds to the combined thickness of the bilayer and single water layer (i.e., the "lamellar repeat" distance D) through the relationship $D = 2\pi/q$. If two phases with a sufficiently different lamellar repeat distance coexist within the same bilayer, the scattering pattern displays two sets of Bragg reflections (see Fig. E3). Therefore, in favorable cases simple inspection of the 1D scattering patterns can be used to identify the onset of phase separation from the respective binary mixture series around the LHS and RHS boundaries. The resolved phase boundaries are shown in Table E3.

7.2.6 Isolation of ESR signal from the inner and outer leaflets of asymmetric liposomes

To obtain an ESR spectrum for each leaflet in the asymmetric liposomes, two separate samples were prepared for each aLUV composition (Table E1). In the first sample, the spin probe was added only to the acceptor vesicles. Thus, after the

exchange of donor lipid, most of the spin probe was present in the inner leaflet of the aLUVs while a residual amount remained in the aLUV outer leaflet. To isolate the signal from the inner leaflet, 8 μL of the sample (prepared with 5 mg acceptor lipid) were incubated with 2 μL of an ascorbate solution (40 mM ascorbate in 20 mM HEPES and 2.4 mM EDTA at pH 7.3) at ascorbate:lipid ratio of ~ 1:2, for 3 h at 4°C. This resulted in the reduction of the spin probe on the outer leaflet and the suppression of its signal (which was less than half of the total signal intensity, see Fig. 7.2 and E4). The remaining ESR spectrum was thus taken as representative of the inner leaflet of the aLUVs.

In the second sample, the spin probe was added only to the donor vesicles, which resulted in its exchange into the outer leaflet of the aLUVs. When the sample was subjected to the same incubation with ascorbate as described above, the majority of the signal disappeared indicating that the spin probe was confined to the outer leaflet (Fig. E4). Thus, the ESR spectrum of the sample collected immediately after preparation (i.e. without any ascorbate incubation) was taken to be representative of the outer leaflet of the aLUVs.

7.2.7 ESR data collection

ESR experiments were performed at the National Biomedical Research Center for AdvanCed ESR Technology (ACERT) at Cornell University. Data were collected at a microwave frequency of 9.4 GHz on a Bruker ELEXSYS-II E500 CW EPR Spectrometer with 0.8 Gauss modulation. The spectrometer was equipped with a nitrogen gas flow temperature unit from Varian. Each sample was loaded into a small open-ended glass capillary, one end was flame sealed and the capillary was gently centrifuged to move its contents to the bottom. The capillary was then placed into a larger glass capillary and inserted into the instrument. The power was set to 20 dB and

the number of scans was adjusted based on the signal intensity, and typically ranged between 8 and 64. The sweep width was set to 100 G and 1024 points were collected in each scan. The final spectrum was an average over all scans. Measurements were performed either at 19-20°C (for binary mixtures with SOPC and DEPC) or 5°C (for binary mixtures with POPC and DOPC) to ensure the impermeability of ascorbate into the vesicle lumen.

7.2.8 Analysis of ESR data

The raw ESR data was imported into MATLAB with the EasySpin toolbox, and the baseline (defined by the average of the first and last 10 points from the spectrum) was subtracted from all points. In addition, an appropriately scaled spectrum of ascorbate was subtracted from the spectrum of each aLUV inner leaflet (obtained after incubation with ascorbate as described above) to recover the line shape at center field in those samples and facilitate data analysis (Fig. E5).

Model-free order parameters were obtained from hyperfine splittings analysis as described in [330] (see Eq. 14 and Figures 2-4). The hyperfine tensor (A_{xx}, A_{yy}, A_{zz}) was taken as (5.5 G, 5.5 G, 33.3 G) ([331]; Boris Dzikovski, personal communication). The positions of the outer and inner hyperfine extrema were determined with a mathematical routine implemented in Mathematica and kindly provided by Fred Heberle. In the routine, an arbitrary range around each peak was first selected manually. Since the analyzed ESR spectrum of intensity vs. field position is the first derivative of the absorbance spectrum of the sample, multiple Lorentzians were fitted to the absorbance spectrum in the specified field range to generate an analytical function that traces smoothly through the experimental data. The peak position in the first derivative of the absorbance spectrum was then identified from the zeroes in the second derivative of this analytical function. After the identification of

all peaks, the data were exported to Excel and the apparent order parameters were calculated from the corresponding hyperfine splittings distances using Eq. 14 from Ref. [330].

Model-based order parameters and rotational diffusion coefficients were obtained by fitting the ESR spectra to the model of microscopic order with macroscopic disorder (MOMD) using the non-linear least squares algorithm implemented in the NLSL software [332]. During the fitting procedure, some parameters were kept fixed while subsets of the remaining parameters were optimized one by one to avoid overfitting and keep the correlation between simultaneously varied parameters minimal (see Tables E4-E5). The NLSL software allows for modeling the spin probe environment as a uniform mixture or a combination of coexisting phases, each with its own characteristic structure. For all spectra, fitting was initially performed by assuming a single phase and only if the resulting best fit was not satisfactory (i.e., it failed to capture the main features of the spectrum), the data was fit with two phases. The goodness-of-fit was monitored with both a reduced chi square statistic as explained in Ref. [332], and visual inspection to ensure that regardless of the amount of spectral noise, all features of the data were preserved in the fit. The best-fit results are shown in Tables E4-E5 and Fig. E6.

7.2.9 Calculation of spin probe partition coefficients

The compositions of the two coexisting phases in a phase-separated binary mixture at a given temperature are determined by the compositions at the LHS and RHS endpoints of the tieline. Thus, to quantify the preference of the spin probe for the fluid phase in a symmetric bilayer with co-existing fluid (L_α) and gel (L_β) domains, the probe's partition coefficient was estimated as follows. ESR spectra were collected at 19-20°C for symmetric LUVs with the compositions of: (1) the LHS boundary of the

binary mixture, s_{LHS}; (2) the RHS boundary of the binary mixture, s_{RHS}; and (3) the outer leaflet of the corresponding aLUV sample, s_{sym}. These compositions are given in Table E3. The latter was modeled as a linear combination of the LHS and RHS spectra:

$$s_{sym} = f_p^{L\alpha} s_{LHS} + \left(1 - f_p^{L\alpha}\right) s_{RHS}, \tag{7.1}$$

where $f_p^{L\alpha}$ is the effective fraction of the L_α phase in the phase-separated sample, determined from the probe partitioning. The fractions of the two phases ($f^{L\alpha}$ and $f^{L\beta}$) are determined from the mole fractions of the high melting lipid in the sample (χ) and in the LHS ($\chi^{L\alpha}$) and RHS ($\chi^{L\beta}$) boundaries using the Lever Rule, as illustrated in the schematic below:

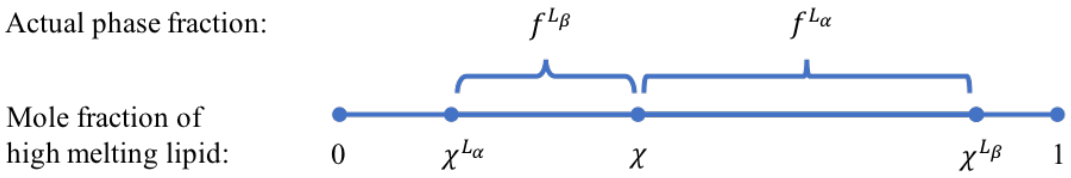

If the probe partitions equally between the gel and fluid phases, then $f_p^{L\alpha} = f^{L\alpha} = \chi^{L\beta} - \chi$. Thus, the probe's partition coefficient K_p is obtained from the formula (Eq. 5 in [83]):

$$K_p = \frac{f_p^{L\alpha}(\chi - \chi^{L\alpha})}{\left(1 - f_p^{L\alpha}\right)(\chi^{L\beta} - \chi)}. \tag{7.2}$$

The results for all 4 binary mixtures are listed in Table E3.

7.2.10 MD simulations

All-atom MD simulations were performed on the symmetric and asymmetric bilayers studied experimentally (Table E6). The bilayers were built with CHARMM-

GUI [141-144] by specifying the number of lipids in each leaflet and the level of hydration of the system (45 waters per lipid). The number of lipids that ensure a minimal leaflet tension in the asymmetric bilayers was identified with the protocol from Chapter 6.

The systems were simulated with the NAMD software [155] using the CHARMM36 force field for lipids [156, 195]. Initial equilibration was carried out following CHARMM-GUI's protocols. The parameters for the subsequent production run were the same as the ones described in Chapter 3.2. The fixed temperature for the simulations, as well as the total simulation time and the simulation time used for analysis, are listed in Table E6.

The fraction overlap of the two leaflets mass density distributions was calculated with the MEMBPLUGIN tool [197] implemented in the Visual Molecular Dynamics (VMD) software [333]. The fraction overlap is a correlation-based measure defined as:

$$I_p^2 = 4 \int \frac{\rho_a(z)\rho_b(z)}{(\rho_a(z) + \rho_b(z))^2} \mathrm{d}z, \tag{7.3}$$

where ρ_a and ρ_b are the mass density profiles of the two leaflets.

7.2.11 Analysis of the properties of coexisting phases in the simulated bilayers

Phase separation was present in some of the binary mixtures of DPPC/POPC and DPPC/DEPC and was detected with both visual inspection and analysis of the distribution of leaflet thicknesses (see Fig. E7). The following steps were performed to dynamically identify the lipids in each phase:

(1) Voronoi analysis was performed in every trajectory frame. Namely, the 2D coordinates of the lipid centers-of-mass were used to partition the

membrane plane into *Voronoi cells* in which the region of each cell corresponds to all points in space that are closest to the center of this cell than to the centers of any other cell. In the partitioning algorithm, the periodic images of the simulation box were explicitly taken into account to avoid edge effects. Thus, each Voronoi cell corresponded to a single lipid and its area was used as an estimate of the instantaneous lipid area. The immediate neighbors of a lipid were defined as the lipids whose Voronoi cells shared an edge with the Voronoi cell of the lipid. This definition was used to estimate the local concentration of DPPC around each lipid.

(2) A concentration cutoff was identified such that all lipids with local concentration above the cutoff were assigned to the gel (L_β) phase, and the remaining lipids were assigned to the fluid (L_α) phase. To find this cutoff, a range of sample cutoff values between 0.1 and 1 in increments of 0.1 were tested. For each sample cutoff the lipids were first assigned to L_α or L_β based on the cutoff. Then the membrane plane was divided into grid points spaced 8×8 Å apart (the spacing used for analysis of the area compressibility modulus as described in Chapter 3.2). Each grid point was assigned to L_β if there was at least one L_β lipid within 8 Å of the grid point (as determined by the lipid's 2D center of mass), or to L_α otherwise. In addition, the interpolated z-position of the leaflet's phosphorous atoms at the grid point was calculated as described in Chapter 3.2. After performing the analysis on all grid points and all frames of the trajectory, the correlation between phase assignment and phosphorous z-position was calculated. A high correlation indicated a good separation of the lipids based on differences in the local leaflet thickness. The sample cutoff that

produced the maximum correlation was thus chosen as the concentration cutoff based on which lipids were formally assigned to L_α or L_β.

Once the lipids in each phase were identified, average lipid properties in the L_α and L_β phases were calculated from the properties of all lipids in the respective phases. In particular, areas per lipid were obtained from the areas of the lipids' Voronoi cells, and the lipids' acyl chain order parameters were calculated with the MEMBPLUGIN tool.

To get the area compressibility of each phase, $K_A^{L\alpha}$ and $K_A^{L\beta}$, the membrane plane was again divided into grid points spaced 8×8 Å apart. As described above, each grid point was assigned to L_β if there was at least one L_β lipid within 8 Å of the grid point, or to L_α otherwise. The computational framework for calculating K_A from Chapter 3.2 was then applied separately to the two sets of grid points assigned to L_α and L_β. The area fraction of each phase was estimated from the time-averaged fraction of lipids in each phase and their respective areas per lipid. The leaflet compressibility was then calculated as the weighted average of $K_A^{L\alpha}$ and $K_A^{L\beta}$ with the weights being the phase area fractions.

7.2.12 Constrained MD simulations of symmetric bilayers

Constrained MD simulations were performed on two symmetric bilayers, POPC and POPE/POPS 0.7/0.3 from Chapter 3, Table 3.1.1. Starting from the last frame of the equilibrated trajectory, a new simulation was performed for each bilayer in which forces were applied to the carbon 14 atoms and their two associated hydrogen atoms on the palmitoyl chains of all lipids only in the top bilayer leaflet. The forces restrained the average order parameter at these carbon atoms to a specific value (0.1772 for POPC and 0.1177 for POPE/POPS) and were applied by implementing a

custom function in NAMD's module for collective variables [334]. The new collective variable applied the specific forces (see Appendix E for a description of how they were calculated) with a force constant of 1.5 and a *width* parameter of 0.01. The constrained simulations were run for 150 ns each by outputting the atomic coordinates every 20 ps. The last 50 ns (for POPC) and 25 ns (for POPE/POPS) where the bilayer area fluctuations had converged were used for analysis. The order parameter (S_{CD}) profiles of the lipids in each leaflet were calculated in VMD with an in-house Tcl script:

$$S_{\mathrm{CD}} = \langle \frac{3\cos^2\alpha - 1}{2} \rangle \tag{7.4}$$

where α is the angle between the CH bond and the bilayer normal (taken to be the z dimension of the simulation box) and $\langle \cdot \rangle$ denotes an ensemble average. The bending rigidity of each leaflet was obtained from analysis of lipid splay fluctuations using the methodology from Chapter 3.1.

7.3 Results

7.3.1 Symmetric bilayers provide insight into the mechanisms of interleaflet communication

The concept of interleaflet communication has been discussed mostly in the context of asymmetric membranes. However, the ability of the two bilayer leaflets to interact with one another is universal across lipid bilayers and does not depend on the leaflets lipid compositions. Indeed, common construction principles such as the hydrophobic effect, dictate that the hydrocarbon chains of the two leaflets face each other and interact at the bilayer midplane. Since the midplane is the only point of physical contact between them, its properties can be used to inform on the

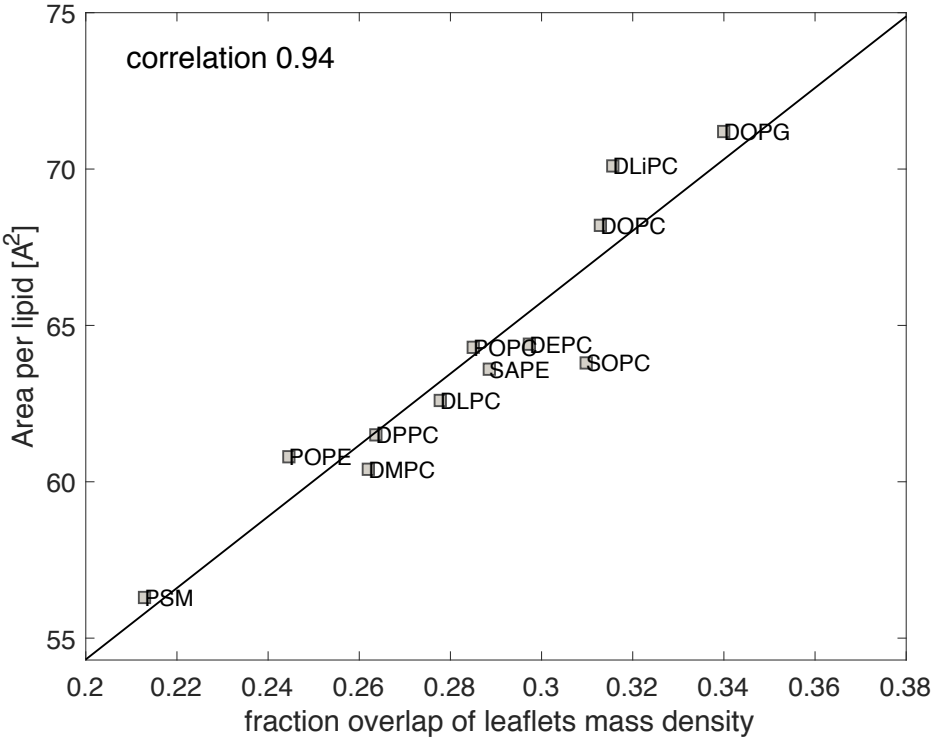

Figure 7.1. The amount of overlap of the two leaflets' mass density profiles correlates with lipid packing in symmetric bilayers. Shown is the average area per lipid as a function of the fraction overlap of the two leaflets' mass density distributions in all single component bilayers from Table 3.2.1 in Chapter 3, except for cardiolipin which has 4 acyl chains. The fraction overlap is a correlation-based measure as defined in Section 7.2.10 and represents the relative size of the interaction region between the leaflets. The Pearson correlation between area per lipid and fraction overlap is denoted on the plot.

mechanisms of interleaflet communication (or coupling). Thus, we examined the size of the interaction region between the leaflets by analyzing the fraction overlap of the leaflets' mass density distributions (see Section 7.2.10). A comparison among different single component bilayers revealed that the mass density overlap was strongly correlated (with a Pearson correlation coefficient of 0.94) with lipid packing (Fig. 7.1), suggesting that when the two leaflets are more tightly packed, the interaction region between them is narrower. This result is supported by the increase in pressure at the midplane accompanying a decrease in the number of double bonds in the lipids' acyl chains (see Fig. B5), and the observed increase in terminal methyl

groups exploring the hydrocarbon/water interface when the acyl chain order of the lipids decreases [335]. Since a narrower interaction region implies more concentrated interleaflet atomic contacts, we hypothesized that the more ordered the two leaflets are, the more capable they are to influence each other's properties.

Table 7.1. Effect of structural perturbation to one leaflet on the properties of the two bilayer leaflets in a fluid POPC bilayer and a more tightly packed POPE/POPS bilayer. Shown is the bending rigidity (κ_C) for each leaflet in the original unperturbed bilayer, and in the perturbed bilayer (pert.) in which the average order parameter of carbon 14 on the palmitoyl chains in the lipids in the top leaflet was constrained to a different value (higher in POPC, and lower in POPE/POPS as explained in the text). The difference between the leaflets' bending rigidities is listed as $\Delta\kappa_C$. κ_C was calculated as in Chapter 3.1 and is given in units of k_BT. The corresponding errors are shown in parenthesis. Also shown is the difference between the average order parameter of the plateau region of the S_{CD} profiles from Fig. E8 (i.e. carbons 4 through 10) in the perturbed and original bilayers (ΔS_{CD}) for both the oleoyl (ole) and palmitoyl (pal) lipid chains.

leaflet	POPC bilayer				POPE/POPS bilayer			
	pert.	original	$\Delta\kappa_C$	ΔS_{CD}	pert.	original	$\Delta\kappa_C$	ΔS_{CD}
top	13.5 (0.6)	12.4 (0.5)	1.1	0.006 ole 0.005 pal	14.2 (0.2)	20.3 (0.3)	-6.1	-0.005 ole -0.010 pal
bottom	12.7 (0.5)	12.0 (0.5)	0.7	0.001 ole 0.002 pal	15.5 (0.3)	19.8 (0.4)	-4.3	-0.007 ole -0.009 pal

To test this hypothesis, we first performed a computational experiment in which we examined the effect of a small structural perturbation to one leaflet in two symmetric membranes, POPC and POPE/POPS. The bilayers had different lipid packing densities (average areas per lipid of 64.4 Å^2 and 55.6 Å^2, respectively) and acyl chain order parameters (Fig. E8). We picked one carbon atom on the palmitoyl chain of the lipids, carbon 14, which was close to the interaction region, yet not completely at the end of the chains. Its order parameter in the POPC and POPE lipids in the two bilayers was 0.1177 and 0.1772, respectively. Starting from the end of the equilibrated trajectories, we continued the simulation runs by gently restricting the

average order parameter of carbon 14 in the palmitoyl chains of the lipids in the top leaflet of the POPC bilayer to 0.1772 and in the top leaflet of the POPE/POPS bilayer to 0.1177 (see Section 7.2.12). Thus, the perturbation aimed to increase the order of carbon 14 in the POPC top leaflet to that of POPE, and to decrease it in the POPE/POPS top leaflet to that of POPC. This perturbation produced only minor overall changes in the POPC bilayer. In contrast, both leaflets of the POPE/POPS membrane were more dramatically affected as evidenced by the changes in their order parameters and bending rigidity moduli (Table 7.1 and Fig. E8). The effect of this structural perturbation confirmed our hypothesis that in the more ordered, tightly packed bilayer the leaflets are more strongly coupled (i.e. can communicate more effectively) and influence each other's properties to a larger extent than in a less tightly packed bilayer.

7.3.2 A new experimental strategy enables the examination of individual leaflet properties with ESR

To enable the in vitro exploration of the mechanistic hypothesis from the previous section, we pursued the application of Electron Spin Resonance (ESR) spectroscopy to measure the structural properties of the bilayer leaflets. In an ESR experiment, a paramagnetic probe added to a sample absorbs energy when the sample is placed in a magnetic field at a specified frequency, thus producing a distinct spectral profile that contains information about probe motions. In the case of a lipid bilayer, the probe is often a lipid with a nitroxide radical attached to one of the chains' carbons that informs on the motional freedom of that carbon.

We used the spin probe C5PC, which structurally resembles a DPPC lipid (with two saturated 16-carbon chains) but has a nitroxide label attached to the 5th carbon on the *sn*-2 chain (see Fig. E1). A small amount of C5PC (0.5-0.9 mol%) in a liposome,

while assumed to have minimal perturbing effects on its surrounding lipid environment, serves as an indirect reporter on the order parameter of the upper part of the hydrocarbon region of the host lipid. In particular, analysis of the ESR spectra can reveal both the orienting potential (and order parameter) of the probe and by extension, the host lipid, and the rate of its rotational diffusion.

In a conventional liposome preparation the spin probe gets distributed equally between the two bilayer leaflets. While this does not present problems for symmetric bilayers whose two leaflets are generally assumed to have the same properties, in an asymmetric bilayer (or a symmetric membrane in which one leaflet has been somehow perturbed) it becomes essential to isolate the ESR signals of the individual leaflets to separately quantify their properties. To achieve this, we used the protocol from Chapter 5 to prepare two types of liposomes. In one of them, the spin probe was added only to the donor vesicles, which, following the exchange of lipids between the donor and acceptor pools, resulted in its confinement to the outer leaflet of the final liposomes (see Section 7.2.6). Thus, the resulting spectral profile corresponded to the motion of the lipids in the liposomes' outer leaflet.

In the second preparation, the spin probe was added only to the acceptor vesicles. After lipid exchange, most of the probe on the outer leaflet was replaced with donor lipid, although some of it remained. To isolate the signal from the inner leaflet, we added externally a chemical reagent that 'silenced' the remaining probe contained in the outer leaflet. In particular, we used ascorbate to reduce the nitroxide label and thus suppress its signal. During a 3 h incubation with the sample at 5°C, ascorbate reduced the C5PC on the outer leaflet without permeating through the bilayer (Fig. 7.2). Note that after 3 h the intensity of a symmetric bilayer with the probe equally distributed between the two leaflets was reduced in half. Consequently, the resulting spectral

profile obtained 3 h post ascorbate addition was used to infer the structural parameters of the lipids in the inner leaflet of the liposome.

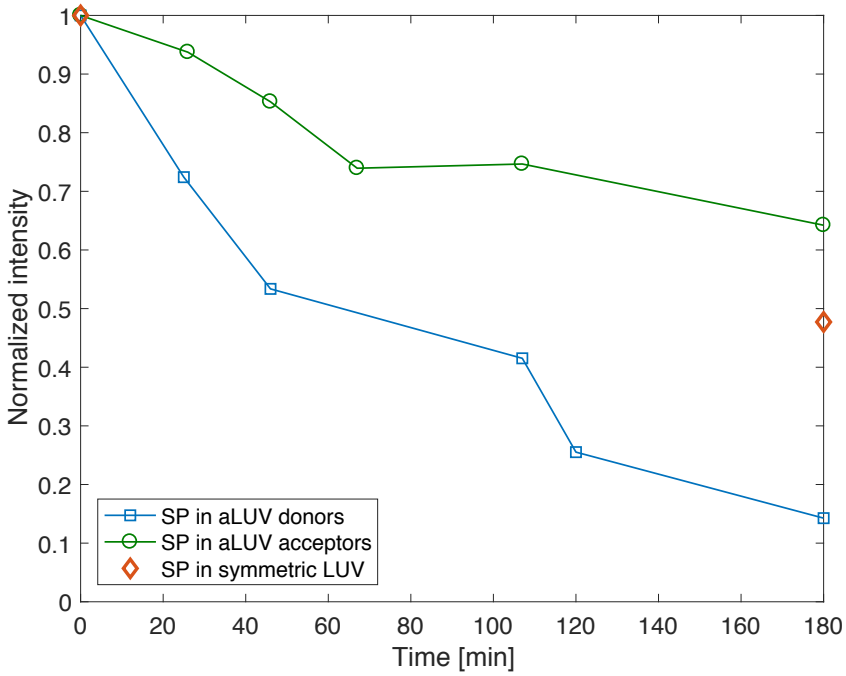

Figure 7.2. Successful silencing of C5PC on the outer leaflet of extruded vesicles. Shown are data for the DPPC/POPC aLUVs with spin probe (SP) in the donors (blue) and acceptors (green). Also shown are results for a symmetric LUV with the same overall composition as the DPPC/DEPC aLUVs (Table E1). The normalized intensity, relative to time 0, was calculated from the first spectral peak (see Fig. E4) after fitting each spectrum to a smoothing spline function in MATLAB with a smoothing parameter of 0.6.

7.3.3 Analysis of the spectral profiles of asymmetric bilayers reveals the presence of interleaflet coupling

To test whether higher order in the two bilayer leaflets leads to more effective interleaflet communication (stronger interleaflet coupling) in asymmetric bilayers, we examined the structural changes in a series of asymmetric liposomes with increasing packing density of their inner leaflets. To this end, we exchanged DPPC (with melting

temperature, Tm, of 42°C) into extruded liposomes made of DOPC (Tm -17°C), POPC (Tm -2°C), SOPC (Tm 6°C) or DEPC (Tm 12°C), as described in Section 7.2.2 (see Fig. E1 for lipid structures). Using the approach outlined in the previous section, we isolated the signals from the outer and inner leaflets of the aLUVs and compared them to the corresponding symmetric bilayers (Fig. 7.3 and E9). To quantify the changes in the spectral profiles, we first performed a model-free analysis of the probe's order parameter by measuring certain peak distances in the spectra and relating them to the hyperfine splitting distances of C5PC (see Section 7.2.8). The order parameters (listed on the respective plots) revealed larger changes as a result of asymmetry in the DEPC bilayer compared to the POPC bilayer, consistent with our mechanistic hypothesis. However, in the DOPC and SOPC liposomes (Fig. E9) the probe motion seemed to remain unchanged, producing almost identical spectral profiles.

Since the outer leaflets of the aLUVs (as well as both leaflets of the corresponding symmetric vesicles) had a higher mole fraction of DPPC, they were likely phase separated into two types of domains, which for convenience we will refer to as gel (L_β) and fluid (L_α) even though their properties in the asymmetric membranes may be different from the canonical properties associated with gel and fluid phases in symmetric membranes [4]. Because of its different properties, each phase should have a characteristic spectral profile, and if the probe partitions equally between the two phases, the ESR spectrum of the sample should be a linear combination of the spectra of the phases weighted by their respective area fractions. However, if the probe has a strong preference for one phase, the ESR spectrum of the sample would report mostly on the properties of that phase. To estimate the partition coefficient (K_p) of C5PC between the two co-existing environments, we first used small-angle X-ray scattering (SAXS) to identify the boundaries of the binary mixtures for which there are disparate

results in the literature (Table E3). We then measured the ESR spectra of the two boundaries and of a symmetric phase separated liposome of that binary composition, and applied the Lever Rule as described in Section 7.2.9. The analysis revealed a very strong preference of the spin probe for the fluid phase in the DPPC/SOPC and DPPC/DOPC mixtures (K_p of 4 and 5.6, respectively), which could help explain the seemingly identical spectral profiles in Fig. E9. In contrast, the partition coefficient of C5PC in DPPC/POPC indicated only a two-fold preference for the fluid phase ($K_p = 2.4$), while in DPPC/DEPC the probe partitioned equally between the phases ($K_p = 1$, Table E3).

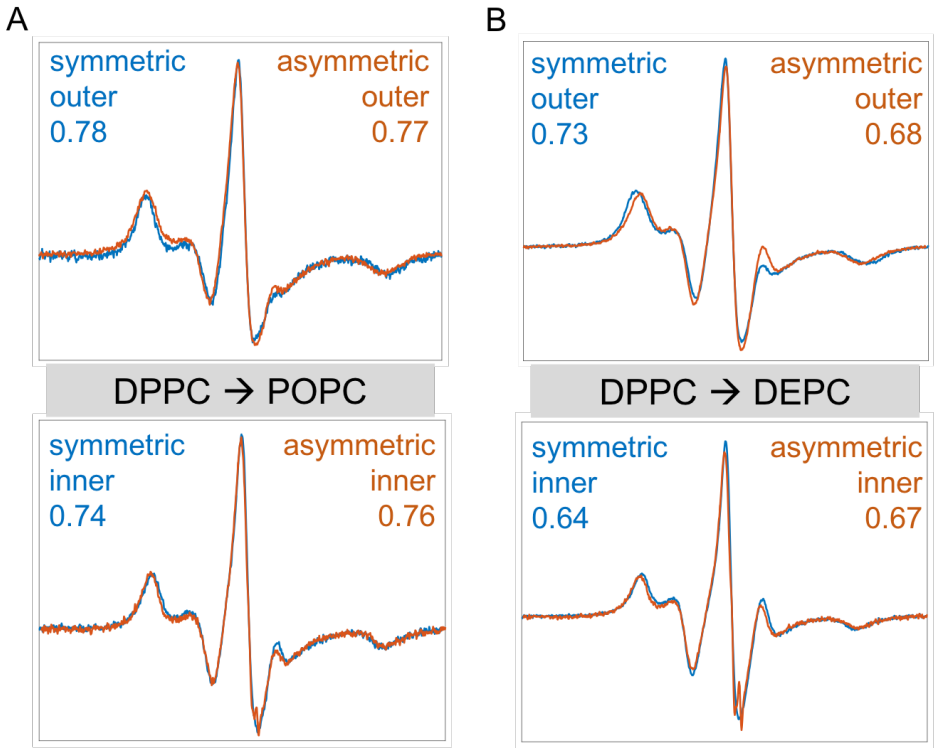

Figure 7.3. Model-free analysis of the ESR spectra for the DPPC/POPC (A) and DPPC/DEPC (B) bilayers. Shown are the spectra of the outer (top plot) or inner (bottom plot) leaflets of the aLUVs (in red) and the spectra of their corresponding symmetric bilayers (in blue). Results for the probe's order parameter obtained from model-free analysis based on hyperfine splittings distances as explained in the text, are listed for each spectrum on each plot.

Table 7.2. Structural parameters obtained from ESR by fitting the raw data to the MOMD model as explained in the text. Shown are the order parameter and rotational diffusion rate of the spin probe, C5PC, in each leaflet of the aLUVs (asym) made of DPPC/POPC and DPPC/DEPC, and their corresponding symmetric counterparts (sym). "POPC in" (DEPC in) and "POPC out" (DEPC out) refer to the compositions of the inner and outer leaflets of the aLUVs, respectively, assuming 100% asymmetry (Table E1). In the samples with co-existing phases the properties of each phase are listed separately, together with the recovered apparent (app) phase fractions obtained from the best fits. Also shown for the symmetric samples is the actual (act) phase fraction calculated from the apparent one by multiplying it by the C5PC's partition coefficient from Table E3. All spectra, except for "POPC in", were collected at 19-20°C.

leaflet	**phase**	**Order parameter**		**Rot. Diffus. [s^{-1}]**		**Phase fraction**	
		sym	asym	sym	asym	Symmetric app / act*	Asym. app
POPC in (5°C)	-	0.50	0.51	7.37	7.31	-	-
POPC out	L_β	0.72	0.62	7.59	7.63	15.80 / 37.92	31.80
	L_α	0.48	0.43	7.68	7.76	84.20 / 62.08	68.20
DEPC in	-	0.51	0.53	7.71	7.65	-	-
DEPC out	L_β	0.56	0.54	7.35	7.57	57.60 / 57.60	56.40
	L_α	0.41	0.43	7.81	7.78	42.40 / 42.40	43.60

To examine in more detail the effect of asymmetry on the properties of the heterogeneous bilayer leaflets, we modeled the ESR spectra using a well-established model of microscopic order with macroscopic disorder (MOMD) that allows for multiple co-existing phases, as described in Section 7.2.8. We focused exclusively on the DPPC/POPC and DPPC/DEPC mixtures because of their lower K_p values. Non-linear least squares analysis with the MOMD model revealed the co-existence of two different probe environments in the outer leaflet of the aLUVs and in their corresponding symmetric liposomes, and a single homogenous phase in the inner leaflet of the aLUVs and in their symmetric counterparts. Table 7.2 shows the order

parameter and rotational diffusion rate of C5PC in each leaflet and phase, as well as the recovered phase fractions obtained from the best fits.

In agreement with our mechanistic hypothesis, compared to the more densely packed DEPC lipids, the acyl chain order of the POPC lipids was less affected by the presence of DPPC on the outer leaflet. At the same time, the DPPC-rich gel phase on the outer leaflet became more fluid (less ordered and with faster rotational diffusion) in both asymmetric bilayers. Interestingly, in the POPC system this lead to an apparent increase in the fraction of the ordered phase. An intriguing possibility is that this increase could be due to a change in the partition coefficient of the spin probe: while in the symmetric bilayer C5PC has a stronger preference for the fluid L_α phase which results in a seemingly smaller fraction of L_β obtained by modeling the ESR data, in the asymmetric bilayer this preference disappears and the apparent fraction of L_β almost doubles (Table 7.2). The fluidization of the gel phase is consistent with a decrease in lipid packing of the DPPC-rich phase on the outer leaflet of the aLUVs observed with SANS [4]. For comparison, the apparent fraction of the gel phase in the DEPC bilayers remained the same after the exchange of DPPC, in agreement with the probe's partition coefficient of unity. However, the properties of the phase changed more dramatically as evidenced by the relative larger increase in the probe's rotational diffusion and the modest increase in its order parameter (see Section 7.4 for further discussion). These results clearly demonstrate the presence of interleaflet-coupling-induced changes in the leaflet properties in both bilayers, and suggest larger deviations from the symmetric systems when both leaflets are more tightly packed.

7.3.4 Small-angle scattering data validates MD simulations of asymmetric bilayers

Table 7.3. Comparison of the structural parameters of an asymmetric DMPC/POPC bilayer obtained from SANS/SAXS experiments and MD simulations. Shown are results for the inner (Asym inner) and outer (Asym outer) leaflets of the asymmetric bilayer, and symmetric bilayers made of these compositions (Sym inner and Sym outer, see Table E1 and Table E6). The structural parameters shown for each system are: total lipid volume (V_L); headgroup volume (V_{HL}); area per lipid (A_L); total leaflet thickness (D_B); leaflet hydrocarbon thickness (D_C); and headgroup thickness (D_H). Results from the experimental data were obtained by a joint refinement of multiple SANS and SAXS datasets (Table E2), as explained in the text. Results from the simulations were calculated from the time-averaged number density profiles of the systems following [149, 336]. Both the experiments and simulations were performed at 25°C. Note that structural parameters for "Sym inner" liposomes (DMPC/POPC 0.1/0.9) were not measured experimentally, however they are expected to be similar to the structural parameters of pure POPC bilayers which can be found in [145].

Parameter	Experiment			Simulation			
	Asym inner	Asym outer	Sym outer	Asym inner	Asym outer	Sym inner	Sym outer
V_L[a] [Å^3]	1235.3	1130	1130	1222.7	1110.5	1217.6	1114.7
V_{HL}[a] [Å^3]	331	331	331	306.4	309.6	306.7	309.1
A_L [Å^2]	63.9[b]	61.3[c]	62.0[c]	63.8	61.3	63.8	61.4
D_B [Å]	19.3	18.4	18.2	19.1	18.1	19.1	18.2
D_C [Å]	14.2	13.0	12.9	14.3	13.0	14.3	13.1
D_H [Å]	5.2[c]	8.5[d]	10.0[d]	-	-	-	-

[a] Hard constraint from experiment; [b] Hard constraint from simulation; [c] Free parameter; [d] Soft constraint (with a quadratic penalty)

While the ESR results provide evidence for the existence of interleaflet coupling, the experimental data informs on the properties of the lipid bilayers only indirectly, through the motion of the spin probe. A more direct analysis on the behavior of the individual lipids requires the application of a different technique such as Molecular Dynamics (MD) simulations. In Chapter 6 we discussed some of the challenges in studying asymmetric bilayers in silico and presented a novel approach for their construction that enables the analysis of interleaflet coupling by ensuring a robust comparison with symmetric model membranes. To experimentally validate the new protocol, we used small-angle scattering techniques (SANS and SAXS) to obtain information about the structural properties of individual bilayer leaflets in the absence

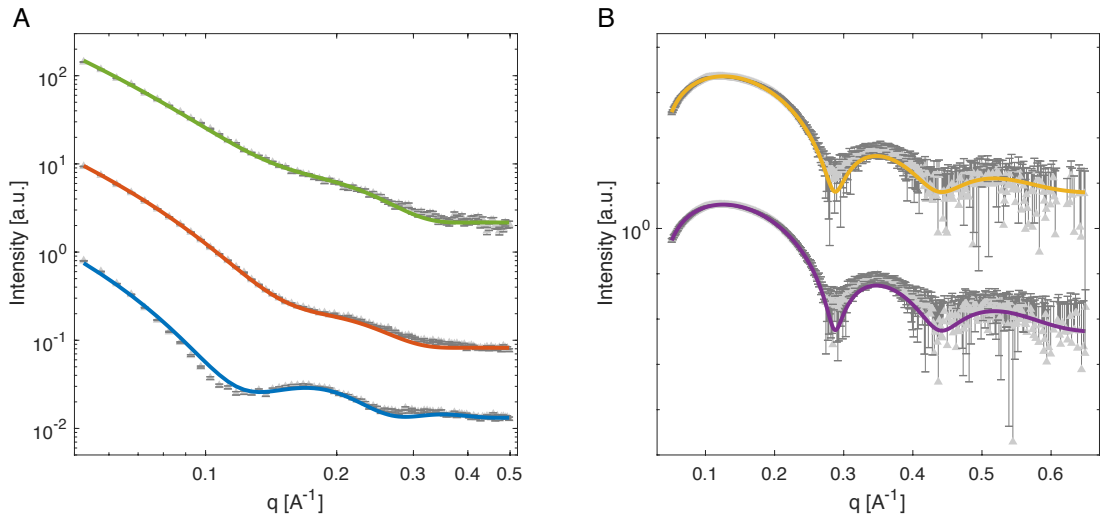

Figure 7.4. Best fits of small-angle scattering data for DMPC/POPC aLUVs. Shown is the raw data (in grey) and the corresponding fits (in color) for the SANS (A) and SAXS (B) datasets analyzed jointly to recover the structural parameters of the two bilayer leaflets. See text for details and Tables E1-E2 for the sample compositions.

of probe molecules, and to compare them to the simulation results. Used together, SANS and SAXS inform on the structure of freely-floating, probe-free liposomes by exploiting the different scattering signatures of atoms upon interaction with neutrons and X-rays. We thus examined aLUVs with an outer leaflet of DMPC/POPC 0.75/0.25 and an inner leaflet of DMPC/POPC 0.90/0.10 (see Tables E1-E2 and Sections 7.2.3-7.2.4). Joint analysis of the scattering data revealed unique structural properties of the two bilayer leaflets, which were virtually the same as the properties of the respective symmetric bilayers, implying weak interleaflet coupling (see Table 7.3 and Fig. 7.4). Importantly, as seen from the results listed in Table 7.3, the recovered structural parameters from the aLUVs are in an excellent agreement with those obtained from an MD simulation of the same asymmetric bilayer constructed with the protocol from Chapter 6. The agreement between simulation and experiment is also evident for the corresponding symmetric bilayers. Thus, the experimental data validated the new in

silico approach and allowed us to apply the computational methodology to further probe the ESR systems.

7.3.5 In silico exploration of interleaflet coupling reveals the elastic energy of mixing the two leaflets in asymmetric membranes

Having validated the simulation protocol for asymmetric membranes, we constructed and simulated bilayer patches of the DPPC/POPC and DPPC/DEPC aLUVs studied with ESR (Table E6). Consistent with the results from the NLSL analysis from Section 7.3.3, the simulations revealed co-existence of two different lipid environments (for convenience, we will refer to them as phases) in the outer leaflets of the asymmetric membranes and in both leaflets of their symmetric counterparts (Table 7.4). Using Voronoi analysis, we identified the lipids in each phase (Section 7.2.11), which allowed us to examine the phase properties. Table 7.4 shows the average area per lipid, average order parameter at the fifth carbon on both chains (the carbon at which the spin probe is attached in C5PC), and the respective phase fractions recovered from the analysis. Similar to the results from the ESR data, the simulations revealed that the DEPC-rich leaflet undergoes bigger changes compared to POPC, as a result of coupling to a DPPC-containing leaflet. This can be seen both from the relative changes in the leaflets' areas per lipid and order parameters. Larger deviations from the symmetric systems were also observed in the top phase-separated leaflet of the asymmetric bilayers: the order parameter of the L_β phase decreased from 0.39 to 0.37 in the POPC system, and from 0.42 to 0.35 in the DEPC system while the corresponding areas per lipid increased accordingly. As in the ESR systems (Table 7.2), the phase fraction of the DPPC-rich phase in the DPPC/POPC bilayer did not change dramatically, reaffirming the hypothesized effect of the asymmetry-induced differential partitioning of the spin probe in the latter. At

the same time, the increase of the L_β fraction in the simulated DPPC/DEPC bilayer was consistent with the corresponding asymmetry-induced changes in the phase packing and order parameter of the lipids (see Section 7.4).

Table 7.4. Structural parameters of asymmetric DPPC/POPC and DPPC/DEPC bilayers and their symmetric counterparts obtained from MD simulations. "POPC in" (DEPC in) and "POPC out" (DEPC out) refer to the compositions of the inner and outer leaflets of the asymmetric bilayers as listed in Table E6. Shown are individual leaflet properties: average area per lipid; order parameter at carbon 5 averaged over the two hydrogens and all lipid chains; and phase fractions calculated as the fraction of total lipids in the leaflet found in either phase, L_β and L_α. See text for more details. The properties of the symmetric bilayers are averaged over their two leaflets. All simulations were performed at 20°C.

leaflet	**phase**	**Area per lipid [Å²]**		**Order parameter**		**Phase fraction**	
		sym	asym	sym	asym	sym	asym
POPC in (20°C)	-	63.5	63.0	0.21	0.21	-	-
POPC out	L_β	48.7	49.8	0.39	0.37	0.26	0.21
	L_α	58.4	59.7	0.28	0.23	0.74	0.79
DEPC in	-	64.3	62.4	0.21	0.23	-	-
DEPC out	L_β	47.2	49.0	0.42	0.35	0.29	0.50
	L_α	56.9	55.9	0.29	0.25	0.71	0.50

The agreement with the experimental data allowed us to use the simulation trajectories to further examine the elastic energy of mixing two leaflets with different composition and properties – a quantity currently inaccessible to experimental techniques. Applying the new computational framework for area compressibility from Chapter 3.2, we calculated the K_A of each leaflet in the asymmetric bilayers (Table 7.5). If a leaflet was phase separated, its K_A was obtained from the weighted average

of the compressibility moduli of the two phases as described in Section 7.2.11. Knowing the equilibrium leaflet properties in the asymmetric and corresponding symmetric bilayers, the excess elastic energy of mixing the leaflets, E_{mix}, in the asymmetric bilayer can be estimated from:

$$E_{mix} = E_{mix}^{\mathrm{TOP}} + E_{mix}^{\mathrm{BOT}} \tag{7.5}$$

where:

$$\begin{aligned} E_{mix}^{\mathrm{TOP}} &\propto K_{A,asym}^{\mathrm{TOP}} - K_{A,sym}^{\mathrm{TOP}} \\ E_{mix}^{\mathrm{BOT}} &\propto K_{A,asym}^{\mathrm{BOT}} - K_{A,sym}^{\mathrm{BOT}} \end{aligned} \tag{7.6}$$

are the elastic energies of coupling each leaflet with a different opposing leaflet.

Table 7.5. Elastic energy of mixing the two leaflets in asymmetric bilayers. Shown are results from MD simulations of five asymmetric bilayers: DPPC/POPC and DPPC/DEPC from Section 7.3.5, DMPC/POPC from Section 7.3.4 and the tension-free DOPC/SOPC and DPPC+Chol/SOPC systems from Chapter 6. Listed for each bilayer are the area compressibility moduli of the top ($K_{A,asym}^{\mathrm{TOP}}$) and bottom ($K_{A,asym}^{\mathrm{BOT}}$) leaflets, as well as the average leaflet moduli of their symmetric counterparts ($K_{A,sym}^{\mathrm{TOP}}$ and $K_{A,sym}^{\mathrm{BOT}}$). K_A values are given in mN/m and their errors (where available) are shown in parenthesis. The elastic energy of coupling each leaflet with the opposing leaflet (E_{mix}^{TOP} and E_{mix}^{BOT}) and the elastic energy of mixing the two leaflets (E_{mix}) are defined in Eqs. 7.5-7.6 in Section 7.3.5.

bilayer	$K_{A,sym}^{\mathrm{TOP}}$	$K_{A,asym}^{\mathrm{TOP}}$	E_{mix}^{TOP}	$K_{A,sym}^{\mathrm{BOT}}$	$K_{A,asym}^{\mathrm{BOT}}$	E_{mix}^{BOT}	E_{mix}
DPPC/POPC	1325	418	< 0	226	225 (32)	~0	< 0
DPPC/DEPC	655	480	< 0	205 (16)	184 (18)	~0	< 0
DMPC/POPC	262 (24)	286 (32)	~0	210 (22)	230 (26)	~0	~0
DOPC/SOPC	256 (17)	260 (32)	~0	245 (21)	236 (32)	~0	~0
DPPC+Chol/ SOPC	3126 (281)	3360 (338)	~0	245 (21)	414 (66)	> 0	> 0

Comparison of E_{mix} of the DPPC/POPC, DPPC/DEPC and DMPC/POPC asymmetric bilayers shows that the elastic energy of mixing the two leaflets is significantly different from 0 only if one leaflet contains a more ordered phase (Table 7.5). In that case coupling the non-uniform leaflet to the more fluid leaflet results in a

lower K_A and more favorable mixing energy while the elastic properties of the uniform leaflet remain mostly unchanged. Similarly, in the DMPC/POPC bilayer in which both leaflets are uniformly mixed, E_{mix}~0. The same result holds for asymmetric bilayers with single component leaflets in the fluid state (Table 7.5). Interestingly, when one leaflet is very tightly packed and contains cholesterol and the other leaflet is more fluid, E_{mix} of the Chol leaflet is insignificant while the elastic energy of the fluid leaflet is less favorable making the mixing energy of the two leaflets greater than 0. These results provide new insights into the construction principles of asymmetric membranes in vivo and in vitro, as discussed in Section 7.4.

7.4 Discussion

Understanding the principles governing the communication between the two leaflets and their ability to affect each other is important for predicting the properties of the two leaflets in a heterogenous environment like the PM, and the role of the membrane in the transmission of signals between the extracellular and intracellular spaces. It is likely that there exist multiple mechanisms that facilitate interleaflet coupling, such as redistribution of cholesterol and interdigitation of lipids with long acyl chains [327, 328]. There are also different phenotypes that can be examined to determine the effect of interleaflet coupling, e.g. phase separation, curvature and lipid diffusion [295, 324, 337]. Here we focused on one particular mechanism of coupling, namely the relative packing (order) of the two leaflets that mediates the communication between the leaflets through the properties of the interaction region between them. The phenotypes that we monitored were the structural properties of the leaflets, including acyl chain order and lipid packing. Our results are consistent with the hypothesis that the more ordered the two leaflets are, the more likely they are to affect each other and thus adopt structural properties that deviate to a larger extent

from those of the corresponding symmetric systems. These findings imply that only the properties of certain types of asymmetric bilayers (those that have two less tightly packed leaflets) can be predicted reasonably well from the known properties of symmetric bilayers. They also reaffirm the potential of the PM to dynamically regulate interleaflet coupling by altering the local lipid composition. One intriguing possibility for instance, is that tension-mediated cholesterol redistribution between the leaflets could be used as a dynamic switch for tuning the strength of interleaflet coupling by mediating the packing and order of the two leaflets. How such mechanism relates to other means of leaflet-leaflet communication like acyl chain interdigitation remains to be explored.

The ability to isolate the ESR signals from the two leaflets in LUVs opens up new directions for exploration. Successful reduction of a spin probe attached to a two-acyl-chain lipid on the outer leaflet of liposomes with ascorbate has so far been achieved mostly with sonicated vesicles containing headgroup-labeled spin probes [338]. However, the high curvature of the vesicles and the location of the spin probe in these experiments limit the range of conditions that can be tested and consequently, the type of information that can be obtained. Reducing the temperature of ascorbate-lipid incubation allowed us to suppress the signal of C5PC in the outer leaflet of larger (100 nm diameter) extruded liposomes without inducing penetration of ascorbate to the vesicles lumen. This approach should be applicable to other spin probes with the label attached to any carbon above the fifth carbon and possibly to some carbons below it (the deeper within the bilayer the SP is situated, the longer it would take for ascorbate to interact with it and oxidize it). Thus, the effects of interleaflet coupling could be further explored as a function of depth in the bilayer.

As illustrated by our results, it is important to consider any potential contributions of specific SP-lipid interactions in the analysis of ESR data. In the presence of phase

separation the probe may partition differentially between the phases, limiting its ability to accurately report on the properties of the two lipid environments. Regardless of the level of non-ideal mixing in the leaflets however, a probe has a unique chemical structure and it may locally perturb the leaflet properties [339]. Unless this effect varies widely with lipid composition, reliable trends in the probe's order parameter and rotational diffusion upon changes in the experimental conditions could still be obtained and analyzed. Alternatively, more direct information about the order parameter of the lipids at different carbon atoms (in the absence of the indirect SP reporter) could be obtained from deuterium NMR [340, 341] by preparing aLUVs with appropriately varied level of deuteration in their two leaflets.

While the results for the asymmetric DPPC/POPC and DPPC/DEPC bilayers are consistent with our hypothesis about the effect of the relative leaflet order on the strength of interleaflet coupling, the two bilayers had different amounts of DPPC in their outer leaflets (a result of different exchange efficiency in the aLUV preparation) and that should be taken into account. The underlying assumption is that as long as the sample is phase separated and the properties of the two phases are analyzed separately, the strength of interleaflet coupling deduced by the changes in the phase properties would be independent of the exchange efficiency. More experiments of aLUVs with systematically varied exchange efficiencies need to be performed to test the validity of this assumption.

SANS and SAXS are powerful techniques that can be used to examine the structural properties of individual bilayer leaflets in freely-floating stress-free liposomes. Combined with our recent protocol for preparing aLUVs (Chapter 5), they provide an excellent and much needed tool for validating asymmetric bilayer simulations. As discussed in Chapter 6, biophysical principles dictate that the proper construction of asymmetric bilayers for MD simulations requires extra rigor in

ensuring that the tension in each bilayer leaflet is zero. In the new methodology that we proposed tension is calculated as the integral of the lateral pressure profile of the bilayer. While such pressure calculations may suffer from some limitations [199, 342], the excellent agreement of the simulation results with the small-angle scattering data confirms the applicability of the analysis to the computational construction of the bilayers. Through the use of scattering techniques, simulations of even more complex asymmetric membranes can be validated and used to further examine properties inaccessible to quantification in vitro.

The simulations of the bilayers examined with ESR are more complex due to the phase separation in their top leaflets. Despite the inherent difficulties in reproducing experimental phase boundaries with MD simulations, the observed fluidization of the gel phase in both systems is consistent with the results from the ESR analysis and with previous results from SANS experiments [4]. However, in the simulations the fraction of gel phase decreases in the POPC system and increases in the DEPC system, contrary to the experimental data. As mentioned earlier, this discrepancy may be attributed in part to the specific partitioning of the spin probe between the two types of environments whose properties change in the aLUVs. At the same time, fluidization of a gel phase can be accompanied by both disordering of the high-melting lipid in the domain and an influx of the low-melting lipid inside the domain, the latter of which would lead to an effective increase in the fraction of the ordered phase. The slight asymmetry-induced decrease in the fraction of the L_β phase in the simulated DPPC/POPC asymmetric bilayer could simply be a result of the difficulty of simulating and analyzing the symmetric gel-fluid phase separated membrane. For example, the two 1.5 μs replica simulations that we performed of this symmetric bilayer produced L_β phases with similar lipid packing but different phase fractions (19% and 33%). In contrast, the two replica simulations of the asymmetric POPC

systems gave identical results for both the ordered phase properties and fraction. Thus, even longer simulation time and a more sophisticated analysis pipeline that does not rely on Voronoi tessellation may be better suited for identifying and characterizing gel domains in the simulated symmetric bilayers. Robust determination of phase fractions and compositions in vitro is also challenging due to the different partition coefficients of the spin probe and the sophisticated modeling approach necessary to recover the structural parameters. A more complete characterization of the co-existing environments could be obtained by combining ESR with SANS and SAXS data, and differential scanning calorimetry.

The ability to estimate the elastic energy of mixing different leaflets provides a new tool for reasoning about the organization of the cellular plasma membrane and the in vitro preparation of aLUVs. The favorable energy of coupling a phase-separated leaflet to a more fluid one is in line with the known distribution of different types of lipids in the PM [33] and with studies showing that a large part of the extracellular PM leaflet is more ordered [343]. At the same time, the positive mixing energy of the asymmetric bilayer with a very tightly packed gel-like DPPC/Chol 0.8/0.2 leaflet indicates that it is unfavorable to have a monolayer that is not amenable to change through coupling, opposing a more fluid one. This could help explain the differences in exchange efficiency in the DPPC/POPC and DPPC/DEPC aLUVs: since the strength of interleaflet coupling is stronger in the latter (i.e. DEPC, having a higher melting temperature than POPC, is able to induce larger changes in the opposing DPPC-containing leaflet), it is easier to replace more of the outer leaflet of the liposomes with DPPC under the same experimental conditions (67% in the DEPC bilayers as opposed to only 46% in the POPC bilayers, see Table E1). Thus, it may be generally easier to prepare asymmetric model membranes with two more strongly coupled leaflets. Note that due to the similarity between the chain lengths of POPC

and DEPC, it is unlikely that differences in exchange efficiency would be due to very different affinities of cyclodextrin for the two types of lipids (relative to DPPC), but this assumption could be tested explicitly.

The definition of E_{mix} itself further implies that the mixing energy becomes favorable when, as a result of interleaflet coupling, the leaflets' area compressibility moduli decrease, that is they become easier to compress. Comparison of the compressibility moduli of the two leaflets in an aLUV with those of the leaflets of a symmetric membrane made of the same overall composition as the aLUVs (i.e. a chemical scramble) may thus indicate how stable the asymmetry will be over time. In a real PM such analysis would instead provide insight into the amount of energy that is needed to maintain the asymmetry. As it is currently impossible to measure individual leaflet compressibility moduli in vitro or in vivo, MD simulations remain an indispensable tool in this effort.

7.5 Conclusions

The existence of membrane asymmetry and its role in mediating processes that involve the exposure of phosphatidylserine on the extracellular leaflet of cells have been known since the 1970s. However, the effects of this transverse lipid organization on the biophysical properties of the membrane and consequently, their functional implications for cellular processes, have just recently begun to be appreciated and studied. Gaining insight into the physical mechanisms by which the two leaflets can communicate with and affect each other provides a segway into understanding the role of membrane asymmetry in spite of the complexity of the PM. Here we used model membranes to investigate one such mechanism, namely the relative packing (order) of the two bilayer leaflets. A combination of experimental and computational techniques allowed us to examine the changes in lipid structure in asymmetric bilayers with

heterogeneous leaflets. Together with analysis of the elastic energy of interleaflet mixing, our results provide new insights into the principles of PM organization and the in vitro preparation of asymmetric model membranes.

CHAPTER 8
GRAMICIDIN INCREASES LIPID FLIP-FLOP IN SYMMETRIC AND ASYMMETRIC LIPID VESICLES

8.1 Abstract

Unlike most transmembrane proteins, phospholipids can move from one leaflet of the membrane to the other. Because this spontaneous lipid translocation (flip-flop) tends to be very slow, cells facilitate the process with enzymes that catalyze the transmembrane movement and thereby regulate the transbilayer lipid distribution. Non-enzymatic membrane-spanning proteins with unrelated primary functions have also been found to accelerate lipid flip-flop, in a non-specific manner and by various hypothesized mechanisms. Using deuterated phospholipids we examined this flip-flop acceleration by gramicidin channels which have well-defined structures and known function, a combination that makes them ideal candidates for probing the protein-membrane interactions underlying lipid flip-flop. To study compositionally and isotopically asymmetric proteoliposomes containing gramicidin, we expanded a recently developed protocol for the preparation and characterization of lipid-only asymmetric vesicles. Channel incorporation, conformation, and function were examined with small-angle X-ray scattering, circular dichroism and a stopped-flow spectrofluorometric assay, respectively. As a measure of lipid scrambling we used differential scanning calorimetry to monitor the effect of gramicidin on the melting transition temperatures of the two bilayer leaflets. The merger of the two calorimetric peaks of the individual leaflets into a single peak over time indicated scrambling activity, and the effect of the channel on the transbilayer lipid distribution in both symmetric POPC and asymmetric POPC/DMPC vesicles was quantified from proton NMR measurements. Our results show that gramicidin increases lipid flip-flop in a complex, concentration-dependent manner. To consider the molecular mechanism

of the process we used molecular dynamics simulations and further computational analysis of the trajectories to estimate the amount of membrane deformation in the samples. Together, the experimental and computational approaches were found to constitute an effective means for studying the effects of transmembrane proteins on lipid distribution in both symmetric and asymmetric model membranes.

8.2 Introduction

Membranes are an essential component of all living organisms. Their structure and organization serve many functions and are tightly regulated by the cell. One prominent example is the transverse lipid distribution in cell membranes: while a self-assembled lipid bilayer has the same lipid composition in its two leaflets (i.e., it is symmetric), the leaflet compositions in the plasma membranes of eukaryotic cells differ (i.e., the bilayer is asymmetric), and this difference is actively maintained by the cell. Not surprisingly, the biophysical properties of membrane asymmetry are the subject of intense studies [12, 48, 265, 304, 324] which are rapidly increasing in number thanks to recent advances that enable the preparation and biophysical characterization of asymmetric lipid-only model membranes in vitro [287, 344, 345]. Since such model membranes are not at chemical equilibrium and their asymmetry is not actively maintained, the time window for examining their properties is limited by the gradual redistribution of the lipids between the two leaflets until a symmetric composition is achieved. Such unassisted interleaflet lipid movement is often referred to as *spontaneous lipid flip-flop (SLF)* [346].

The key lipid and bilayer properties that determine the kinetics of SLF are still under active investigation and include chain length, headgroup size and charge, and cholesterol concentration (see Ref. [347] for a current review of both experimental and computational studies on the topic). In general, the flip-flop rates of phospholipids

are many orders of magnitude slower than other typical lipid motions, such as rotation or lateral diffusion [282], due to the large energy barrier for translocating a polar lipid headgroup from one side of the bilayer to the other through the hydrophobic bilayer core. In cells, the one-directional movement of lipids between the extracellular and intracellular leaflets is catalyzed by ATP-dependent enzymes such as flippases (e.g., P-type ATPases) [348] and floppases (e.g., ABC transporters) [349], respectively. An additional bi-directional, and often non-specific movement of lipids across the two leaflets is catalyzed by ATP-independent scramblases, which include the Ca^{2+} activated TMEM (TransMEMbrane) family of proteins [282]. It is through this careful balance between the activity of the enzymes and scramblases that cells maintain the desired lipid compositions in their two membrane leaflets.

In addition to the flippases, floppases and scramblases, a wide variety of proteins with non-related primary functions can also catalyze lipid flip-flop through different mechanisms including the so-called credit-card lipid movement [282] and pore-mediated scrambling [350, 351]. For some proteins this "side" function has been hypothesized to have biological implications [352]; for others the physiological role is still unclear. Still, the ability of such proteins to scramble lipids has direct implications for the design and interpretation of model studies employing asymmetric protein-laden membranes and therefore needs to be carefully examined. A particularly interesting case are single-span transmembrane (TM) proteins that are often used to study protein-membrane interactions in vitro [47]. Such proteins can facilitate lipid flip-flop through the so-called perturbation-mediated mechanisms, that is, lowering the energy barrier for lipid translocation between the leaflets by changing the bilayer structure and/or dynamics in the vicinity of the protein [353-357].

One single-span TM protein that reportedly affects lipid flip-flop only under certain conditions is the functional dimer form of the bacterial ion-channel gramicidin

(gA) [358]. The channel has been shown to accelerate lipid translocation in three separate studies (to our knowledge), but to different extents: up to 30-fold in erythrocytes at moderate gA concentrations (gA:lipid ratio of roughly 1:200) [359]; from 2 to 10-fold in supported lipid bilayers at high gA:lipid ratios (of about 1:50) [360]; and to a somewhat lesser extent in 400 nm diameter liposomes with high gramicidin mole fractions (with ratios of 1:20) in which flip-flop was unmeasurable in the absence of gA [350]. At the same time, flip-flop enhancement was not detected in erythrocytes at the gA concentrations at which the channel performs its ion-conducting function [359]. The disparate results from these studies highlight limitations in the experimental methodologies that include quantifying the distribution of lipids in the two leaflets using a rather indirect method based on extraction with albumin (which in its own right could perturb the bilayer) [359], or approximating the kinetics of lipid flip-flop by measuring the translocation rate of a chain-labeled fluorescent lipid analog [350]. The choice of system is also very important: complex and asymmetric cell membrane environments like erythrocytes present challenges both for the interpretation of the results and the quantification of the gA:lipid ratio, while the unavoidable bilayer defects in supported lipid bilayers prepared with the Langmuir-Blodgett/Langmuir-Schaefer (LB/LS) technique are particularly worrisome as they could accelerate lipid flip-flop in a hard-to-control manner [361].

Here we address these challenges by presenting a new platform for measuring protein-mediated lipid flip-flop in vitro. The approach utilizes free-floating and stress-free large unilamellar vesicles with precisely controlled symmetric and asymmetric lipid composition, in the presence or absence of protein. This experimental setup allows for a wide range of biophysical assays and importantly, enables the direct measurement of the flip-flop kinetics of unlabeled lipids in chemically symmetric and asymmetric bilayers using ^{1}H NMR. Thus, the framework overcomes the limitations in

the previous approaches by providing a robust model system for studying the effects of proteins on the transverse bilayer organization. Using this protocol, we examined the effect of gramicidin on lipid flip-flop in both isotopically and compositionally asymmetric vesicles. Though our results show that gramicidin speeds up lipid translocation in both systems, the corresponding rates are not directly proportional to gA concentration. Further computational analysis revealed that membrane deformations likely play a role in the observed effects at high gA mole fractions, suggesting the existence of mechanistically different regimes of gA-mediated changes in bilayer organization.

8.3 Materials and methods

8.3.1 Materials

Gramicidin and all phospholipids (POPC, POPG, POPC-d31, POPC-d13 and DMPC-d54, see Table 8.1 for a list of abbreviations) were purchased from Avanti Polar Lipids (Alabaster, AL) as dry powders and used as supplied. The phospholipids were dissolved in HPLC-grade chloroform and gramicidin was dissolved in HPLC-grade methanol. Both phospholipids and gramicidin were stored at −80°C until use. Methyl-β-cyclodextrin (MβCD), praseodymium(III) nitrate hexahydrate {$Pr(NO_3)_3$ $6H_2O$}, sucrose, NaCl, and hydrochloric acid were purchased from Fisher Scientific. Thallium nitrate ($TlNO_3$) and ANTS were purchased from Sigma Aldrich and Invitrogen, respectively. Ultrapure H_2O was obtained from a High-Q purification system (Wilmette, IL) and D_2O (99.9%) was purchased from Cambridge Isotopes (Andover, MA).

Table 8.1. List of abbreviations

POPC	1-palmitoyl-2-oleoyl-*sn*-glycero-3-phosphocholine
POPC-d13	1-palmitoyl-2-oleoyl-*sn*-glycero-3-phosphocholine-1,1,2,2-d4-N,N,N-trimethyl-d9 (headgroup-deuterated POPC)
POPC-d31	1-palmitoyl-d31-2-oleoyl-*sn*-glycero-3-phosphocholine (chain-deuterated POPC)
DMPC-d54	1,2-dimyristoyl-d54-*sn*-glycero-3-phosphocholine (chain-deuterated DMPC)
POPG	1-palmitoyl-2-oleoyl-*sn*-glycero-3-phospho-(1'-rac-glycerol)
LUV	Large unilamellar vesicle
sLUV	Compositionally symmetric LUV
s*LUV	Compositionally symmetric but isotopically asymmetric LUV
aLUV	Asymmetric LUV
gA	Gramicidin A
gA-LUV	Large unilamellar vesicle with gA
gA-sLUV	Compositionally symmetric LUV with gA
gA-s*LUV	Compositionally symmetric but isotopically asymmetric LUV with gA
gA-aLUV	Asymmetric LUV with gramicidin
MLV	Multilamellar vesicle
MβCD	Methyl beta cyclodextrin
GC/MS	Gas chromatography/mass spectrometry
SAXS	Small-angle X-ray scattering
CD	Circular dichroism
GBFA	Gramicidin-based fluorescence assay
DSC	Differential scanning calorimetry
^{1}H NMR	Proton nuclear magnetic resonance
MD	Molecular Dynamics
CTMD	Continuum theory of membrane deformations
C_{out}	Area of shifted peak in ^{1}H NMR spectra after addition of shift reagent
C_{in}	Area of unshifted peak in ^{1}H NMR spectra after addition of shift reagent
ΔC	Difference between C_{out} and C_{in} relative to time 0, $(C_{out} - C_{in})/(C_{out}(0) - C_{in}(0))$
k_f	Rate of lipid flip-flop
$t_{1/2}$	Half-time of lipid flip-flop

8.3.2 Preparation of liposomes without gramicidin

Large unilamellar vesicles (LUVs) with symmetric lipid distribution (sLUVs) were prepared by first mixing appropriate volumes of lipid stocks in organic solvent with a glass Hamilton syringe. The solvent was evaporated with an Ar stream followed by high vacuum overnight. The dry lipid film was hydrated at room temperature (for POPC) or 35-40°C (for mixtures with DMPC) for at least 1 h with intermittent vortexing every 15 min. The resulting multilamellar vesicle (MLV) suspension was subjected to at least 5 freeze/thaw cycles using a –80°C freezer, then extruded through a 100 nm pore-diameter polycarbonate filter with a mini-extruder (Avanti Polar Lipids) by passing the suspension through the filter 31 times. All sLUVs were doped with 5 mol% POPG to ensure unilamellarity [293].

Asymmetric LUVs (aLUVs) were prepared following the protocol described in Chapter 5 with slight modifications. Briefly, an MLV suspension of the donor lipid (i.e., the lipid to be exchanged into the outer leaflet of the aLUVs) was prepared in a 20% w/w sucrose solution as described above. The sample was diluted 20-fold with water and centrifuged at 20°C for 30 min at 20K × g. The supernatant was discarded, the pellet was re-dissolved using a 35 mM MβCD solution in water at a nominal donor lipid:MβCD ratio of 1:8, and the MβCD/donor mixture was incubated at room temperature for 2 h with gentle stirring. sLUVs of the acceptor lipids (i.e., the lipids to be present on the inner leaflet of the aLUVs) were prepared in a 25 mM NaCl solution as described above. These were added to the MβCD/donor mixture at a nominal donor:acceptor ratio of 2:1 or 3:1 (see Table F1). The MβCD/donor/acceptor slurry was incubated for 30 min at room temperature with gentle stirring. Immediately after that the sample was filtered with a centrifugal filter device (Amicon Ultra-15, 100,000 Da molecular weight cutoff, pre-washed with water 7 times) for 25 min at 2.5K × g. The retentate was diluted with water 8-fold and centrifuged for 30 min at 20K × g and 20°C. The supernatant was carefully transferred to centrifugal devices (as described

above), concentrated to 250-500 μL and washed with H_2O or D_2O a minimum of 3 times. The aLUVs were recovered from the final retentate and stored in a plastic centrifuge tube at room temperature until further use.

8.3.3 Preparation of liposomes with gramicidin

Symmetric large unilamellar vesicles with gramicidin (gA-sLUVs) were prepared as follows. The lipids were first mixed in organic solvent, and gA was added from a methanolic solution with a glass Hamilton syringe at the appropriate gA:lipid ratio. The organic solvent was evaporated on a rotary evaporator, followed by high vacuum overnight. The dry sample was gently hydrated on a rotary evaporator for 30-60 min, then incubated at room temperature until the film was fully dissolved and the solution looked uniform (typically overnight). Vortexing was performed only occasionally and at the lowest setting. The sample was subjected to at least 5 freeze/thaw cycles using a −80°C freezer and then extruded with a 100 nm pore-diameter polycarbonate filter as described above. All gA-sLUVs were doped with 5 mol% POPG to ensure unilamellarity.

Asymmetric LUVs with gramicidin (gA-aLUVs) were prepared following the protocol described above with the only modification that gramicidin was added to the symmetric acceptor liposomes. That is, instead of acceptor sLUVs, acceptor gA-sLUV vesicles were added to the MβCD/donor mixture after the 2 h incubation. All other steps of the protocol were the same (see Fig. F1).

8.3.4 Gas chromatography-mass spectrometry (GC/MS)

The overall lipid composition of the aLUVs and gA-aLUVs was determined from GC/MS analysis of fatty acid methyl esters (FAMEs) generated by acid catalyzed methanolysis of the samples. The detailed protocol is described in Chapter 5. Briefly,

about 100 μg of the sample were dried on a rotary evaporator, dissolved in 1 mL of 1 M methanolic HCl, flushed with Ar and incubated at 85°C for 1 h in a glass culture tube sealed with a Teflon-lined cap. After allowing the sample to cool for a few minutes, 1 mL water was added and the sample was briefly vortexed. Then, 1 mL hexane was added and the sample was vortexed vigorously to form an emulsion and extract the FAMEs. The solution was centrifuged at low speed (~ 400 × g) for 5 min to break the emulsion, and the upper (hexane) phase containing the FAMEs was transferred to a GC autosampler vial. The total volume in the vial was brought up to 1 mL with hexane. FAME analysis was performed using an Agilent 5890A gas chromatograph (Santa Clara, CA) with a 5975C mass-sensitive detector operating in electron-impact mode and an HP-5MS capillary column (30 m × 0.25 mm, 0.25 μm film thickness). After injection of a 5 uL aliquot into the chromatograph, a pre-programmed column temperature routine was initiated as described in Chapter 5. Total ion chromatogram peaks were assigned and integrated using GC/MSD ChemStation Enhanced Data Analysis software. The ratio of the different lipid components was determined from the ratio of the respective peak areas of the FAMEs corresponding to the lipid fatty acid chains.

8.3.5 Small-angle X-ray Scattering (SAXS)

LUV samples for small angle X-ray scattering (SAXS) measurements were prepared as described above and concentrated to 15-20 mg/mL. SAXS measurements were performed using a Rigaku BioSAXS-2000 home source system with a Pilatus 100K 2D detector and a HF007 copper rotating anode (Rigaku Americas, The Woodlands, TX). SAXS data were collected at a fixed sample-to-detector distance (SDD) using a silver behenate calibration standard, with a typical data collection time of 3-4 h. The one-dimensional scattering intensity $I(q)$ [$q = 4\pi \sin(\theta)/\lambda$, where λ is

the X-ray wavelength and 2θ is the scattering angle relative to the incident beam] was obtained by radial averaging of the corrected 2D image data, an operation that was performed automatically using Rigaku SAXSLab software. Data were collected in 10 min frames with each frame reduced separately to assess radiation damage; there were no significant changes in the scattering curves over time. Background scattering from water collected at the same temperature was subtracted from each frame, and the background-corrected $I(q)$ from the individual frames was then averaged, with the standard deviation taken to be the measurement uncertainty.

8.3.6 Circular dichroism (CD)

Samples for CD were first diluted to 1 mg/mL lipid concentration, for a protein concentration between 5-13 μM. The lipid concentration was estimated from dynamic light scattering (DLS). gA conformation was measured using a J-815 spectropolarimeter equipped with a PTC-423S Peltier temperature controller (Jasco, Easton, MD). CD spectra (raw ellipticity θ in units of millidegree vs. wavelength) were collected at 25°C using a 2 mm path length cuvette, a scan rate of 100 nm/min, and 30 accumulations. The spectrum of each gA-containing sample was first corrected for the lipid background by subtracting the spectrum of a corresponding lipid-only sample. The only exception was the gA-aLUV sample, for which the background was taken to be the spectrum of the POPC acceptor sLUVs which were similar in size to the gA-aLUVs as determined from DLS. The background-corrected data were then converted to mean residue molar ellipticity $[\theta]$ (in units of degree cm^2 $dmol^{-1}$) using the relationship:

$$[\theta] = \frac{10^6\theta}{lcN}, \tag{8.1}$$

where l is the cell path length in mm, c is the protein concentration in μM, and $N = 15$ is the number of amino acids in the gA protein.

8.3.7 Gramicidin-based fluorescence assay (GBFA)

Gramicidin function was quantified using a fluorescence quench protocol as described in [362]. To adapt the samples for this assay, the acceptor sLUVs were prepared with gA:lipid ratio of 1:20,000 and hydrated with 25 mM ANTS instead of 25 mM NaCl. After the last concentration step the gA-aLUVs were washed once with H_2O and 3 times with elution buffer (35 mM $NaNO_3$ and 6 mM HEPES at pH 7.0). The rate of quenching of the ANTS trapped inside the vesicles was measured with a Tl^+ buffer (35 mM $TINO_3$ and 6 mM HEPES at pH 7.0) in a single-mixing experiment and quantified with a regular stretched exponential [362]. As a control, gA-sLUV acceptors hydrated with ANTS were also washed 3 times with elution buffer and the rate of ANTS quenching was measured as described above.

8.3.8 Differential scanning calorimetry (DSC)

Samples for DSC were diluted to ~ 5 mg/mL and measured using a Nano DSC (TA Instruments, New Castle, DE). The LUV suspension was loaded into the sample capillary cell, and degassed solvent was loaded into the reference capillary cell. The cells were pressurized to 3 atm to suppress the formation of air bubbles, and a cooling scan was initiated from 30°C to –8°C at a rate of 0.2°C/min. All thermograms showed either a series of peaks or a single broad peak between ~ –5°C and 20°C. A sloping background contribution was accounted for by fitting a portion of the thermogram on either side of these peaks to a third-order polynomial which was then subtracted from the raw data.

8.3.9 ^{1}H NMR

The interleaflet lipid distribution in the aLUVs and gA-aLUVs was quantified with a shift reagent assay performed on either a Bruker Avance III 400 MHz spectrometer (at ORNL) or a Bruker Avance III HD 500 MHz spectrometer (at Weill Cornell Medical College) as described in [361]. Briefly, a standard ^{1}H pulse sequence with a 30º flip angle and 2 s delay time was collected at 35°C first for the sample itself diluted with D_2O or H_2O to 600 µL and ~ 0.5 mg/mL. Following that, a small aliquot (1-2 µL) of 20 µM Pr^{3+}/D_2O was added to the NMR tube and mixed with its contents by inverting the tube 3 times. The sample was measured again, another aliquot of Pr^{3+} was added, and the procedure was repeated. A total of at least three Pr^{3+} titrations were performed, and their spectra recorded. Each Pr^{3+} titration resulted in a shift of the resonance peak of the protiated choline headgroups exposed on the outer leaflet of the vesicles. The ratio of exposed and protected choline headgroups was quantified from the ratio of the areas of the shifted and unshifted choline peaks and, together with the GC results, used to approximate the composition of the two bilayer leaflets as described in Chapter 5. The NMR analysis was performed by fitting multiple Lorentzians to the data with Origin or custom Mathematica scripts. For all samples measured in H_2O, the signal from the solvent was suppressed using the standard excitation sculpting sequence *zgesgp*.

8.3.10 Analysis of lipid flip-flop kinetics

The rate k_f of lipid flip-flop was measured from the time-dependent changes in the transverse distribution of protiated-headgroup lipid in each sample as described in [361]. Briefly, the NMR time traces of relative changes in the lipid distribution were expressed as:

$$\Delta C(t) = \frac{C_{out}(t) - C_{in}(t)}{C_{out}(0) - C_{in}(0)}, \tag{8.2}$$

where $C(t)$ is the ratio of the areas of the shifted (outer leaflet) and unshifted (inner leaflet) choline peaks at time t with subscripts *out* and *in* denoting the outer and inner leaflet, respectively. The data was modeled as:

$$\Delta C(t) = e^{-2k_f t}, \tag{8.3}$$

with the corresponding half-time $t_{1/2}$ given by

$$t_{1/2} = \frac{\ln(2)}{2k_f}. \tag{8.4}$$

All samples were kept on the bench between NMR measurements, and consequently the flip-flop kinetics reported here correspond to sample behavior at an ambient temperature of ~ 22°C.

8.3.11 Molecular Dynamics (MD) simulations

All-atom MD simulations of gramicidin in the symmetric and compositionally asymmetric bilayers from the *in vitro* experiments were performed as described below.

For the symmetric system, a POPC bilayer with 100 lipids per leaflet (200 lipids total) was first constructed with CHARMM-GUI [141, 142, 144]. The bilayer was hydrated with 70 waters per lipid, and a total of 35 Na^+ and 35 Cl^- ions for a salt concentration of 138 mM. After a short initial equilibration with CHARMM-GUI's protocol, the system was run for 226 ns. From the last frame of the trajectory all water and ion atoms were removed, and a single gramicidin dimer (PDB: 1JNO) was manually inserted in the bilayer by replacing 10 lipids from each leaflet with a gA monomer. The system was then hydrated and ionized with VMD's *solvate* and *autoionize* plugins, respectively, resulting in a bilayer patch with 90 lipids per leaflet

(180 lipids total), 1 gA dimer, 67 waters per lipid and 30 Na^+ and 30 Cl^- ions for a salt concentration of 138 mM NaCl.

For the asymmetric system, we identified first the appropriate number of lipids in the asymmetric lipid-only bilayer with top leaflet composed of DMPC/POPC 75/25 mol%, and a bottom leaflet composed of DMPC/POPC 10/90 mol%, following the protocol in Chapter 6. The resulting tension-free bilayer contained 104 and 100 lipids in the top and bottom leaflets respectively, and was constructed and equilibrated with CHARMM-GUI's protocols. After a production run of 445 ns, gramicidin was manually inserted in the bilayer by removing 8 lipids from each leaflet while maintaining the overall leaflet compositions. The system was hydrated with VMD's *solvate* plugin, resulting in a bilayer patch with 96 lipids in the top leaflet, 92 lipids in the bottom leaflet, 1 gA dimer and 55 waters per lipid.

All simulations were performed with the NAMD software [155] and the CHARMM36 force field for lipids [156, 195] in the NPT ensemble under constant pressure of 1 atm and temperature of 25°C. The force field parameters for gA were kindly provided by Andrew Beaven and were based on those used in [363], made compatible with the CHARMM36 force field. Namely, the D-amino acids were treated in the same way as L-amino acids (except for their chirality) whereas the parameters for the two gA termini (formyl and ethanolamine) were the same as in [363] with the particular atom types renamed to conform to the CHARMM36 atom notation. For both the symmetric and asymmetric bilayers with gA, the system was first energy minimized for 10^4 steps, then run for 100 ps with a 1 fs time step. Following this initial relaxation, the POPC/gA bilayer was simulated for 887 ns and the asymmetric bilayer with gA was simulated for 705 ns with a 2 fs time step. For more details on all simulated systems and the corresponding simulation parameters, see Section F.1 in Appendix F.

8.3.12 Quantification of membrane deformation from simulations

To quantify the deformation of the membrane around gramicidin, the trajectories were first centered and aligned on the backbone of gA. Since gA can tilt with respect to the bilayer normal in the course of the simulations, special care was taken to ensure that the alignment step did not result in abnormal tilting of the membrane effectively leading to artificial changes in the bilayer thickness in the vicinity of the protein. The gA-lipid boundary was identified separately for each leaflet as the outermost layer of the time-averaged occupancy map (constructed on a 2 x 2 grid) of the respective gA monomer atoms projected onto the *xy* plane. The leaflet thickness at the gA-lipid boundary was calculated from the interpolated z-positions of the lipid atoms in the respective grid points, as described in Section F.2 in Appendix F. The leaflet thickness at the gA-lipid boundary was used to obtain the optimal deformation profile around a gA monomer by a self-consistent free energy minimization procedure as described in Section F.3 in Appendix F. The leaflet deformation around gA at distance r from the gA center was calculated as the squared deviation in thickness averaged over the area between the grid points at distance r from the gA center and the gA-lipid boundary (the bulk leaflet thickness was taken from the corresponding lipid-only simulations). The membrane deformation was taken as the sum of the deformations of the two leaflets.

8.3.13 Quantification of membrane deformation in experiments

To estimate the amount of membrane deformation at each of the gA:lipid ratios used in the experiments, we first approximated the number N of gA dimers on a vesicle from: 1) the total surface area of a vesicle with diameter 130 nm (the average vesicle size measured with DLS); 2) the average area per lipid 64 $Å^2$ (calculated from

MD simulations for a POPC bilayer); and 3) the area per gA monomer 208 Å^2 approximated from the occupancy map of the gA monomers described above. N gA dimers were then distributed uniformly on the surface of a sphere with diameter 130 nm using MATLAB, and the distance d between them was recorded. The membrane deformation at a given gA:lipid ratio was estimated as the membrane deformation at a distance $d/2$ from the gA center.

8.4 Results

8.4.1 Gramicidin incorporation, conformation, and function are the same in symmetric and asymmetric liposomes

We modified a recently developed protocol for the construction of asymmetric lipid-only vesicles [4] to enable the preparation of asymmetric proteoliposomes. As described in Methods, the protocol involves mixing two populations of symmetric vesicles (only one of which contains pre-incorporated protein) and exchanging the lipids between their outer leaflets with MβCD (Fig. F1). Using this procedure we prepared two types of gramicidin-containing vesicles: 1) *compositionally symmetric* but *isotopically asymmetric* liposomes (s*LUVs) with inner leaflet composed of POPC or its headgroup-perdeuterated variant (POPC-d13), and outer leaflet exchanged with its chain-perdeuterated variant (POPC-d31); and 2) *compositionally asymmetric* vesicles (aLUV) with the same inner leaflet composition and an outer leaflet exchanged with the chain-perdeuterated variant of DMPC (DMPC-d54). Table F1 shows the donor mole fraction in the final samples as determined from GC/MS (see Methods) which ranged between 0.32 and 0.4 for the s*LUVs and between 0.35 and 0.45 for the aLUVs. The size of the vesicles was measured with DLS and was on average 130 nm with polydispersity index below 0.2.

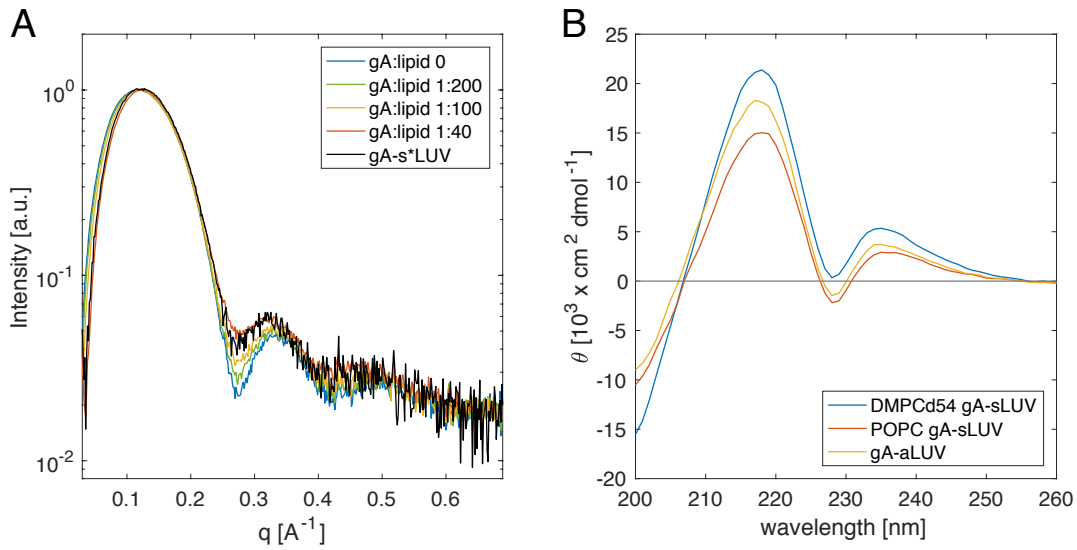

Figure 8.1. Gramicidin incorporation and conformation remain the same in symmetric and asymmetric liposomes. A) Color-coded SAXS form factors of a series of POPC gA-sLUVs with increasing concentration of gA and isotopically asymmetric LUVs, gA-s*LUV, composed of deuterated variants of POPC and prepared with a nominal gA:lipid ratio of 1:40. B) Circular dichroism spectra of gA-containing DMPC-d54 (blue) and POPC (red) sLUVs, and compositionally asymmetric LUVs composed of DMPC-d54 and POPC (yellow). All liposomes were prepared at a gA:lipid ratio of 1:40, and all measurements were performed at 25°C. See text for details.

To examine the effect of the sample preparation protocol on gramicidin, we assayed its incorporation, conformation, and function in the asymmetric proteoliposomes. Fig. 8.1A shows evidence of unaltered bilayer incorporation of gA from small-angle X-ray scattering (SAXS) data. In a SAXS experiment, hydrogen and deuterium scatter X-rays in the same way and the form factor of an isotopically asymmetric sample is indistinguishable from the form factor of the corresponding protiated sample. Moreover, because of the short length of gA relative to the bilayer thickness, larger amounts of the channel in the bilayer lead to systematic lift-off (i.e. increase in the intensity) of the first minimum in the SAXS form factor, as shown in the series of symmetric POPC LUVs with increasing gA mole fractions (Fig. 8.1A).

Comparing (in Fig 8.1A) the isotopically asymmetric gA-containing LUVs (gA-s*LUV) prepared with gA:lipid ratio of 1:40, with the series of symmetric LUVs, shows that the concentration of gA in the asymmetric LUVs is very close to the nominal mole fraction of gA initially incorporated in the acceptor vesicles; the incorporation was efficient and very little (if any) gA was lost during the asymmetric proteoliposome preparation.

Next we examined the structural properties of the incorporated gA. In addition to its canonical helical dimer conformation, gramicidin can exist in other non-functional conformations such as a dimeric helix in which two gA monomers are intertwined into a single extended helix [364]. The dimeric helix conformation can arise from hydrophobic mismatch (or from keeping gA in some nonpolar solvents) and has a distinct CD spectrum [365]. Fig 8.1B shows the CD spectrum of gA in the compositionally asymmetric LUVs in comparison with the spectra of gA in symmetric LUVs made of either just POPC or DMPCd54. The data clearly show that most of the 0.025 mol% gA in the symmetric samples existed in a helical dimer conformation, and that the conformation remained unchanged during the steps of the gA-aLUVs preparation protocol.

To evaluate the function of gA in the asymmetric liposomes, we measured the rate with which a fluorophore (ANTS) trapped inside the vesicles was quenched by an externally added quencher (Thallium, Tl^+). This assay provides a measure of the equilibrium dimer-to-monomer ratio of gA in the bilayer by taking advantage of the fact that Tl^+ can enter the vesicles and quench ANTS only through functional gA dimers [362]. Fig. 8.2A shows the ANTS fluorescence decay as a function of time in the initially symmetric acceptor vesicles (66.1) and the final isotopically asymmetric gA-s*LUVs (62.9). According to the ratio of the two rates (0.95), the dimer-to-monomer equilibrium of gA in the isotopically asymmetric vesicles was essentially

unaffected by the cyclodextrin-mediated lipid exchange. We obtained a similar ratio of 0.99 for the compositionally asymmetric liposomes (Fig. 8.2B), confirming that in both asymmetric samples gA function remained intact.

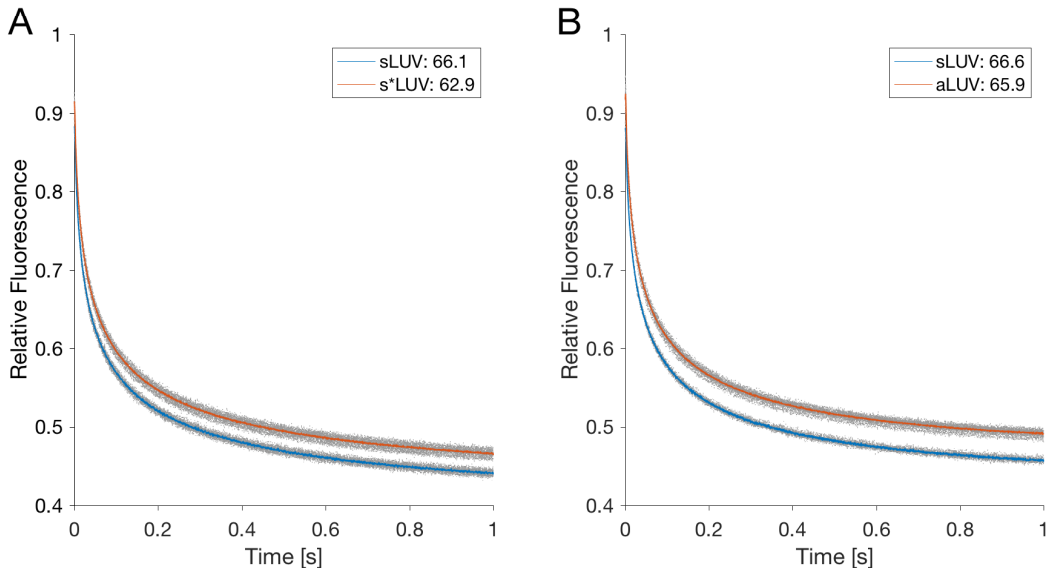

Figure 8.2. Gramicidin channel function remains intact in asymmetric liposomes. Changes in ANTS fluorescence over time for the isotopically (A) and compositionally (B) asymmetric samples (in red) and their corresponding symmetric acceptor vesicles (in blue). Replicate traces are shown in grey while their averages are shown in color. A constant background fluorescence measured before addition of Tl^+ has been subtracted from all traces. The average rates calculated from the traces are indicated in the legends. All measurements were performed at ambient temperature of ~ 22°C.

8.4.2 gA scrambles lipids in compositionally asymmetric vesicles

That gramicidin can scramble lipids first became evident in differential scanning calorimetry experiments. In a DSC experiment, thermodynamic phase transitions (such as transitions between gel and fluid) are detected by monitoring the release of heat from a sample as a function of temperature. Fig. 8.3 shows a cooling temperature scan performed after sample preparation (scan 1) for compositionally asymmetric vesicles without (Fig. 8.3A) and with (Fig. 8.3B) gramicidin (see Methods). Two

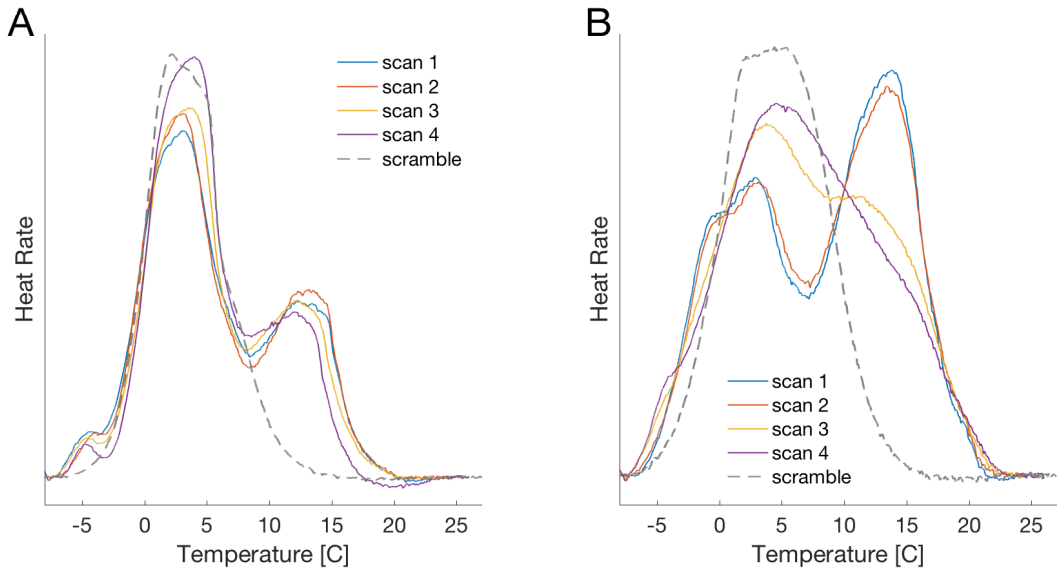

Figure 8.3. Gramicidin scrambles lipids in compositionally asymmetric vesicles. DSC data of compositionally asymmetric LUVs with DMPC-d54 and POPC, and without (A) or with (B) gramicidin at gA:lipid ratio of 1:40. Four consecutive cooling scans were performed as follows: after the asymmetric vesicle preparation (scan 1, blue); after scan 1 (scan 2, red); after subsequent incubation at 20°C for 12 h followed by incubation at 45°C for 5 h (scan 3, yellow); and after another set of incubations at 20°C for 12 h and 45°C for 5 h (scan 4, purple). Also shown for comparison with grey dashed lines is data for the symmetric samples (scramble) with the same overall composition as the asymmetric vesicles (Table F1).

transition peaks are visible in both samples, likely coming from the different melting temperatures of the POPC-rich inner leaflet (POPC melting temperature is -2°C) and the DMPC-d54-rich outer leaflet (DMPC-d54 melting temperature is 19°C), see Fig. F2. After the first scan, the temperature was again brought to 30°C and a second cooling scan (scan 2) was performed without any observable changes in the DSC spectra, indicating that cycling through the temperature range of -8°C to 30°C (and

consequently through the gel-liquid crystalline transition of each leaflet) by itself did not result in any major redistribution of the lipids between the two leaflets. In the gA-

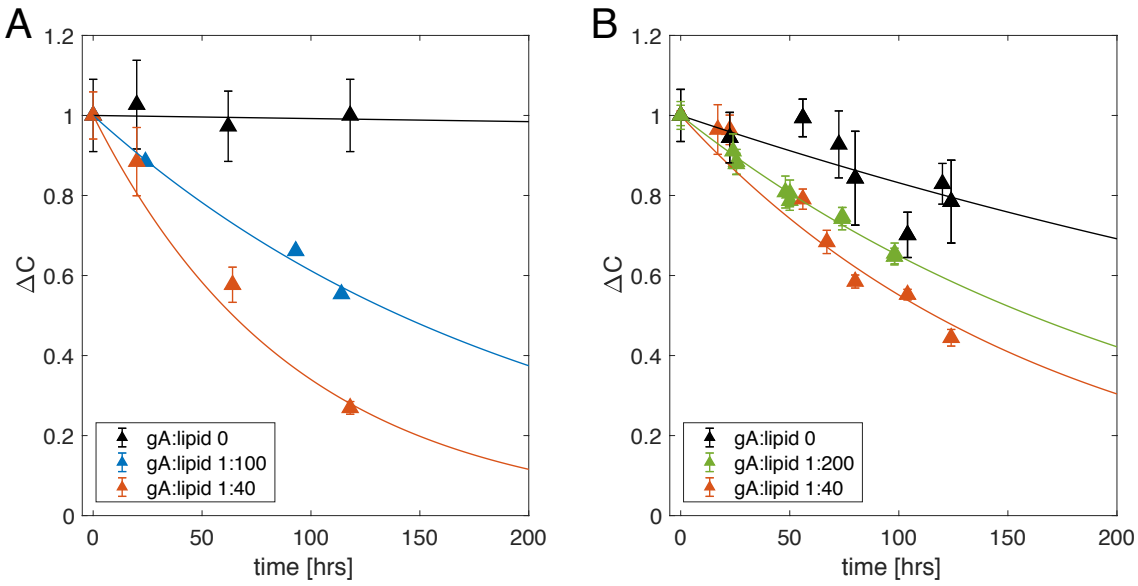

Figure 8.4. Gramicidin increases the rate of lipid flip-flop in isotopically and compositionally asymmetric vesicles. Time evolution of the interleaflet distribution of POPC-d31 in s*LUVs (A) and DMPC-d54 in aLUVs (B) either without gA (black) or with gA at gA:lipid ratio of 1:40 (red), 1:100 (blue) and 1:200 (green). Both plots show the time-dependent changes in the distribution of POPC-d31 between the outer and inner leaflets, relative to the first time point measured after vesicle preparation (ΔC). See text for details. Error bars represent standard deviations of at least 3 consecutive Pr^{3+} additions. Each time trace in panel A is from a single sample. The time traces of the compositionally asymmetric vesicles in panel B are from 1 (gA:lipid 1:40), 2 (no gA) and 3 (gA:lipid 1:200) separately prepared samples, respectively. The kinetics reported here correspond to sample behavior at an ambient temperature of ~ 22°C.

aLUV sample, however, after a set of fixed temperature incubations (20°C for 12 hrs, followed by 45°C for 5 hrs), the two peaks began to merge (scan 3, Fig. 8.3B) while those of the aLUV sample without gA remained unchanged (scan 3, Fig. 8.3A). The changes in the gA-aLUV sample were even more pronounced after subjecting the samples to another set of fixed temperature incubations (scan 4). These results indicate that gramicidin facilitated the equilibration of the two leaflet compositions,

presumably through its ability to accelerate lipid flip-flop, which eventually would result in a symmetric bilayer with a single transition temperature peak (grey dashed lines in Fig. 8.3).

8.4.3 gA increases the rate of lipid flip-flop in compositionally asymmetric vesicles

In order to quantify the effect of gA on lipid flip-flop, we used ^{1}H NMR to measure the rate of lipid translocation in the presence and absence of the channel (see Methods). The nine equivalent protons on a protiated choline headgroup produce a clearly defined resonance peak at ~ 3.1-3.6 ppm. The shift reagent Pr^{3+} added externally to the sample interacts only with the lipid headgroups exposed on the outer leaflet of the vesicles and shifts their resonance downfield [10, 366]. After exchanging lipids with protiated choline headgroups (POPC-d31 or DMPC-d54) into acceptor vesicles composed of the headgroup-deuterated POPC-d13, the only detectable resonance comes from the exchanged donor lipids. The distribution of the protiated-headgroup lipids across the two bilayer leaflets thus can be determined from the ratio of the areas of the shifted (C_{out}) and unshifted (C_{in}) choline peaks in the NMR spectrum. Repeating the shift experiment on different aliquots from the sample over time allows for direct quantification of the lipid flip-flop rate [10].

Table 8.2. Translocation kinetics in the examined systems. Shown are the corresponding half times and rates of lipid flip-flop calculated from the NMR data shown in Fig. 4 as described in Methods. The numbers in brackets represent 95% confidence intervals.

Outer leaflet	gA:lipid	$t_{1/2}$ [h]	k_f / 10^{-7}s^{-1}
POPC-d31 / POPC-d13	0	~ 8900	~ 0.1
	1:100	141 [125; 163]	6.8 [5.9; 7.7]
	1:40	64 [55; 76]	16.0 [12.6; 17.4]
DMPC-d54 / POPC-d13	0	376 [251; 748]	2.6 [1.3; 3.8]
	1:200	160 [153; 168]	6.0 [5.7; 6.3]
	1:40	116 [104; 132]	8.3 [7.3; 9.2]

Fig. 8.4 shows the relative changes in transverse lipid distribution ΔC (see Eq. 8.2) as a function of time t for both the chemically symmetric (Fig. 8.4A) and asymmetric (Fig. 8.4B) liposomes with different amounts of gramicidin (see Methods). Table 8.2 lists the corresponding lipid flip-flop rates and half-times calculated as described in Methods. While the spontaneous lipid flip-flop rate in the absence of gA is almost unmeasurably slow in the s*LUVs, it is clearly increased when DMPC is exchanged in the outer leaflet of POPC. Importantly, the rate of lipid translocation in both samples increases in the presence of the channel, in a gA-concentration dependent manner.

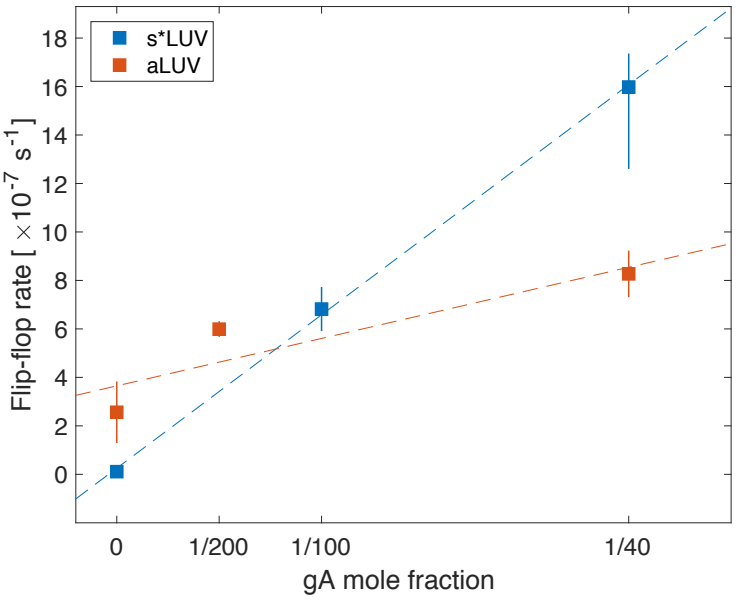

Figure 8.5. Rate of lipid flip-flop shows a complex relationship with gA mole fraction. Flip-flop rates calculated from the data in Fig. 8.4 for the compositionally symmetric (blue) and asymmetric (red) LUVs (see Table 8.2) as a function of the nominal gA mole fraction in the samples. Error bars represent 95% confidence intervals.

8.4.4 Models for gA-mediated lipid flip-flop

If every gA dimer accelerated the movement of lipid between the leaflets, the rate of lipid flip-flop would vary linearly with gA mole fraction [355]. Fig. 8.5 shows the

flip-flop rates calculated from the NMR data (Table 8.2), as a function of the gA:lipid ratio. Indeed, the data for the s*LUV samples (shown in blue) are consistent with the model of single gA channel-mediated lipid translocation. However, in the aLUV samples (shown in red) the linear relationship predicted from the model is not as clear, and the uncertainty in the data precludes any firm conclusions. Considered together, the two data sets introduce a conundrum: in the absence of gramicidin, the flip-flop rate in the compositionally asymmetric bilayers is clearly faster than the rate in the symmetric membranes, yet in the presence of gA at gA:lipid ratio of 1:40 this trend is reversed and the flip-flop kinetics in the aLUVs are much slower than those in the s*LUVs. This result suggests a mechanism different from a single channel-induced perturbation by which gramicidin catalyzes lipid translocation, based on the following considerations: 1) as the gA channel is relatively short, it is likely to cause thickness deformations in the membrane; and 2) the thickness deformations in a POPC bilayer could be alleviated in the presence of a shorter-chain lipid like DMPC. Thus gA-induced bilayer stress could be a plausible contributing factor in the observed trends.

8.4.5 Membrane deformations are likely to play a role in gA-mediated lipid flip-flop

Gramicidin has been routinely used as a model peptide to study local bilayer deformations that result from protein-membrane interactions [106, 367]. In particular, gA has been shown to induce thinning in a pure DMPC bilayer [368] and one would expect that the same effect would be observed in bilayers with hydrophobic thickness greater than DMPC, such as a membrane composed of POPC [145]. Such local deformations produce a stress on the membrane that will increase with increasing gA concentration in the membrane and could potentially affect lipid flip-flop. We therefore investigated the response of the bilayer to the presence of a single gA channel in the two experimentally studied systems.

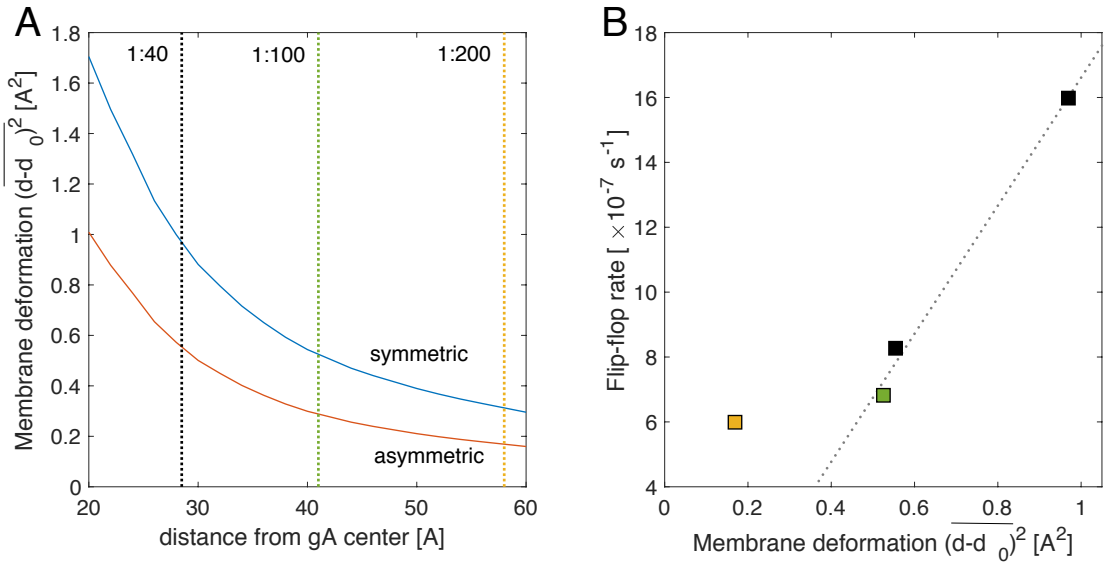

Figure 8.6. Membrane deformation correlates with the rate of gA-mediated lipid flip-flop at high gA concentrations. (A) Average squared deviations in bilayer thickness as a function of distance from the center of gA in a symmetric POPC bilayer (blue) and in an asymmetric bilayer (like in the one used in the NMR experiments in Fig. 8.4) (red). The thickness deviations were calculated from the membrane deformation profiles around a single gA channel obtained from a CTMD-guided free energy minimization utilizing information from the MD simulations (see Section 8.3). Dashed lines indicate the approximated half-distances between gA channels on the surface of the LUVs at three different gA:lipid ratios: 1:40 (black), 1:100 (green) and 1:200 (yellow). (B) gA-mediated lipid flip-flop rate from Fig. 8.5 as a function of the corresponding membrane deformation from panel (A). The data points are color coded according to gA concentration as in panel (A).

MD simulations, in combination with the continuum theory of membrane deformations (CTMD) [369], were used to estimate the amount of membrane deformation at the different gA mole fractions from the experiments by first quantifying the changes in membrane thickness as a function of distance from the channel, and then relating them to the average distances between channels in the samples. To enable this protocol, MD simulations were performed on a system containing a single gA channel embedded in a symmetric POPC bilayer, or in an asymmetric membrane with a top leaflet of DMPC/POPC 0.75/0.25 and a bottom leaflet of DMPC/POPC 0.10/0.90. The compositions of the two leaflets were based on

a different set of samples prepared for small-angle neutron scattering experiments (unpublished), and were similar to the leaflet compositions of the samples examined with NMR in the present work (Table F1). At the end of the simulations, the thickness of each leaflet at the gA-lipid boundary was analyzed and used to calculate the optimal thickness deformation profile around gA using the CTMD formalism, as described in Methods and Section F.3 in Appendix F. Since the energy of membrane deformation varies with the square of the hydrophobic mismatch (see Eq. F3 in Appendix F), Fig. 8.6A shows the resulting average squared deviations in thickness as a function of distance from the gA center in both systems. While the amount of membrane deformation decreases gradually further away from the protein in the two bilayers, it is less in the asymmetric membrane, indicating that gA is able to adapt more easily to the asymmetric bilayer environment.

To examine whether membrane deformation plays a role in the ability of gramicidin to scramble lipids, we approximated the packing density of gA dimers within the experimentally prepared LUVs. In particular, we estimated the distance between the channels at each gA mole fraction by assuming that they are uniformly distributed on the surface of the vesicles (see Methods). The dashed lines on Fig. 8.6A indicate the respective half distances between the gA centers. The compositionally symmetric sample with gA at gA:lipid ratio of 1:40 in which the rate of lipid flip-flop was highest (Table 8.2) also seemed to have the largest membrane deformation among the examined asymmetric proteoliposomes. Fig. 8.6B shows the relationship between the measured rates of lipid flip-flop in the four gA-aLUVs and the corresponding amounts of membrane deformation as quantified by the analysis in Fig. 8.6A. While the correlation between gA-mediated lipid scrambling and membrane deformation at gA mole fractions of 0.01 and higher is very strong (0.998), the sample with gA:lipid ratio of 1:200 did not follow the same relationship and appeared as an outlier (Fig.

8.6B). This result suggests that the stress induced in the membrane as a result of gA-membrane interactions is an important contributor to the observed effects of gA on lipid scrambling, and that at high mole fractions the channels accelerate lipid flip-flop in a mechanistically different way than at low gA concentrations.

8.5 Discussion

In the study of protein-membrane interactions, the effects of the membrane (e.g. its composition and structure) on protein function and oligomerization have been examined extensively. However, it is equally important to account for the protein effect on the membrane, because a protein embedded in a bilayer is prone to introduce defects that can perturb the bilayer structure and affect its transverse and lateral organization. We have, therefore, developed new protocols for the systematic investigation of protein-mediated changes in the lipid compositions of the two bilayer leaflets by utilizing model systems that allow for fine tuning of various membrane parameters. As discussed below, these protocols have been devised to exploit specific biophysical properties that bring to light specific elements of the complex interplay between the protein and the membrane, and to quantify the consequences.

8.5.1 Preparation and biophysical characterization of asymmetric proteoliposomes

Asymmetric membranes containing transmembrane (TM) proteins have been successfully prepared in the past. Two general types of approaches have been adopted. In one, the protein (either soluble or micelle-stabilized) is added externally to pre-formed asymmetric membranes including LUVs filled with sucrose [267], droplet interface bilayers [370] and planar supported bilayers [266]. In the other one, also employed here, the protein is first reconstituted into symmetric vesicles, then the outer leaflet of the vesicles is exchanged for specific lipids. For example, following the

latter approach Vitrac et al. prepared sonicated small unilamellar vesicles (SUVs) with the 12-transmembrane protein LacY from *E. coli* and examined the effect of asymmetric charge distribution on the topology of the protein [48, 299]. In a different study, asymmetric SUVs with the nicotinic acetylcholine receptor (AChR) were prepared by using MβCD-loaded lipid complexes to exchange the lipids on the outer leaflet of symmetric SUVs containing AChR, with sphingomyelin [265]. While these examples illustrate that a variety of TM proteins can be incorporated into asymmetric model membranes of different geometries, the effect of the protein (and protein incorporation) on the lipid compositions of the two bilayer leaflets can vary and therefore has to be examined explicitly. With respect to this effect, the protocol and assays presented here constitute an advantageous platform for the biophysical characterization of the sample, much improved by utilizing large tensionless proteoliposomes free from either the potential effects of curvature, or the commonly found residues of organic solvents, or polymer cushion supports. Thus, we found only minimal effects of the preparation protocol on the incorporation, conformation and function of gramicidin (Figs. 8.1 and 8.2), but as these are likely to depend on the types of lipids in the vesicles their negligible magnitude cannot be taken for granted. Indeed, the energy cost of gA dimer formation increases with increasing bilayer thickness, meaning that the monomer-to-dimer equilibrium of gA is shifted towards the monomeric state [365, 371], and in such cases the gA monomers have been shown to more easily exchange between vesicles [372]. This could result in a loss of the protein during the CD-mediated lipid exchange between donor and acceptor vesicles. Furthermore, a preference of a gA monomer for the composition of one leaflet vs. another in the gA-aLUVs may require additional tests of the interleaflet gA localization and vesicle stability. The thermodynamic phase properties of the bilayer in the presence of gA (whether in dimeric or monomeric state), should also be

considered. For example, we found that gA broadens and slightly lowers the transition temperature of DMPCd54 (Fig. F3), but this effect is likely to depend on both the protein type and concentration in the membrane and may be different for other proteins. A gel environment could affect not only the protein dynamics but also the efficiency of lipid exchange during the aLUV preparation protocol (Chapter 5).

8.5.2 Rates of lipid flip-flop measured with NMR

The slow rate of spontaneous lipid flip-flop that we measured in the chemically symmetric vesicles in the absence of gA is consistent with previous reports [285, 350]. Interestingly, we found that the flip-flop kinetics in the compositionally asymmetric membranes were significantly faster (Fig. 8.5). Since both POPC and DMPC have phosphocholine headgroups, this increase is likely due to differences in the chain lengths of the lipids (16 and 18 carbons for POPC and 14 carbons for DMPC) and the corresponding leaflet thicknesses (Table F2). This explanation is consistent with results from small-angle neutron scattering experiments showing a faster flip-flop rate in DMPC LUVs compared to POPC LUVs [285], and the corresponding free energy for flip-flop in the two bilayers, quantified with MD simulations [373].

Our result for the gA-mediated half time of lipid translocation in the POPC liposomes ($t_{1/2} \approx 64$ h) is comparable to that obtained by Fattal and coworkers with the chain-labeled fluorescent lipid analog NBD-PC ($t_{1/2} > 96$ h) [350]. This similarity is curious in light of the different chemical structure of the acyl chains of NBD-PC relative to POPC and suggests that the nature of the lipid headgroup is the dominant factor in determining the flip-flop rate, in agreement with earlier experimental observations [281]. Chain structure has also been shown to strongly affect flip-flop for lipids with multiple double bonds [374]. In contrast, the reported kinetics of lipid translocation in the presence of gA in erythrocytes [359] and

supported lipid bilayers [360] are much faster, likely due to the specific experimental conditions in the studies as discussed in the Introduction.

The lipid flip-flop rates accessible to NMR measurements are limited by the time needed to perform a single shift experiment. Depending on the type of instrument (i.e. the strength of the magnet) and sample concentration, one measurement in the absence of shift reagent, followed by 3 Pr^{3+} titrations (needed to obtain error bars, for example) could take anywhere from 15 min to 1 hour. Thus this technique can be used to measure only slower time-dependent translocation processes. However, since lipid flip-flop is a thermodynamic event and increases at higher temperatures, different samples with expected faster rates can still be compared if incubated at lower temperatures. The samples in this study were incubated on the benchtop at an ambient temperature of ~ 22°C.

8.5.3 Mechanisms of gA-induced lipid scrambling

It has previously been proposed that the ability of gA to scramble lipid analogs is not due to bilayer perturbations induced by individual gA channels because [358, 359]: 1) gA increases the translocation rate of lysophosphatidylcholine only at concentrations much higher than those where gA performed its normal function as a conducting channel, but where gA produces non-specific solute leakage; and 2) formylation of gA's tryptophan residues, which prevents formation of gA clusters, abolished the gA-catalyzed lyso-lipid scrambling. Instead, it was proposed that gA at gA:lipid mole fractions of 1:2000 or higher forms some sort of aggregate(s) in the erythrocyte membrane, which may be intermediates for the formation of hexagonal phases. The proposed clusters would induce transient defects in the bilayer with subsequent formation of aqueous leaks that allow for the passage of molecules as large as choline and sucrose across the cell membrane, as well as the translocation of lipid

analogs [359]. The proposed formation of gA clusters would depend on channel-bilayer hydrophobic mismatch because gA did not cause detectable aggregates in DMPC bilayers, where there is minimal channel-bilayer hydrophobic mismatch [368] and little accumulation of stress in the membrane. Though we cannot exclude the existence of gA aggregates in our samples, their presence is unlikely [368, 375] and the lamellar SAXS form factors (Fig. 8.1A) definitively exclude the presence of non-lamellar phases shown to form at high gA concentrations under different experimental conditions [354]. Our NMR and computational analysis further illuminate the importance of the frustration energy in the bilayer: At high channel densities, the bilayer thickness is not able to relax to its unperturbed state between the channels (Fig. 8.6), leading to bilayer-deformation-induced stress. This stress would increase the probability of transient clusters of bilayer-spanning gA channels, e.g. [376, 377], which could serve to decrease the energy barrier for lipid translocation and thereby increase the lipid flip-flop rate [378]. The deviation of the gA-aLUVs at gA:lipid ratio of 1:200 from the other samples in Fig. 8.6B further suggests that at this lower gA mole fraction the role of the frustration energy is different, resulting in a mechanistically distinct route for the observed gA effect.

8.6 Conclusion

Application of the new methodology and protocols developed for preparing and characterizing asymmetric proteoliposomes to the system of gramicidin channels, revealed the ability of gA to accelerate inter-leaflet lipid translocation in both chemically symmetric and asymmetric membranes. The mechanistic details illuminated by the work show the mode in which the channel-induced bilayer deformation contributes to the rate of lipid flip-flop. The ability to characterize and quantify the interplay between transmembrane proteins and their solvating lipid

environment allows us to determine the properties of the protein-laden bilayers. If such properties are considered properly, e.g., with the type of methodology illustrated here, the mechanistic understanding of much more complex biomimetic systems becomes feasible and practical.

CHAPTER 9
CONCLUSION

Lipid membranes are ubiquitous molecular assemblies. Once considered to be featureless barriers between the cell interior and the external environment, they are now known to be indispensable players in a multitude of cellular processes. Our understanding of their complexity and functional diversity has evolved slowly over the years, hand in hand with the technological advancements in assaying biological systems. The growing appreciation for the different ways in which membranes contribute to cellular homeostasis has pushed forward the use of model systems for elucidating the properties of the heterogeneous lipid matrix and its interactions with other membrane-associated components. Together with the continuing development of experimental techniques, a large body of foundational knowledge has been created for the physicochemical properties of the different types of lipids found in natural membranes, including their mixing behavior and interactions with proteins in symmetric bilayers. The results presented in this thesis fill some of the gaps in this foundational knowledge database and establish the means for expanding a new subsection of it that is focused on membrane asymmetry. The contributions to the field of membrane research in this work can be summarized as follows.

In Chapter 2, we provided evidence that a low-melting non-hybrid lipid (one with two identical fully saturated chains) has the same effect on domain size and morphology as a hybrid lipid (i.e., having one saturated and one unsaturated chain), thus refuting a previously hypothesized special role for hybrid lipids in controlling raft size, and helping steer research efforts in more fruitful directions. For example, our results suggest that theoretical work should not focus on the supposed "line activity" of hybrid lipids (e.g., a proposed orientational alignment of these lipids at domain

boundaries), but rather on the differential effects these lipids have on the bulk structural and mechanical properties of the coexisting phases.

In Chapter 3, we established robust computational methodologies for calculating the bending rigidity and area compressibility moduli of lipid bilayers and their leaflets from MD simulations. This work has a number of important implications: 1) the thorough characterization of the mechanical properties of single and multi-component symmetric bilayers, which is becoming increasingly easier with advances in computational resources, provides a basis for evaluating their role in various experimental observations such as changes in domain size and vesicle morphology; 2) the complete set of results from the simulated bilayers (most of which cannot be investigated in vitro due to practical limitations) enabled analysis that helps resolve discrepancies in the field regarding the definition of the tilt modulus and mechanical thickness of the bilayer; 3) the new method for calculating area compressibility makes possible the construction of tension-free asymmetric bilayers for MD simulations, and the analysis of their mechanical properties as well as the elastic energy of interleaflet mixing; 4) in both methodologies, the ability to resolve properties of individual leaflets enables the calculation of the free energy of protein-induced membrane deformation in both symmetric and asymmetric bilayers in a self-consistent manner (i.e. without having to rely on the availability of experimental data for the particular system of interest).

The uncovered general mechanism by which cholesterol mediates the electrostatic interaction of the Rous Sarcoma Virus matrix protein with bilayers, described in Chapter 4, reveals an important and previously unconsidered role of this ubiquitous membrane component in the binding of peripheral proteins to membranes. This result has implications for both the design and interpretation of in vitro studies, and for the

potential regulation of protein binding to the inner leaflet of the cell plasma membrane through changes in the local lipid composition.

The novel protocols for the preparation of asymmetric large unilamellar vesicles (Chapter 5) and tension-free asymmetric bilayers for MD simulations (Chapter 6) provide much needed tools for advancing the investigation of the functional implications of membrane asymmetry. Hypotheses about its mechanistic roles in cellular processes (e.g. binding of proteins and permeation of small molecules) can now be probed with both symmetric and asymmetric model systems. Together with the established experimental approaches for the robust characterization of the lipid composition and structure of the two bilayer leaflets, these protocols enable the validation of MD simulations, the exploration of interleaflet coupling and the mechanisms of leaflet-leaflet communication (Chapter 7), as well as the analysis of protein-membrane interactions in more physiologically relevant asymmetric bilayer environments (Chapter 8). Furthermore, the measurement of lipid flip-flop kinetics with nuclear magnetic resonance enables the study of the effects of various proteins and small molecules on the transverse bilayer organization.

The powerful combination of experimental and computational techniques that so far has been applied mostly in symmetric systems, relies on the continuing validation and refinement of the relevant computational representations and methodologies. As illustrated by the entire work in this thesis, such validation is now possible for asymmetric membranes and it is important to incorporate it in the design of any study by seeking principles and mechanistic insights from systems for which there is an experimental equivalent that can be appropriately interrogated.

Being relatively unexplored and hard to study, membrane asymmetry represents one example of a complex biological phenomenon that must be carefully and systematically investigated with a broad suite of techniques. For this reason, I had

selected bilayer systems that could be examined both with different experiments in vitro and with computational modeling, which enabled the robust determination of the effects of membrane asymmetry. The two types of approaches often nicely complement each other, for example when models for analyzing small-angle scattering data can be rigorously tested with simulated bilayers, or when MD simulations can explain experimental observations at the molecular level. It is important to note that both in vitro assays and computational (or theoretical) experiments have their strengths and weaknesses and can yield valuable information only if conducted appropriately with their respective controls. The more complex the problem, the more critical it is to approach it with multiple techniques and examine it from different angles. SANS and SAXS, ESR and NMR, MD simulations and other forms of theoretical modeling are all complementary biophysical tools that can be put to this task.

The utility of model membranes stems from their relative simplicity and amenability to biophysical characterization. We have learned much from them and continue to adapt them to new problems. However, in the quest for understanding membrane asymmetry in living cells, model membranes are only as useful to the extent that they capture the salient features of real plasma membranes. The widely cited results from the 1970s concerning the types of lipids found in the cytosolic and exoplasmic leaflets of the PM are insufficient to support the continued move of the field forward. We have reached the point where, in order to formulate realistic hypotheses and make predictions about the role of asymmetry in cellular processes, we must gather more detailed information about the lipid composition (including the corresponding chain compositions) in the two PM leaflets. Glycolipids and plasmalogens are examples of relatively overlooked but ubiquitous membrane components that are likely to affect leaflet-leaflet communication. A related open

question with profound implications for interleaflet coupling is the distribution of cholesterol in the PM. Future research efforts are needed to address this careful compositional characterization first. The methods I developed, in combination with other experimental approaches focused on the same mechanisms, are able to then use this information to formulate and test hypotheses about the functional implications of membrane asymmetry.

Once assays are developed to robustly probe the composition of each PM leaflet at this level of detail, the next step is to examine the ways in which cells can dynamically regulate their membrane composition during the processes of interest. Lipid modification by enzymes, turning flippases and scramblases on and off, lipid sequestration by proteins or delivery of new lipid pools via vesicle fusion are all potential means of achieving dynamic compositional control. In combination with appropriate experiments with model membranes in vitro and in silico, these studies can help us begin to unravel the mystery surrounding the various physiological roles of membrane asymmetry.

APPENDIX A

Abbreviations:

BoDIPY-PC	2-(4,4-difluoro-5,7-dimethyl-4-bora-3a,4a-diaza-s-indacene-3-pentanoyl)-1-hexadecanoyl-*sn*-glycero-3-phosphocholine
C12:0-DiI	1,1′-didodecyl-3,3,3′,3′-tetramethylindocarbocyanine perchlorate
Chol	cholesterol
DHE	dehydroergosterol, ergosta-5,7,9(11),22-tetraen-3β-ol
DLPC	1,2-dilauroyl-*sn*-glycero-3-phosphocholine
DOPC	1,2-dioleoyl-*sn*-glycero-3-phosphocholine
DSC	differential scanning calorimetry
DSPC	1,2-distearoyl-*sn*-glycero-3-phosphocholine
DSPC-d70	1,2-distearoyl(d70)-*sn*-glycero-3-phosphocholine
FRET	Förster resonance energy transfer
GUV	giant unilamellar vesicle
Ld	liquid-disordered
Lo	liquid-ordered
LUV	large unilamellar vesicle
MLV	multilamellar vesicle
PLV	paucilamellar vesicle
REE	region of enhanced FRET efficiency
RRE	region of reduced FRET efficiency
RSE	rapid solvent exchange
SAE	sensitized acceptor emission
SANS	small-angle neutron scattering
SLD	neutron scattering length density
TLC	thin-layer chromatography
Vpp	volts peak-to-peak

Table A1. Sample compositions examined in this study.

Composition	Technique	Vesicle prep	χDSPC	χ(DLPC+DOPC)	χChol
A	Fluor. microscopy	GUV	0.5	0.3	0.2
B	Fluor. microscopy	GUV	0.45	0.3	0.25
C	Fluor. microscopy	GUV	0.35	0.4	0.25
D	SANS	LUV	0.39	0.39	0.22
E	SANS	LUV	0.325	0.325	0.35
F	FRET	PLV	0	0.905	0.095
G	FRET	PLV	0.685	0	0.315

Table A2. Microscopy data obtained in this study.

Composition	ρ	Counts (uniform/mod./macro)	Proportions (uniform/mod./macro)	St. Dev. (uniform/mod./macro)
A	0.1	214/1/0	0.955/0.005/0	0.005/0.005/0
A	0.15	293/273/2	0.516/0.481/0.004	0.021/0.021/0.002
A	0.2	58/93/0	0.384/0.616/0	0.040/0.040/0
A	0.25	34/274/12	0.106/0.856/0.038	0.017/0.020/0.011
A	0.3	7/92/107	0.034/0.447/0.519	0.013/0.035/0.035
A	0.35	4/8/111	0.033/0.065/0.902	0.016/0.022/0.027
A	0.355	2/12/147	0.012/0.075/0.913	0.009/0.021/0.022
A	0.4	0/73/39	0/0.652/0.348	0/0.045/0.045
B	0	40/0/0	1/0/0	N/A
B	0.1	59/0/0	1/0/0	N/A
B	0.15	94/34/0	0.734/0.266/0	0.039/0.039/0
B	0.2	26/29/114	0.154/0.172/0.675	0.028/0.029/0.036
B	0.25	24/22/133	0.134/0.123/0.743	0.025/0.025/0.033
B	0.3	10/21/55	0.116/0.244/0.640	0.035/0.046/0.052
B	0.35	21/37/130	0.112/0.197/0.691	0.023/0.029/0.034
B	0.4	69/108/43	0.314/0.491/0.195	0.031/0.034/0.027
C	0.1	35/0/0	1/0/0	N/A
C	0.15	32/0/0	1/0/0	N/A
C	0.2	120/0/0	1/0/0	N/A
C	0.25	172/18/6	0.878/0.092/0.031	0.023/0.021/0.012
C	0.3	59/60/13	0.447/0.455/0.098	0.043/0.043/0.026
C	0.35	44/50/66	0.275/0.313/0.413	0.035/0.037/0.039
C	0.4	5/12/138	0.032/0.077/0.890	0.014/0.021/0.025
C	0.45	0/8/58	0/0.121/0.879	0/0.040/0.040
C	0.5	1/2/90	0.011/0.022/0.968	0.011/0.015/0.018

Table A3. SANS data obtained in this study.

Composition	ρ	Pore diameter (nm)	ULV diameter (nm)	Rel. polydispersity	Domain diameter (nm)
D	0	50	65.2	0.21	18.7
D	0.1	50	60.9	0.23	22.6
D	0.25	50	59.9	0.23	26.5
E	0	50	67.7	0.20	---

Table A4. Comparison of results for hybrid and non-hybrid mixtures.

	Modulated phases in GUVs		Domain diameter (nm) in LUVs				
	DSPC/Chol	ρ	DSPC/Chol	ρ=0	ρ=0.1	ρ=0.2	ρ=0.25
Hybrid[a]	0.375/0.225	0.15-0.40[c]	0.39/0.22	13.6[d]	17[d]	24.8[d]	--
Non-hybrid[b]	0.35/0.25	0.20-0.40	0.39/0.22	18.7	22.6	--	26.5

[a]DSPC/(POPC+DOPC)/Cholesterol. [b]DSPC/(DLPC+DOPC)/Cholesterol. [c]Taken from ref [94]. [d]Taken from ref [8].

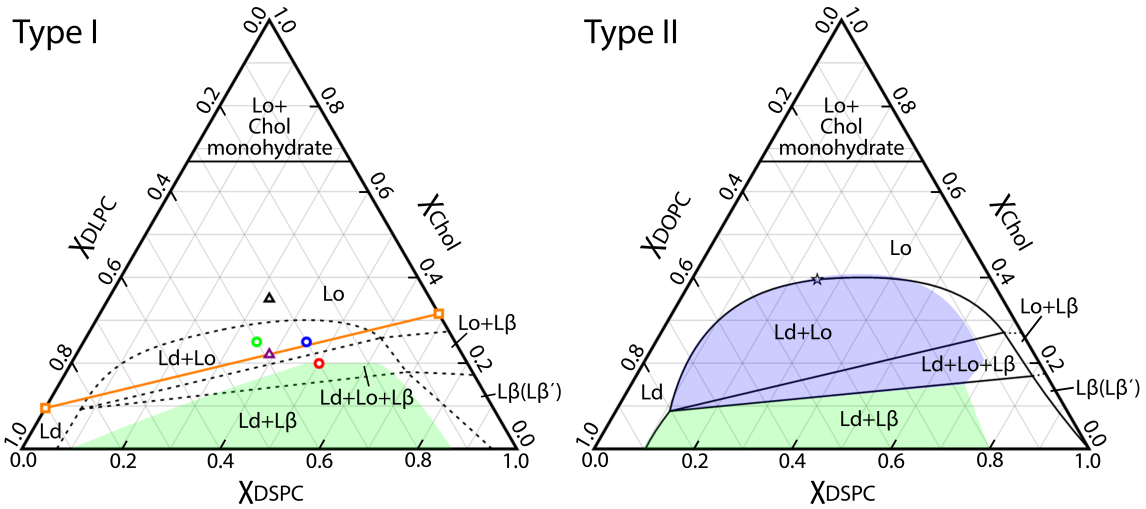

Figure A1. Room temperature phase diagrams for multicomponent lipid bilayer mixtures examined in this study. Phase diagrams for DSPC/DLPC/Chol and DSPC/DOPC/Chol [77] are respectively classified as Type I or Type II [75] to indicate the number of microscopic phase coexistence regions (shaded green and blue areas), where micron-sized domains are visible with fluorescence microscopy [77, 79]. Compositions examined in this study include: A, B and C (red, blue and green circles, respectively), with fluorescence microscopy; D and E (purple and black triangles, respectively), with SANS; and a sample trajectory (orange line) prepared from endpoints F and G (orange squares), with FRET. All sample compositions are listed in Table A1. Dashed phase boundaries for DSPC/DLPC/Chol are based on DSC [379] and fluorescence spectroscopic data, and are considered tentative.

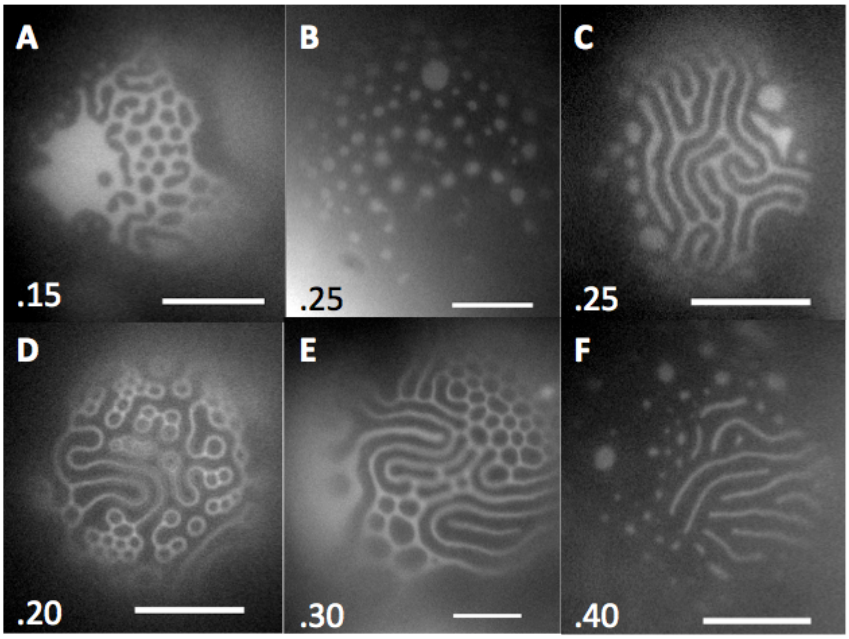

Figure A2. Fluorescence micrographs of GUVs show modulated phase patterns in the non-hybrid lipid mixture DSPC/(DLPC+DOPC)/Chol. When liquid phases coexist, the fluorescent dye C12:0-DiI partitions strongly into the Ld phase (bright regions) and is excluded from Lo phase. Images were taken at sample compositions A (upper panel, *A-C*) and B (lower panel, *D-F*) as listed in Table A1. Corresponding ρ values are indicated in the lower left corner of each image. Temperature 23 ºC; scale bar 10 μm.

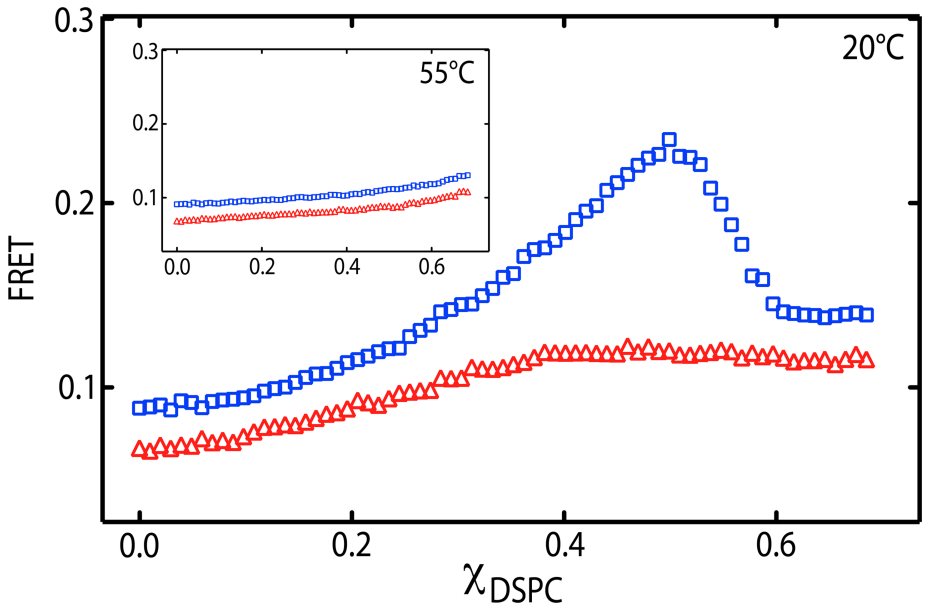

Figure A3. FRET reveals nanodomain formation in a non-hybrid lipid mixture. Sensitized acceptor emission is plotted *vs.* DSPC mole fraction for a sample trajectory composed of DSPC/(DLPC+DOPC)/Chol, at ρ = 0 (red triangles) and 0.25 (blue squares). Plots are offset by 0.02 y-units for clarity. Sample compositions are shown in Fig. A1 (orange line), and follow the approximate direction of tielines in the Ld+Lo region, passing through the SANS sample composition at DSPC/(DLPC+DOPC)/ Chol = 0.39/0.39/0.22. FRET efficiency is enhanced in phase coexistence regions where BoDIPY-PC donor and C12:0-DiI acceptor partition into the same (Ld) phase, behavior that is clearly observed in both sample trajectories at 20 ºC. *Inset*: the same samples measured at 55 ºC, revealing gradual changes consistent with uniform mixing.

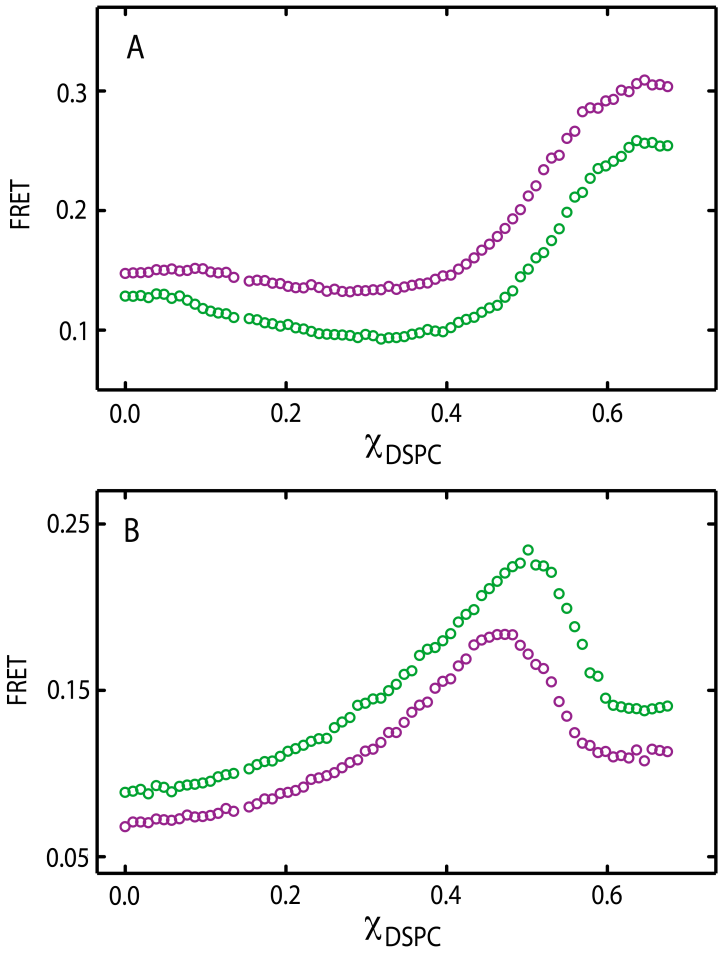

Figure A4. A comparison of FRET profiles between hybrid and non-hybrid lipid mixtures reveal similar trends in probe partitioning behavior. Sensitized acceptor emission is plotted *vs.* DSPC mole fraction for sample trajectories composed of DSPC/(POPC+DOPC)/Chol at 23 ºC for ρ = 0.20 (purple) and DSPC/(DLPC+DOPC)/Chol at 20 ºC for ρ = 0.25 (green). Plots are offset by 0.04 y-units (*A*) and 0.02 y-units (*B*) for clarity. Sample compositions follow the approximate direction of tielines in the Ld+Lo region of each mixture. (*A*) Regions of reduced FRET efficiencies are observed in both mixtures, where DHE donor and BoDIPY-PC acceptor partition into Lo and Ld phases, respectively. (*B*) Regions of enhanced FRET efficiencies are observed in both mixtures, where BoDIPY-PC donor and C12:0-DiI partition into the same (Ld) phase. Data for the DSPC/(POPC+DOPC)/Chol mixture taken from ref [380].

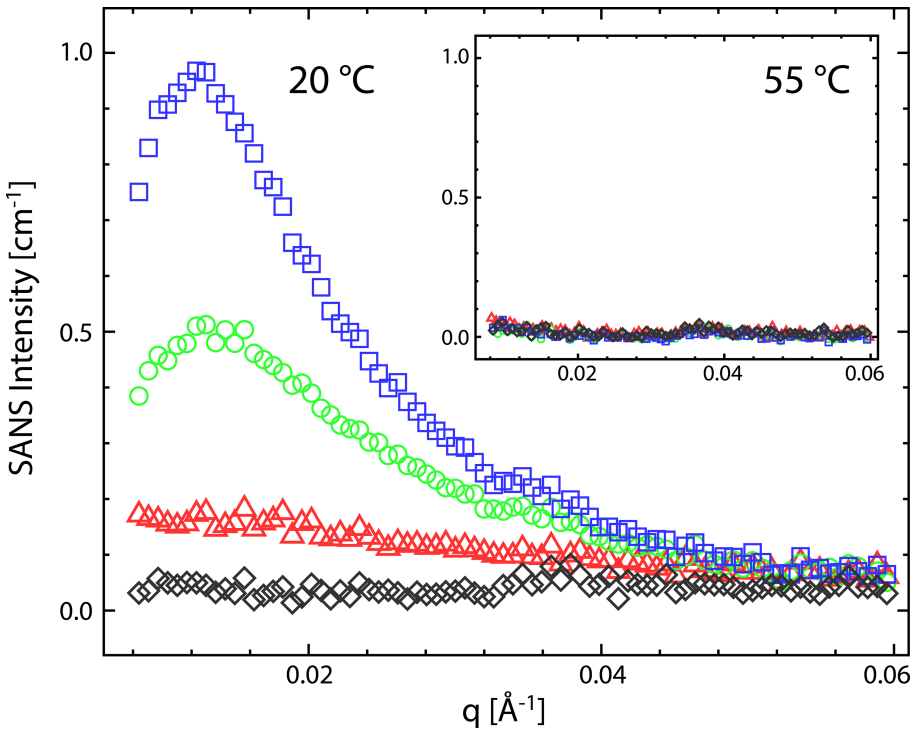

Figure A5. SANS reveals nanodomains in a non-hybrid lipid mixture. SANS intensity *vs.* momentum transfer vector q is shown for LUVs composed of DSPC/(DLPC+DOPC)/Chol = 0.39/0.39/0.22 at 20 ºC, for ρ = 0 (red triangles), 0.1 (green circles), and 0.25 (blue squares), and a single-phase control sample composed of DSPC/DLPC/Chol = 0.325/0.325/0.35 (black diamonds). *Inset*: the same samples measured at 55 ºC, revealing flat intensity consistent with uniform mixing. The small increase in scattering at $q < 0.02$ Å^{-1} seen in the 55 ºC data is likely the result of a small radial scattering length density contrast between the headgroup and acyl chain regions of the bilayer, while the small increase in scattering at $q \sim 0.035$ Å^{-1}, present in all curves, is an artifact from the data reduction software. Before fitting, these spurious contributions were corrected, as described in Section A1.3.

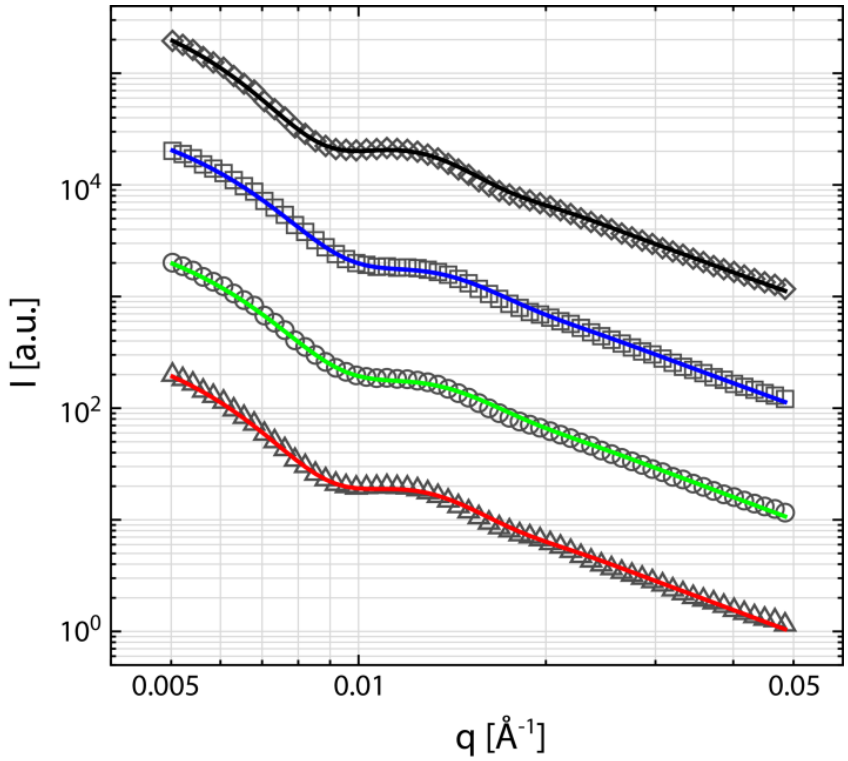

Figure A6. SANS data used to determine vesicle size and polydispersity. Shown are experimental SANS intensity I vs. momentum transfer vector q (symbols) and fits to the data (solid lines) for vesicles composed of: DSPC/(DLPC+DOPC)/Chol = 0.39/0.39/0.22 at 20 ºC, for ρ = 0 (triangles, red line), 0.1 (circles, green line), and 0.25 (squares, blue line); and DSPC/DLPC/Chol = 0.325/0.325/0.35 (diamonds, black line). Log-log curves are offset by powers of ten for clarity. Vesicle size and polydispersity were determined as described in Section A1.3; best-fit values are listed in Table A3.

A1. MATERIALS and METHODS

DSPC, DSPC-d70, DOPC, and DLPC were purchased as lyophilized powders or chloroform stocks from Avanti Polar Lipids (Alabaster, AL). Cholesterol was purchased from Nu Chek Prep (Elysian, MN). Stock solutions were prepared by dissolving lipid or cholesterol in HPLC-grade chloroform. Phospholipid purity of ≥ 99% was confirmed by TLC on washed, activated Adsorbosil TLC plates (Alltech, Deerfield, IL), developed with chloroform/methanol/water in a 65/25/4 ratio. Concentration of phospholipid stocks was determined to within 1% by inorganic phosphate assay [237]. Ultrapure H_2O was obtained from a Barnstead purification system (Dubuque, IA), and 99.8% D_2O was purchased from Alfa Aesar (Ward Hill, MA).

A1.1 Fluorescence microscopy

A1.1.1 Preparation of GUVs. GUVs were prepared using a modified version of the electroformation method [381]. Lipid films were swelled at 55 ºC in 100 mM sucrose in an AC field of 5 Hz (1 Vpp) for 2 h to form GUVs, then cooled to room temperature (23 ºC) over 12 h. The GUVs were then diluted into 100 mM glucose before imaging. The difference in solution density allows vesicles to settle more efficiently and also creates a sufficient refractive index difference to enable locating and focusing on GUVs without intense illumination [382].

A1.1.2 Image data collection. Wide-field microscopy was performed on a Nikon Diaphot-TMD (Micro Video Instruments Inc., Avon, MA and Rochester, NY) at 23 °C using a 60× 1.4 numerical aperture oil immersion objective. GUVs were labeled with C12:0-DiI at 0.02 mol%; the dye partitions preferentially into the Ld phase. To minimize light-induced artifacts, GUVs were located with transmitted light prior to exposure to the intense illumination needed for fluorescence imaging. Images were taken with a Photometrics (Tucson, Arizona) CoolSNAP HQ2 charge-coupled device camera. C12:0-DiI was imaged with 530-550 nm excitation and 565-610 nm emission. Images were contrast-enhanced and analyzed with NIS Elements Basic Research Software (MVI, Inc.).

A1.2 Förster resonance energy transfer (FRET)

A1.2.1 Preparation of PLVs. FRET samples were prepared as previously described [83], with the following modifications. Two series of samples (trajectories) were prepared at $\rho = 0$ and $\rho = 0.25$, each at ~ 1% compositional resolution along a presumed tieline within the Ld+Lo region of DSPC/(DLPC+DOPC)/Chol. Endpoint compositions of this tieline trajectory were (DLPC+DOPC)/Chol = 0.905/0.095 and DSPC/Chol = 0.685/0.315. FRET samples received fluorescent dyes in the following dye:lipid ratios: DHE, 1:100; BoDIPY-PC, 1:1500; and C12:0-DiI, 1:2000. Single-dye controls with the same dye:lipid ratios were prepared at ~ 10% compositional

resolution along the trajectory. For samples or controls containing 1% DHE (a cholesterol analog), cholesterol concentrations were reduced by 1%.

Paucilamellar vesicles (PLVs) in aqueous suspension were formed using the rapid solvent exchange (RSE) method [383], in order to avoid a dried lipid film state that may accelerate the precipitation of cholesterol crystals. Briefly, 0.500 mL of aqueous RSE buffer (5 mM PIPES, 200 mM KCl, 1 mM EDTA, pH 7.0) was added to lipid mixtures dissolved in < 0.1 mL chloroform. The sample was then subjected to vacuum for ~ 1 min while vortexing to remove the chloroform, resulting in the formation of fully hydrated bilayers containing one to a few lamellae. Samples were then ramped from 50 to 20 °C at 2 °C/h in a water bath, and held at 20 °C for at least 36 h before data collection.

A1.2.2 FRET data collection. Fluorescence data were collected on a F7000 spectrofluorimeter (Hitachi High Technologies America, Schaumburg, IL) equipped with a temperature-controlled cuvette holder (Quantum Northwest, Inc., Liberty Lake, WA). Prior to measurement, samples were diluted to 25 μM total phospholipid in the cuvette with RSE buffer, while applying gentle stirring. Fluorescence intensity was measured in 6 excitation/emission channels (λ, nm), using 5 nm bandpass for excitation and emission slits, and 2 s integration time: DHE fluorescence (327/393); BoDIPY-PC sensitized emission (327/517); BoDIPY-PC fluorescence (505/517); C12:0-DiI sensitized emission (505/565); C12:0-DiI fluorescence (549/565); and vesicle scattering (430/420).

A1.2.3 FRET data analysis. The characteristic profiles of steady-state probe-partitioning FRET (SP-FRET) have been used to determine phase coexistence regions for samples prepared along a trajectory in composition space [83, 384]. Abrupt changes in the lateral distribution of mixture components occurs at phase boundaries, resulting in changes in the energy transfer efficiency between fluorescent donor and acceptor lipids. For donor and acceptor that partition favorably into the same phase, a hill-shaped region of enhanced FRET efficiency (REE) is observed for samples located between phase boundaries, while a valley-shaped region of reduced FRET efficiency (RRE) is observed when donor and acceptor prefer different phases. We utilized two sensitized acceptor emission (SAE) channels for comparing SP-FRET along tieline trajectories. SAE channels contain non-FRET contributions from vesicle scattering, as well as direct donor and acceptor fluorescence emission; these spurious contributions were corrected using control samples [83]. Furthermore, an internal normalization that corrects for some sample-to-sample variation (*e.g.*, small concentration errors due to liquid transfers and differences in applied vacuum) was applied:

$$FRET = \frac{F_{SAE}}{\sqrt{F_D \cdot F_A}}$$

where F_{SAE}, F_D and F_A are scattering-corrected intensities from the SAE, donor and acceptor channels, respectively. The corrected FRET signal is plotted in Figs. 2.3 and S3.

To determine the location of the Ld+Lo phase boundaries, we used the SP-FRET profile of DHE donor and BoDIPY-PC acceptor, which displayed an RRE (Fig. 2.3). The phase boundaries at the left and right end of the trajectory were determined using the segmental linear regression function in Prism (v5.0d, GraphPad Software Inc., San Diego, CA). The intersection point of two straight-line regions in the vicinity of a phase boundary was determined for the data collected at 20 °C (see Fig. 2.3).

A1.3 Small-angle neutron scattering (SANS)

A1.3.1 Preparation of LUVs. Large unilamellar vesicles (LUVs) were prepared by extrusion as follows. Lipid mixtures were prepared by transferring desired volumes of chloroform stock solutions to a glass culture tube with a syringe (Hamilton USA, Reno, NV). Chloroform was removed with an N_2 stream and gentle heating, followed by drying *in vacuo* for a minimum of 12 h. Dry lipid films were hydrated with an appropriate D_2O/H_2O mixture (see below) preheated to 50 °C, followed by vigorous vortexing to disperse the lipid. The resulting multilamellar vesicle (MLV) suspension was incubated at 50 °C for 1 hour, and then subjected to 5 freeze/thaw cycles between –80 and 50 °C to reduce the average number of lamellae and facilitate extrusion. LUVs were prepared with a hand-held miniextruder (Avanti Polar Lipids, Alabaster, AL), assembled with a 50 nm pore-diameter polycarbonate filter and heated to 50 °C. The suspension was passed through the filter a minimum of 31 times, in all cases using an odd number of passes to minimize contamination with unextruded starting material. Data was collected within 24 h of extrusion. Final sample concentrations were 10-15 mg/mL, which allows for sufficient water between vesicles to eliminate the interparticle structure factor, thereby simplifying data analysis.

We performed two different types of SANS experiments, designed to isolate either the lateral bilayer structure (for examining domain formation), or the transverse bilayer structure (for vesicle size determination). Interrogation of lateral structure requires the use of a chain-perdeuterated species to provide neutron scattering length density (SLD) contrast upon demixing of lipids. Here, the high-melting lipid component was composed of DSPC and DSPC-d70 in a 42/58 ratio, yielding an average SLD for the bilayer's acyl chain region that is simultaneously equal to (1) the SLD of the bilayer's headgroup region, and (2) the SLD of water composed of 34.6 volume percent D_2O. This simultaneous contrast matching minimizes scattering associated with transverse structure, and enhances scattering due to demixing of saturated and unsaturated lipids (*i.e.*, domain formation). To determine the vesicle size distribution for each sample, a 0.200 mL aliquot was diluted with 0.400 mL of D_2O for a final D_2O concentration of 78 volume percent, thereby providing a large SLD contrast between the water and bilayer, and enhancing the spherical vesicle form factor.

A1.3.2 SANS data collection. Neutron scattering experiments were performed at the CG-3 Bio-SANS instrument of the High Flux Isotope Reactor (HFIR), located at Oak Ridge National Laboratory (ORNL). LUV suspensions were loaded into 1 mm path-length quartz banjo cells (Hellma USA, Plainview, NY) and mounted in a temperature-controlled cell holder with ~ 1 °C accuracy. Sample-to-detector distances of 2.5 and 15.3 m, and 6 Å wavelength neutrons (FWHM 15%) were used to obtain the relevant momentum transfer vector, $q = 4\pi \sin(\theta)/\lambda$, where λ is the neutron wavelength and 2θ is the scattering angle relative to the incident beam. Scattered neutrons were collected with a two-dimensional (1 m × 1 m) ^{3}He position-sensitive detector with 192 × 256 pixels. The 2D data were reduced following standard procedures using MantidPlot (http://www.mantidproject.org/). During reduction, the measured scattering intensity was corrected for detector pixel sensitivity, dark current, sample transmission, and background scattering contributions from the water and empty cell. The one-dimensional scattering intensity $I(q)$ was obtained by radial averaging of the corrected 2D data.

A1.3.3 SANS data analysis. The average vesicle radius and polydispersity were determined using the method of separated form factors described previously [229]. Briefly, data from high-contrast LUVs (*i.e.*, LUVs in 78 volume percent D_2O, Fig. A6) were fit to a spherical shell form factor with a Schulz size distribution, using a standard three-shell model (headgroup/hydrocarbon/ headgroup) to represent the flat bilayer form factor.

Domain sizes were determined by fitting data from radially contrast-matched samples (*i.e.*, LUVs in 34.6 volume percent D_2O, Fig. A5). Prior to analysis, SANS curves were corrected for small, spurious scattering contributions seen most clearly in the 55 ºC data (Fig. A5). A small increase in scattering at $q < 0.02$ Å^{-1} is likely the result of a residual radial SLD contrast between the headgroup and acyl chain regions of the bilayer (*i.e.*, incomplete contrast matching), while the small increase in scattering at $q \sim 0.035$ Å^{-1}, present in all curves, is an artifact from the data reduction software. These temperature-independent contributions were eliminated by subtracting the 55 ºC data from the corresponding 20 ºC data. We also fit the uncorrected data and found no significant differences in the obtained domain sizes, compared to the corrected data.

Corrected SANS data were modeled with a Monte Carlo method previously described in detail [8]. Briefly, vesicles were approximated as spherical shells of radius R and thickness t corresponding to the hydrophobic thickness of the bilayer, with polydispersity assumed to follow a Schulz distribution [229]. The shell volume was further divided into N monodisperse, randomly placed, non-overlapping caps (domains), each subtending an angle 2α. For the compositions studied, these domains are considered to be Ld phase dispersed in a continuous Lo matrix; the composition and total area fraction of the domains were calculated from phase boundaries determined by FRET data (Section A1.2) and published lipid volumes [145]. With the size and location of domains specified, random points were generated within the shell

volume in proportion to the SLD contrasts of the phases using a rejection algorithm (*i.e.*, points were uniformly generated within the shell and tested for inclusion in a domain until both the Ld and Lo volumes accumulated the desired number of points). The SLD-contrast-weighted pair distance distribution *P(r)* for the vesicle was then calculated from the set of random points following Henderson [385], and the procedure was repeated for 10^5 vesicles to obtain an ensemble average. The scattering intensity is the Fourier transform of the averaged *P(r)*:

$$I(q) = \frac{1}{4\pi}\int P(r)\frac{\sin(qr)}{qr}\,dr$$

I(q) was smeared with the instrumental resolution function [386] and compared to experimental data using a standard χ^2 goodness-of-fit criterion, varying *N* until a best fit was achieved. The reported domain size is that corresponding to a Schulz distribution of vesicles, each containing *N* monodisperse domains, and therefore represents an average domain size consistent with the experimental data.

APPENDIX B

Table B1. Bilayer information for all simulated systems: number of lipids per leaflet (Lip/Leaf), temperature (Temp), salt concentration, trajectory length (both total and analyzed) and average area per lipid (APL). All bilayers were hydrated with at least 45 waters/lipid. Also shown are the standard errors for the area per lipid, calculated from consecutive time blocks of length determined by the effective number of uncorrelated data points [196].

Bilayer	Lip/Leaf	Temp [ºC]	Salt [mM]	Traj. Length [ns]		APL [Å^2]
				analysis	total	
DLPC◆	64	30		278	278	62.6 ± 0.1
DMPC◆	64	30	140	200	200	60.4 ± 0.1
DPPC◆	100	50		238	335	61.5 ± 0.1
DLiPC◆	100	25		245	278	70.1 ± 0.1
DOPC◆	100	25		517	523	68.2 ± 0.1
DOPC replica 1	100	25		269	275	68.1 ± 0.1
DOPC replica 2	100	25		267	274	68.1 ± 0.1
SOPC◆	100	25		464	490	63.8 ± 0.1
DEPC◆	100	25		680	680	64.4 ± 0.1
POPC◆ 1	208	25		520	520	64.4 ± 0.1
POPC◆ 2	100	25	140	183	226	64.3 ± 0.2
POPC 3	64	25		281	281	64.3 ± 0.1
POPC 4	64	30		293	293	64.7 ± 0.1
POPE◆	100	55		184	190	60.8 ± 0.1
DOPG◆	100	25	140	231	246	71.2 ± 0.1
TOCL◆	50	30	140	310	310	130.5 ± 0.2
PSM	100	55		235	324	56.3 ± 0.1
SAPE	100	37		563	928	63.6 ± 0.1
POPC/Chol 70/30	100	15		252	1157	45.1* ± 0.1
DOPC/Chol 90/10	100	25		336	336	62.3* ± 0.1
DOPC/Chol 80/20	100	25		350	350	56.9* ± 0.1
DOPC/Chol 70/30	100	15		329	676	50.8* ± 0.1
DOPC/Chol 60/40	100	25		179	465	47.1* ± 0.1
DOPC/Chol 50/50	100	15		859	948	43.8* ± 0.0
DPPC/Chol 80/20◆	100	25		124	683	40.8* ± 0.0
POPE/POPG 70/30◆	100	37		274	280	61.2 ± 0.1
POPC/POPS 70/30◆	70	20	50	175	191	60.9 ± 0.1
POPE/POPS 70/30◆	210	25		250	690	55.3 ± 0.1
DMPC/POPC 10/90	100	25		471	471	63.8 ± 0.1
DMPC/POPC 43/57	100	25		556	696	62.6 ± 0.1
DMPC/POPC 75/25	100	25		738	738	61.4 ± 0.1

◆ Bilayers taken from Ref [318].

* The given APLs include cholesterol.

Table B2. Information for all NPγT simulations. For each bilayer shown are the set of applied non-zero tensions (γ), the respective average areas per lipid (APL) and lengths of the last part of the trajectories used for analysis, as identified by the method from Ref. [196] (see Simulations analysis and method implementation section in Chapter 3.2).

Bilayer	γ [mN/m]	APL [Å^2]	Lengths of analyzed trajectories [ns]
DMPC	-5, 3, 5, 12	58.7, 61.0, 61.6, 63.2	168, 314, 100, 302
DPPC	-3, 5, 9	60.8, 62.8, 64.1	267, 239, 244
DLiPC	-3, 4, 8, 12	69.5, 71.0, 72.4, 73.9	172, 173, 180, 183
DOPC	-7, 7, 15	66.3, 70.2, 72.2	138, 144, 129
POPC	-5, 4, 8	62.8, 65.1, 66.8	91, 191, 234
POPE	-3, 3, 5, 9	60.1, 61.3, 61.9, 62.7	198, 196, 193, 168
PSM	-3, 3, 10	55.6, 56.7, 57.9	342, 221, 128

Table B3. Bilayers used for comparison with PBM (Fig. 4). Shown are the average phosphate-to-phosphate distance (t_{pp}), length of the double bond region approximated as described in the caption of Fig. B7 (t_{DB}), length of cholesterol's ring body (t_{Chol}), the difference between t_{pp} and $2t_{DB}$ (t_m^{DB}) or t_{pp} and $2t_{Chol}$ (t_m^{Ch}), the effective mechanical thickness of the bilayers (t_m^{eff}), and bilayer bending rigidity (κ_C) calculated from splay fluctuations [137-139]. Errors for all thicknesses shown in parenthesis are the standard deviations from consecutive time blocks of length determined by the effective number of samples [196]. Errors on κ_C were calculated as described in Ref. [137]. In the first column, DOPC/Chol, POPC/Chol and DPPC/Chol mixtures are denoted with 'DO', 'PO' and 'DP' respectively.

Bilayer	t_{pp} [Å]	t_{DB} [Å]	t_{Chol} [Å]	t_m^{DB} [Å]	t_m^{Ch} [Å]	t_m^{eff} [Å]	κ_C [k_BT]
DLPC	31.4 (0.4)					31.4 (0.4)	25.8 (0.6)◆
DMPC	35.9 (0.4)					35.9 (0.4)	34.7 (1.2)◆
DPPC	39.5 (0.4)					39.5 (0.4)	34.1 (1.1)◆
DLiPC	37.0 (0.3)	5.0 (0.1)		27.0 (0.4)		27.0 (0.4)	16.3 (0.3)◆
DOPC	38.5 (0.3)	6.8 (0.1)		24.9 (0.4)		24.9 (0.4)	18.3 (0.3)◆
SOPC	40.8 (0.4)	4.2 (0.1)		32.4 (0.4)		32.4 (0.4)	26.4 (0.7)◆
DEPC	40.3 (0.4)	4.0 (0.1)		32.3 (0.4)		32.3 (0.4)	24.2 (0.6)◆
POPC	38.9 (0.4)	4.1 (0.1)		30.7 (0.4)		30.7 (0.4)	24.3 (0.6)◆
PO 7:3	46.1 (0.3)	5.3 (0.1)	8.4 (0.1)	35.5 (0.4)	29.3 (0.4)	29.3 (0.4)	73.7 (1.3)
DO 9:1	39.9 (0.4)	7.1 (0.1)	7.9 (0.2)	25.7 (0.4)	24.1 (0.6)	25.7 (0.4)	22.5 (0.4)
DO 8:2	41.5 (0.4)	7.6 (0.1)	8.0 (0.1)	26.3 (0.4)	25.5 (0.4)	25.5 (0.4)	30.5 (0.6)
DO 7:3	43.4 (0.4)	8.2 (0.1)	8.2 (0.1)	27.0 (0.4)	27.0 (0.4)	27.0 (0.4)	41.6 (0.7)
DO 6:4	44.7 (0.3)	8.7 (0.1)	8.3 (0.1)	27.3 (0.4)	28.1 (0.4)	28.1 (0.4)	51.0 (0.6)
DO 5:5	45.3 (0.3)	9.0 (0.1)	8.4 (0.0)	27.3 (0.4)	28.5 (0.3)	28.5 (0.3)	70.1 (1.1)
DP 8:2	49.0 (0.2)		14.4 (0.1)*		20.2 (0.4)	20.2 (0.4)	142.1 (3.1)◆

◆ Taken from Ref [318].

* t_{Chol} includes both the ring (8.4 Å) and tail (6 Å) regions of cholesterol.

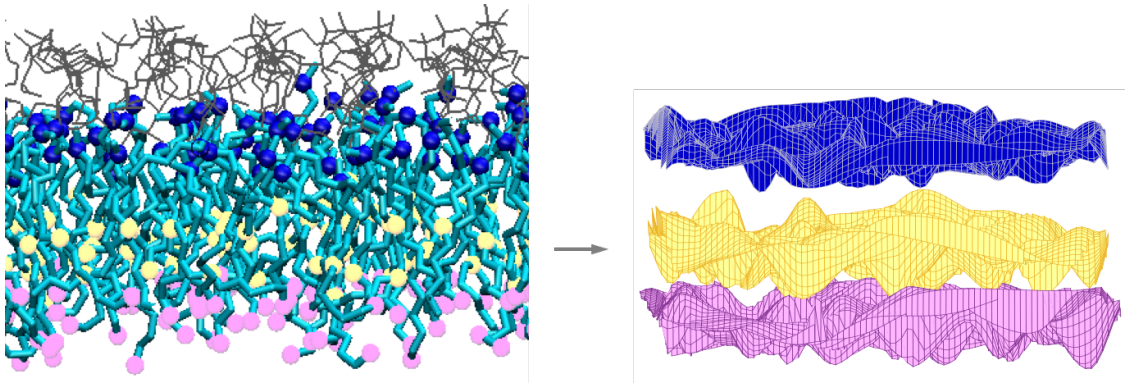

Figure B1. Transformation of a leaflet from an all-atom MD simulation trajectory frame into a set of surfaces. Left, a schematic representation of a DPPC leaflet. Lipid chains are shown in Licorice (cyan), the first carbons not attached to oxygen are shown as blue spheres, the 10th carbons (representing the surface for the relevant thickness fluctuations for this membrane, see Chapter 3.2) are shown as yellow spheres and the terminal methyl carbons are shown as pink spheres. The glycerol backbone atoms, phosphates and lipid headgroups are shown as grey lines. Right, three interpolated surfaces corresponding to the blue, yellow and pink spheres on the left.

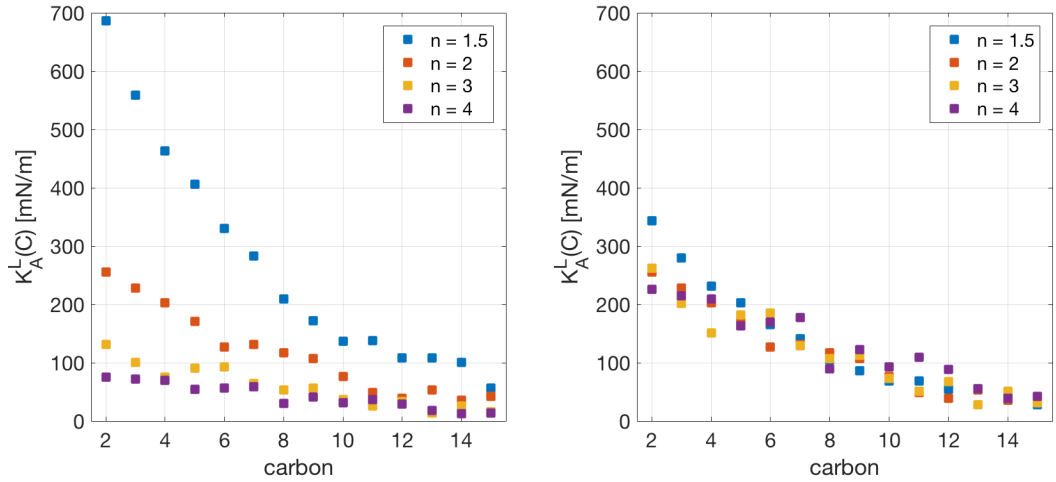

Figure B2. Effect of the interpolation order n on the calculated effective leaflet compressibilities (y-axis) at different carbon surfaces (x-axis) by setting a_0 to either A_{lip}^L (left) or $a_{0,n}$ (right). The data shown is for the top leaflet of a DOPC bilayer.

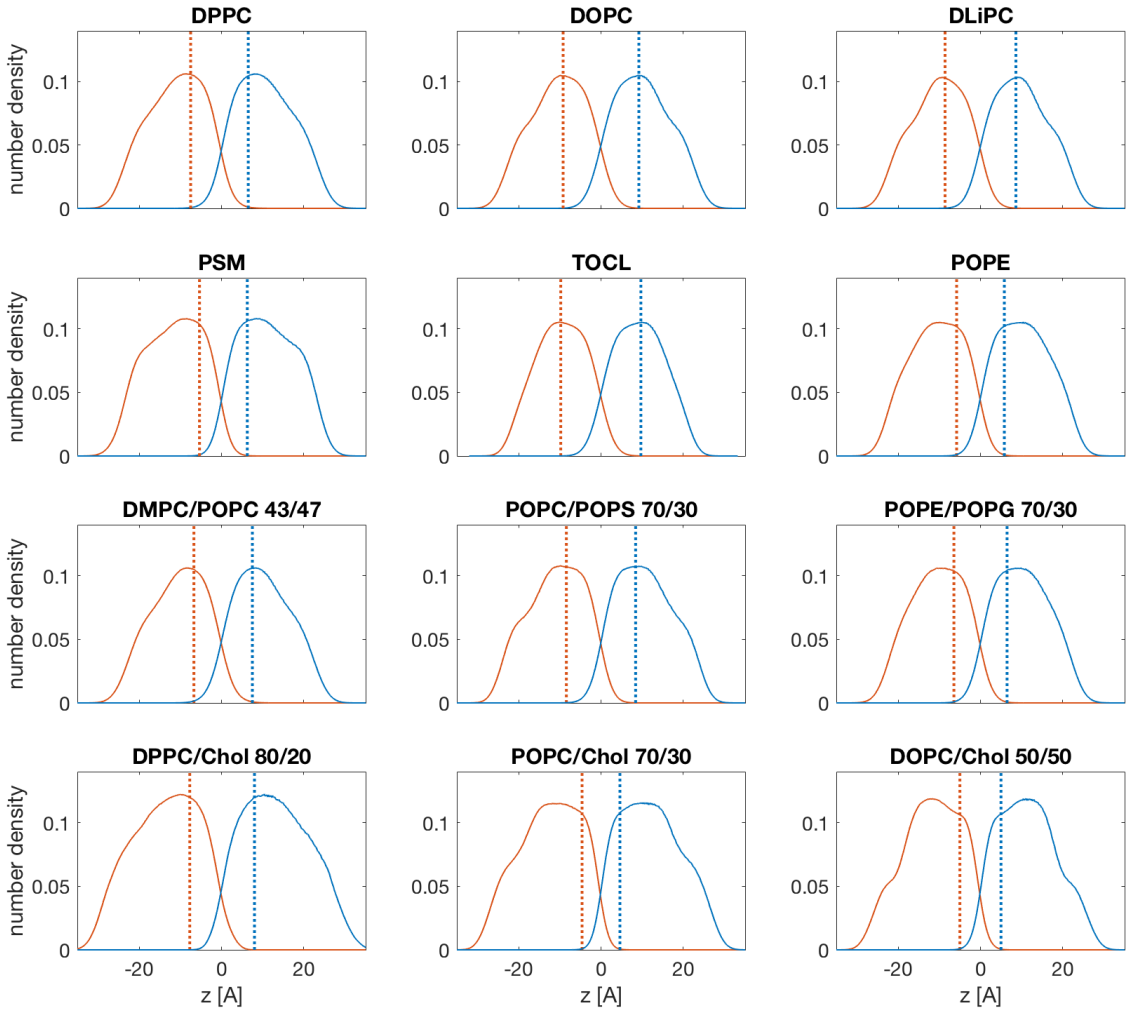

Figure B3. Identified leaflet thicknesses whose fluctuations are relevant for the calculation of the leaflet compressibility moduli for a set of representative bilayers from Tables 3.2.1-3.2.2. Shown are the number density profiles of the top (blue) and bottom (red) bilayer leaflets. The corresponding locations of the identified relevant leaflet thicknesses are shown as dotted lines.

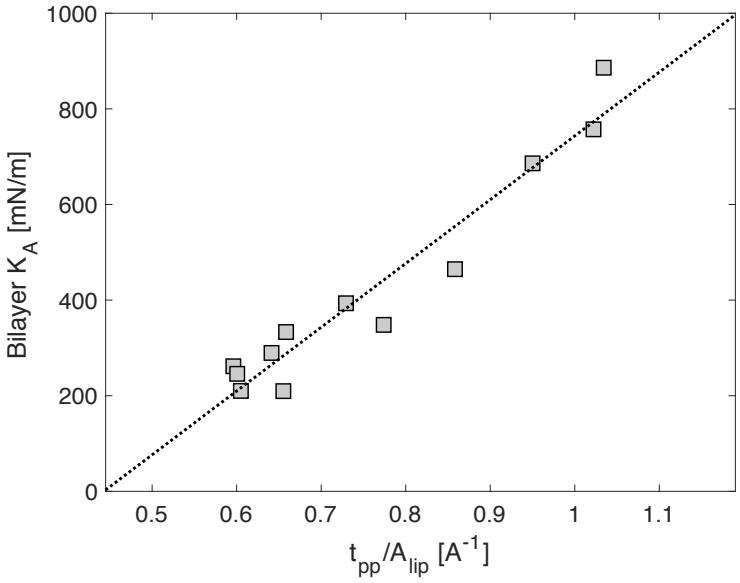

Figure B4. Bilayer area compressibility modulus K_A as a function of the ratio of bilayer thickness (phosphate-to-phosphate distance, t_{pp}) and average area per lipid (A_{lip}) for all fluid multi-component bilayers from Table 3.2.2, except for DPPC/Chol. The correlation between K_A and t_{pp}/A_{lip} is 0.965. The best linear fit to the data is shown as a dotted black line.

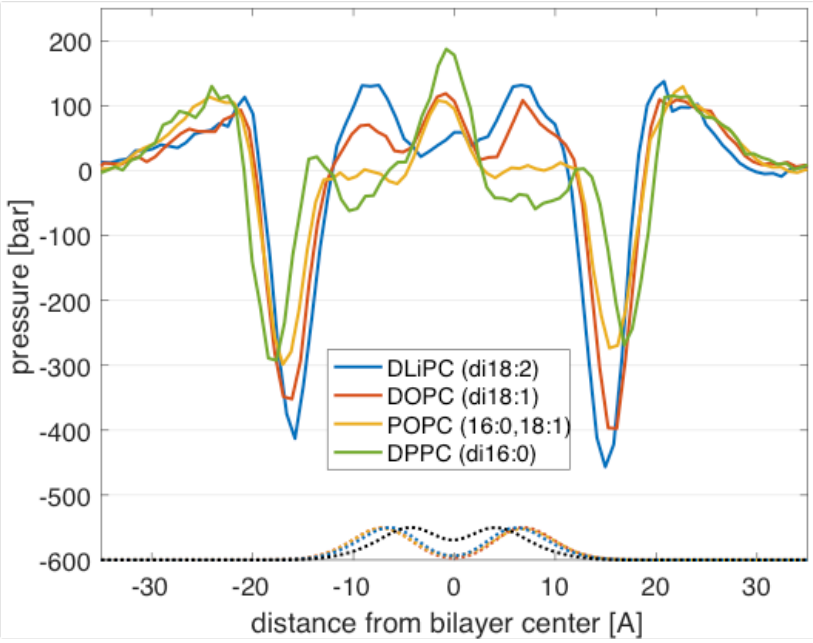

Figure B5. Lateral pressure profiles of bilayers with increasing level of unsaturation. All double bonds are between carbons 9-10, or 9-10 and 12-13 for DLiPC. An increase in pressure is observed with an increase in the number of double bonds (see text for more details). Also shown with correspondingly colored dotted lines are the rescaled and translated number density profiles of the double bonds at carbons 9-10 for all unsaturated bilayers. The number density of the second double bond at carbons 12-13 for DLiPC is shown in black. The pressure profiles have been smoothed for visualization purposes.

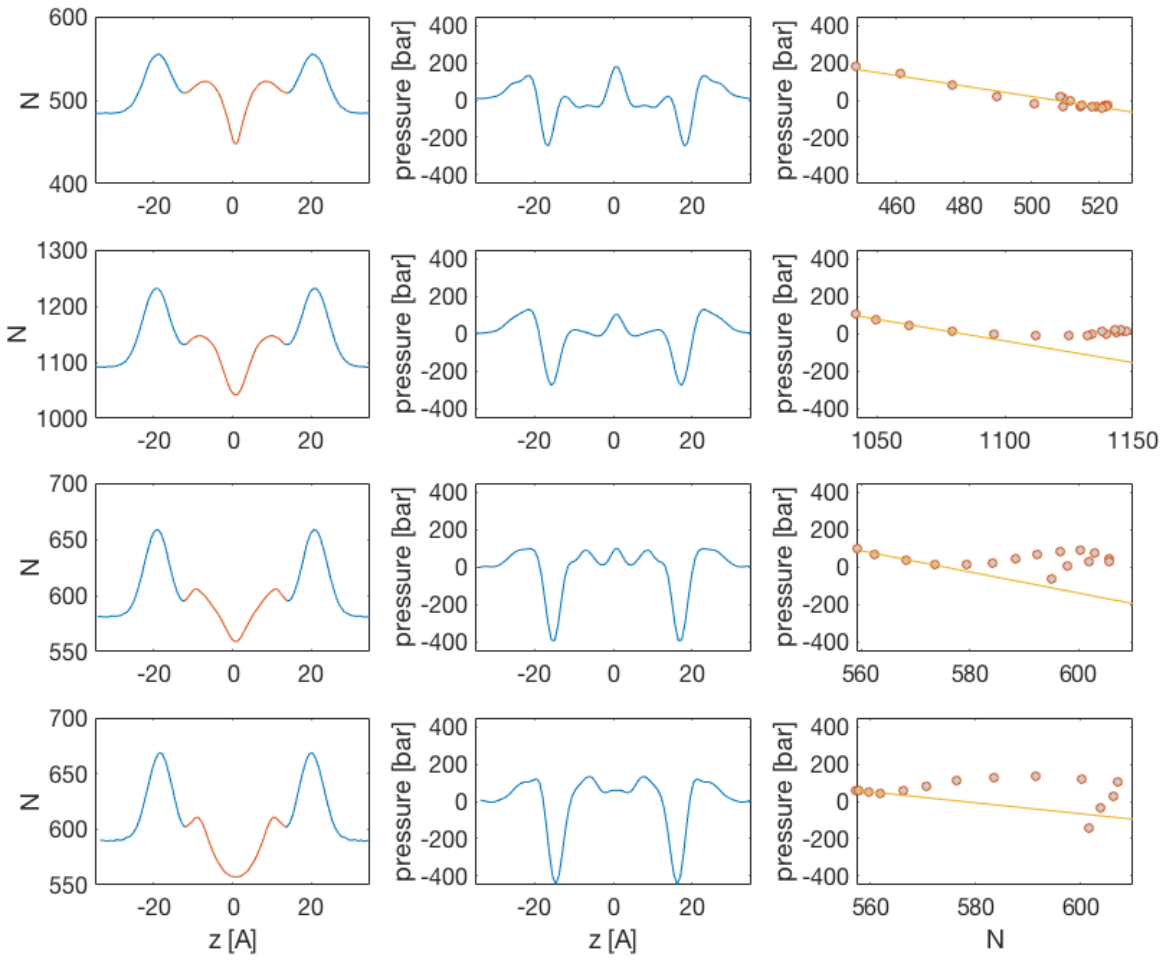

Figure B6. Total number of atoms N (first column) and lateral pressure p (second column) calculated from the same equal volume slabs along the bilayer normal for bilayer with increasing number of double bonds: DPPC (first row), POPC (second row), DOPC (third row) and DLiPC (fourth row). The third column shows the corresponding relationship between N and p in the region colored in red in the N vs z plots in the first column. A best-fit line through the left-most points on the plots in the third column (corresponding to the slabs around the bilayer midplane at z=0) is shown in yellow to guide the eye.

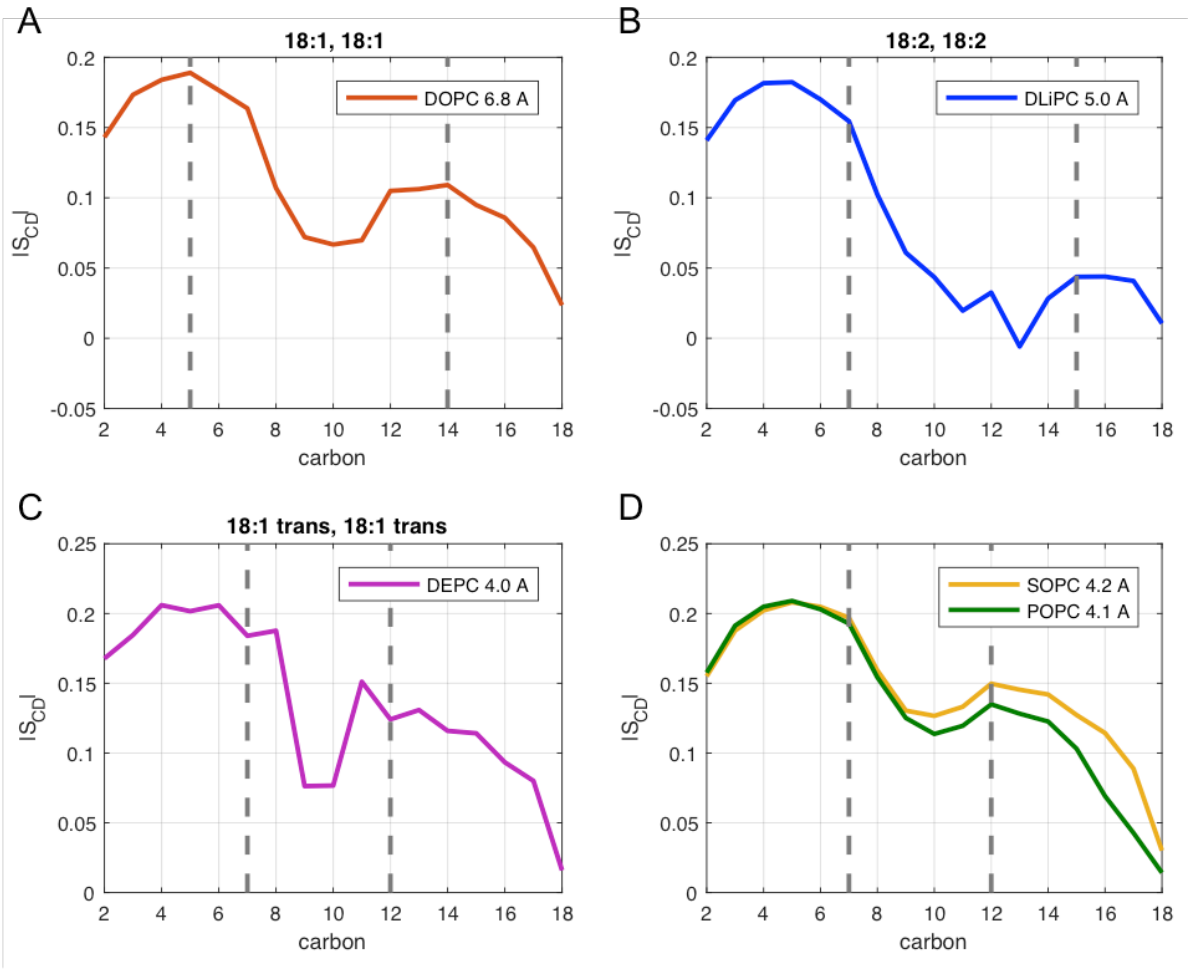

Figure B7. Heuristic approximation of the double bonds region (DB) in all unsaturated PC bilayers from Fig. 3.2.4. For lipids with two cis-unsaturated chains DB extends 4 carbons above and below the midpoint of all double bonds; for bilayers with one saturated chain or two trans-unsaturated chains DB extends 2 carbons above and below the midpoint of all double bonds. Shown are the acyl chain order parameter (S_{CD}) profiles of the bilayers. Each profile is averaged over the two acyl chains of the lipids. Dashed lines surround the approximated double bonds region.

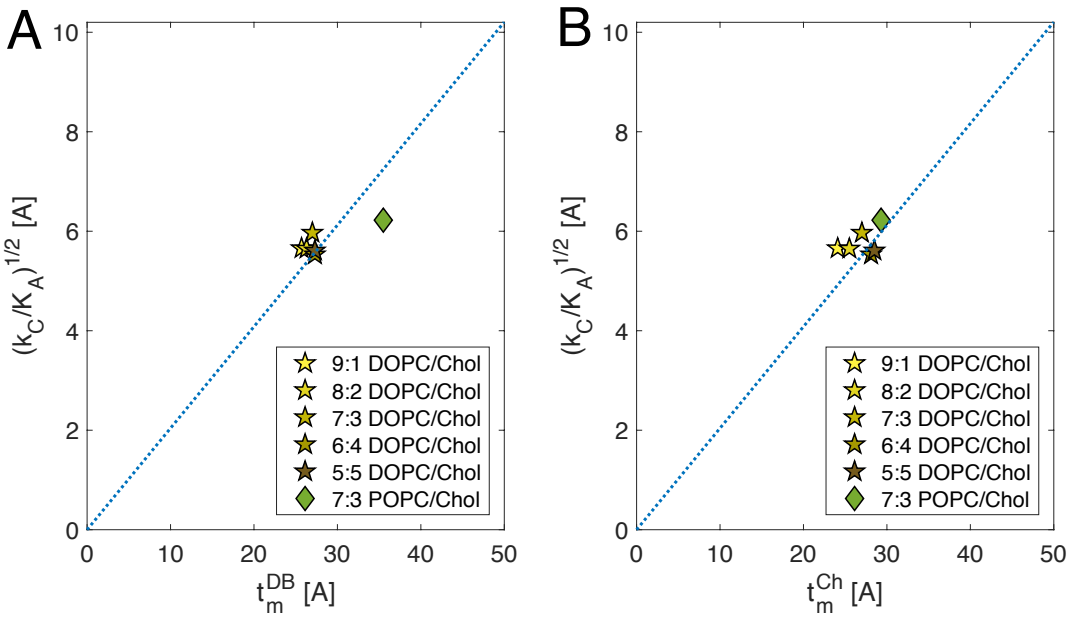

Figure B8. Polymer brush model (Eq. 3.2.17) applied to unsaturated bilayers with cholesterol using different definitions of t_m: the phosphate-to-phosphate distance excluding either (A) the perturbed region around the double bonds (t_m^{DB}), or (B) the length of Chol's ring body (t_m^{Ch}). See Table B3 for exact quantities and discussion in Chapter 3.2 for more details.

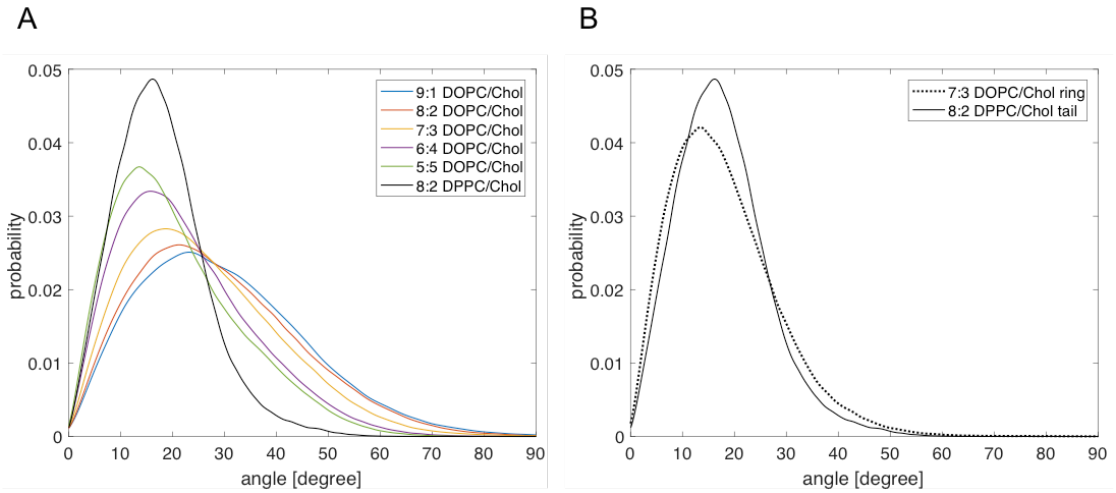

Figure B9. A, Distribution of tilt angles of cholesterol's tail (director vector connecting carbons 17 and 25 in CHARMM36 notation) with respect to bilayer normal (taken as the z dimension of the simulation box) for indicated cholesterol bilayers calculated from the simulation trajectories. The distribution of Chol's tail tilt angles for the DPPC/Chol bilayer is narrower than in the other bilayers and comparable to the distribution of Chol's ring tilt angles (B) (director vector connecting carbons 3 and 17 in CHARMM36 notation).

Method Sections

B.1 Inter-block correlations and extended theoretical model. In order to evaluate the magnitude of the Q term appearing in Eq. 3.2.8 in Chapter 3.2, we calculated the sum of the covariances of local areas in a leaflet, taking advantage of the relationship $\sigma^2(a_{xi}) = a_{x0}\sigma^2\left(\frac{a_{xi}-a_{x0}}{a_{x0}}\right)$. Since the relative changes in area can be expressed as characteristic changes in thickness (Eq. 3.2.11 in Chapter 3.2), $\sigma^2(a_{xi}) = a_{x0}\sigma^2\left(\frac{t_{x0}-t_{xi}}{t_{xi}}\right)$ where t is thickness. Following the same approach as the one outlined in Section 3.2.3.3, we calculated the characteristic changes in the *relevant* leaflet thickness (see "Identifying the relevant thickness for fluctuations analysis" in Section 3.2.3.3) on an 8x8 Å^2 grid in the leaflet. From that, we obtained the sum of the covariances of local areas as $\sum_{ij}\sigma^2(a_{xi}, a_{xj}) = a_{x0}\sum_{ij}\sigma^2\left(\frac{t_{x0}-t_{xi}}{t_{xi}}, \frac{t_{x0}-t_{xj}}{t_{xj}}\right)$. We then performed the 2D-bootstrapping algorithm outlined in Section B.7 to get the corresponding 95% confidence interval (CI). For three different bilayers representing very low (DPPC/Chol), medium (DPPC) and high (DOPC) fluidity, the 95% CI-s were [-0.002; 0.003], [-0.012; 0.018] and [-0.010; 0.014], respectively. Since all intervals contained 0, we can conclude that, empirically, the sum of the covariances of local areas within a leaflet is approximately 0 and consequently, $Q \approx 0$.

The derivation of Eq. 3.2.10 in the main text (in particular, the transition from Eq. 3.2.7 to Eq. 3.2.8) assumes that the two leaflets are composed of the same number of elastic blocks. Since the smallest physically meaningful average unit area of a block is the average area of a lipid, and in an asymmetric membrane the two leaflets may have different number of lipids, in the following we extend the formulation to allow for different number of blocks in the two leaflets. Let n_x and n_y be the number of blocks in the two leaflets such that $n_x \neq n_y$. Since all blocks within a leaflet have the same compressibility modulus, i.e. the same variance, Eq. 3.2.7 can be written as:

$$\sigma^2(A) = \frac{n_x\sigma^2(a_x) + n_y\sigma^2(a_y)}{2} + Q. \tag{B1}$$

Further, since $\sigma^2(a_x) = a_{x0}\sigma^2\left(\frac{a_x-a_{x0}}{a_{x0}}\right)$,

$$A_0\sigma^2\left(\frac{A-A_0}{A_0}\right) = \frac{a_{x0}n_x\sigma^2\left(\frac{a_x-a_{x0}}{a_{x0}}\right) + a_{y0}n_y\sigma^2\left(\frac{a_y-a_{y0}}{a_{y0}}\right)}{2} + Q. \tag{B2}$$

However, since $a_{x0}n_x = a_{y0}n_y = A_0$ and $\frac{a_x-a_{x0}}{a_{x0}} = \frac{n_xa_x-n_xa_{x0}}{n_xa_{x0}}$, Eq. B2 simplifies to:

$$A_0\sigma^2\left(\frac{A-A_0}{A_0}\right)=\frac{A_0\sigma^2\left(\frac{n_x a_x-A_0}{A_0}\right)+A_0\sigma^2\left(\frac{n_y a_y-A_0}{A_0}\right)}{2}+Q. \tag{B3}$$

Since $\sigma^2\left(\frac{A-A_0}{A_0}\right)=\frac{1}{K_A A_0}$, the above leads to:

$$\frac{1}{K_A}=\frac{1}{2}\left(\frac{1}{K_A^x}+\frac{1}{K_A^y}\right)+Q, \tag{B4}$$

which is the same expression as Eq. 3.2.8.

B.2 Two approaches for calculating K_A. As mentioned in the main text, K_A^L can be obtained either from the equipartition theorem (Eq. 3.2.12) or from statistical mechanics (Eq. 3.2.13). Eq. 3.2.12 relies on an accurate estimation of the mean of the squared characteristic changes in thickness $\langle(t^L-t_0^L)^2/(t^L)^2\rangle$. However, this calculation becomes problematic because of numerical issues. We illustrate the problem in Fig. B10 by using as an example the local relevant thicknesses calculated for the top leaflet of DPPC as discussed in the main text. Fig. B10A shows the distribution of the *relative* changes in thickness while Fig. B10B shows the corresponding distribution of *characteristic* changes in thickness. The latter is more skewed and has a long tail to the right (beyond the x-axis limits on the plot) coming from outliers, e.g. very small local thicknesses τ_{ς_s} that produce very large characteristic changes since τ_{ς_s} appears in the denominator. Once squared, the

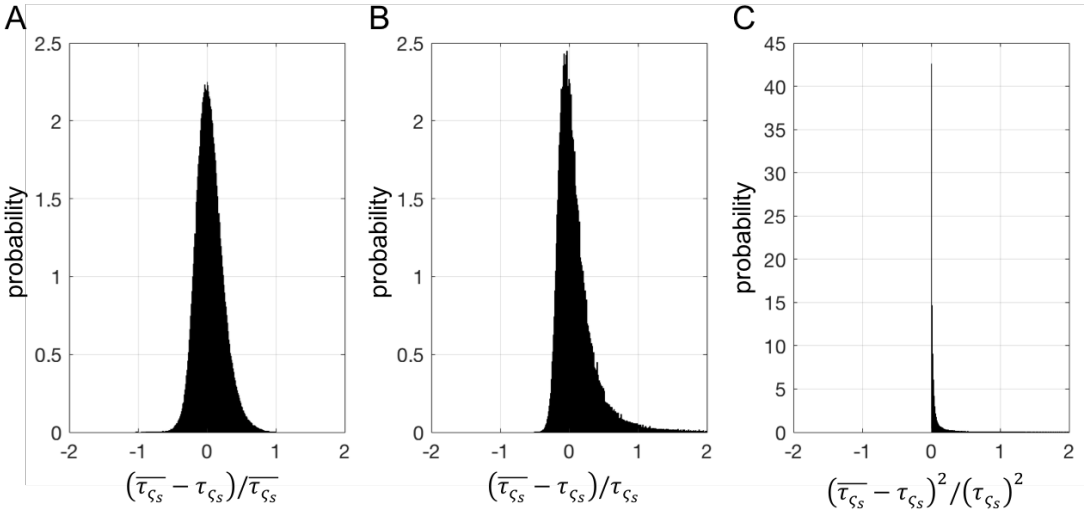

Figure B10. Probability density functions of different changes in relevant thickness for the top leaflet of DPPC: relative (A), characteristic (B) and squared characteristic (C) changes in thickness.

distribution becomes even more skewed and sensitive to outliers as illustrated in Fig. B10C (it again has a very long tail that is truncated in the figure). The accurate estimation of the mean from the distribution in Fig. B10C thus becomes challenging. Recognizing the fact that theoretically Eqs. 3.2.12-3.2.13 are valid only in the regime of small deformations around the mean thickness, and that $\langle (t^L - t_0^L)^2/(t^L)^2 \rangle = \langle |(t^L - t_0^L)/t^L| \rangle^2$, we calculated K_A^L from Eq. 3.2.12 by considering only t^L within some p percent of t_0^L. As can be seen in the examples in Fig. B11, the results depend strongly on p.

In contrast, obtaining K_A^L from Eq. 3.2.13 requires an accurate representation of the *non-squared* distribution within a small region around 0. Furthermore, Taylor expansion of the expression for the energy (Eq. 3.2.11) shows that the distributions of relative and characteristic changes in thickness are the same for thicknesses around the mean t_0^L, i.e.:

$$\text{For } t^L \sim t_0^L: \quad K_a^L a_0^L \left(\frac{t_0^L - t^L}{t^L} \right)^2 \sim K_a^L a_0^L \left(\frac{t_0^L - t^L}{t_0^L} \right)^2. \tag{B5}$$

This allows us to use the distribution of relative thicknesses (Fig. B10A) to obtain K_A^L without running into issues arising from outliers in the local thicknesses (note that small local thicknesses result in relative changes ~1 that do not affect the PMF analysis which is done on thicknesses with relative changes within the range -0.07 and 0.07).

B.3 Averaging lipid chains for different lipids and lipid mixtures. Eq. 3.2.15 can be applied directly to single component bilayers with lipids that have multiple chains of the same length such as DPPC, DOPC, DMPC, or TOCL (with the special treatment of double bonds as described in the text). For lipids that have different length chains we use the following algorithm. If N_1 and N_2 are the lengths of chains 1 and 2 of a two-tailed lipid (i.e. the number of carbon atoms in the chain after any averaging for the double bonds), and $N_1 < N_2$, then:

$$\text{For } \varsigma \le N_1, \qquad h_\varsigma = \frac{1}{2}\left(h_{\varsigma(1)} + h_{\varsigma(2)}\right) \tag{B6}$$

$$\text{For } \varsigma > N_1, \qquad h_\varsigma = \frac{1}{2}\left(h_{N_1(1)} + h_{\varsigma(2)}\right) \tag{B7}$$

In other words, for carbons 1 through N_1 we average the heights of the two chains. For carbons on chain 2 greater than N_1, we average the height of the carbon with the height of the terminal methyl carbon of chain 1.

For PSM, the first carbons not attached to oxygen on the two chains are C4S and C2F (using CHARMM36 atom name notation). Hence, both chains have the same length and their heights are averaged using Eq. 3.2.15.

For lipid mixtures, we do not perform the interpolation separately for the different lipid components but instead treat all of them the same way: Assuming that all lipids

have the same number of chains (e.g. 2 as in most cases), the height of the C carbon of

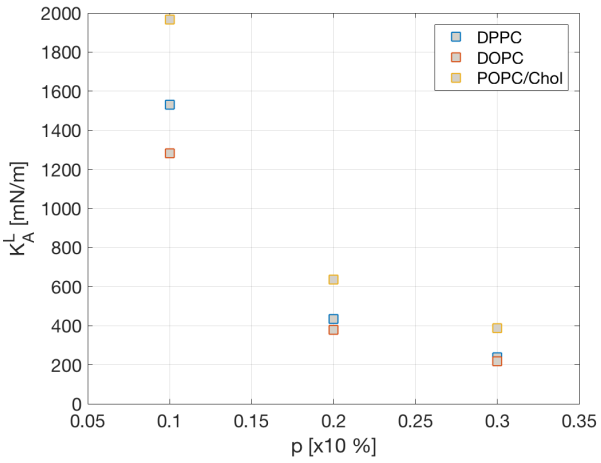

Figure B11. K_A^L calculated with Eq. 3.2.12 in the main text by using only thicknesses within p percent of the mean thickness t_0^L. Results are shown for the top leaflets of DPPC (blue), DOPC (red) and POPC/Chol (yellow) bilayers.

chain CH is calculated from the surface constructed from the C carbons of chain CH on all lipids in the leaflet. If chain CH of one of the lipids (lipid X) is shorter than the CH chains of the other lipids, for the interpolated surfaces of subsequent carbons further down the chain, we use the methyl carbon of the CH chain of lipid X. This ensures that the interpolated surface always contains exactly 1 atom from each lipid molecule irrespective of the lipid type. This leads to interpolated surfaces for the carbons of two chains (if one of the chains is unsaturated for all lipids in the mixture, we apply the same treatment to the double bonds as in the single component unsaturated bilayers) and we proceed with the averaging of their heights as described above.

If cholesterol is present in a leaflet, we exclude it from the calculation of the interpolated heights. That is, the interpolation is performed only on the non-cholesterol components. Therefore, in order to calculate K_a^L with Eq. 3.2.13 we need to find the average area per non-Chol molecules $a_{0(nonCh)}^L$. To this end, we use the simple model proposed by Alwarawrah et al. whereby the partial area of Chol, $a_{0(Ch)}^L$, is approximated from Chol's average tilt angle (Eq. 3.2.8 in Ref [201]). $a_{0(nonCh)}^L$ is then obtained from the relationship:

$$a_0^L = \chi_{nonCh} a_{0(nonCh)}^L + \chi_{Ch} a_{0(Ch)}^L \tag{B8}$$

where χ_{Ch} is Chol's mole fraction in the leaflet and $\chi_{nonCh} = 1 - \chi_{Ch}$ is the mole fraction of the non-Chol components. Note that the influence of cholesterol on the membrane compressibility is still considered in the formulation implicitly through its effect on the local thickness/area fluctuations of the membrane surface (see Simulations analysis and method implementation section in the text for more details, including a necessary correction applied for high mole fractions of Chol).

B.4 Determining the effective area of normalization. In Eq. 3.2.14, ς is unique for a lipid. The summations are performed over all lipids in the leaflet with the contribution of each lipid being weighted by $1/d_{iG(x,y)}^{n}$ and thus decreasing the further away the lipid's atom ς is from the grid point. Therefore, the *effective* area over which the surface heights h_{ς} and consequently, thicknesses τ_{ς}, are calculated depends on the interpolation order n: The higher the interpolation order, the more local the analysis, i.e. the higher the relative contribution of the atoms closest to the grid point. The effective area can thus be approximated by $a_0 \sim N_{\text{eff}} A_{lip}^{L}$ where A_{lip}^{L} is the equilibrium area per lipid in the leaflet, and $N_{\text{eff}} = \sum_{\varsigma} 1/d_{iG(x,y)}^{n}$ is the sum of all weights that represents the *effective* number of lipids contributing to $h_{\varsigma,G(x,y)}$. For example, if $n = 0$ then $N_{\text{eff}} = \sum_{\varsigma} 1/1 = N$ where N is the total number of lipids in the leaflet, and $a_0 = NA_{lip}^{L}$. Stated differently, with 0th order interpolation the heights at all grid points are the same and equal to the average z position across all atoms of type ς in the leaflet. For $n > 1$,

$$N_{\text{eff}} = \sum_{i} \frac{1}{d_{i,(x,y)}^{n}} \sim \int_{1}^{L_{\max}} \frac{1}{r^{n}} dr = \frac{(L_{\max})^{-n+1}}{-n+1} - \frac{1^{-n+1}}{-n+1} \approx \frac{1}{n-1} \qquad \text{(B9)}$$

where the second equality comes from the power rule, r is a variable of integration representative of distance, and $L_{\max} = \sqrt{(L_x/2)^2 + \left(L_y/2\right)^2}$ is the maximum 2D distance between two points on the leaflet surface, given periodic boundary conditions (L_x and L_y are the lateral dimensions of the simulation box). If $a_{0,n}$ denotes the *effective* area in the interpolation scheme with interpolation order n, then from Eq. B9 it follows that:

$$a_{0,1.5} = 2A_{lip}^{L} \qquad a_{0,2} = A_{lip}^{L} \qquad a_{0,3} = \frac{A_{lip}^{L}}{2} \qquad a_{0,4} = \frac{A_{lip}^{L}}{3} \qquad a_{0,5} = \frac{A_{lip}^{L}}{4} \qquad \ldots$$

Note that $n = 1$ is a special case where the integral in Eq. B9 can be approximated with $\ln L_{\max}$ and $a_{0,1} = \ln L_{\max} A_{lip}^{L}$. Fig. B2 shows a comparison between the *effective* compressibilities calculated with different n at different carbons. Since $a_{0,2}$ is equal to the equilibrium area per lipid, for convenience we choose $n = 2$ and perform all subsequent analysis using the equation:

$$h_{\varsigma,(x,y)} = \frac{\sum_i \frac{z_{\varsigma,i}}{d_{i,(x,y)}^{2}}}{\sum_i \frac{1}{d_{i,(x,y)}^{2}}} \qquad \text{(B10)}$$

B.5 Testing the volume incompressibility condition. The conversion from changes in area to changes in thickness in Eq. 3.2.11 of the main text relies on the assumption of volume incompressibility that enforces the preservation of the product of area and thickness. To check whether the interpolated thicknesses satisfy this condition, we use a simple algorithm. Since $NA_{lip}^{L}=\overline{L_x L_y}$ where N is the total number of lipids in the leaflet and the right-hand-side is the mean lateral area of the simulation box, the sum of the instantaneous areas of the lipids in a single frame of the trajectory should be equal to the instantaneous lateral dimensions of the box. We set $V = A_{lip}^{L}\overline{\tau_P}$ where $\overline{\tau_P}$ is the mean thickness of a leaflet (equivalently, of a lipid) at the level of the phosphate surface calculated with Eq. 3.2.16. If volume conservation holds, then the instantaneous area at a grid point G_i would be $a_{P,G_i} = V/\tau_{P,G_i}$ and in every frame of the trajectory the sum of the instantaneous areas of all grid points, normalized to the number of lipids, should equal the instantaneous lateral area of the box, i.e. $L_x L_y - \frac{N}{N_G}\sum_{i=1}^{N_G} V/\tau_{P,G_i} \approx 0$ where N_G is the number of grid points and the pre-factor N/N_G accounts for any difference between the number of lipids and the number of grid points. Fig. B12 shows the distribution of these differences for a few different bilayers. The distributions are centered very close to 0, indicating that volume incompressibility does indeed hold, and confirming the applicability of the interpolation scheme to the calculation of the leaflet's compressibility modulus.

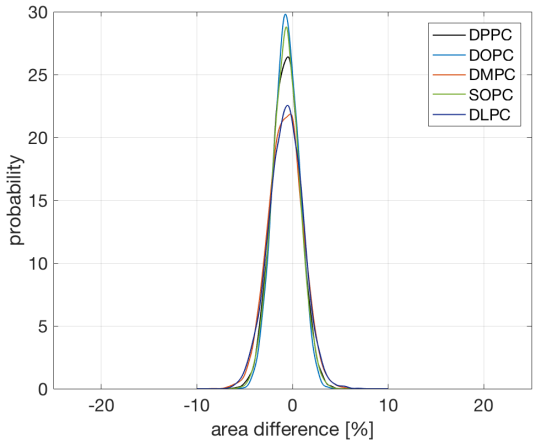

Figure B12. Probability distribution of the deviation of the instantaneous lateral box area from the area estimated from the interpolated thicknesses assuming that volume incompressibility holds, i.e. the product of average lipid area and average thickness (calculated at the level of the phosphate surface) is preserved locally. See Chapter 3.2 for details.

B.6 Calculating K_A^L from the relevant local thicknesses. Once the relevant thickness has been identified and the corresponding PMF is estimated (see Fig. 3.2.2B in the main text), we fit a quadratic function to the PMF in a small region around the mean thickness in order to recover K_A^L. As mentioned above (see Fig. B10 and Eq.BS5), for small thicknesses around the mean thickness the distributions of relative and characteristic changes are the same. For practical reasons (see above) we use the relative thickness changes for the PMF fitting. In particular, from the kernel density of the thicknesses (Fig. 3.2.2A), we estimate the PMF of the relative changes in thickness (similar to the left-hand-side of Eq. 3.2.13). To identify the region for fitting, we search within a small range of thicknesses between 5 and 7% of the mean thickness.

This range ensures that the analyzed thickness deformations are small enough to satisfy the theoretical requirements of the model (i.e. quadratic approximation of the energy), while at the same time providing sufficient sampling of the data, minimally affected by noise features in the underlying distribution. The full protocol goes as follows:

1. Estimate the thickness distribution with a kernel density estimation using the *ksdensity* function in MATLAB. The bandwidth, bw (i.e. smoothing parameter) of the kernel density is determined automatically based on the data. From the kernel density, find $\overline{\tau_{\zeta_s}}$ corresponding to the peak of the kernel distribution.
2. Use the kernel weights to estimate the probability distribution of the relative thickness changes, $P\left(\frac{t_0^L - t^L}{t_0^L}\right)$, and the corresponding PMF: $-\frac{k_B T}{a_0^L} \ln P\left(\frac{t_0^L - t^L}{t_0^L}\right)$.
3. Select a range of relative thickness changes (between 0.05 and 0.07), corresponding to changes in thickness within 5 to 7% of the mean thickness.
4. Sample from the estimated probability distribution within the thickness range (i.e. sample the relative thickness changes (raw data) within the selected range and add Gaussian noise to them with bandwidth equal to $\left(\overline{\tau_{\zeta_s}} - bw\right)/\overline{\tau_{\zeta_s}}$).
5. Construct a qqplot of the sampled data, i.e. compare the quantiles of the sampled distribution to those of a normal distribution. Calculate the fraction, $fracq$ of the sampled data quantilies that are within 0.01 of the normal distribution quantilies. The larger $fracq$, the closer the sampled distribution is to a normal distribution.
6. For each range (in step 3), repeat steps 4-5 ten times and find the mean $fracq$. The range with maximum mean $fracq$ (i.e. closest to a normal distribution) is the range that we choose for subsequent PMF fitting.
7. Fit a quadratic function of the form $f(x) = c_1 x^2 + c_2$ to the PMF in the identified region. K_A^L is the coefficient of the quadratic term (c_1) in the best fit.

B.7 Error on leaflet compressibility. The calculation of K_A^L from local changes in thickness is based on sampling both in time (N time points over the course of the trajectory) and space ($G_x G_y$ grid points across the two dimensional grid on the leaflet surface). However, there can be correlations both in time (slow motions leading to autocorrelation) and in space (local correlated motions due to interaction between atoms), and thus the effective number of independent observations of the leaflet thickness may be less than NG_xG_y. In order to account for these correlations in our estimate of the error on K_A^L, we use a 2-dimensional non-parametric moving block bootstrapping approach in which we resample blocks of data in both time and space. The procedure goes as follows:

1. We first find for each height h the median autocorrelation time ξ_h across all grid points. The largest ξ_h determines the number of consecutive time points, N_{SEG}, in a resampled time block.

2. We then find the maximum number of grid points G_{SEG}, such that $\sqrt{G_{SEG}} \leq \frac{1}{2} G_x$ and $\sqrt{G_{SEG}} \leq \frac{1}{2} G_y$.
3. We resample a block of $N_{SEG} G_{SEG}$ data points by picking a random point in time (T_p) between 1 and $N - N_{SEG}$, and space (S_p), and taking N_{SEG} consecutive frames starting from T_p and a square patch of G_{SEG} grid points with a top left corner at S_p (using periodic boundary conditions).
4. We repeat step 3 η times where $\eta = \max(N/(N_{SEG} G_{SEG}))$ is an integer, to construct a resampled data set D' with approximately the same size as the original data set, i.e. $\eta N_{SEG} G_{SEG} \approx N G_x G_y$. We calculate the compressibility modulus from D', i.e. $K_A^L(D')$.
5. We repeat step 4 one hundred times and obtain the error of K_A^L from the standard deviation of the set of $\{K_A^L(D')\}$ values.

APPENDIX C

DETAILED METHODS

SANS data analysis. SANS data were modeled with a heterogeneous core-shell (HCS) form factor [240] with modifications discussed here. This model is appropriate for describing scattering from a "patchy" spherical shell particle, such as a phase-separated or protein-bound unilamellar lipid bilayer vesicle, shown schematically in Fig. C2A. The coherent scattered intensity of such a particle contains three contributions:

$$I(q) = I_{hom}(q) + I_{intra}(q) + I_{inter}(q). \qquad (C1)$$

The first term in Eq. C1 accounts for the *homogeneous* contribution to the total scattering arising from structure normal to the plane of the bilayer. Differences in the atomic composition of lipid headgroups and chains generally results in different average neutron scattering length densities (NSLDs) for these layers, with the NSLD variation along the bilayer normal described quantitatively by a radial NSLD profile $\rho(r)$, where r is the radial distance from the center of a vesicle. In a phase-separated vesicle with two coexisting environments, the transverse structure from each phase contributes to the homogeneous scattering, which can be expressed as:

$$I_{hom}(q) = 4\pi\left[2\sqrt{\pi}M_0(q) + 2\sqrt{\pi}a_d W_0(q)\right]^2, \qquad (C2)$$

$$M_0(q) = \int_0^\infty [\rho_c(r) - \rho_s] r^2 j_0(qr) dr, \qquad (C3)$$

$$W_0(q) = \int_0^\infty [\rho_d(r) - \rho_c(r)] r^2 j_0(qr) dr. \qquad (C4)$$

Here, ρ_d, ρ_c, and ρ_s refer respectively to the NSLD of the domain phase, continuous phase, and surrounding aqueous solvent, a_d is the fraction of the vesicle surface area occupied by the domain phase, and j_0 is the zeroth order Bessel function. From Eqs. C2-4, it is clear that I_{hom} depends only on the radial (transverse) bilayer structure and relative amounts of the two phases, but not on the size or spatial organization of domains. The latter information is accounted for by the second and third terms in Eq. C1, I_{intra} and I_{inter}. Making use of a spherical harmonic expansion of the vesicle scattering amplitude, the intradomain scattering contribution is given by:

$$I_{intra}(q) = 4\pi N_d \sum_{l=1}^{\infty} \left|\widetilde{w}_l^0(\alpha_d)\right|^2 |W_l(q)|^2, \qquad (C5)$$

$$W_l(q) = \int_0^\infty [\rho_d(r) - \rho_c(r)] r^2 j_l(qr) dr, \qquad (C6)$$

$$\widetilde{w}_l^0(\alpha_d) = \frac{\sqrt{(2l+1)}}{2l}[\cos\alpha_d\, P_l(\cos\alpha_d) - P_{l+1}(\cos\alpha_d)], \qquad (C7)$$

where N_d is the number of domains, α_d is the angle formed by vectors pointing from the vesicle center to the domain center and edge, and P_l is the Legendre polynomial of degree l. Finally, the interdomain scattering arising from coherent interference between different domains is given by:

$$I_{inter}(q) = 4\pi \sum_{J\neq K} \sum_{l=1}^{\infty} \left|\widetilde{w}_l^0(\alpha_d)\right|^2 |W_l(q)|^2 P_l\left(\cos\theta_{JK}\right), \qquad (C8)$$

where θ_{JK} is the angle between the vesicle center and the centers of domains J and K. The effects of vesicle size polydispersity are included by averaging the monodisperse intensity $I(q,R)$ (i.e., Eqs. C1-8) over a Schulz distribution:

$$G(R) = \left(\frac{1}{R_m\sigma^2}\right)^{(1/\sigma^2)} \frac{R^{(1/\sigma^2-1)}}{\Gamma(1/\sigma^2)} exp\left[\frac{-R}{R_m\sigma^2}\right], \qquad (C9)$$

where R_m is the most probable vesicle radius, σ is the root mean square deviation from R_m, and Γ is the gamma function. The polydisperse intensity $I_P(q)$ is then given by:

$$I_P(q) = \int_0^{\infty} I(q,R)G(R)dR. \qquad (C10)$$

To summarize, the HCS model requires as input:

1. Radial SLD profiles for the domain and continuous phases, $\rho_d(r)$ and $\rho_c(r)$. Assuming that the radial bilayer structure does not depend on vesicle size R, then $\rho(r;R) = \rho(z+R)$ for all R, where $\rho_d(z)$ and $\rho_c(z)$ are transverse SLD profiles centered at $z = 0$. Diverse models for transverse SLD profiles can be found in the literature (reviewed in [387]); our analysis used a simple "slab" model described below.
2. The size and spatial arrangement of domains on the vesicle surface, given by the angle α_d and the distribution of domain center-center angles θ_{JK}. Our analysis assumed circular domains with a fixed area of 1375 Å^2 (corresponding to the cross-sectional area of an MA monomer), randomly arranged on the vesicle surface.
3. A vesicle size distribution $G(R;R_m,\sigma)$. We note that for vesicles larger than ~ 300 Å diameter, the precise values of R_m and σ do not affect $I(q)$ for q > 0.05 Å^{-1}. In our analysis, we fixed these parameters at 500 Å and 125 Å, respectively (i.e., a relative polydispersity of 0.25).

Transverse bilayer structure was modeled for each phase separately, using volume probability distributions for different lipid and protein "quasi-molecular fragments". The lipid headgroups and hydrocarbon chains were modeled as separate fragments with uniform probability distributions:

$$P_i(z) = \frac{N_i V_i}{A_L \sigma_i}[\Theta(\mathrm{z} - \mathrm{z}_i) - \Theta(\mathrm{z} - \mathrm{z}_i - \sigma_i)], \qquad (C11)$$

$$\Theta(x) = \begin{cases} 0, & x < 0 \\ 1, & x \geq 0 \end{cases}, \qquad (S12)$$

where V_i is the fragment volume, σ_i is the fragment width along the bilayer normal, A_L is the unit cell area, z_i is the fragment's lower boundary ($z_i + \sigma_i$ is the upper boundary), and Θ is the unit step function. For the domain phase, externally-bound protein was modeled with a Gaussian probability distribution:

$$P_P(z) = \frac{2\chi_P V_P}{\sqrt{2\pi} A_L \sigma_p} exp\left[\frac{-(z - z_p)^2}{2{\sigma_p}^2}\right]. \qquad (C13)$$

In Eq. C13, χ_P is the protein mole fraction in the protein+lipid sample; because the bilayer unit cell by definition contains exactly two lipids, the (fractional) number of proteins per unit cell is given by $N_P = 2\chi_P$. All lipid and protein fragment volume probability functions satisfy the following relationships:

$$\int P_i(z)dz = \frac{N_i V_i}{A_L}, \qquad (C14)$$

$$P(z) = \sum_i P_i(z) + P_w(z) = 1, \qquad (C15)$$

where N_i is the number of fragment i contained in the unit cell, P_w is the water probability, and P is the total probability. These equations enforce local volume conservation: any volume not occupied by a lipid or protein fragment must be occupied by water. Equation C15 can be rearranged to define the water probability function in terms of lipid and protein fragment probabilities:

$$P_w(z) = 1 - \sum_i P_i(z). \qquad (C16)$$

The scattering length density profile is then given by a weighted sum of the lipid and protein fragment probabilities:

$$\rho(z) = \sum_i \rho_i P_i(z), \qquad (C17)$$

$$\rho_i = \frac{b_i}{V_i}, \qquad (C18)$$

where b_i is the fragment's coherent scattering length. In the case of mixtures of two or more lipids, the lipid fragments are composites whose properties represent average properties of the mixture, and are approximated as mole fraction-weighted sums of individual lipid properties, i.e.:

$$V_i = \sum_j \chi_j V_{ij}, \qquad (C19)$$

$$b_i = \sum_j \chi_j b_{ij}, \qquad (C20)$$

where V_{ij} and b_{ij} are the fragment i volume and scattering length of mixture component j, respectively, and χ_j is the component j mole fraction. Values for the volumes and scattering length densities of the different lipid and protein species are given in Table C3. The total bilayer (Luzzati) thickness D_B is calculated from the total lipid volume V_L and area per lipid:

$$D_B = V_L/A_L, \qquad (C21)$$

where V_C and V_H are the lipid chain and headgroup volumes, respectively, and $V_L = V_C + V_H$. Similarly, the hydrocarbon chain thickness $2D_C$ is calculated from the hydrocarbon chain volume and area per lipid:

$$2D_C = 2V_C/A_L. \qquad (C22)$$

Finally, to account for the smearing effects of thermal disorder, the NSLD profile was smoothed by convolution with a Gaussian function:

$$\tilde{\rho}(z) = \rho * g = \int_{-\infty}^{\infty} \rho(x) g(\sigma_s; z - x) dx, \qquad (C23)$$

with the width of the smoothing window σ_s fixed at 2 Å.

X-ray crystallography. All crystals were grown using the sitting-drop vapor diffusion technique. Crystallization conditions were identified using screening experiments based on orthogonal arrays [388]. Details are given in Table C1. Prior to data collection crystals were transferred into cryo-protective solutions, and vitrified by direct immersion in liquid nitrogen. Diffraction data were collected by the oscillation method, using both laboratory and synchrotron radiation sources (Table C1), with crystals maintained at 100–110 K in a cold gas stream throughout. Data integration and scaling were performed with the program HKL2000 [389].

The structure of RSV MA was determined by the method of Multiple Isomorphous Replacement with Anomalous Scattering (MIRAS). To produce isomorphous derivatives, the crystals were soaked for 2-10 minutes in cryo-protective solutions incorporating either 1 M NaI or 1 M NaBr, prior to immersion in liquid nitrogen. Diffraction data on NaBr-soaked crystals were collected at several wavelengths near the Bromine K edge, while diffraction data on NaI-soaked crystals were collected at wavelengths of 1.033 and 1.653 Å. The program SHELXD [390] was used to identify the halide-binding sites. The NaI and NaBr-derivatized crystals shared a common site, with an additional unique site for the NaI derivative. The program SHARP 2.0 [391] was used to refine site occupancies and calculate phases, producing a partially interpretable electron density map in which helices were clearly visible. Repeat rounds of model building and refinement using the programs Coot [392] and Refmac [393] allowed for the completion of a structural model for the N-terminal region of the molecule (amino acids 1-102). There was no interpretable electron density associated with the remainder of the sequence (amino acids 103-155). Subsequently structures of a truncated variant (MA2-102) were determined by the method of molecular replacement, using the program Phaser [394] to position the structural model where required. Statistics associated with the native data sets and refined structural models are shown in Table C1.

MD simulations. All MD simulations were performed with the NAMD software, versions 2.7-2.10,[155] and analyzed with VMD [333] and custom Tcl scripts. Protein secondary structure was calculated using DSSP [395].

The two bilayers, POPC/POPS 70/30 mol% and POPC/POPS/Chol 34/30/36 mol%, were constructed with CHARMM-GUI [141] and simulated as described in [247]. The bilayers contained 70 and 100 lipids per leaflet, respectively, and were solvated with 45 waters/lipid and 50 mM NaCl. The POPC/POPS bilayer was simulated for a total of 191 ns and the POPC/POPS/Chol bilayer for a total of 270 ns. The last 100 ns of each simulation were used for subsequent analysis.

MA was placed on top of each bilayer using coordinates taken from the last frames of the two bilayer-only simulations. MA was oriented with respect to the membrane surface as previously done [248]. The systems were energy minimized for 24000 steps and run for 1.2 ns with a 1 fs time step before the production runs. Three replica simulations were run for the POPC/POPS +MA system with total simulation times of 184 ns, 242 ns and 198 ns. The POPC/POPS/Chol +MA system was simulated for 74 ns, after which time two replica simulations were started and run for an additional 132 and 141 ns respectively. The last 100 ns of the trajectories were used for subsequent analysis.

To ensure that the applied periodic boundary conditions did not affect the interaction of the protein with the bilayer, an additional simulation was performed in which two MA proteins were placed as described above, but on each side of a POPC/POPS/Chol bilayer (i.e., one on the top leaflet and one on the bottom leaflet). Thus, any modes of

interaction that could cause large leaflet deformations and accumulation of pressure if applied only on one side of the bilayer, would be counterbalanced and not suppressed. The simulation was run for a total of 204 ns and the interaction of each of the two MA proteins with their respective leaflets was analyzed separately. Since the results were the same as in the systems with a single MA, they were treated as two additional replicas of the POPC/POPS/Chol +MA system and were analyzed jointly with the other simulations.

Calculations of electrostatic potential and fraction of bound protein. The electrostatic potential on the membrane surface was calculated using the analytical solution to the non-linear Poisson-Boltzmann equation (Eq. 15 in [255]) with the membrane surface taken as z = 0. Surface charge density was calculated as the mole fraction of charge divided by the average area per lipid of the bilayer, with units of $e^-/Å^2$. Unless otherwise noted, the areas per lipid calculated from MD simulations were used.

To generate the contour plots in Fig. 4.6B in Chapter 4, the fraction of bound protein f from protein binding assays (i.e., the data in Fig. 4.5F in Chapter 4) was modeled as a sigmoidal function of the membrane surface potential ψ:

$$f(\psi) = \frac{a}{1 + e^{b(\psi - \psi^*)}}, \qquad (C24)$$

where a is a scaling factor representing the maximum bound fraction, b is a stretching factor representing the width of the sigmoidal binding transition, and ψ^* is the surface potential at half-maximum binding. The three adjustable parameters were optimized with Mathematica's built-in NonlinearModelFit function using a Levenberg-Marquardt algorithm. The best-fit parameter values were: a = 70.9%, b = 0.285, and ψ^* = –55.9 mV (Fig. C10). This parameter set was used with Eq. C24 to map the calculated membrane surface potential (Fig. 4.6B, left-hand plot) to the percentage of bound protein, generating the right-hand plot in Fig. 4.6B (Chapter 4).

Monte Carlo simulations of equilibrium lipid distributions. Monte Carlo simulations of a 100 × 100 triangular lattice in the canonical ensemble were performed using custom code written in Mathematica and available from the authors upon request. Each lattice site represented either a PC or PS lipid, with the composition fixed at 70/30 mol% PC/PS. Neglecting multibody and long-range electrostatic interactions, the total energy of a lattice composed of a fixed number of PS and PC lipids (N_{PS} and N_{PC}, respectively) is given by the sum of unique nearest-neighbor pairwise interactions [51]:

$$U^T = \frac{ZN_{PS}U_{PS-PS}}{2} + \frac{ZN_{PC}U_{PC-PC}}{2} + N_{PS-PC}\Delta E_m, \qquad (C25)$$

$$\Delta E_m = U_{PS-PC} - (U_{PS-PS} + U_{PC-PC})/2, \qquad (C26)$$

where U_{PS-PS} and U_{PC-PC} are the interaction energies for a neighboring pair of PS and PC lipids, respectively, N_{PS-PC} is the total number of PC/PS contacts, and Z is the number of nearest neighbors in a lattice site (6 for a triangular lattice). The sole adjustable parameter ΔE_m is the excess mixing energy of a PC/PS pair. The first two terms in Eq. C25 do not depend on the lipid distribution and therefore do not contribute to non-ideal mixing. As a result, only the third term was updated. For each proposed update, the position of two randomly chosen lipids was exchanged, generating a change in the lattice energy $\Delta U^T \equiv U^T_{new} - U^T_{init}$ that was either favorable/neutral ($\Delta U^T \leq 0$) or unfavorable ($\Delta U^T > 0$). Importance sampling was based on the Metropolis criterion, whereby a favorable move was always accepted, and an unfavorable move was accepted with probability $P = \exp\left(-\Delta U^T / k_B T\right)$ by first drawing a random number R from a uniform probability distribution $R \sim U[0,1]$ and then performing the exchange if $R \leq P$. Each simulation was equilibrated for a minimum of 10^3 MC cycles, where a cycle is defined as a number of proposed exchanges equal to the lattice size (here, 10^4 exchanges). Equilibrium was judged by convergence of the lattice energy upon starting from either (a) a completely random distribution of the lipids, or (b) a block distribution of the lipids. The number of MC cycles required to reach convergence increased with increasing ΔE_m, varying from ~ 300 cycles for ΔE_m = + 0.1 k_BT to ~ 10^4 cycles for ΔE_m = + 0.5 k_BT. For additional details on MC lattice simulations, we point the reader toward several studies relevant to lipid bilayers [51, 92, 251, 396-403].

Calculation of relative surface potential from Monte Carlo snapshots. To calculate a surface potential map from MC snapshots, lattice sites were assigned relative real space coordinates $\boldsymbol{l} = (l_x, l_y, 0)$ using the relationship between the triangular lattice spacing λ and the unit cell area A:

$$\lambda = \left(\frac{2A}{\sqrt{3}}\right)^{1/2}, \qquad (C27)$$

and taking A to be the area per lipid (63 Å^2). The potential V at an arbitrary point $\boldsymbol{p} = (p_x, p_y, p_z)$ is then given by:

$$V = k_e \sum_j \frac{q_j}{r_j}, \qquad (C28)$$

where k_e is Coulomb's constant, $r_j = \left\| \boldsymbol{l_j} - \boldsymbol{p} \right\|$ is the distance between point $\boldsymbol{p}$ and lattice site j, q_j is the charge at lattice site j (i.e., 0 for a neutral PC lipid and the elementary charge e$^-$ for an acidic PS lipid), and the sum is over all lattice sites j. Because the absolute potential depends strongly on the lattice size, V was normalized to a reference potential $\bar{v}$ arising from a uniformly charged lattice calculated as:

$$\bar{v} = k_e \chi e^- \sum_j r_j^{-1}, \qquad (C29)$$

where χ is the mole fraction of charged lipid in the mixture (here, 0.3). Finally the relative potential $\tilde{V}$ at point $\boldsymbol{p}$ was calculated as $\tilde{V} = V/\bar{v}$.

MM/GBSA calculations. The molecular mechanics-generalized Born and surface area (MM-GBSA) method [256, 257] is a so-called end-point free energy approach to estimate the binding free energy between two molecular binding partners, based on a sample of molecular conformations of the complex generated by all-atom molecular dynamics simulation. The MM-GBSA method has been used successfully to estimate the binding free energy of ligands to proteins, and to calculate single-residue contributions to binding free energies of large protein-protein complexes [256-258]. For each trajectory frame, the solvent and ions are stripped away and only the coordinates of the binding partners are kept. In the one-trajectory MM-GBSA approach employed here, coordinates for each partner in isolation are extracted from the same trajectory frames of the complex, assuming that these are also acceptable conformations for the molecules in solution. As in the preceding molecular mechanics-Poisson Boltzmann surface area (MM-PBSA) method [404], the solvation effects are approximated by immersing the molecules in a continuous medium with high relative dielectric constant $\varepsilon_r^{\text{solv}} = 80$. Following the thermodynamic cycle shown in Fig. C11, the binding free energy between two binding partners, here membrane (M) and protein (P), is expressed as

$$\Delta G_{\text{bind}} = \Delta E_{\text{int}}^{\text{vac}} + \Delta G_{\text{desolv}}(M) + \Delta G_{\text{desolv}}(P) - \Delta G_{\text{desolv}}(MP) + \Delta S_{\text{bind}}^{\text{vib}}\,. \qquad (C30)$$

In general, $\Delta E_{\text{int}}^{\text{vac}}$ is the difference in internal bonded and non-bonded energies in M and P upon binding, calculated with the same Charmm36 parameters [246] as in the MD simulation. Here, a lot of terms cancel out since we use the same coordinates for bound and unbound molecules, such that $\Delta E_{\text{int}}^{\text{vac}}$ boils down to the Van der Waals and electrostatic interaction energies between M and P. $\Delta S_{\text{bind}}^{\text{vib}}$ is the difference in internal vibrational entropy upon binding, which we neglect in the present application. The desolvation penalty for molecular system X is composed of a polar and a non-polar term,

$$\Delta G_{\text{desolv}}(X) = \Delta G_{\text{P,desolv}}(X) + \Delta G_{\text{NP,desolv}}(X). \qquad (C31)$$

The non-polar term accounts for energetic and entropic effects in the solvent related to creating the cavity occupied by X. This term is simply proportional to the SASA,

$$\Delta G_{\text{NP,desolv}}(X) = \gamma\, SASA(X), \qquad (C32)$$

with $\gamma = -0.0072$ kcal/mol/Å^2 [405]. The SASA is calculated by rolling a virtual 1.4 Å radius ball over the molecules. The polar solvation term is calculated using the

generalized Born (GB) equation [256, 404] with an additional Debeye-Hückel correction to account for ionic screening [256]:

$$\Delta G_{\mathrm{P,desolv}}(X) = \frac{c}{2}\left(\frac{1}{\varepsilon_r^{\mathrm{vac}}} - \frac{e^{-\kappa r_{ij}^{\mathrm{GB}}}}{\varepsilon_r^{\mathrm{solv}}}\right)\sum_{i,j\in X}\frac{q_i q_j}{r_{ij}^{\mathrm{GB}}}\,. \qquad (C33)$$

Here, the q_i are atomic partial charges, $c = 332.0672$ kcal/mol Å / u^2, and κ is the Debeye-Hückel screening constant expressed in Å^{-1} as $\kappa = 0.316\sqrt{[\mathrm{salt}]}$, where [salt] is the monovalent ion concentration in mol/L [406]. The modified atomic distances entering the GB equation are given by

$$r_{ij}^{\mathrm{GB}} = \sqrt{r_{ij}^2 + \alpha_i\alpha_j \exp\left\{-\frac{r_{ij}^2}{8\alpha_i\alpha_j}\right\}}. \qquad (C34)$$

Critical quantities for the accuracy of the GB model are the Born radii α_i, which essentially express how far each atom is from the molecular surface. To calculate these, we use the GB-MV2 method [407, 408] implemented in the CHARMM software [409], which was shown to yield very good accuracy compared to Poisson-Boltzmann results.

Because all energies in the MM-GBSA framework are expressed in terms involving single atoms or pairs of atoms, ΔG_{bind} can be decomposed in contributions from separate groups of atoms [257, 258]. For the Van der Waals, electrostatic, and GB pair terms, half of the interaction energy is attributed to each atom of the pair. When applied to amino acid side chains, this decomposition yields contributions comparable to those obtained by computational alanine scanning [410]. In the present case, summing over all residues in M or P allows us to attribute contributions of each binding partner to ΔG_{bind}. These contributions can differ due to different desolvation penalties on each side. The MM-GBSA free energy decomposition were carried out using a custom set of scripts built upon the original implementation of V. Zoete [258, 410, 411] and the CHARMM version 37 software [409].

To perform the MM-GBSA analysis on each of the two MA/membrane systems, we first created a single trajectory file by concatenating the last ~150 ns from the respective replica simulations of a single MA and the bilayer. The trajectories of the –Chol and +Chol systems consisted of a total of 5929 and 3450 frames, respectively, all output with a stride of 80 ps. Only the top membrane leaflet was considered in the reported energy analysis (taking the bottom leaflet into account had an insignificant effect on the energies). The calculation was set up and run with 50 mM salt and a 20 Å cutoff for VdW and electrostatics.

ESR measurements. ESR was performed as previously described [231] with the following changes. Multilamellar vesicles were extruded to form 100 nm large

unilamellar vesicles (LUVs). The LUVs were incubated with MA protein at a ratio of 0.31 mg protein to 1 mg lipid (the same ratio used for SANS measurements) in buffer (20 mM Tris HCl pH 8, 50 mM NaCl, 2 mM TCEP) for no less than 30 minutes at ambient room temperature (~22 °C) prior to loading into glass ESR capillary tubes. The final protein concentration in the ESR experiment was ~ 68 μM, or approximately three times the MA binding constant measured by SPR [245] for similar binding reactions. The model-free order parameters for POPC/POPS LUVs with and without MA were each 0.11, and the model-free order parameters for POPC/POPS/Chol LUVs with and without MA were each 0.22 [412].

Continuum mean-field modeling of MA protein-membrane interactions. To quantify the extent of lipid segregation around the MA protein adsorbed to a membrane, we used a previously developed continuum mean-field (CMF) computational approach [252, 253]. The CMF method quantifies essential components of the energetics of protein-lipid interactions and describes the combined kinetic effect of many lipid species interacting with the membrane-adsorbed protein. The protocol defines the steady state of the system consisting of the membrane-associated protein, and includes all important degrees of freedom (electrostatics, mixing entropy of lipids and solution ions), as described in detail in our publications [252, 253, 413-415]. To this end, a hybrid representation of the computational model is constructed in which membrane-associated proteins are treated at detailed atomic level in three dimensions, and the lipid membrane is considered as a continuum elastic medium comprised of two-dimensional smooth charged surfaces representing the lipid polar headgroups, and a low-dielectric hydrocarbon core volume.

This system is subjected to a self-consistent minimization of the governing mean-field-based free energy functional F that depends on local lipid component densities $\varphi(x,y)$ and mobile ion concentrations c_+ and c_- (for positive and negative ionic species, respectively) in the solution. In particular, as detailed in [252, 253], F can be written as the sum of electrostatic energy (F_{el}), lipid mixing entropy (F_{lip}), and salt ion translational entropy (F_{ion}) contributions:

$$F = F_{el} + F_{lip} + F_{ion}, \quad (C35)$$

where,

$$F_{el} = \frac{1}{2}\epsilon_0\epsilon_w\left(\frac{k_BT}{e^2}\right)\int_V (\nabla\Phi)^2 dv, \quad (C36)$$

$$F_{lip} = \frac{k_BT}{a}\int_A \left[\varphi\, ln\frac{\varphi}{\varphi_0} + (1-\varphi)\, ln\frac{(1-\varphi)}{(1-\varphi_0)}\right] dA, \quad (C37)$$

$$F_{ion} = k_B T \int_V \left[c_+ \, ln \frac{c_+}{c_0} + c_- \, ln \frac{c_-}{c_0} - (c_+ + c_- - 2c_0) \right] dv. \qquad (C38)$$

In the above, k_B is the Boltzmann constant, T is the temperature, e is the elementary charge, ϵ_0 is the permeability of free space, and $\epsilon_w = 80$ is the dielectric constant of the aqueous solution. Φ represents reduced (dimensionless) electrostatic potential in space, a denotes the area per lipid, c_0 is the salt concentration in the bulk, and φ_0 represents bulk concentration of a charged lipid species. The $\varphi(x,y)$ local field relates to the surface charge densities $\sigma(x,y)$ through $\sigma(x,y) = (e/a)\varphi(x,y)z(x,y)$, where $z(x,y)$ denotes valency of the lipid at (x,y). Minimization of F with respect to c_+ and c_- leads to the non-linear Poisson-Boltzmann (NLPB) equation [416]:

$$\nabla \Phi = \lambda^{-2} \, sinh \, \Phi, \qquad (C39)$$

which is solved to obtain Φ in space (λ being the Debye length of the electrolyte solution). As seen from Eqs. C35-38, this electrostatic potential is self-consistently dependent on the local lipid concentrations through the entropic penalty (F_{lip}) due to lipid segregation or de-mixing. Thus, a self-consistent search for the free energy minimum is conveniently carried by linking Φ (obtained from the NLPB equation) and spatial charged-lipid compositions φ on each leaflet of the membrane to the respective electrochemical potentials μ through the Cahn-Hilliard (CH) equation [417]:

$$\frac{\partial \varphi(\vec{r}, t)}{\partial t} = D_{lip} \nabla^2 \mu(\vec{r}, t). \qquad (C40)$$

To quantify interactions between MA protein and the membrane composed of 70/30 mol% mixture of POPC/POPS lipids with the CMF approach, we took one of the top 5 simulation frames with the lowest MA-bilayer total interaction energy (as calculated from MM/GBSA). Then, by applying only global transformations to the protein, we positioned MA in a manner where we maximized the exposure of its lysine residues to a flat lipid surface of $\sigma(x,y) \sim 4.93 \times 10^{-3}$ e^- charge density, corresponding to ~30 mol% PS lipid content (assuming a = 60.9 Å^2).

The self-consistent minimization of F was then carried out for the protein by solving the NLPB equation using the multigrid solver of the Adaptive Poisson-Boltzmann Solver (APBS) suite [418] on 1 Å-spaced cubic 256 Å^3 mesh as described previously [253]. This was done using a 0.05 M ionic solution of monovalent counterions (corresponding to λ = 13.49 Å Debye length), and a dielectric constant of 2 for the membrane interior and protein, and 80 for the solution. The protein models were positioned so that the minimum distance between the protein and the lipid surface was 2 Å [253, 415].

The CMF calculation shows the adsorption free energy of MA protein, $\Delta F = F-(F_{prot}+F_{memb})$ (F_{prot} and F_{memb} representing the free energy of protein and membrane system in separation) onto the POPC/POPS 70/30 mol% lipid membrane is ~ –9 k_BT (see Fig. C4A). Importantly, lipid de-mixing had an insignificant effect on ΔF (the minimization procedure resulted in a change in ΔF of < 1 k_BT, Fig. C4A) as the local concentration of PS under the adsorbed protein calculated by integrating the charge map of the smallest rectangle enclosing the protein shadow, was ~ 31%, or only slightly higher than the bulk PS concentration of 30% (see Fig. C4B). The minor extent of lipid segregation, together with the concomitant insignificant change in the adsorption free energy, suggests that MA protein adsorbs onto the PC/PS membrane mainly through the electrostatic sensing of PS lipid domains.

Table C1. Protein crystallization conditions, and statistics associated with the X-ray diffraction data and atomic models.

Protein	**RSV MA**	**RSV MA_{2-102}**	**RSV MA_{2-102}**
Crystallization Conditions			
Protein concentration (μM)	680	540	540
Reservoir Solution	2.60 M Ammonium formate 0.20 M β-Alanine/KOH pH 10.3	18%(w/v) PEG 8000 0.2 M Succinic acid/KOH pH 5.5 1.0 M Ammonium nitrate	0.6 M Malonic acid /KOH pH 9.1 0.1 M Boric acid /KOH pH 9.1
Temperature (°C)	Ambient	18	18
X-ray diffraction data			
Cryoprotectant	4.00 M Ammonium formate 0.20 M β-Alanine/KOH pH 10.3 30 %(v/v) Ethylene glycol	20%(w/v) PEG 8000 0.1 M Succinic acid/KOH pH 5.5 1.0 M Ammonium nitrate 20 %(v/v) Ethylene glycol	0.6 M Malonic acid /KOH pH 9.1 0.1 M Boric acid /KOH pH 9.1 20 %(v/v) Ethylene glycol
Space group	$I4_122$	$I4_1$	$I4_122$
Unit cell lengths (Å)	a=b= 66.2, c= 218.8	a=b= 79.0, c= 27.8	a=b= 67.4, c=220.8
X-ray source	ALS Beamline 8.2.1	Rigaku MicroMax-007 HF Rotating Copper Anode	Rigaku MicroMax-007 HF Rotating Copper Anode
X-ray wavelength (Å)	1.03320	1.54179	1.54179
Sample Temperature (K)	100	110	110
Data resolution limits (Å) [a]	49.0 - 2.85 (2.95 - 2.85)	39.5 - 1.86 (1.93 - 1.86)	49.7 - 3.20 (3.31 - 3.20)
Number of unique observations [a]	6104 (582)	7363 (681)	4535 (429)
Mean Redundancy [a]	8.7 (9.0)	12.4 (11.4)	10.1 (10.5)
Completeness (%) [a]	99.9 (100.0)	99.5 (94.6)	99.9 (100.0)
$R_{measure}$ [a]	ND (ND)	0.058 (0.289)	0.139 (0.703)
R_{merge} [a]	0.070 (0.455)	0.055 (0.277)	0.132 (0.678)
Mean I / σI [a]	34.0 (4.1)	56.0 (10.0)	22.2 (4.5)
Crystallographic models			
Number of protein molecules in the asymmetric unit	1	1	1
R_{work} / R_{free} [b]	0.195 / 0.239	0.164 / 0.210	0.202 / 0.249
Total number of protein atoms	767	741	791
Number of water molecules	7	54	6
Other ligands	-	Ethylene Glycol NO_3^-	-
Disorder Model	Individual Isotropic B-factors	Individual Isotropic B-factors	Individual Isotropic B-factors
Mean total isotropic B-factor, all protein atoms ($Å^2$):	67.4	23.1	74.7
Bulk Solvent model	Mask	Mask	Mask
RMSD from ideal geometry : Bond lengths (Å) / Bond angles (°)	0.008 / 1.325	0.011 / 1.392	0.013 / 1.695
Residues in Favoured / Allowed regions of Ramachandran plot (%)[c]	100.0 / 100.0	97.1 / 100.0	95.3 / 100.0
PDB ID code	5KZ9	5KZA	5KZB

[a]Numbers in parentheses are for the highest resolution shell. [b]Calculated from a randomly selected 5% of observations omitted from all model refinement. [c]Defined by the MolProbity web-server [419].

Table C2. Bilayer structural parameters obtained from the refinement of SANS data. Italicized values indicate constrained parameters, and asterisks indicate parameters that were varied during the fitting routine (all remaining structural and compositional values are obtained through mathematical relationships).

Parameter	– Cholesterol		+ Cholesterol	
	– RSV-MA	+ RSV-MA	– RSV-MA	+ RSV-MA
global				
χ_{POPC}	*0.7*	*0.7*	*0.34*	*0.34*
χ_{POPS}	*0.3*	*0.3*	*0.3*	*0.3*
χ_{CHOL}	--	--	*0.36*	*0.36*
POPC-rich domain				
χ_{POPC}	0.9 ± 0.1*	0.9 ± 0.1*	0.46 ± 0.02*	0.45 ± 0.07*
χ_{POPS}	0.1 ± 0.1	0.1 ± 0.1	0.18 ± 0.02	0.19 ± 0.07
χ_{CHOL}	--	--	*0.36*	*0.36*
V_L [Å^3] [a]	1234 ± 2	1236 ± 2	1012 ± 1	1012 ± 2
A_L [Å^2] [b]	63.1 ± 1.4*	61.5 ± 2.0*	48.2 ± 0.6*	47.7 ± 0.9*
D_B [Å] [c]	39.2 ± 0.9	40.3 ± 1.2	42.0 ± 0.5	42.4 ± 0.8
$2D_C$ [Å] [d]	29.0 ± 0.7	29.9 ± 0.9	33.8 ± 0.4	34.1 ± 0.6
D_H [Å] [e]	6.9 ± 1.5*	6.2 ± 0.6*	7.2 ± 1.4*	6.6 ± 1.3*
POPS-rich domain				
χ_{POPC}	0.3 ± 0.3	0.3 ± 0.3	0.08 ± 0.03	0.19 ± 0.09
χ_{POPS}	0.7 ± 0.3	0.7 ± 0.3	0.56 ± 0.03	0.45 ± 0.09
χ_{CHOL}	--	--	*0.36*	*0.36*
V_L [Å^3] [a]	1222 ± 5	1222 ± 5	1003 ± 2	1005 ± 3
A_L [Å^2] [b]	63.0 ± 4.3*	65.2 ± 2.3*	48.8 ± 4.4*	47.4 ± 2.9*
D_B [Å] [c]	38.9 ± 1.4	38.6 ± 0.9	41.7 ± 1.9	42.2 ± 1.3
$2D_C$ [Å] [d]	29.1 ± 1.1	29.0 ± 0.6	33.8 ± 1.5	34.2 ± 1.0
D_H [Å] [e]	9.2 ± 1.0*	6.4 ± 1.3*	7.8 ± 1.7*	7.6 ± 1.8*
Protein bound to POPS-rich domain				
A_P [Å^2] [f]		*1375*		*1375*
z_P [Å] [g]	--	35.9 ± 0.8*	--	38.0 ± 0.6*
σ_P [Å] [h]	--	7.2 ± 0.6*	--	6.6 ± 0.4*
N_L [i]	--	21 ± 1	--	29 ± 2
N_{POPS} [j]	--	15 ± 5	--	13 ± 3
f_P [k]	--	0.47 ± 0.04*	--	0.50 ± 0.05*
a_P [l]	--	0.35 ± 0.04	--	0.40 ± 0.04

[a]average lipid volume calculated as mole fraction-weighted sum of lipid and chol molecular volumes [b]average area per lipid [c]total bilayer (Luzzati) thickness [d]bilayer hydrocarbon thickness [e]headgroup thickness [f]area per protein [g]center of Gaussian protein volume distribution [h]width of Gaussian protein volume distribution [i]average number of outer leaflet lipids in protein shadow [j]average number of outer leaflet POPS in protein shadow [k]fraction of protein bound to vesicle [l]vesicle area fraction bound by protein

Table C3. Molecular volume V, neutron scattering length b, and neutron scattering length density ρ of different species.

	V [Å^3]		b [fm]		ρ [fm Å^{-3}]	
D_2O	30.1		19.145		0.636	
RSV-MA in D_2O	20280[a]		6325[b]		0.312	
	Head	*Chains*	*Head*	*Chains*	*Head*	*Chains*
POPC[c]	331	916	60.072	-26.624	0.181	-0.029
POPC-D31[c]	331	916	60.072	296.086	0.181	0.323
POPS[d]	278	917	115.789	-26.624	0.417	-0.029
POPS-D31[d]	278	917	115.789	296.086	0.417	0.323

[a]sum of residue volumes taken from ref. [420] [b]accounts for exchangeable protons following ref. [421] [c]volume data from ref. [145] [d]volume data from ref. [249]

Table C4. Estimated composition [45, 221, 260] and surface charge density (calculated from the mole fraction-weighted charge and area) of the mammalian plasma membrane inner leaflet.

lipid	mole fraction χ	charge [e$^-$]		area [Å^2]	
		per lipid	χ-weighted	per lipid	χ-weighted
Chol	0.4	0	0	27[a]	10.8
(PO)PE	0.28	0	0	59[b]	16.5
(PO)PC	0.05	0	0	65[c]	3.3
(PO)PS	0.18	-1	0.18	64[d]	11.5
(SA)PI	0.08	-1	0.08	68[e]	5.4
(SA)PIP2	0.02	-3	0.06	68[e]	1.4
Total	1.0		0.32		48.9

[a]ref. [193] [b]ref. [147] [c]ref. [145] [a]ref. [249] [e]ref. [422]

Table C5. Decomposition of the interaction energy of MA and the lipids calculated with the MM-GBSA method from the simulation trajectories as described in the text. Shown are the Van der Waals (VdW) and electrostatic (Elec) energies calculated in vacuum and their sum, $\Delta E_{\text{int}}^{\text{vac}}$; the polar (P) and nonpolar (NP) desolvation penalties and their sum, $\Delta\Delta G_{solv}$; and the total binding free energy approximated by $\Delta E_{\text{int}}^{\text{vac}}+\Delta\Delta G_{solv}$. All energy units are in kcal/mol.

system	component	Interaction energy in vacuum			Desolvation penalty			total
		VdW	Elec	ΔG_{in}^{vac}	P	NP	$\Delta\Delta G_{solv}$	
MA and PC/PS	MA	-9.3	-607.8	-617.1	620.9	-4.8	616.1	-1.0
	lipids	-9.3	-607.8	-617.1	620.6	-4.2	616.4	-0.7
MA and PC/PS/Chol	MA	-8.5	-765.6	-774.1	779.1	-5.1	774.0	-0.1
	lipids	-8.5	-765.7	-774.1	773.1	-4.8	768.3	-5.8

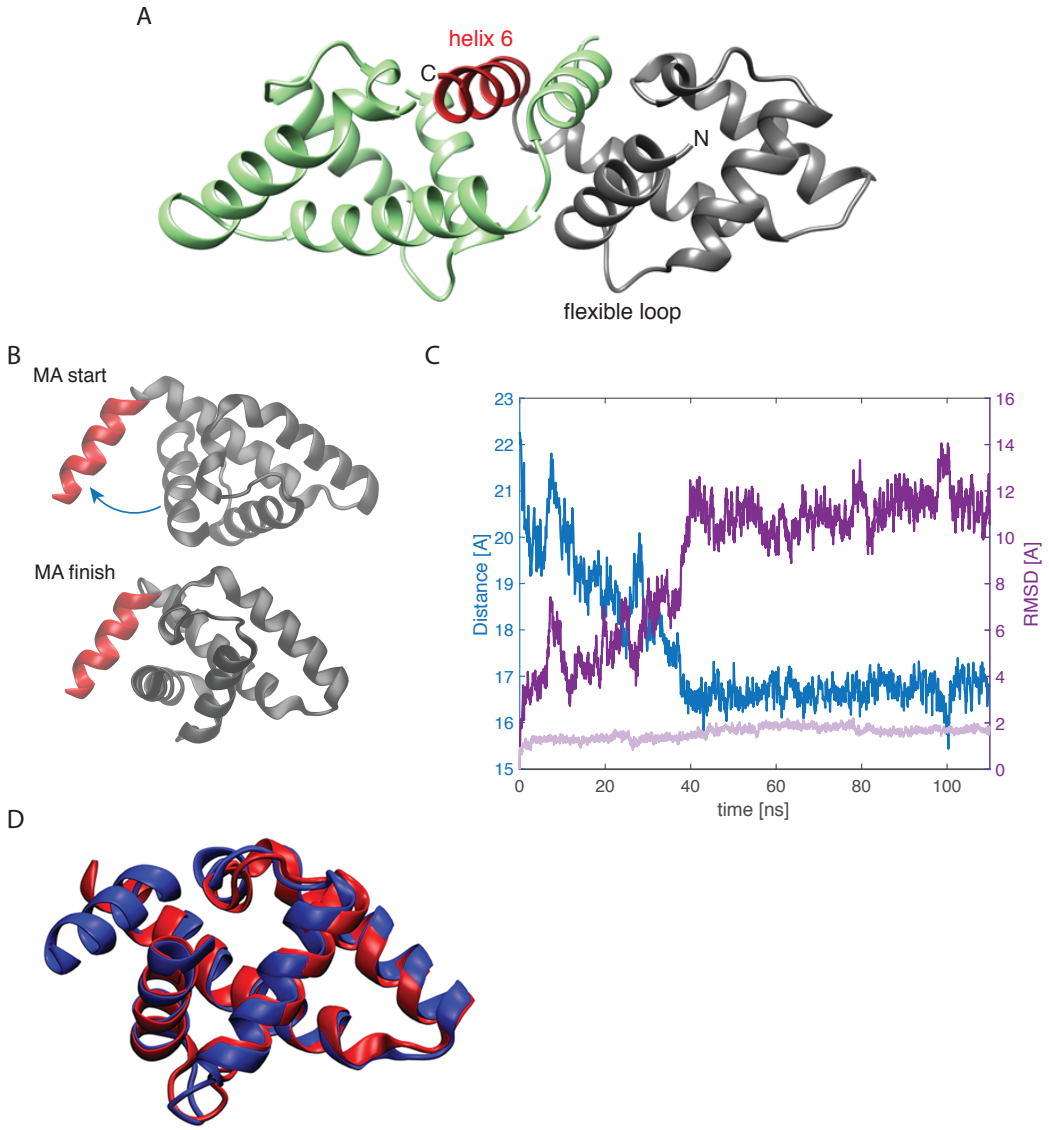

Figure C1. (A) Crystal structure of the resolved MA dimer, with monomers colored in green and grey. Helix 6 of the grey-colored monomer is shown in red. (B) Snapshots of the protein at the start and finish of the water box simulation. Helix 6 (red) is fixed during the simulation and is displayed in the same plane while the rest of the protein (referred to protein *body* from here on) rotates ~ 30 degrees. An arrow denotes the observed structural change. (C) Time evolution of the distance between the centers of mass of helix 6 and the protein body (residues 1-90, blue). Also plotted are the *full protein backbone* RMSD with respect to the starting structure after alignment on helix 6 (dark purple) and the *protein body* RMSD after alignment on the protein body (light purple). (D) Overlay of the monomer crystal structure of MA (red) and the structure of MA used in the simulations (blue). The backbone RMSD between the two structures (excluding helix 6 which is not present in the monomer crystal structure) is 2.8 Å.

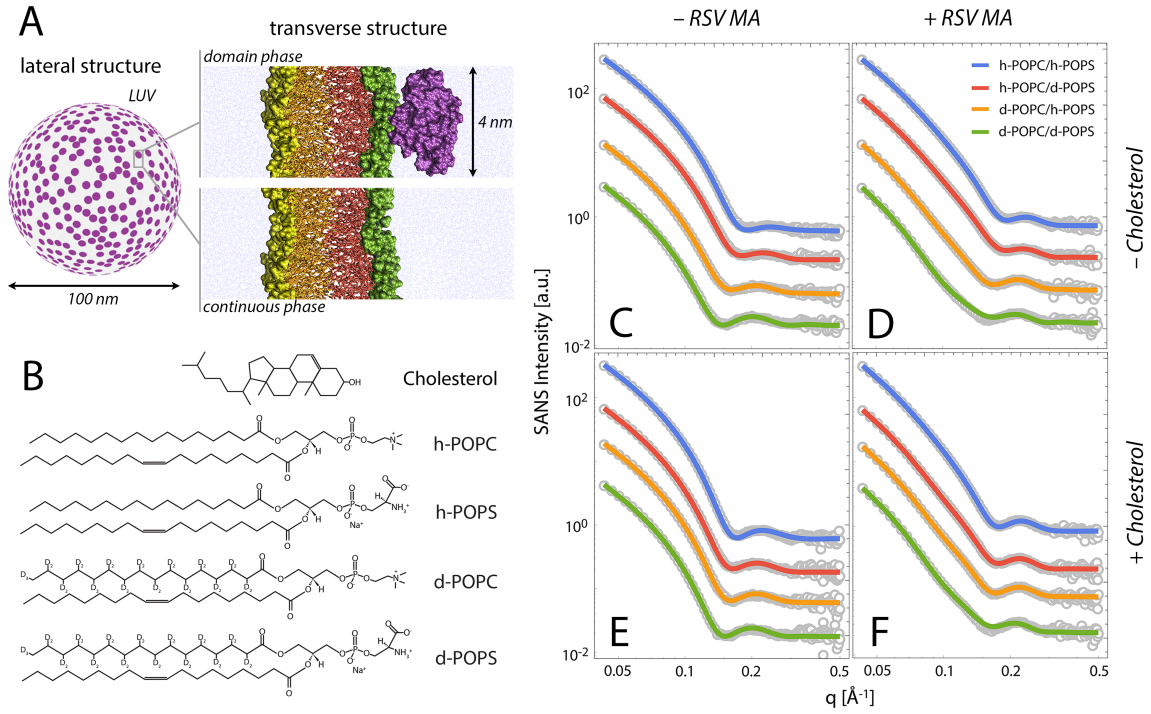

Figure C2. Bilayer structure from analysis of SANS data. (A) Schematic illustration of a 100 nm LUV and the two environments used in the model to analyze the SANS data. The structural model accounts for both transverse and lateral structure. Transverse structure arises from the layered distribution of matter projected onto the bilayer normal, and is mathematically described by parameters related to the volume probability distributions of inner and outer leaflet lipid headgroups, and hydrocarbon chains, in addition to bound protein. Lateral structure can arise from lipid clustering or phase separation, as well as partial surface coverage of bound protein monomers; it is mathematically described by parameters related to the domain size, shape and spatial arrangement (here, domains were modeled as circular disks, randomly arranged on the vesicle surface). Two distinct coexisting environments were modeled—the domain and the surrounding continuous phase—with the lipid composition and transverse structure of each allowed to vary as described in the text. (B) Structures of lipids used in SANS experiments. Palmitoyl chain-perdeuterated variants of POPC and POPS (i.e., d-POPC and d-POPS) were used to provide a scattering length density contrast in order to highlight lateral structure. (C-F) Scattering data (open circles) and fits (solid lines) for four different neutron contrast data sets, with different sample compositions: POPC/POPS 70/30 mol% (C); POPC/POPS 70/30 mol% + RSV MA (D); POPC/POPS/Chol 34/30/36 mol% (E); POPC/POPS/Chol 34/30/36 mol% + RSV MA (F).

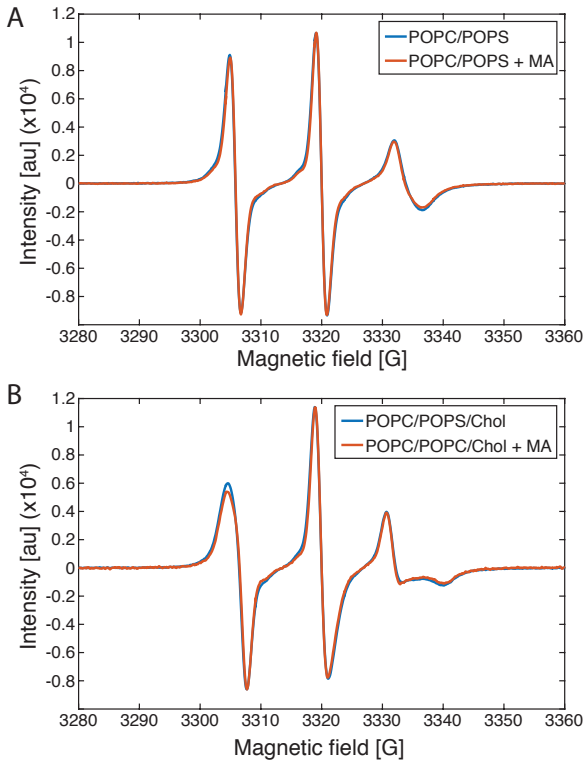

Figure C3. ESR spectra of (A) POPC/POPS with and without MA, and (B) POPC/POPS/Chol with and without MA. All LUVs contained 0.5 mol% of 16:0-16 Doxyl PC.

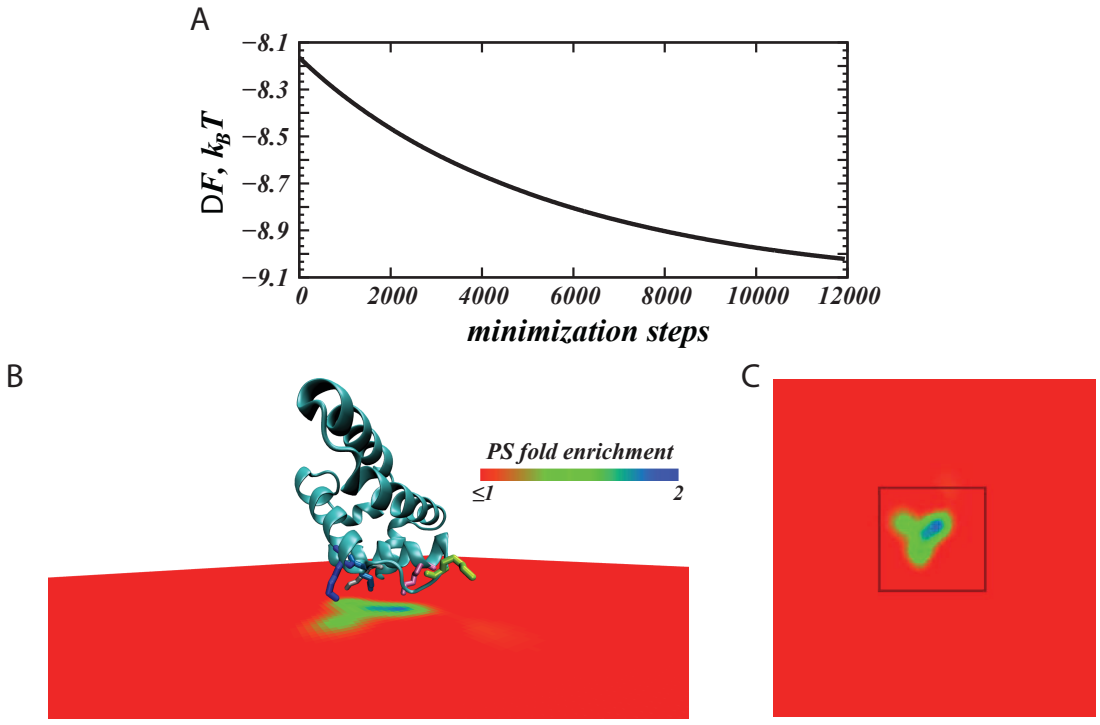

Figure C4: (A) Convergence of the adsorption free energy (ΔF) in the CMF calculations. Shown is the change in ΔF as the mean-field free energy functional is minimized. Value of ΔF at 0^{th} minimization step corresponds to the adsorption free energy onto homogeneous membrane composed of charged and neutral lipids generating a surface charge density of 4.93×10^{-3} e^- (corresponding to a PC/PS lipid mixture with ~30 mol% PS). (B) View of the MA protein (cartoon) adsorbing on the lipid membrane (as seen from the side). The level of PS lipid segregation by the protein, calculated with CMF approach, is illustrated (as ratios of local and bulk lipid fraction values) in color code. Lysine residues close to the surface are shown in licorice and color according to the following: K6 – gray, K13 – purple, K18 – green, K23 – light blue, K24 – dark blue. (C) View of the lipid membrane (as seen from above). Highlighted with a black box is the smallest rectangle enclosing the protein shadow , whose charge density was integrated to calculate the local concentration of PS under MA (~31 mol%).

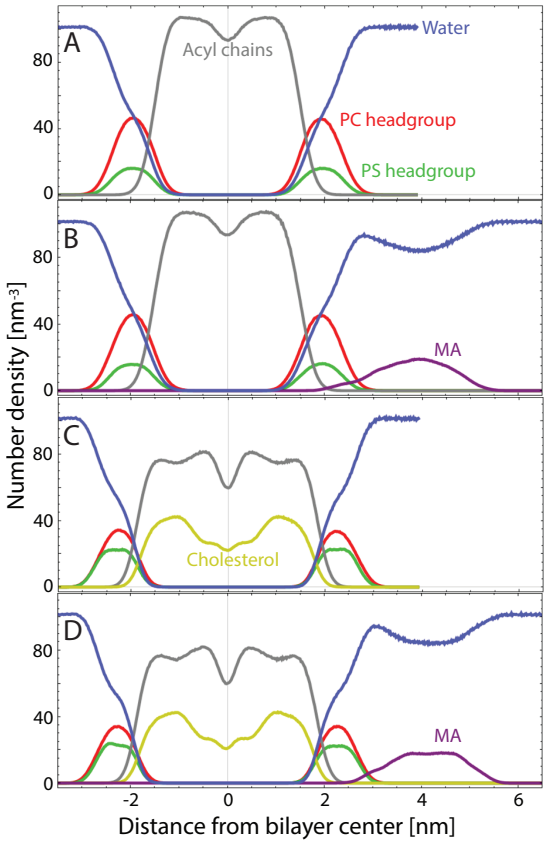

Figure C5. Number density profiles calculated from four different MD simulations. Color coded are the profiles of lipid acyl chains (grey), water (blue), POPC headgroups (red), POPS headgroups (green), Chol (yellow) and MA (purple) calculated from the last 100 ns of each simulation: (A) POPC/POPS 70/30 mol%; (B) POPC/POPS 70/30 mol% with MA; (C) POPC/POPS/Chol 34/30/36 mol%; and (D) POPC/POPS/Chol 34/30/36 mol% with MA.

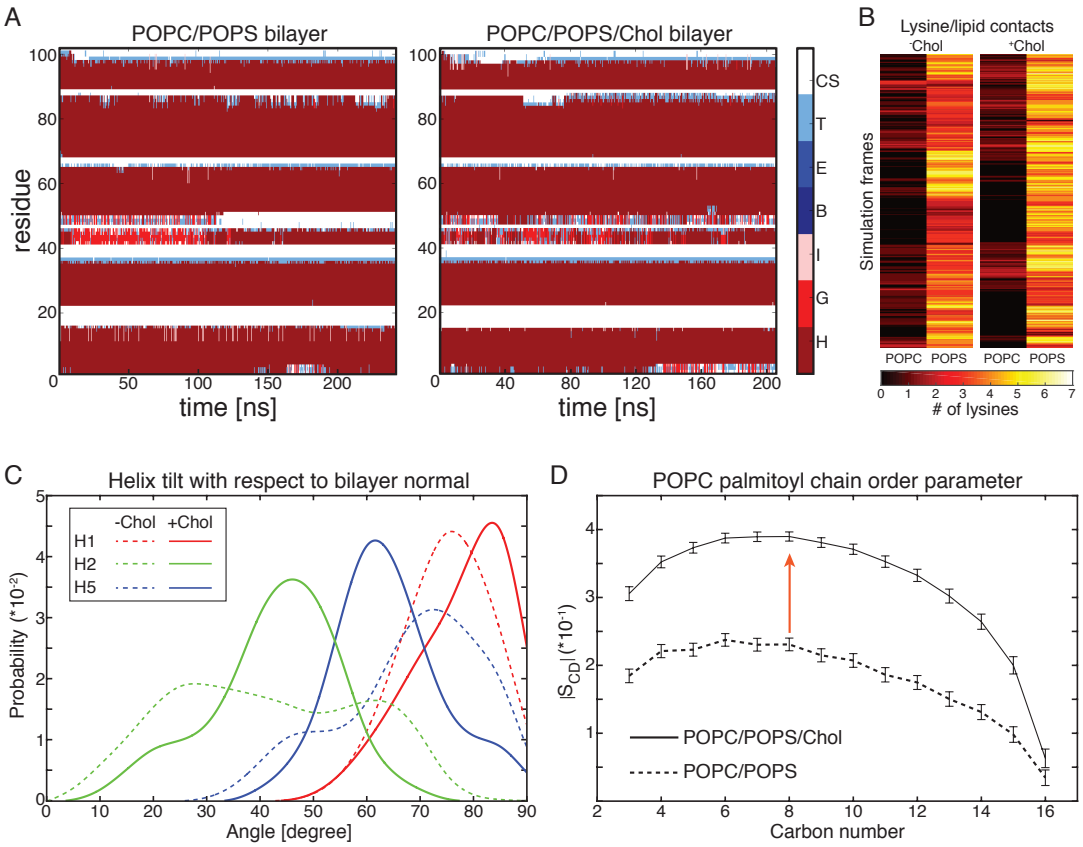

Figure C6. (A) Time evolution of MA's secondary structure in bilayers composed of POPC/POPS 70/30 mol% (left) or POPC/POPS/Chol 34/30/36 mol% (right). The secondary structure assignment of each residue was calculated with the DSSP software. They are as follows: H, alpha helix; G, 3-turn helix; I, pi helix; B, residue in isolated beta-bridge; E, extended beta sheet; T, hydrogen bonded turn; and CS, coil and bend. (B) Heat map of lysine-lipid contacts defined as having no more than 4 Å distance between the centers of mass of the NH_3 Lysine group and either the serine or phosphate groups on the lipid headgroups. Each row represents a single frame and the color denotes the number of instantaneous lysine-POPC or lysine-POPS contacts. Shown is data from the last 100 ns of three replica simulations for each system. (C) Tilt distributions of helices 1, 2 and 5 with respect to bilayer normal. The helices direction vectors are defined by the Cα atoms of residues E2 and K13, K23 and Q34, and E70 and A84, respectively, and the bilayer normal is the z-dimension of the simulation cell. The broad distributions in the absence of Chol indicate the dynamic nature of MA orientation with respect to the membrane (dashed lines, Movie S1A), which becomes more stable upon the addition of Chol (solid lines, Movie S1B). (D) The acyl chain order parameter of the palmitoyl chain of POPC, S_{CD}, increases by more than 65% in the presence of Chol as denoted by the red arrow.

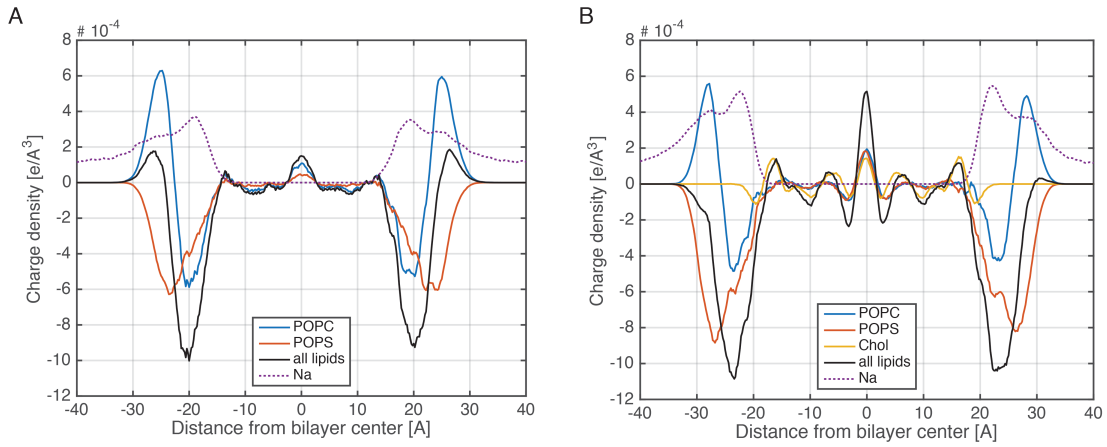

Figure C7. Charge density of POPC (blue), POPS (red), Chol (yellow), all lipids (black) and sodium (dashed purple line) from the two bilayer-only simulations of POPC/POPS (A) and POPC/POPS/Chol (B). The positively charged choline group on the POPC headgroups counteracts the negatively charged serine group on the POPS headgroups, and depending on the PC/PS ratio, the net effect is the accumulation of a higher (A) or lower (B) positive charge density on the bilayer surface (~ 27 and 30 Å, respectively). Note that since the charge density calculation is performed at high resolution (slabs in z with thickness of 0.2 Å) on individual atoms with assigned partial charges, relative imbalances in the distributions of hydrogen and carbon atoms result in a peak of positive charge density at the interface between the two leaflets. If the calculation is instead performed on the neutral chemical atomic groups (e.g. methylene, methyl), instead of the individual atoms, the positive density at the midplane would disappear.

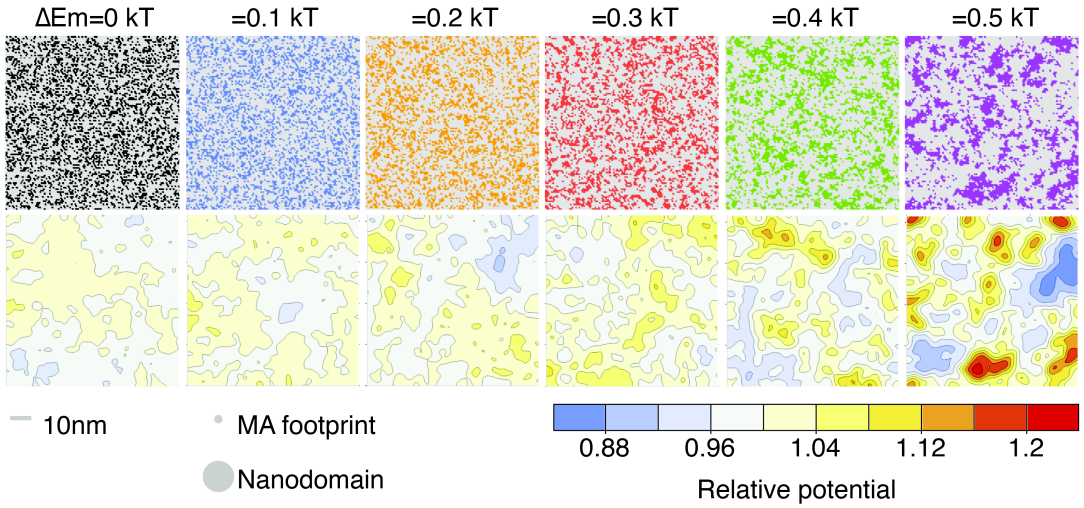

Figure C8. Non-ideal mixing does not induce large changes in membrane surface potential but may influence the spatial organization of bound protein. *Upper*, plots of the lateral distribution of a binary lipid mixture (70/30 mol% neutral/charged) obtained from Monte Carlo lattice simulations. Increasing the unfavorable pairwise interaction energy ΔEm results in larger clusters of the charged lipid (colored regions) within the neutral lipid matrix (gray regions). *Lower*, corresponding maps of the relative electrostatic surface potential calculated 3 Å above the bilayer surface and normalized to the potential of a uniformly mixed bilayer having the same average charge density. Also displayed for reference are the relative sizes of the MA protein (4 nm diameter) and a lipid nanodomain (15 nm diameter [8]). Scale bar 10 nm.

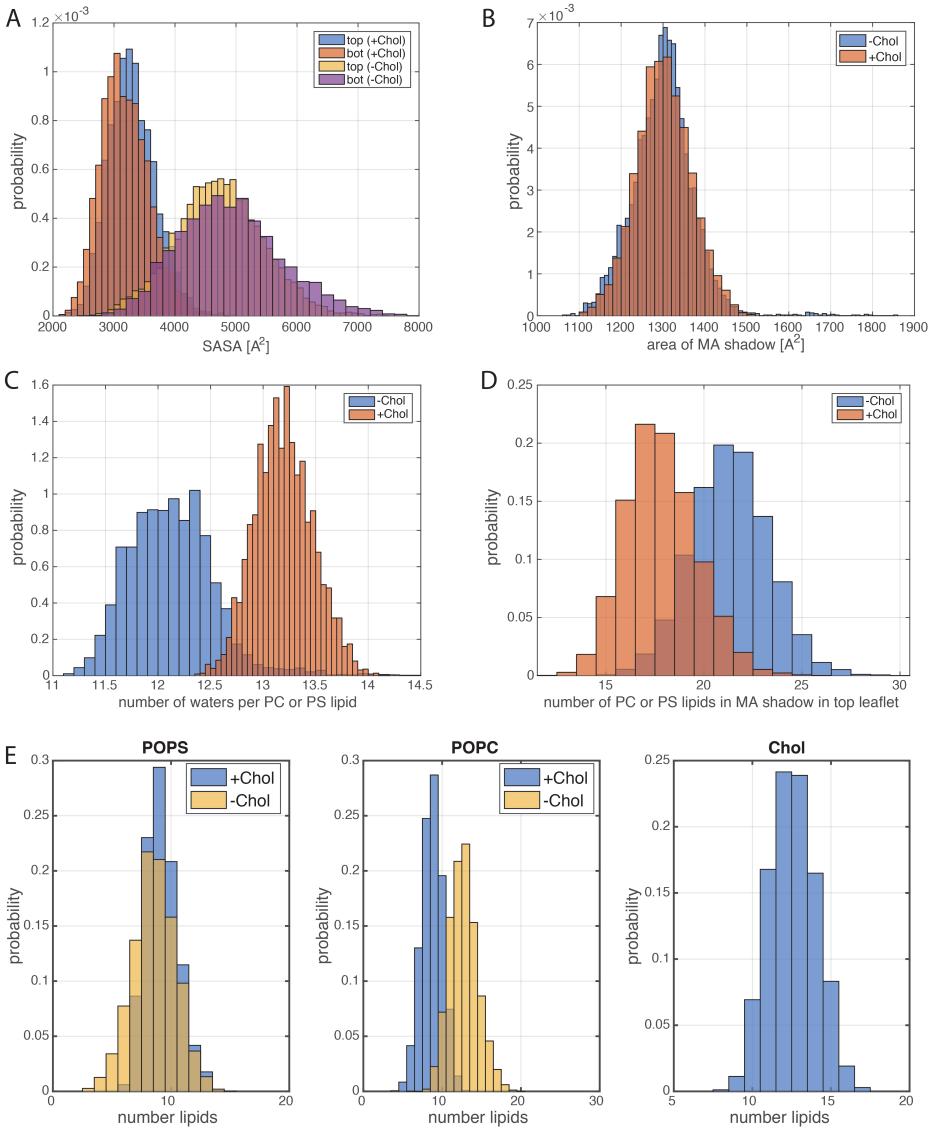

Figure C9. (A) Solvent exposed surface area (SASA) of each leaflet of the bilayer patch in the MA shadow. The MA shadow is defined as the set of atoms whose x and y coordinates are within 3 Å of the x and y coordinates of any protein atom. MA is interacting directly with the top leaflet. (B) Area of the MA shadow calculated as the area of the convex hull containing all 2D atomic coordinates in the MA shadow. (C) Distribution of the number of water molecules per POPC or POPS headgroup calculated from the bilayer-only simulations. A water per headgroup is defined as a water molecule within 3 Å of any lipid atom of a POPC or POPS lipid. (D) Distribution of the number of POPC or POPS lipids in the top leaflet from the MA-bilayer trajectories, whose phosphate atoms are within the MA shadow. (E) Number of different lipid counts in the top leaflet of the bilayer patch in the MA shadow in the two systems. POPS and POPC are represented with their phosphate atoms and Chol with its O3 atom. All distributions in this figure were constructed from calculations performed across all frames of the respective simulation trajectories.

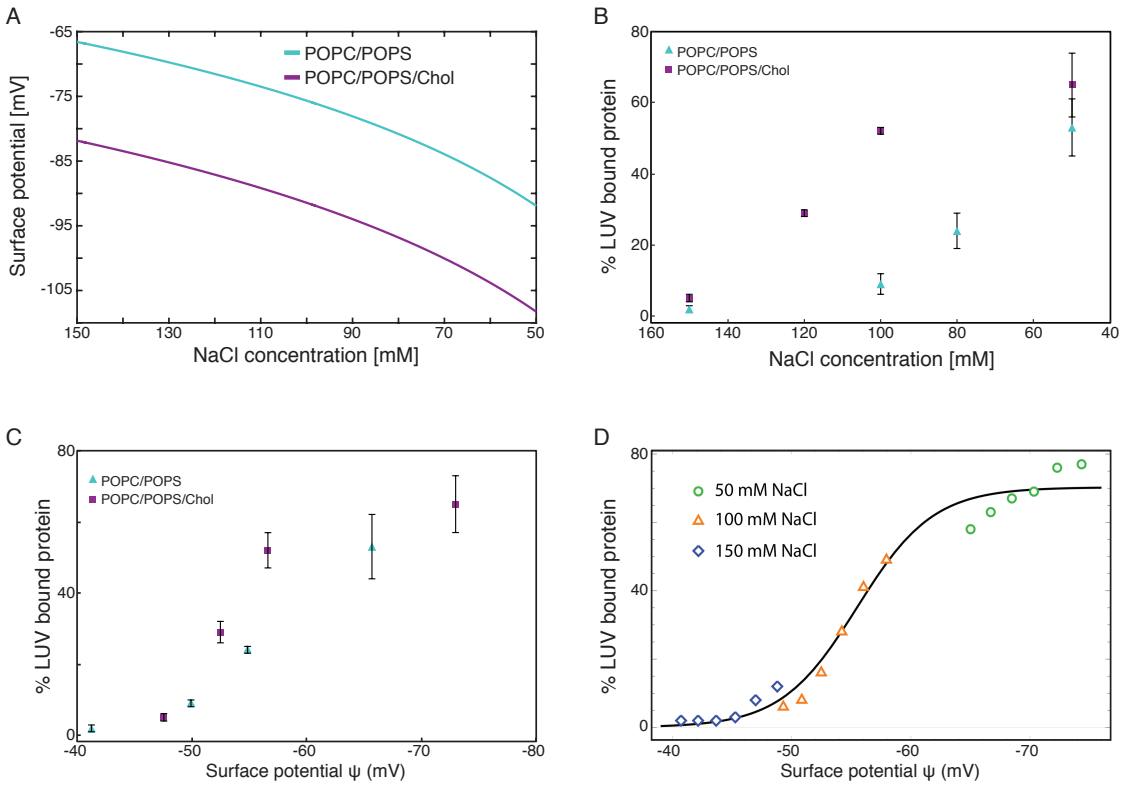

Figure C10. RSV MA membrane association as a function of NaCl concentration. (A) Example of a calculated membrane surface potential as a function of increasing NaCl concentrations for POPC/POPS (70/30 mol%) (light blue) and POPC/POPS/Chol (34/30/36 mol%) (purple) bilayers. (B) % of LUV-bound MA plotted against decreasing NaCl concentration. (C) Binding data from B plotted against calculated membrane surface potential. (D) Best sigmoidal fit to the MA binding data versus surface potential from Fig. 4.5F (see text for more details).

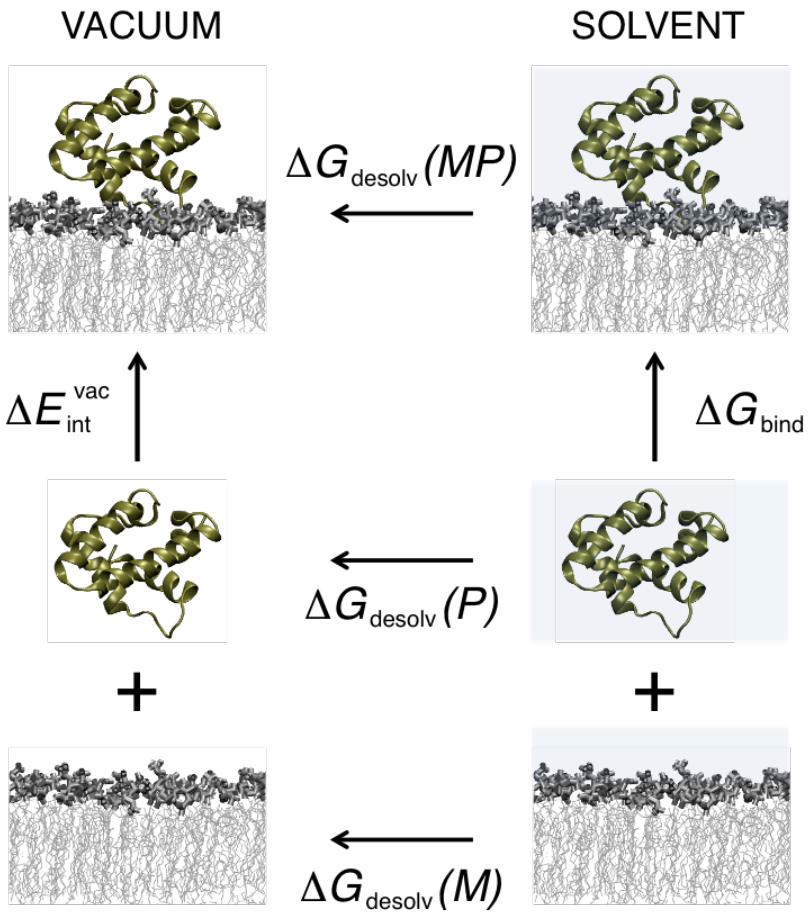

Figure C11. Thermodynamic cycle underlying the MM-GBSA method. For each frame of the trajectory, the binding free energy ΔG_{bind} is estimated from the vacuum interaction energy and the desolvation penalties for each binding partner and the complex.

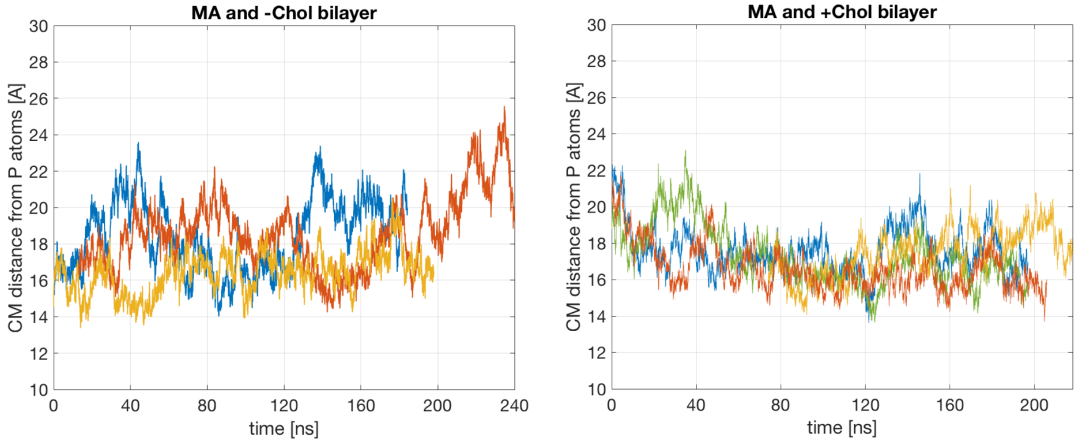

Figure C12. Fluctuations of the distance between MA and bilayer surface. Time evolution of the MA-bilayer distance defined as the distance in z between the center of mass of the protein and the center of mass of the phosphate atoms in the MA-proximal leaflet. Data is shown for the –Chol (left) and +Chol (right) systems. Colors denote different replica simulations (or in the latter also proteins interacting with different leaflets).

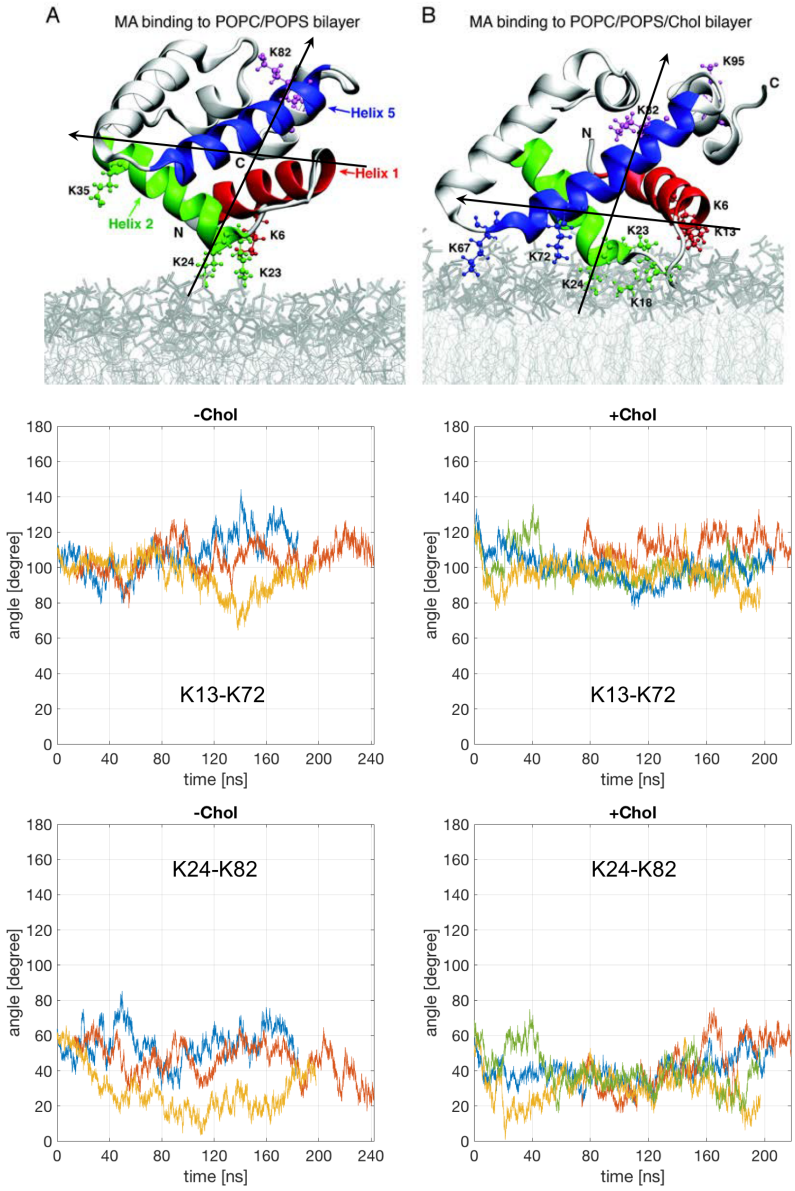

Figure C13. Orientation of MA with respect to the bilayer surface. *Top* Fig. 4.2AB with two axes (director vectors) shown, defining the orientation of MA relative to the bilayer surface: one, connecting the Cα atoms of K13 and K72, and another one connecting the Cα atoms of K24 and K82. Time evolution of the tilt angle of each axis (middle and bottom rows) with respect to the bilayer normal (z dimension of the simulation box) is shown for the –Chol (left) and +Chol (right) systems. Colors denote different replica simulations (or in the latter also proteins interacting with different leaflets). After about 80 ns of initial relaxation, the tilts fluctuate ~103º for K13-K72 and ~41º for K24-K82 with standard deviations within 10 degrees for individual replicas, and within 16 or 10 degrees across different replicas for –Chol and +Chol systems respectively.

APPENDIX D

Table D1. Information and results for 3 different simulations run for the asymmetric bilayers in Example #1 and Example #2 from Chapter 6: number of lipids in the top (Ntop) and bottom (Nbot) leaflets; total simulation time, last converged portion of the trajectory (convergence of box fluctuations is determined with the method from [196]) and number of frames used for analysis; local leaflet K_A-s and their errors calculated with the method from Chapter 3.2; tension of the top and bottom leaflets; bilayer K_A calculated as the harmonic mean of the local leaflet K_A-s as explained in Chapter 3.2 and used to estimate the ideal number of lipids; bilayer K_A calculated from the fluctuations of the simulation box and displayed for comparison with errors calculated as explained in Chapter 3.2; and the fixed and predicted number of lipids in the two leaflets.

Example #1	Simulation 1	Simulation 2	Simulation 3
Ntop start (DOPC)	94	95	61
Nbot start (SOPC)	100	100	64
simulation time, total [ns]	112	287	432
simulation time, analysis [ns]	112	225	193
number of frames for analysis	11265	11225	9692
Local K_A of top leaflet [mN/m]	224 (26)	320 (30)	260 (32)
Local K_A of bottom leaflet [mN/m]	232 (32)	218 (32)	236 (32)
Tension of top leaflet, T_T [mN/m]	1.2	0.5	-0.9
Tension of bottom leaflet, T_B [mN/m]	-1.2	-0.5	0.9
Bilayer K_A (harmonic mean)	228 (20)	259 (25)	247 (23)
Bilayer K_A (box fluctuations)	216 (35)	270 (33)	289 (33)
Ntop (predict)	**95**	**95**	**61**
Nbot (fix)	100	100	64

Example #2	Simulation 1	Simulation 2	Simulation 3
Ntop start (8:2 DPPC/Chol)	135	135	135
Nbot start (SOPC)	100	99	86
simulation time, total [ns]	548	573	1008
simulation time, analysis [ns]	138	140	660
number of frames for analysis	6913	7000	11000
Local K_A of top leaflet [mN/m]	3282 (184)	3360 (338)	11,696 (894)
Local K_A of bottom leaflet [mN/m]	646 (92)	414 (66)	112 (24)
Tension of top leaflet, T_T [mN/m]	5.7	2.2	-10.7
Tension of bottom leaflet, T_B [mN/m]	-5.7	-2.2	10.7
Bilayer K_A (harmonic mean)	1080 (129)	737 (105)	222 (47)
Bilayer K_A (box fluctuations)	782 (112)	731 (114)	1147 (80)
Ntop (fix)	135	135	135
Nbot (predict)	**99**	**98-99**	***93-97****

* The bilayer looks unstable (Fig. D1B), which prevents the accurate calculation of its properties

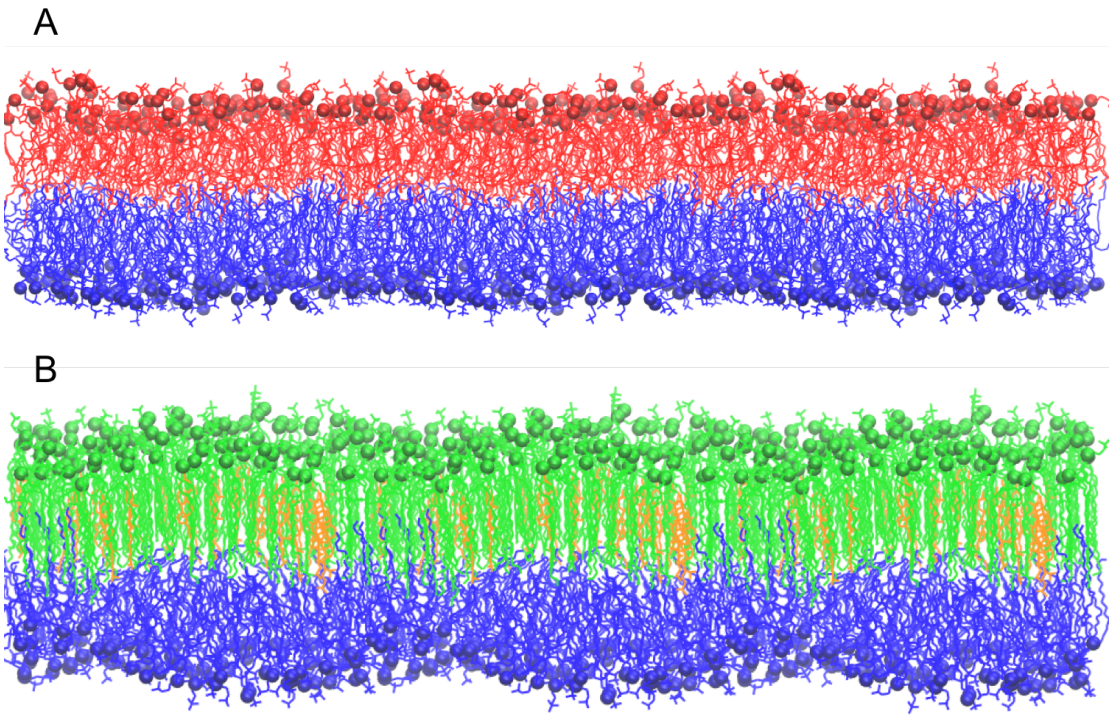

Figure D1. Snapshots of the last frames of Simulation 1 from Example #1 (A) and Simulation 3 from Example #2 (B). DOPC is shown in red, SOPC in blue, DPPC in green and Chol in orange. Phosphate atoms on the lipid headgroups are displayed as spheres while Chol and the lipid acyl chains are shown as sticks. Water and hydrogen atoms are omitted for clarity. Each snapshot consists of the main simulation cell and two periodic images.

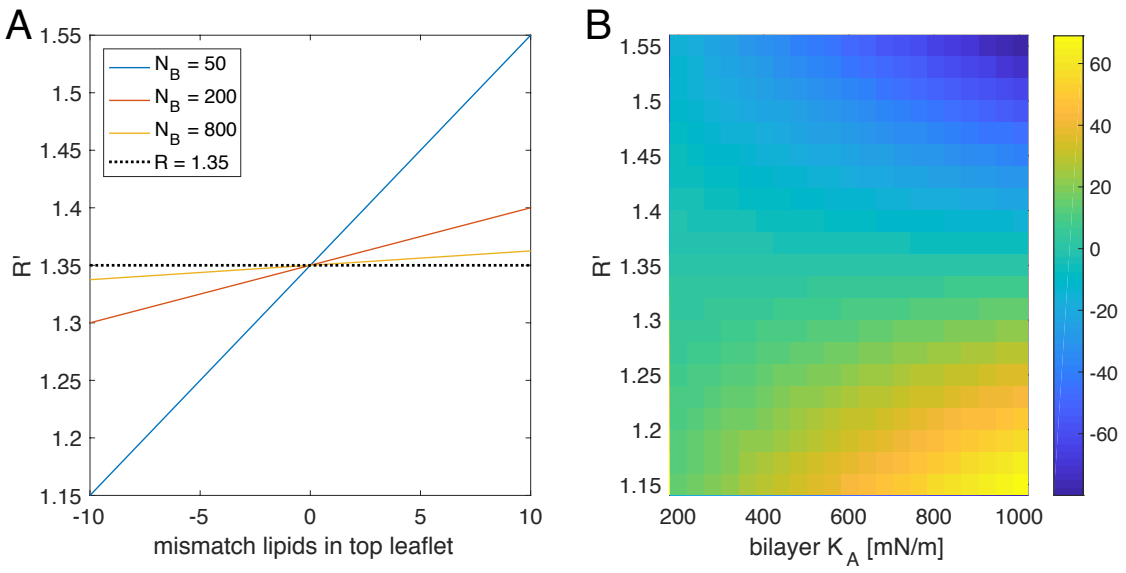

Figure D2. Effect of deviations from the ideal lipid ratio on leaflet tension. A. Changes in the lipid ratio $R' = N'_T/N'_B$ as a function of the number of mismatch lipids in the top leaflet for bilayers with ideal lipid ratio $R = 1.35$ and different size. B. Effect of R' and the bilayer K_A on the tension of the top leaflet, T_T, using Eq. 6.4. The color scale denotes T_T in units of mN/m. See Chapter 6 for more details.

Simulation details and analysis

All bilayers were constructed with CHARMM-GUI [141, 142, 144] by specifying the number of each type of lipid in each leaflet and setting the number of water molecules per lipid to 45. The systems were simulated with NAMD [155] using the CHARMM36 force field for lipids [156, 195]. The initial equilibration followed the protocol provided by CHARMM-GUI. The parameters for the subsequent production run were the same as the ones described in Chapter 3.2. All simulations were performed at 25°C (298.15 K).

The tension of each bilayer leaflet was obtained from the lateral pressure profile of the bilayer. The latter was calculated as described in Chapter 3.2. Briefly, the trajectory was first centered on the average z position of all terminal methyl groups of the lipids in both leaflets. The system was divided into a fixed number of slabs with thickness around 0.8 Å, and the three components of the pressure tensor were calculated in each slab with NAMD using the stored atomic coordinates and velocities. The normal component of the pressure tensor $p_N = p_{zz}$ was corrected to a constant value and the pressure in each slab z was obtained from $p(z) = p_L(z) - p_N$ where $p_L = (p_{xx} + p_{yy})/2$ is the tangential component of the pressure tensor. The tension in the two leaflets is then:

$$T_B = \int_{-\infty}^{0} p(z)\, dz \qquad T_T = \int_{0}^{\infty} p(z)\, dz$$

APPENDIX E

Calculation of forces restraining the order parameter at lipid chain carbon atoms

Let $S_{l,c,h}$ be the order parameter of lipid l at carbon c relative to hydrogen h.

Let α be the angle between the ch bond and the bilayer normal (assumed to be the z axis).

$$S_{l,c,h} = \frac{3\cos^2\alpha}{2} - \frac{1}{2}$$

Let R be the ch bond length and z_i be the z coordinate of atom i.

Then, $\cos\alpha = \left(z_{l,c,h} - z_{l,c}\right)/R$ and:

$$S_{l,c,h} = \frac{3\left(z_{l,c,h} - z_{l,c}\right)^2}{2R^2} - \frac{1}{2}$$

$$\frac{\partial S_{l,c,h}}{\partial z_{l,c,h}} = \frac{3\left(z_{l,c,h} - z_{l,c}\right)}{R^2}$$

$$\frac{\partial S_{l,c,h}}{\partial z_{l,c}} = -\frac{3\left(z_{l,c,h} - z_{l,c}\right)}{R^2}$$

Let U^{tot} be the total potential energy of the atoms to be modified, N is the number of lipids in the bilayer, and C is the number of carbon atoms whose order is to be restrained. Then,

$$U^{\text{tot}} = \sum_{l=1}^{N}\sum_{c=1}^{C}\sum_{h=1}^{2}\frac{1}{2}\kappa\left(S_{l,c,h}\left(z_{l,c}, z_{l,c,h}\right) - S_c^0\right)^2$$

The corresponding forces to be applied are as follows:

$$F_{l,c,h} = \frac{\partial U^{\text{tot}}}{\partial z_{l,c,h}} = \kappa\left(S_{l,c,h}\left(z_{l,c}, z_{l,c,h}\right) - S_c^0\right)\frac{3\left(z_{l,c,h} - z_{l,c}\right)}{R^2}$$

$$F_{l,c} = \frac{\partial U^{\text{tot}}}{\partial z_{j,k}} = -\sum_{h=1}^{2}\frac{\partial U^{\text{tot}}}{\partial z_{l,c,h}} = -\sum_{h=1}^{2}F_{l,c,h}$$

To preserve the average order parameter without overconstraining the local order of the carbon atoms, the potential energy and associated forces could be written as follows:

$$U^{\text{tot}} = \sum_{c=1}^{C} \frac{1}{2} \kappa \left(\frac{1}{2N} \sum_{l=1}^{N} \sum_{h=1}^{2} S_{l,c,h}\left(z_{l,c}, z_{l,c,h}\right) - S_c^0 \right)^2$$

$$F_{l,c,h} = \frac{\partial U^{\text{tot}}}{\partial z_{l,c,h}} = \kappa \left(\frac{1}{2N} \sum_{l=1}^{N} \sum_{h=1}^{2} S_{l,c,h}\left(z_{l,c}, z_{l,c,h}\right) - S_c^0 \right) \frac{3\left(z_{l,c,h} - z_{l,c}\right)}{2NR^2}$$

$$F_{l,c} = \frac{\partial U^{\text{tot}}}{\partial z_{l,c}} = -\sum_{h=1}^{2} \frac{\partial U^{\text{tot}}}{\partial z_{l,c,h}} = -\sum_{h=1}^{2} F_{l,c,h}$$

Thus, $F_{l,c}$ and $F_{l,c,h}$ were applied to the carbon 14 atoms and their hydrogen atoms, respectively, on the palmitoyl chains of the lipids in the top bilayer leaflet as explained in Chapter 7.

Table E1. aLUVs examined in this study. Shown are the acceptor and donor lipids; the type of the performed experimental measurement (Exp.); the nominal MβCD-to-donor (CD:D) and donor-to-acceptor (D:A) ratios; the overall fraction of donor lipid in the aLUVs measured with GC-MS (χ_{don}); the degree of asymmetry, i.e. fraction of donor lipid on the outer leaflet of the aLUVs (f_{out}), measured with NMR; and the resulting composition of the outer and inner leaflets of the aLUVs.

Acceptor*	Donor	Exp.	CD:D	D:A	χ_{don}	f_{out}	Composition DMPC/POPC or DPPC/(low-TM lip)
POPCd13	DMPC -d54	SAXS SANS	8	3	0.43	89%	0.77 / 0.23 (out) 0.10 / 0.90 (in)
POPCd31					0.42	89%†	0.75 / 0.25 (out) 0.09 / 0.91 (in)
POPC	DPPC/ C5PC	ESR	6	4	0.23	95%††	0.44 / 0.56 (out) 0.02 / 0.98 (in)
DEPC					0.33		0.63 / 0.37 (out) 0.03 / 0.97 (in)
SOPC					0.26		0.49 / 0.51 (out) 0.03 / 0.97 (in)
DOPC					0.24		0.46 / 0.54 (out) 0.02 / 0.98 (in)
POPC/C5PC	DPPC				0.22		0.42 / 0.58 (out) 0.02 / 0.98 (in)
DEPC/C5PC					0.34		0.65 / 0.35 (out) 0.03 / 0.97 (in)
SOPC/C5PC					0.25		0.48 / 0.52 (out) 0.03 / 0.97 (in)
DOPC/C5PC					0.23		0.44 / 0.56 (out) 0.02 / 0.98 (in)

* All acceptors were doped with 5 mol% POPG to ensure that the vesicles had a single bilayer.

† Assumed from the aLUV with POPCd13 acceptor and DMPCd54 donor.

†† Assumed from f_{out} in aLUVs with POPCd13 acceptor and DPPC donor [4].

Table E2. Symmetric (sym) and asymmetric (asym) LUVs examined with small-angle scattering. The composition of the aLUVs is listed in Table E1. Shown are the percent D_2O in the solvent and the types of measurement performed on each sample.

sample	sym/asym	% D_2O	SANS	SAXS
DMPCd54/POPCd13	asym	100	+	+
DMPCd54/POPCd31		100	+	+
		80	+	-
DMPCd54/POPCd13 0.75/0.25	sym	100	+	-
DMPCd54/POPCd31 0.75/0.25		100	+	-

Table E3. Partition coefficients of C5PC in the examined binary mixtures. Shown are the tested ranges of sample compositions guided from literature results; the corresponding fractions of DPPC in the fluid (χ^{L_α}) and gel (χ^{L_β}) phases determined from analysis of SAXS data at 20-22°C (see Fig. E2); the fraction of DPPC (χ_{DPPC}) in a symmetric sample with the composition of the outer leaflet of the aLUVs from Table E1, assuming f_{out} is 100%; the fraction of L_α in the sample obtained from linear combination of the ESR spectra ($f_p^{L_\alpha}$) collected at 19-20°C; and the resulting partition coefficient (K_p) of C5PC (see Section 7.2.9).

Binary mixture	LHS		RHS		χ_{DPPC}	$f_p^{L_\alpha}$	K_p [e]
	Range	χ^{L_α}	Range	χ^{L_β}			
DPPC/POPC	0.15-0.45[a]	0.3	0.80-0.95[a]	0.9	0.45	0.880	2.4
DPPC/DEPC	0.10-0.30[b]	0.2	0.60-0.85[b]	0.8	0.67	0.217	1.0
DPPC/SOPC	0.05-0.35[c]	0.25	0.65-0.95[c]	0.925	0.51	0.865	4.0
DPPC/DOPC	0.25-0.40[d]	0.35	0.80-0.98[d]	1	0.48	0.959	5.6

[a] [423, 424]; [b] [36, 425]; [c] [424, 426]; [d] [427-429]; [e] values greater than 1 indicate preference for L_α phase

Table E4. Best-fit NLSL parameters for uniform mixtures. All common parameters were fixed while individual parameters were varied in small subsets as described in Section 7.2.8. For parameter definitions see Table S1 in Ref. [332]. Data is shown for the binary mixtures of DPPC and POPC, and DPPC and DEPC. Listed are the best-fit parameters for the spectra of the symmetric acceptor samples and the inner leaflet of the aLUVs obtained after incubation with ascorbate as described in Section 7.2.6. The best fits are shown in Fig. E6.

parameter	POPC acceptor LUV	DPPC/POPC aLUV inner leaflet	DEPC acceptor LUV	DPPC/DEPC aLUVs inner leaflet
(g_{xx}, g_{yy}, g_{zz})	(2.0087, 2.00593, 2.0022)			
(A_{xx}, A_{yy}, A_{zz})	(5.5, 5.5, 33.3)			
$(2I, L_{emx}, L_{omx})$	(2, 8, 5)			
$(K_{mx}, M_{mx}, P^I_{mx})$	(4, 3, 2)			
n_{MOMD}	23			
$R_\parallel$	7.8			
$W_\parallel$	0.8	0.8	0.9	0.9
$W_\perp$	0.77	0.77	0.9	0.9
Δ_g	0.524	0.524	0.403	0.4
c20	3.218	3.316	3.319	3.273
c40	-1.16	-1.16	-1.169	-0.9
$R_\perp$	7.3679	7.3073	7.7089	7.6538
D20	0.4977	0.5095	0.5089	0.5332
D40	0.0525	0.0631	0.062	0.105

Table E5. Best-fit NLSL parameters for phase separated mixtures. All common parameters were fixed while individual parameters were varied in small subsets as described in Section 7.2.8. For parameter definitions see Table S1 in Ref. [332]. Data is shown for the binary mixtures of DPPC and POPC, and DPPC and DEPC. Listed are the best-fit parameters for the spectra of: (1) the symmetric samples with the composition of the corresponding aLUV's outer leaflet assuming f_{out} is 100% (symmetric outer), and (2) the outer leaflet of the aLUVs obtained by placing the spin probe only in the donor vesicles as described in Section 7.2.6 (aLUV outer leaflet). The best fit for each sample was achieved by assuming co-existence of two distinct environments of the spin probe, denoted as phase 1 (ph1) and phase 2 (ph2). The best-fits are shown in Fig. E6.

parameter	DPPC/POPC symmetric outer		DPPC/POPC aLUV outer leaflet		DPPC/DEPC symmetric outer		DPPC/DEPC aLUV outer leaflet	
	ph1	ph2	ph1	ph2	ph1	ph2	ph1	ph2
(g_{xx}, g_{yy}, g_{zz})	(2.0087, 2.00593, 2.0022)							
(A_{xx}, A_{yy}, A_{zz})	(5.5, 5.5, 33.3)							
$(2I, L_{emx}, L_{omx})$	(2, 8, 5)							
$(K_{mx}, M_{mx}, P^I_{mx})$	(4, 3, 2)							
n_{MOMD}	23							
$R_{\parallel}$	7.8							
$W_{\parallel}$	0.8		0.8		0.8		0.6	
$W_{\perp}$	0.77		0.801		0.9		0.9	
Δ_g	0.44		0.747		0		0.8	
c20	4.155	3.079	3.5	4.427	2.768	5	2.648	5
c40	-0.073	-1.195	-0.424	-3.142	-0.099	-4.144	-0.099	-3.831
$R_{\perp}$	7.5882	7.6758	7.6301	7.763	7.3456	7.812	7.5736	7.7798
D20	0.7165	0.4768	0.6155	0.4346	0.5602	0.4083	0.5419	0.4274
D40	0.3632	0.0318	0.2229	-0.116	0.1991	-0.1724	0.1844	-0.1454
Phase fraction [%]	15.8	84.2	31.8	68.2	57.6	42.4	56.4	43.6

Table E6. Simulated bilayers. Shown are the leaflet compositions (unless noted otherwise, the composition was the same in the two leaflets); the number of lipids of each type in the leaflet; the fixed temperature of the simulation; the total simulation time and the last portion of it used for analysis. For uniform mixtures the time for analysis was determined from the convergence of the bilayer area (the *xy* area of the simulation box) as estimated with the algorithm from [196]. For bilayers in which at least one leaflet was phase separated (denoted with '*') the time for analysis was determined from the convergence of both the bilayer area and the fraction of L_α (or L_β). Phase fractions were calculated as described in Section 7.2.11. For two of the bilayers (DPPOout and DPPOasym) a second replica simulation was performed of a newly constructed bilayer with the same composition. The two replica simulations were analyzed jointly in the subsequent analysis.

bilayer	composition	# lipids in leaflet	Temp [°C]	Simulation time [ns]	
				Total	Analysis
DMPOout	DMPC/POPC 0.75 / 0.25	75 / 25	25	738	738
DMPOin	DMPC/POPC 0.10 / 0.90	10 / 90	25	471	471
DMPOasym	DMPC/POPC 0.75 / 0.25 (top) 0.10 / 0.90 (bot)	78 / 26 (top) 10 / 90 (bot)	25	423	280
DPPOout*	DPPC/POPC 0.43 / 0.57	43 / 57	20	1499	259
				1557	600
DPPOin	DPPC/POPC 0.02 / 0.98	2 / 98	20	694	694
DPPOasym*	DPPC/POPC 0.43 / 0.57 (top) 0.02 / 0.98 (bot)	46 / 61 (top) 2 / 96 (bot)	20	1015	444
				1555	679
DPDEout*	DPPC/DEPC 0.60 / 0.40	60 / 40	20	659	312
DPDEin	DPPC/DEPC 0.03 / 0.97	3 / 97	20	772	560
DPDEasym*	DPPC/DEPC 0.60 / 0.40 (top) 0.03 / 0.97 (bot)	71 / 48 (top) 3 / 97 (bot)	20	1918	1225

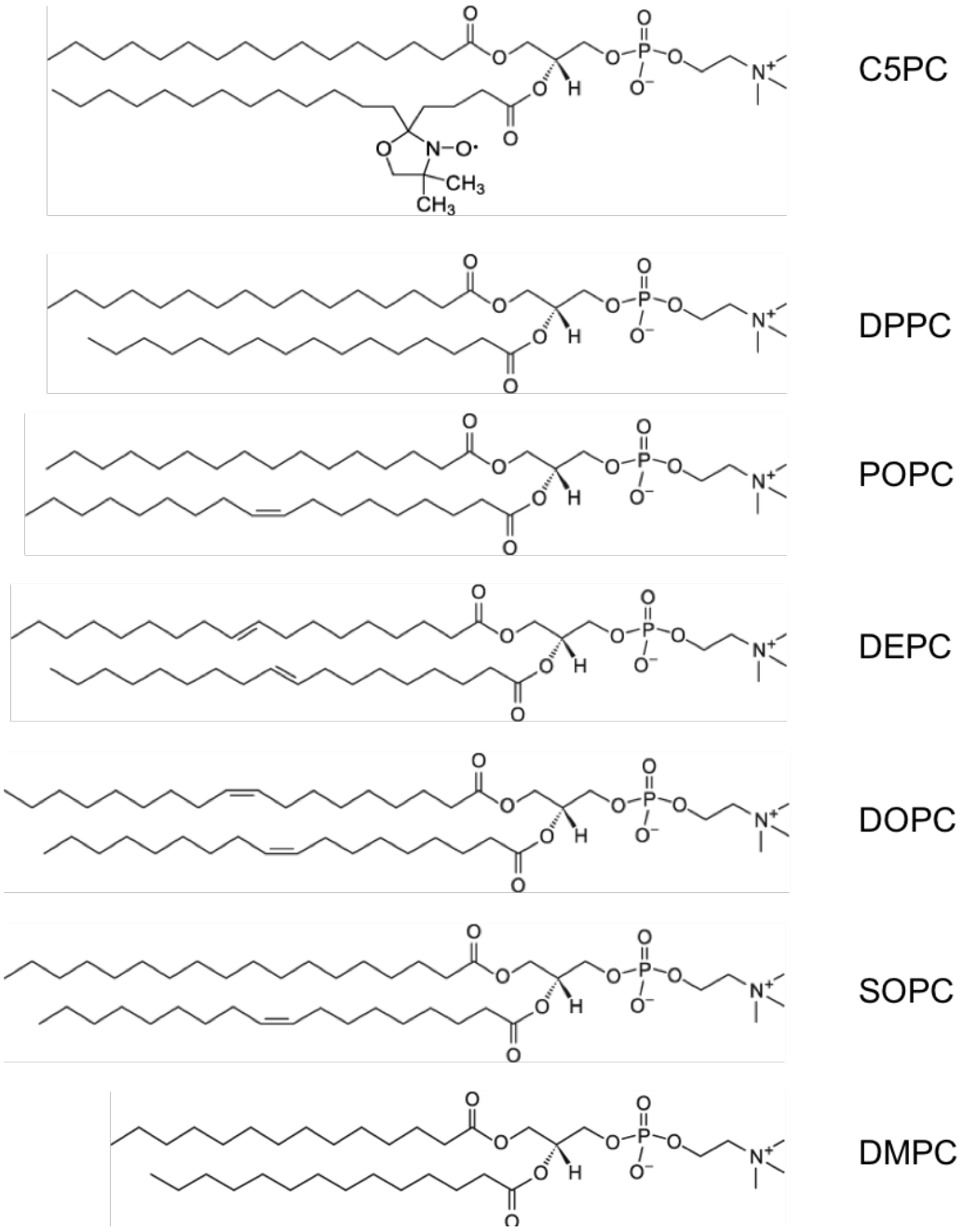

Figure E1. Chemical structures of the lipids examined in this study: 1-palmitoyl-2-stearoyl-(5-doxyl)-*sn*-glycero-3-phocphocholine (C5PC); 1,2-palmitoyl-*sn*-glycero-3-phosphocholine (DPPC); 1-palmitoyl-2-oleoyl-*sn*-glycero-3-phosphocholine (POPC); 1,2-dielaidoyl-*sn*-glycero-3-phosphocholine (DEPC); 1,2-dioleoyl-*sn*-glycero-3-phosphocholine (DOPC); 1-stearoyl-2-oleoyl-*sn*-glycero-3-phosphocholine (SOPC); and 1,2-dimyristoyl-*sn*-glycero-3-phosphocholine (DMPC).

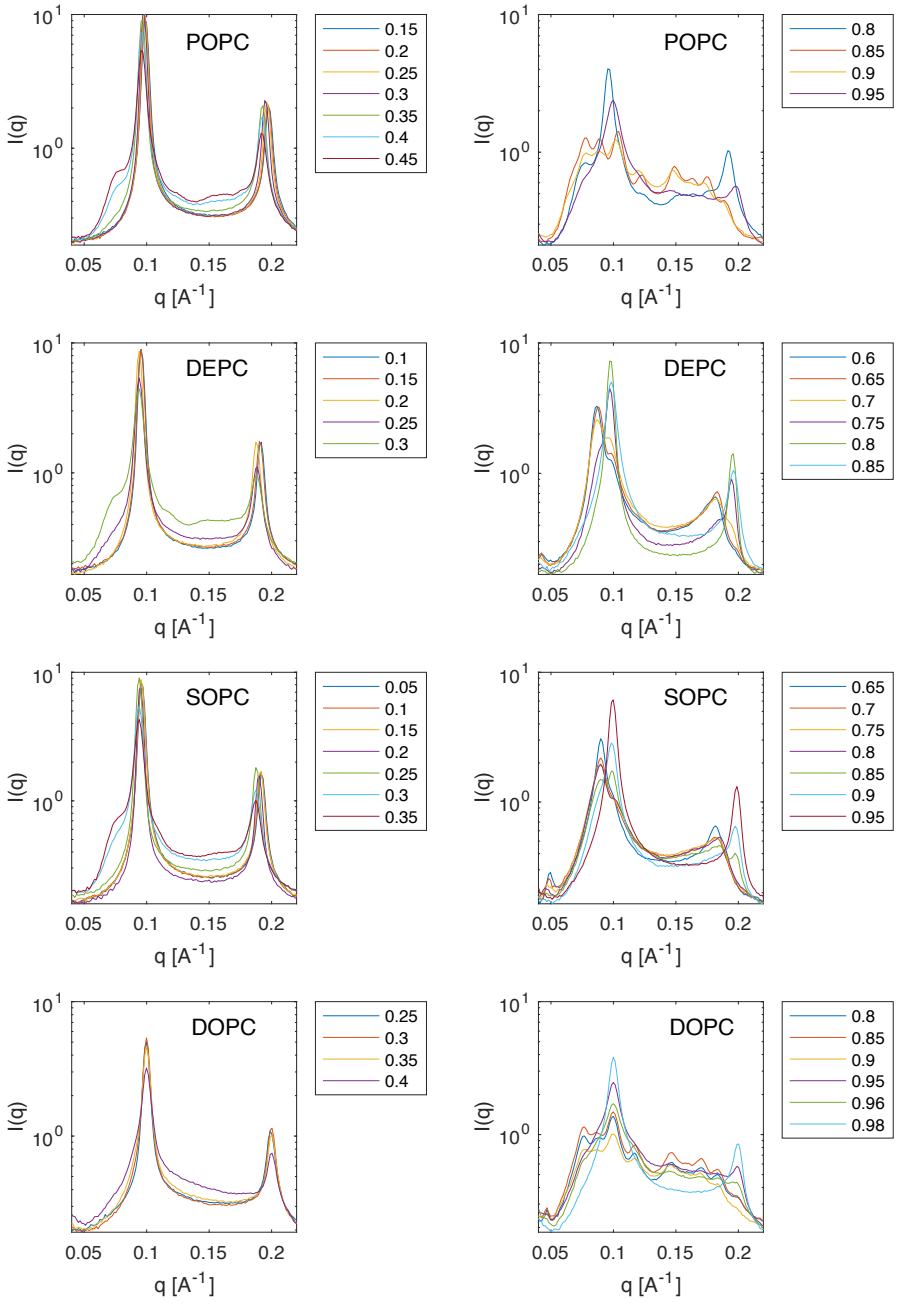

Figure E2. SAXS data for binary mixtures of DPPC and a low-melting lipid (POPC, DEPC, SOPC or DOPC). Each plot shows the variation in intensity as a function of the scattering vector q, and is labeled by the type of low-melting lipid present in the sample. Scattering was measured from MLVs made of a range of compositions around the LHS (left) and RHS (right) boundaries (see Table E3). Different colors denote the mole fraction of DPPC in the samples as indicated in the legend of each plot. All data was collected at 20°C, except for DPPC/POPC which was collected at 22°C.

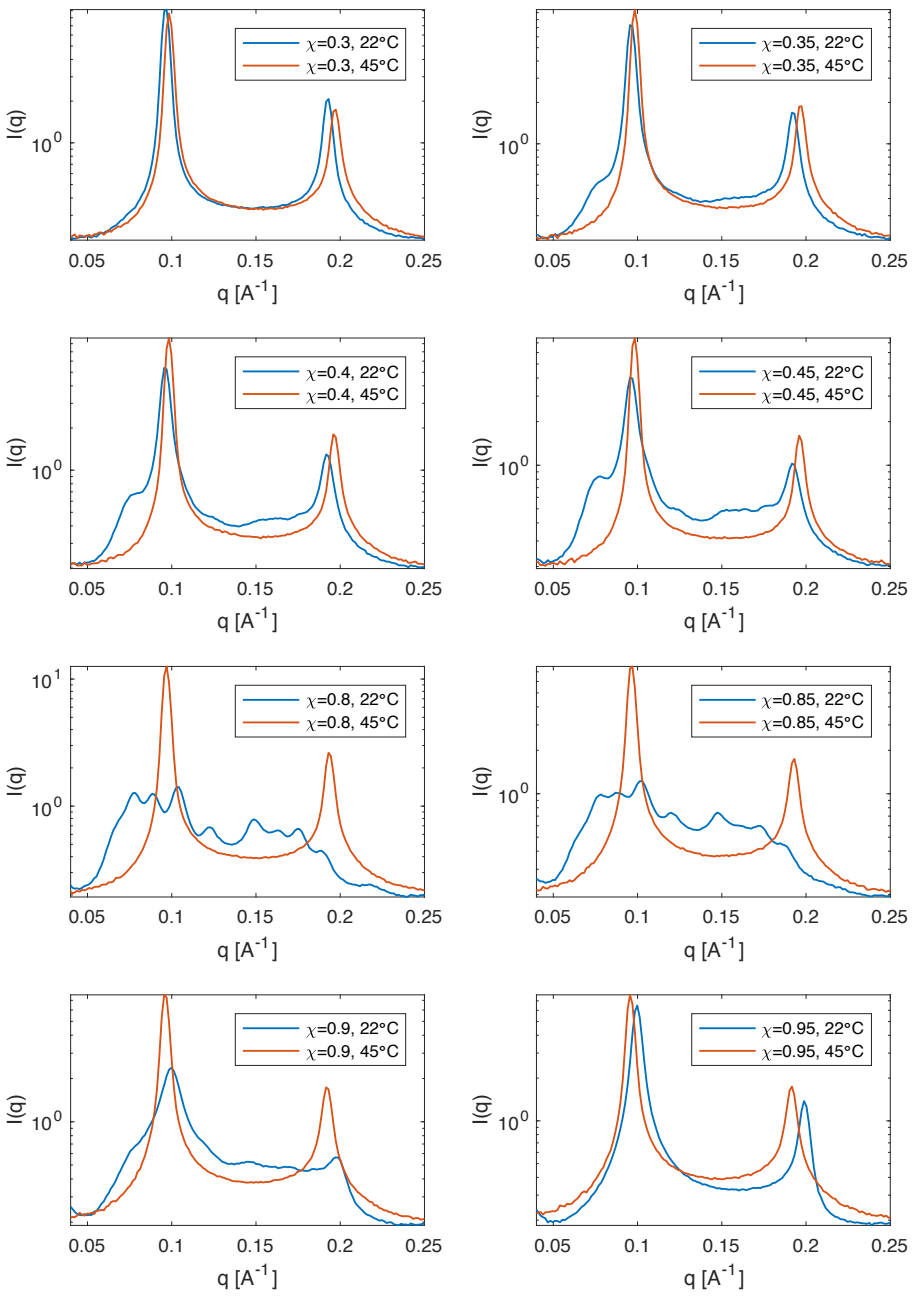

Figure E3. Comparison of SAXS form factors for mixtures of DPPC/POPC with different mole fractions of DPPC (χ) at 22°C and 45°C.

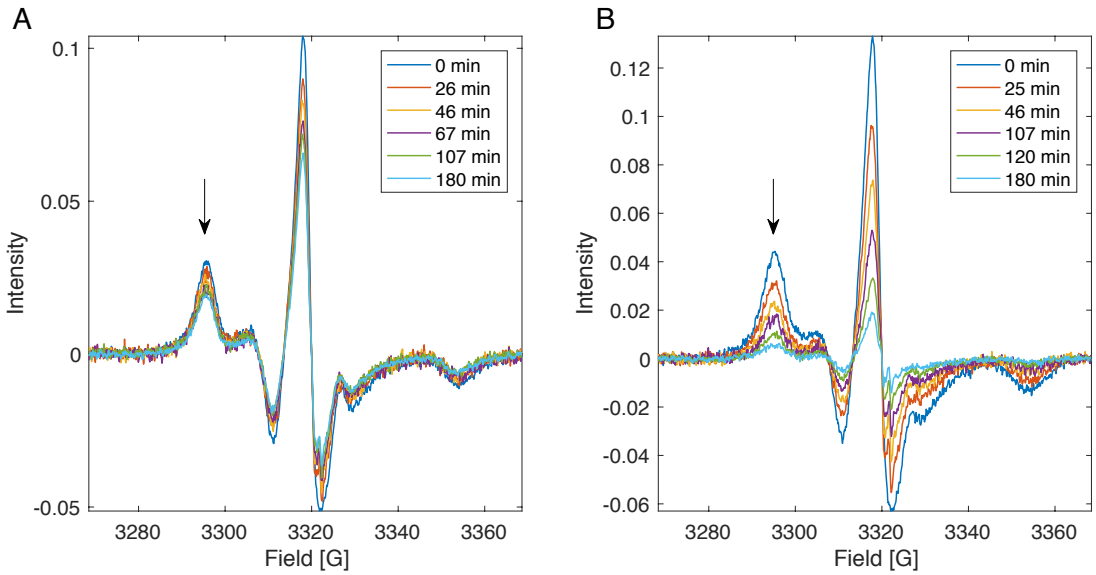

Figure E4. Interaction of ascorbate with the C5PC spin probe (SP). Shown are ESR spectra of the aLUVs with (A) POPC/C5PC acceptors and DPPC donors, and (B) POPC acceptors and DPPC/C5PC donors (see Table E1), measured at different time points after addition of ascorbate. The arrows indicate the peak whose intensity was measured to monitor the time evolution of the signal intensity plotted in Fig. 7.2.

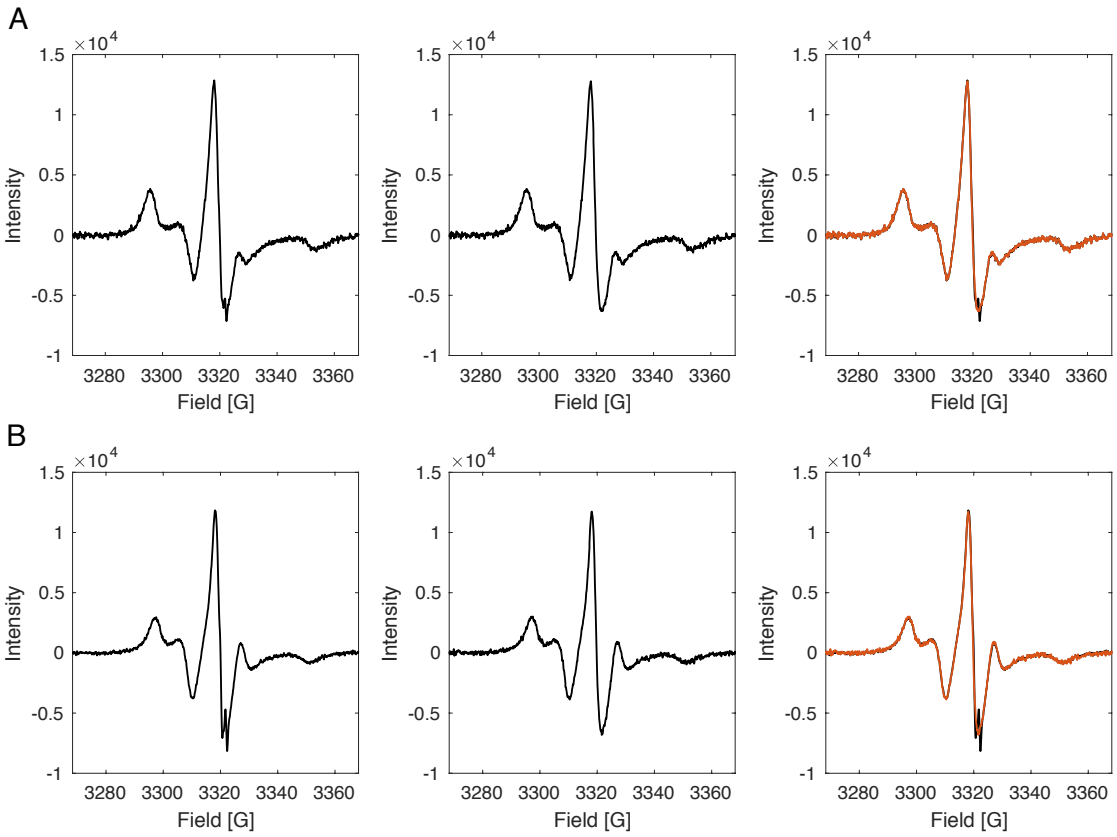

Figure E5. Subtraction of ascorbate signal from the ESR spectra of the DPPC/POPC (A) and DPPC/DEPC (B) aLUVs with the spin probe in the acceptors (see Table E1). The plot on the left shows the spectra after 3 h incubation with ascorbate; the plot in the middle shows the same spectra after the subtraction of the appropriately scaled spectrum of ascorbate in water, and the plot on the right shows an overlay of the original and subtracted spectra.

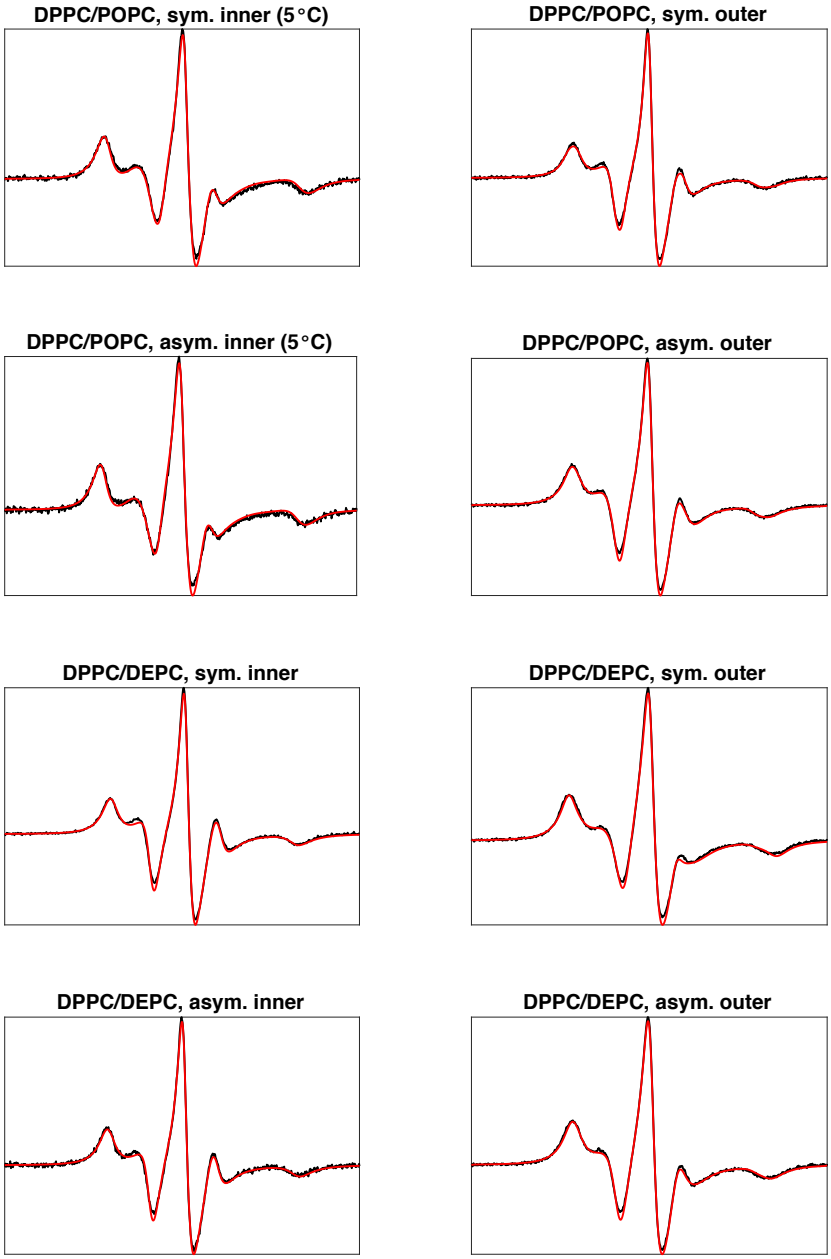

Figure E6. Best fits of the ESR data obtained with the NLSL software as described in Section 7.2.8. Each plot shows the raw data in black and the best fit in red. The sample names correspond to: the acceptor LUVs (sym. inner); the symmetric samples with the composition of the corresponding aLUV's outer leaflet assuming f_{out} is 100% (sym. outer); the aLUVs with SP in acceptors after 3 h incubation with ascorbate (asym. inner); and the aLUVs with SP in donors (asym. outer). All spectra were collected at 19-20°C unless otherwise noted. The corresponding best-fit parameters are listed in Tables E4-E5.

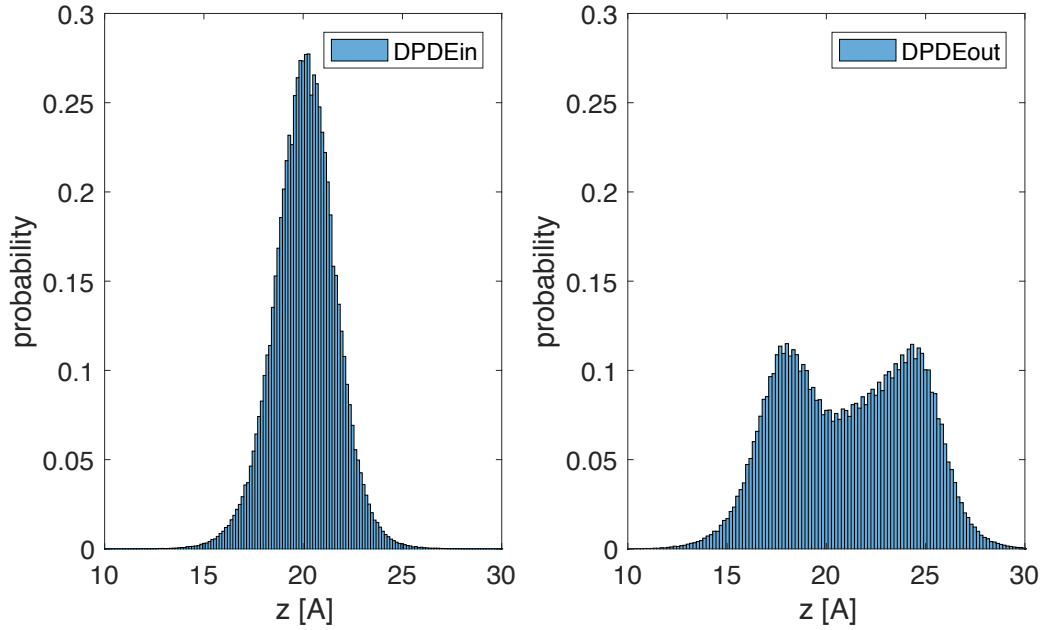

Figure E7. Distribution of the interpolated z-positions of the phosphorus atoms in the top leaflet of the uniformly mixed DPDEin bilayer (left) and the phase-separated DPDEout bilayer (right) (see Table E6 for the respective lipid compositions).

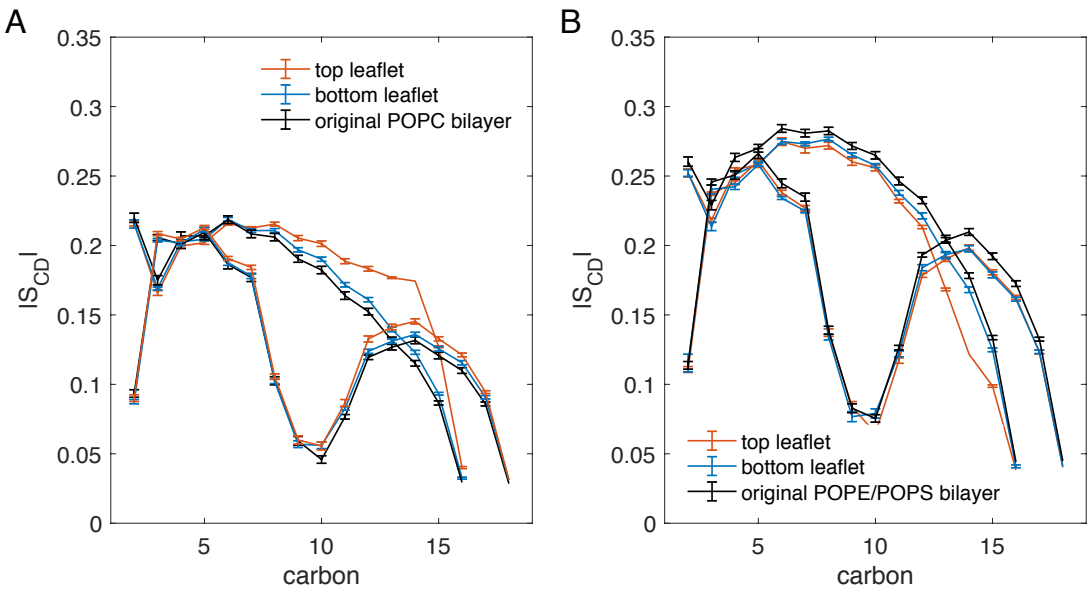

Figure E8. Effect of structural perturbation to one leaflet on the order parameter profiles of the lipids in both leaflets in symmetric POPC (A) and POPE/POPS 0.7/0.3 (B) bilayers. Shown are the profiles of the palmitoyl and oleoyl lipid chains, averaged over all lipids in the top and bottom leaflets of the unperturbed original bilayer (shown in black), and the perturbed bilayer (in red and blue, respectively) in which the average order parameter of carbon 14 in the palmitoyl chains of the lipids in the top leaflet was constrained to a different value (higher in POPC, and lower in POPE/POPS as explained in Chapter 7). The order parameter profiles of the POPE/POPS leaflets were calculated as a weighted average of the profiles of the POPE and POPS lipids with weights being the lipids mole fractions. Error bars are standard errors calculated from consecutive time blocks with length determined by the effective number of uncorrelated data points [196].

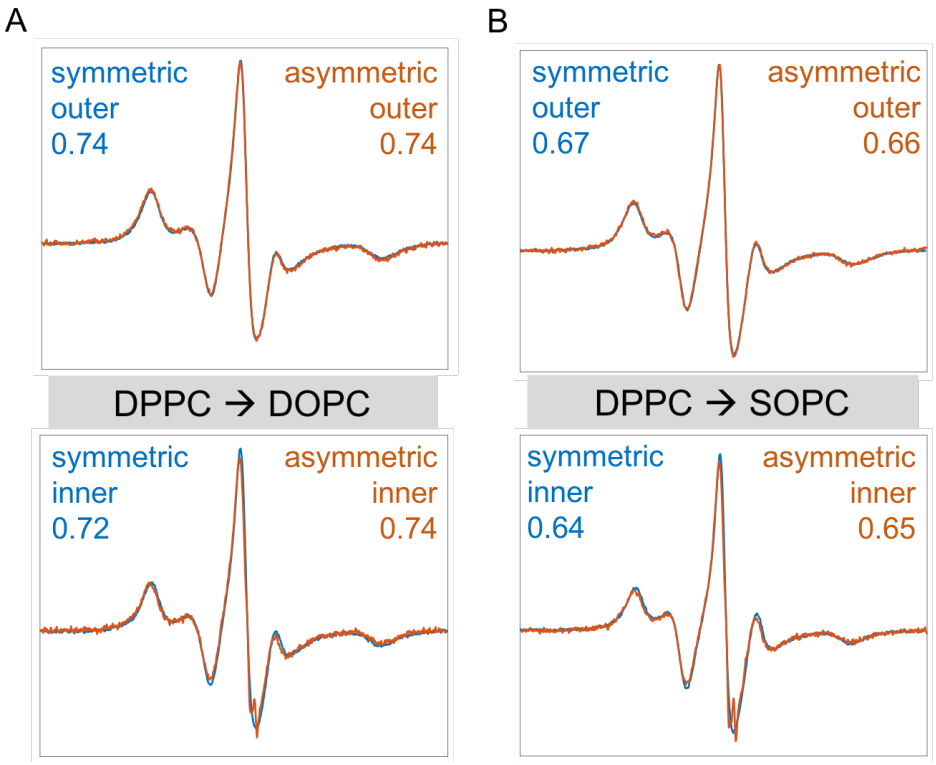

Figure E9. Model-free analysis of the ESR spectra for the DPPC/DOPC (A) and DPPC/SOPC (B) bilayers. Shown are the spectra of the outer (top plot) or inner (bottom plot) leaflets of the aLUVs (in red) and the spectra of their corresponding symmetric bilayers (in blue). Results for the probe's order parameter obtained from model-free analysis based on hyperfine splittings distances as explained in Chapter 7, are listed for each spectrum on each plot.

APPENDIX F

Table F1. Asymmetric samples examined in each experiment. Shown are the corresponding donor and acceptor lipids; corresponding experiment (Exp.); protein-to-lipid ratio (gA:L); nominal donor:acceptor ratio (D:A); mole fraction of donor in the final asymmetric sample determined from GC (χ_{don}); and the area fraction of the shifted choline resonance peak measured with NMR after sample preparation ($C_{\mathrm{out}}(t=0)$) indicating the fraction of donor lipid on the outer leaflet of the vesicles.

Donor	Acceptor	Exp.	gA:L	D:A	χ_{don}	$C_{\mathrm{out}}(t=0)$
POPC-d31	POPC	GBFA	1:20000	2	0.32	-
	POPC-d13	SAXS	1:40	3	0.4	-
		NMR	0	2	0.34	0.87 (0.03)
			1:40	2	0.33	0.76 (0.02)
			1:100	3	0.38	0.76 (0.02)
DMPC-d54	POPC	GBFA	1:20000	2	0.35	-
		CD	1:40	3	0.45	-
		DSC	0	3	0.42	-
			1:40	3	0.4	-
	POPC-d13	NMR	0	3	0.43	0.85 (0.02)
			1:40	3	0.4	0.78 (0.01)
			1:200	3	0.42	0.88 (0.01)

Table F2. Simulated bilayers without gramicidin. Shown are the total simulation time and the last equilibrated portion of the trajectory used for analysis. Equilibration was determined from convergence of the area per lipid quantified with the algorithm from [196]. Also shown for each leaflet are the average area per lipid, A_{lip} (equal to the lateral area of the simulation box divided by the number of lipids in the leaflet); the area compressibility modulus, K_A (calculated from local thickness fluctuations as described in Chapter 3.2); the bending rigidity modulus, κ_C (calculated from local splay fluctuations as described in [138, 139]); and the average leaflet thickness (calculated as described in Section F.2). Errors are shown in parentheses. The errors on A_{lip} are standard errors calculated from consecutive time blocks of length equal to the effective number of samples [196]. Errors on K_A and κ_C were calculated as described in Chapter 3.2 and Refs. [138, 139], respectively.

Bilayer	Leaf	Simulation time [ns]		A_{lip} [A^2]	K_A† [mN/m]	κ_C† [k_BT]	d_0† [A]
		analysis	total				
§POPC	Top	183	226	64.3 (0.2)	236 (26)	12.9 (0.5)	17.8
	Bot				186 (28)	12.4 (0.6)	17.7
§DMPC/POPC 0.75/0.25	Top	738	738	61.4 (0.1)	282 (24)	15.4 (0.6)	16.8
	Bot				244 (38)	14.8 (0.5)	16.8
§DMPC/POPC 0.10/0.90	Top	471	471	63.8 (0.1)	238 (22)	12.8 (0.6)	17.7
	Bot				188 (32)	11.7 (0.4)	17.7
Asymmetric DMPC/POPC	Top	280	445	61.4 (0.1)	286 (32)	15 (0.5)	16.8
	Bot			63.8 (0.1)	224 (26)	12.5 (0.5)	17.7

§ Bilayer systems taken from [318].

† For the symmetric bilayers, the corresponding average leaflet quantity was used in the membrane deformations analysis described in Section F.3.

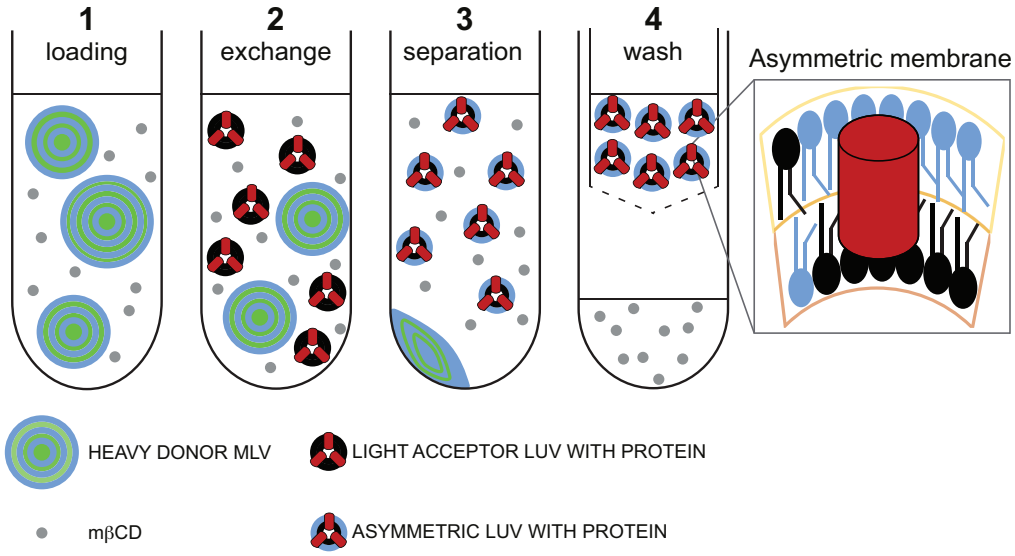

Figure F1. Schematic illustration of the protocol for preparation of asymmetric proteoliposomes. Step 1, MLVs of donor lipid are incubated with MβCD for 2 h at room temperature with gentle stirring. Step 2, extruded symmetric LUVs with gramicidin are added to the donor lipid/MβCD solution, and the acceptor/donor/MβCD mixture is incubated at room temperature with gentle stirring. Step 3, donor MLVs are separated from the asymmetric vesicles and cyclodextrin after an 8-fold dilution with H_2O and centrifugation at 20K x g for 30 min. Step 4, cyclodextrin is removed with centrifugal filter devices, and the sample is washed at least 3 times with water (or another appropriate solvent). The final asymmetric proteoliposomes are recovered from the retentate. The schematic is adapted from Chapter 5.

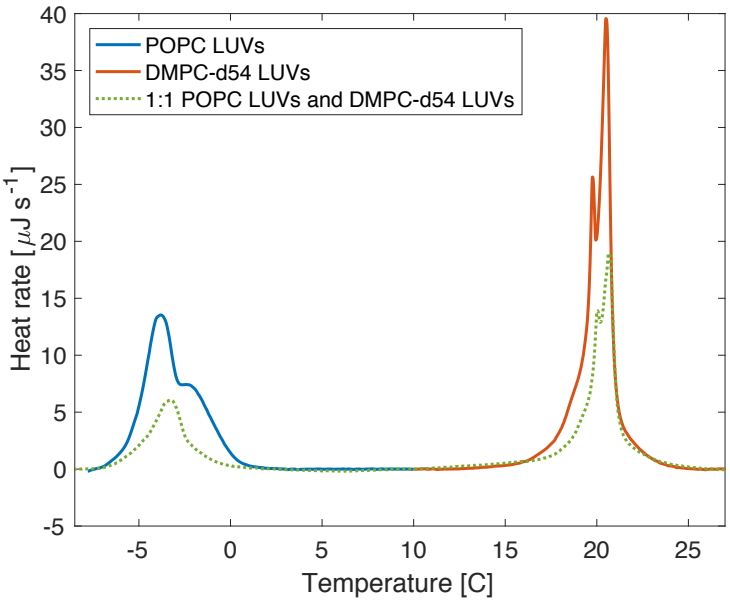

Figure F2. DSC thermograms for POPC LUVs (blue), DMPC-d54 sLUVs (red) and a 1:1 mixture of POPC LUVs and DMPC-d54 LUVs.

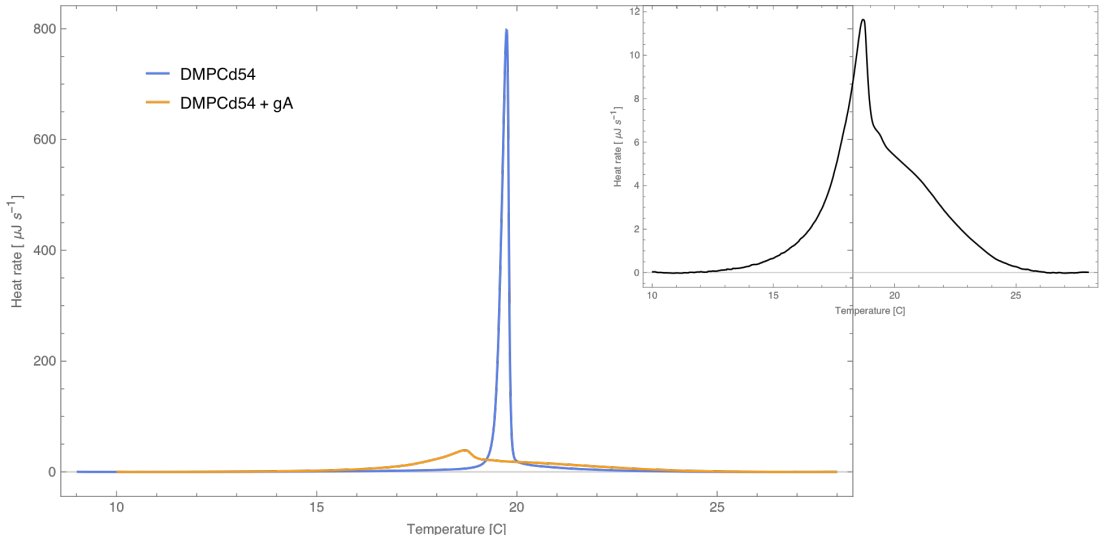

Figure F3. DSC thermograms for DMPCd54 sLUVs (blue) and gA-sLUVs (orange) with gA:lipid ratio of 1:40. The inset shows a zoomed in version of the gA-sLUV thermogram. The presence of gA broadens the melting transition of the sample and slightly decreases it.

F.1. Simulation details. Table F2 lists all simulated bilayer systems without gramicidin. As indicated, the symmetric bilayers were taken from [318]. The asymmetric bilayer was simulated with the same simulation parameters as the symmetric ones: a 10-12 A cutoff with NAMD's *vdwForceSwitchng* option turned on for Van der Waals and electrostatic interactions; Particle Mesh Ewald for long-range electrostatics, with grid spacing of 1 A; Langevin thermostat set to maintain temperature at 25 C and a Nose-Hoover barostat with Langevin dynamics set to maintain pressure at 1 bar with a period of 200 fs and delay of 50 fs; and a time-step of 2 fs with fixed hydrogen bonds (i.e. *rigidbonds* option set to *all*).

The two gA-containing bilayer systems (one gA channel embedded into the symmetric POPC or asymmetric DMPC/POPC membrane as described in Chapter 8) were simulated with the same simulation parameters as outlined above.

F.2. Analysis of leaflet thickness from MD simulations. Local leaflet thicknesses were calculated with a modified version of VMD's MEMBPLUGIN tool for membrane thickness [197] as described in Chapter 3.2. Briefly, the heights h of all heavy atoms on the lipid acyl chains, including the phosphate, were calculated at different grid points on the leaflet surface by interpolation on their z coordinates as follows:

$$h_{\varsigma,(x,y)} = \frac{\sum_i \frac{z_{\varsigma,i}}{d_{i,(x,y)}^2}}{\sum_i \frac{1}{d_{i,(x,y)}^2}}, \tag{F1}$$

where ς denotes the atom type (e.g. phosphate, C1 atom on the sn-1 chain, C2 atom on the sn-2 chain, etc.), x and y are the two-dimensional coordinates of the grid point, the summations are over all lipid atoms of type ς in the leaflet with $z_{\varsigma,i}$ being the z-coordinate of atom i and $d_{i,(x,y)}$ denoting the 2D distance between atom i and the grid point at (x, y). Once all heights have been calculated, the leaflet thickness τ at each grid point was simply the distance between the local height of the phosphate atom and the local height of the lowest-situated atom type at the grid point:

$$\tau_{P,(x,y)} = h_{P,(x,y)} - \min h_{(x,y)}. \tag{F2}$$

The average leaflet thickness d_0 in Table F2 is the space- and time-averaged local thickness τ_P in the leaflet.

F.3 Analysis of membrane deformation. The membrane deformation profile around a single gA channel was calculated by combining information from the simulation trajectories with the CTMD formalism in which the free energy of membrane deformation ΔG_{def} is expressed in terms of the area compressibility (K_A) and bending rigidity (κ_C) moduli of the lipid environment:

$$\Delta G_{\text{def}} = \frac{1}{2}\int_{\Omega} \left\{ K_a \left(\frac{u}{d_0}\right)^2 + \kappa_C \left(\frac{\partial^2 u}{\partial x^2} + \frac{\partial^2 u}{\partial y^2} - c_0\right)^2 - \kappa_C c_0^2 \right\} d\Omega. \tag{F3}$$

In the space integral in Eq. F3, $u = d - d_0$ is deviation from the equilibrium thickness and c_0 is spontaneous curvature. Generally, ΔG_{def} is calculated directly for the whole membrane and used to obtain the optimal membrane deformation profile, i.e. the optimal u that minimizes ΔG_{def} subject to a number of boundary conditions.

Since the two membrane leaflets may deform in a different way around gA (especially in the case of an asymmetric membrane), here we treat each leaflet separately. Thus, if L denotes one leaflet (top or bottom) and ΔG^L_{def} is the corresponding free energy, then:

$$\Delta G^L_{\text{def}} = \frac{1}{2}\int_\Omega \left\{ K^L_a \left(\frac{u}{d_0}\right)^2 + \kappa^L_C \left(\frac{\partial^2 u}{\partial x^2} + \frac{\partial^2 u}{\partial y^2} - c_0\right)^2 - \kappa^L_C c_0^2 \right\} d\Omega, \qquad \text{(F4)}$$

where all mechanical constants, u, d_0 and c_0 represent the per leaflet quantities. Eq. F4 is used to obtain an optimal deformation profile for each leaflet L (as described in detail below) and the membrane deformation profile is then the sum of the deformation profiles of the two bilayer leaflets. In the whole procedure, the input from the MD simulations consists of (1) the mechanical constants (K^L_a and κ^L_C) and d_0 calculated from the bilayer-only trajectories as described in Section F.2. and listed in Table F2; and (2) the leaflet thickness at the gA-lipid boundary which is calculated from the gA containing trajectories as descried below and appears as one of the boundary conditions in the energy minimization procedure.

Thus, the following protocol, inspired by the methodology in [369], was used to calculate the optimal deformation profile for a leaflet L:

1. Identify the gA-lipid boundary in the leaflet and calculate the leaflet thickness at this boundary as described in Chapter 8.
2. Solve the following boundary value problem:

$$\kappa_C \nabla^4 u + \left(\frac{K_a}{d_0^2}\right) u = 0 \qquad \text{where} \qquad \nabla^2 = \frac{\partial^2}{\partial x^2} + \frac{\partial^2}{\partial y^2} \qquad \text{(F5)}$$

subject to the boundary conditions:

$$u|_{\Gamma_{out}} = 0 \quad \nabla u|_{\Gamma_{out}} = 0 \quad u|_{\Gamma_{in}} = u_0(x,y) \quad \nabla^2 u|_{\Gamma_{in}} = v_0(x,y) \qquad \text{(F6)}$$

where Γ_{out} and Γ_{in} denote the bulk and the protein-lipid interface respectively, and u_0 and v_0 are the deviation from d_0 and the curvature at the gA-lipid boundary accordingly. Both u_0 and v_0 can be non-uniform around the protein and are thus functions of x and y. $u_0(x,y)$ is calculated directly from the gA simulations by subtracting d_0 from the corresponding leaflet thickness at (x,y), while κ_C and K_a are calculated from the bilayer-only trajectories as described in the caption of Table F2.

v_0 is obtained through a self-consistent optimization procedure that aims to globally minimize ΔG^L_{def} by following a slightly modified version of the approach in [369]. In short, every (x,y) point on the gA-lipid boundary is first expressed as a function of an

angle θ relative to the center of gA. Then $v_0(\theta)$ is expressed as a Fourier series truncated up to 7th order:

$$v_0(\theta) \sim \sum_{n=0}^{7} (a_n \cos n\theta + b_n \sin n\theta) \tag{F7}$$

and is thus parameterized by only 15 parameters (a_0 through a_7 and b_1 through b_7). The 15 parameters are first chosen at random, then optimized using a quasi-Newton method for unconstrained minimization (the *fminunc* function in MATLAB) to find the minimum ΔG^L_{def}. For each set of parameters, ΔG^L_{def} is obtained by:
(1) calculating $v_0(\theta)$ with Eq. F7,
(2) solving Eq. F5 for u subject to the four boundary conditions in Eq. F6 (which yield a unique solution), and
(3) using the resulting deformation profile u to get ΔG^L_{def} with Eq. F4.
Eq. F5 is solved by using the 5-point stencil method (the 5-point finite difference approximation of the Laplacian operator) in two dimensions and expressing the problem in the form $Au = b$ where A is a nonsingular matrix, b is a vector and thus the solution can be computed as $u = A\backslash b$.

BIBLIOGRAPHY

1. Doktorova, M., et al., *Cholesterol Promotes Protein Binding by Affecting Membrane Electrostatics and Solvation Properties.* Biophys J, 2017. **113**(9): p. 2004-2015.

2. May, S., et al., *Tilt modulus of a lipid monolayer.* Eur Phys J E Soft Matter, 2004. **14**(3): p. 299-308.

3. Szleifer, I., et al., *Molecular Theory of Curvature Elasticity in Surfactant Films.* Journal of Chemical Physics, 1990. **92**(11): p. 6800-6817.

4. Heberle, F.A., et al., *Subnanometer Structure of an Asymmetric Model Membrane: Interleaflet Coupling Influences Domain Properties.* Langmuir, 2016. **32**(20): p. 5195-200.

5. Phillips, R., et al., *Physical biology of the cell*. 2nd ed. 2013, New York, NY: Garland Science.

6. Alberts, B., et al., *Molecular biology of the cell*. sixth ed, ed. B. Alberts. 2015, New York, NY: Garland Science.

7. Nagle, J.F., et al., *What are the true values of the bending modulus of simple lipid bilayers?* Chem Phys Lipids, 2015. **185**: p. 3-10.

8. Heberle, F.A., et al., *Bilayer thickness mismatch controls domain size in model membranes.* J Am Chem Soc, 2013. **135**(18): p. 6853-9.

9. Danielli, J.F. and H. Davson, *A contribution to the theory of permeability of thin films.* Journal of Cellular and Comparative Physiology, 1935. **5**(4): p. 495-508.

10. Marquardt, D., et al., *1H NMR Shows Slow Phospholipid Flip-Flop in Gel and Fluid Bilayers.* Langmuir, 2017. **33**(15): p. 3731-3741.

11. Robertson, J.D. and M. Locke, *Cellular membranes in development*, ed. M. Locke. 1964, New York: Academic Press, Inc.

12. Kiessling, V., C. Wan, and L.K. Tamm, *Domain coupling in asymmetric lipid bilayers.* Biochim Biophys Acta, 2009. **1788**(1): p. 64-71.

13. Tsujimoto, Y. and S. Shimizu, *Role of the mitochondrial membrane permeability transition in cell death.* Apoptosis, 2007. **12**(5): p. 835-40.

14. Singer, S.J. and G.L. Nicolson, *The fluid mosaic model of the structure of cell membranes.* Science, 1972. **175**(4023): p. 720-31.

15. Klausner, R.D., et al., *Lipid domains in membranes. Evidence derived from structural perturbations induced by free fatty acids and lifetime heterogeneity analysis.* J Biol Chem, 1980. **255**(4): p. 1286-95.

16. Zalba, S. and T.L. Ten Hagen, *Cell membrane modulation as adjuvant in cancer therapy.* Cancer Treat Rev, 2017. **52**: p. 48-57.

17. Hebbel, R.P., *Beyond hemoglobin polymerization: the red blood cell membrane and sickle disease pathophysiology.* Blood, 1991. **77**(2): p. 214-37.

18. Jain, S.K. and S.B. Shohet, *Red blood cell [14C]cholesterol exchange and plasma cholesterol esterifying activity of normal and sickle cell blood.* Biochim Biophys Acta, 1982. **688**(1): p. 11-5.

19. Muskiet, F.D. and F.A. Muskiet, *Lipids, fatty acids and trace elements in plasma and erythrocytes of pediatric patients with homozygous sickle cell disease.* Clin Chim Acta, 1984. **142**(1): p. 1-10.

20. Nash, G.B., et al., *Alteration of the mechanical properties of sickle cells by repetitive deoxygenation: role of calcium and the effects of calcium blockers.* Br J Haematol, 1989. **72**(2): p. 260-4.

21. Tomer, A., et al., *Reduction of pain episodes and prothrombotic activity in sickle cell disease by dietary n-3 fatty acids.* Thromb Haemost, 2001. **85**(6): p. 966-74.

22. VanderJagt, D.J., et al., *Phase angle correlates with n-3 fatty acids and cholesterol in red cells of Nigerian children with sickle cell disease.* Lipids Health Dis, 2003. **2**: p. 2.

23. Hulbert, A.J., et al., *Dietary fats and membrane function: implications for metabolism and disease.* Biol Rev Camb Philos Soc, 2005. **80**(1): p. 155-69.

24. Loeb, J., *The Recent Development of Biology.* Science, 1904. **20**(519): p. 777-86.

25. Pfeffer, W., *Osmotic examinations: studies on cell mechanics*, ed. W. Engelmann. 1877.

26. Overton, C.E., *Ueber die osmotischen Eigenschaften der labenden Pflanzen und Tierzelle.* Vierteljahrsschr. Naturforsch. Ges. Zuerich, 1895. **40**: p. 159-201.

27. Overton, C.E., *Studies on anesthesia at the same time contribute to general pharmacology*. 1901: Fischer.

28. Gorter, E. and F. Grendel, *On Bimolecular Layers of Lipoids on the Chromocytes of the Blood.* J Exp Med, 1925. **41**(4): p. 439-43.

29. Langmuir, I., *The constitution and fundamental properties of solids and liquids. II. Liquids.* Journal of the American Chemical Society, 1917. **39**: p. 1848-1906.

30. Bar, R.S., D.W. Deamer, and D.G. Cornwell, *Surface area of human erythrocyte lipids: reinvestigation of experiments on plasma membrane.* Science, 1966. **153**(3739): p. 1010-2.

31. Frye, L.D. and M. Edidin, *The rapid intermixing of cell surface antigens after formation of mouse-human heterokaryons.* J Cell Sci, 1970. **7**(2): p. 319-35.

32. Bretscher, M.S., *Asymmetrical lipid bilayer structure for biological membranes.* Nat New Biol, 1972. **236**(61): p. 11-2.

33. Verkleij, A.J., et al., *The asymmetric distribution of phospholipids in the human red cell membrane. A combined study using phospholipases and freeze-etch electron microscopy.* Biochim Biophys Acta, 1973. **323**(2): p. 178-93.

34. Boon, J.M. and B.D. Smith, *Chemical control of phospholipid distribution across bilayer membranes.* Med Res Rev, 2002. **22**(3): p. 251-81.

35. Lee, A.G., et al., *Clusters in lipid bilayers and the interpretation of thermal effects in biological membranes.* Biochemistry, 1974. **13**(18): p. 3699-705.

36. Wu, S.H.W. and H.M. Mcconnell, *Phase Separations in Phospholipid Membranes.* Biochemistry, 1975. **14**(4): p. 847-854.

37. Karnovsky, M.J., et al., *The concept of lipid domains in membranes.* J Cell Biol, 1982. **94**(1): p. 1-6.

38. Florine, K.I. and G.W. Feigenson, *Protein redistribution in model membranes: clearing of M13 coat protein from calcium-induced gel-phase regions in phosphatidylserine/phosphatidylcholine multilamellar vesicles.* Biochemistry, 1987. **26**(11): p. 2978-83.

39. Dibble, A.R.G., M.D. Yeager, and G.W. Feigenson, *Partitioning of Gramicidin a' between Coexisting Fluid and Gel Phospholipid Phases.* Biochimica Et Biophysica Acta, 1993. **1153**(2): p. 155-162.

40. Simons, K. and G. van Meer, *Lipid sorting in epithelial cells.* Biochemistry, 1988. **27**(17): p. 6197-202.

41. Brown, D.A. and J.K. Rose, *Sorting of GPI-anchored proteins to glycolipid-enriched membrane subdomains during transport to the apical cell surface.* Cell, 1992. **68**(3): p. 533-44.

42. Simons, K. and E. Ikonen, *Functional rafts in cell membranes.* Nature, 1997. **387**(6633): p. 569-572.

43. Simons, K. and D. Toomre, *Lipid rafts and signal transduction.* Nat Rev Mol Cell Biol, 2000. **1**(1): p. 31-9.

44. Shevchenko, A. and K. Simons, *Lipidomics: coming to grips with lipid diversity.* Nat Rev Mol Cell Biol, 2010. **11**(8): p. 593-8.

45. van Meer, G., D.R. Voelker, and G.W. Feigenson, *Membrane lipids: where they are and how they behave.* Nat Rev Mol Cell Biol, 2008. **9**(2): p. 112-24.

46. Botelho, A.V., et al., *Curvature and hydrophobic forces drive oligomerization and modulate activity of rhodopsin in membranes.* Biophys J, 2006. **91**(12): p. 4464-77.

47. Andersen, O.S. and R.E. Koeppe, 2nd, *Bilayer thickness and membrane protein function: an energetic perspective.* Annu Rev Biophys Biomol Struct, 2007. **36**: p. 107-30.

48. Vitrac, H., et al., *Dynamic membrane protein topological switching upon changes in phospholipid environment.* Proc Natl Acad Sci U S A, 2015. **112**(45): p. 13874-9.

49. Yeung, T., et al., *Membrane phosphatidylserine regulates surface charge and protein localization.* Science, 2008. **319**(5860): p. 210-3.

50. Marsh, D., *Handbook of Lipid Bilayers*. Second Edition ed. 2013, Boca Raton, FL, USA: CRC Press.

51. Huang, J. and G.W. Feigenson, *Monte Carlo simulation of lipid mixtures: finding phase separation.* Biophys J, 1993. **65**(5): p. 1788-94.

52. Marsh, D., *Liquid-ordered phases induced by cholesterol: a compendium of binary phase diagrams.* Biochim Biophys Acta, 2010. **1798**(3): p. 688-99.

53. Marsh, D., *Cholesterol-induced fluid membrane domains: a compendium of lipid-raft ternary phase diagrams.* Biochim Biophys Acta, 2009. **1788**(10): p. 2114-23.

54. Konyakhina, T.M., et al., *Phase diagram of a 4-component lipid mixture: DSPC/DOPC/POPC/chol.* Biochim Biophys Acta, 2013. **1828**(9): p. 2204-14.

55. Almeida, P.F., *Thermodynamics of lipid interactions in complex bilayers.* Biochim Biophys Acta, 2009. **1788**(1): p. 72-85.

56. Huang, J. and G.W. Feigenson, *A microscopic interaction model of maximum solubility of cholesterol in lipid bilayers.* Biophys J, 1999. **76**(4): p. 2142-57.

57. Radhakrishnan, A. and H. McConnell, *Condensed complexes in vesicles containing cholesterol and phospholipids.* Proc Natl Acad Sci U S A, 2005. **102**(36): p. 12662-6.

58. Hauser, H. and G.G. Shipley, *Comparative structural aspects of cation binding to phosphatidylserine bilayers.* Biochim Biophys Acta, 1985. **813**(2): p. 343-6.

59. Fujiwara, T., et al., *Phospholipids undergo hop diffusion in compartmentalized cell membrane.* J Cell Biol, 2002. **157**(6): p. 1071-81.

60. Lorent, J.H., et al., *Structural determinants and functional consequences of protein affinity for membrane rafts.* Nat Commun, 2017. **8**(1): p. 1219.

61. Mondal, S., G. Khelashvili, and H. Weinstein, *Not Just an Oil Slick: How the Energetics of Protein-Membrane Interactions Impacts the Function and Organization of Transmembrane Proteins.* Biophysical Journal, 2014. **106**(11): p. 2305-2316.

62. Zwaal, R.F., P. Comfurius, and L.L. van Deenen, *Membrane asymmetry and blood coagulation.* Nature, 1977. **268**(5618): p. 358-60.

63. McEvoy, L., P. Williamson, and R.A. Schlegel, *Membrane phospholipid asymmetry as a determinant of erythrocyte recognition by macrophages.* Proc Natl Acad Sci U S A, 1986. **83**(10): p. 3311-5.

64. Bevers, E.M., et al., *Generation of prothrombin-converting activity and the exposure of phosphatidylserine at the outer surface of platelets.* Eur J Biochem, 1982. **122**(2): p. 429-36.

65. Fadok, V.A., et al., *Exposure of phosphatidylserine on the surface of apoptotic lymphocytes triggers specific recognition and removal by macrophages.* J Immunol, 1992. **148**(7): p. 2207-16.

66. Esteban-Martin, S., et al., *Stability of asymmetric lipid bilayers assessed by molecular dynamics simulations.* J Am Chem Soc, 2009. **131**(42): p. 15194-202.

67. Mui, B.L., et al., *Influence of transbilayer area asymmetry on the morphology of large unilamellar vesicles.* Biophys J, 1995. **69**(3): p. 930-41.

68. Cullis, P.R., et al., *Influence of pH gradients on the transbilayer transport of drugs, lipids, peptides and metal ions into large unilamellar vesicles.* Biochim Biophys Acta, 1997. **1331**(2): p. 187-211.

69. Lingwood, D. and K. Simons, *Lipid rafts as a membrane-organizing principle.* Science, 2010. **327**(5961): p. 46-50.

70. Simons, K. and M.J. Gerl, *Revitalizing membrane rafts: new tools and insights.* Nat Rev Mol Cell Biol, 2010. **11**(10): p. 688-99.

71. Simons, K. and J.L. Sampaio, *Membrane organization and lipid rafts.* Cold Spring Harb Perspect Biol, 2011. **3**(10): p. a004697.

72. Eggeling, C., et al., *Direct observation of the nanoscale dynamics of membrane lipids in a living cell.* Nature, 2009. **457**(7233): p. 1159-62.

73. Sahl, S.J., et al., *Fast molecular tracking maps nanoscale dynamics of plasma membrane lipids.* Proc Natl Acad Sci U S A, 2010. **107**(15): p. 6829-34.

74. Elson, E.L., et al., *Phase separation in biological membranes: integration of theory and experiment.* Annu Rev Biophys, 2010. **39**: p. 207-26.

75. Feigenson, G.W., *Phase boundaries and biological membranes.* Annu Rev Biophys Biomol Struct, 2007. **36**: p. 63-77.

76. Feigenson, G.W., *Phase diagrams and lipid domains in multicomponent lipid bilayer mixtures.* Biochim Biophys Acta, 2009. **1788**(1): p. 47-52.

77. Zhao, J., et al., *Phase studies of model biomembranes: complex behavior of DSPC/DOPC/cholesterol.* Biochim Biophys Acta, 2007. **1768**(11): p. 2764-76.

78. Farkas, E.R. and W.W. Webb, *Precise and millidegree stable temperature control for fluorescence imaging: application to phase transitions in lipid membranes.* Rev Sci Instrum, 2010. **81**(9): p. 093704.

79. Zhao, J., et al., *Phase studies of model biomembranes: macroscopic coexistence of Lalpha+Lbeta, with light-induced coexistence of Lalpha+Lo Phases.* Biochim Biophys Acta, 2007. **1768**(11): p. 2777-86.

80. Silvius, J.R., *Fluorescence energy transfer reveals microdomain formation at physiological temperatures in lipid mixtures modeling the outer leaflet of the plasma membrane.* Biophys J, 2003. **85**(2): p. 1034-45.

81. de Almeida, R.F., et al., *Lipid rafts have different sizes depending on membrane composition: a time-resolved fluorescence resonance energy transfer study.* J Mol Biol, 2005. **346**(4): p. 1109-20.

82. Frazier, M.L., et al., *Investigation of domain formation in sphingomyelin/cholesterol/POPC mixtures by fluorescence resonance energy transfer and Monte Carlo simulations.* Biophys J, 2007. **92**(7): p. 2422-33.

83. Heberle, F.A., et al., *Comparison of three ternary lipid bilayer mixtures: FRET and ESR reveal nanodomains.* Biophys J, 2010. **99**(10): p. 3309-18.

84. Petruzielo, R.S., et al., *Phase behavior and domain size in sphingomyelin-containing lipid bilayers.* Biochim Biophys Acta, 2013. **1828**(4): p. 1302-13.

85. Brewster, R., P.A. Pincus, and S.A. Safran, *Hybrid lipids as a biological surface-active component.* Biophys J, 2009. **97**(4): p. 1087-94.

86. Brewster, R. and S.A. Safran, *Line active hybrid lipids determine domain size in phase separation of saturated and unsaturated lipids.* Biophys J, 2010. **98**(6): p. L21-3.

87. Yamamoto, T., R. Brewster, and S.A. Safran, *Chain ordering of hybrid lipids can stabilize domains in saturated/hybrid/cholesterol lipid membranes.* Epl, 2010. **91**(2).

88. Yamamoto, T. and S.A. Safran, *Line tension between domains in multicomponent membranes is sensitive to degree of unsaturation of hybrid lipids.* Soft Matter, 2011. **7**(15): p. 7021-7033.

89. Hirose, Y., S. Komura, and D. Andelman, *Concentration fluctuations and phase transitions in coupled modulated bilayers.* Physical Review E, 2012. **86**(2).

90. Palmieri, B. and S.A. Safran, *Hybrid lipids increase the probability of fluctuating nanodomains in mixed membranes.* Langmuir, 2013. **29**(17): p. 5246-61.

91. Feigenson, G.W. and J.T. Buboltz, *Ternary phase diagram of dipalmitoyl-PC/dilauroyl-PC/cholesterol: nanoscopic domain formation driven by cholesterol.* Biophys J, 2001. **80**(6): p. 2775-88.

92. Heberle, F.A. and G.W. Feigenson, *Phase separation in lipid membranes.* Cold Spring Harb Perspect Biol, 2011. **3**(4).

93. Konyakhina, T.M., et al., *Control of a nanoscopic-to-macroscopic transition: modulated phases in four-component DSPC/DOPC/POPC/Chol giant unilamellar vesicles.* Biophys J, 2011. **101**(2): p. L8-10.

94. Goh, S.L., J.J. Amazon, and G.W. Feigenson, *Toward a better raft model: modulated phases in the four-component bilayer, DSPC/DOPC/POPC/CHOL.* Biophys J, 2013. **104**(4): p. 853-62.

95. Baumgart, T., S.T. Hess, and W.W. Webb, *Imaging coexisting fluid domains in biomembrane models coupling curvature and line tension.* Nature, 2003. **425**(6960): p. 821-4.

96. Ursell, T.S., W.S. Klug, and R. Phillips, *Morphology and interaction between lipid domains.* Proc Natl Acad Sci U S A, 2009. **106**(32): p. 13301-6.

97. Amazon, J.J., S.L. Goh, and G.W. Feigenson, *Competition between line tension and curvature stabilizes modulated phase patterns on the surface of giant unilamellar vesicles: a simulation study.* Phys Rev E Stat Nonlin Soft Matter Phys, 2013. **87**(2): p. 022708.

98. Pan, J., et al., *Using small-angle neutron scattering to detect nanoscopic lipid domains.* Chem Phys Lipids, 2013. **170-171**: p. 19-32.

99. Honerkamp-Smith, A.R., et al., *Line tensions, correlation lengths, and critical exponents in lipid membranes near critical points.* Biophys J, 2008. **95**(1): p. 236-46.

100. Honerkamp-Smith, A.R., S.L. Veatch, and S.L. Keller, *An introduction to critical points for biophysicists; observations of compositional heterogeneity in lipid membranes.* Biochimica Et Biophysica Acta-Biomembranes, 2009. **1788**(1): p. 53-63.

101. Veatch, S.L., et al., *Critical fluctuations in domain-forming lipid mixtures.* Proc Natl Acad Sci U S A, 2007. **104**(45): p. 17650-5.

102. Honerkamp-Smith, A.R., B.B. Machta, and S.L. Keller, *Experimental observations of dynamic critical phenomena in a lipid membrane.* Phys Rev Lett, 2012. **108**(26): p. 265702.

103. Schick, M., *Membrane heterogeneity: Manifestation of a curvature-induced microemulsion.* Physical Review E, 2012. **85**(3).

104. Simunovic, M., et al., *When Physics Takes Over: BAR Proteins and Membrane Curvature.* Trends in Cell Biology, 2015. **25**(12): p. 780-792.

105. Phillips, R., et al., *Emerging roles for lipids in shaping membrane-protein function.* Nature, 2009. **459**(7245): p. 379-85.

106. Lundbaek, J.A., et al., *Lipid bilayer regulation of membrane protein function: gramicidin channels as molecular force probes.* J R Soc Interface, 2010. **7**(44): p. 373-95.

107. Helfrich, W., *Elastic properties of lipid bilayers: theory and possible experiments.* Z Naturforsch C, 1973. **28**(11): p. 693-703.

108. Faucon, J.F., et al., *Bending Elasticity and Thermal Fluctuations of Lipid-Membranes - Theoretical and Experimental Requirements.* Journal De Physique, 1989. **50**(17): p. 2389-2414.

109. Engelhardt, H., H.P. Duwe, and E. Sackmann, *Bilayer Bending Elasticity Measured by Fourier-Analysis of Thermally Excited Surface Undulations of Flaccid Vesicles.* Journal De Physique Lettres, 1985. **46**(8): p. L395-L400.

110. Schneider, M.B., J.T. Jenkins, and W.W. Webb, *Thermal fluctuations of large cylindrical phospholipid vesicles.* Biophys J, 1984. **45**(5): p. 891-9.

111. Pecreaux, J., et al., *Refined contour analysis of giant unilamellar vesicles.* Eur Phys J E Soft Matter, 2004. **13**(3): p. 277-90.

112. Evans, E., W. Rawicz, and B.A. Smith, *Concluding remarks Back to the future: mechanics and thermodynamics of lipid biomembranes.* Faraday Discussions, 2013. **161**: p. 591-611.

113. Rawicz, W., et al., *Effect of chain length and unsaturation on elasticity of lipid bilayers.* Biophys J, 2000. **79**(1): p. 328-39.

114. Henriksen, J., A.C. Rowat, and J.H. Ipsen, *Vesicle fluctuation analysis of the effects of sterols on membrane bending rigidity.* European Biophysics Journal with Biophysics Letters, 2004. **33**(8): p. 732-741.

115. Henriksen, J.R. and J.H. Ipsen, *Measurement of membrane elasticity by micro-pipette aspiration.* European Physical Journal E, 2004. **14**(2): p. 149-167.

116. Kummrow, M. and W. Helfrich, *Deformation of Giant Lipid Vesicles by Electric-Fields.* Physical Review A, 1991. **44**(12): p. 8356-8360.

117. Gracia, R.S., et al., *Effect of cholesterol on the rigidity of saturated and unsaturated membranes: fluctuation and electrodeformation analysis of giant vesicles.* Soft Matter, 2010. **6**(7): p. 1472-1482.

118. Lyatskaya, Y., et al., *Method for obtaining structure and interactions from oriented lipid bilayers.* Phys Rev E Stat Nonlin Soft Matter Phys, 2001. **63**(1 Pt 1): p. 011907.

119. Liu, Y. and J.F. Nagle, *Diffuse scattering provides material parameters and electron density profiles of biomembranes.* Phys Rev E Stat Nonlin Soft Matter Phys, 2004. **69**(4 Pt 1): p. 040901.

120. Yi, Z., M. Nagao, and D.P. Bossev, *Bending elasticity of saturated and monounsaturated phospholipid membranes studied by the neutron spin echo technique.* J Phys Condens Matter, 2009. **21**(15): p. 155104.

121. Arriaga, L.R., et al., *Stiffening effect of cholesterol on disordered lipid phases: a combined neutron spin echo + dynamic light scattering analysis of the bending elasticity of large unilamellar vesicles.* Biophys J, 2009. **96**(9): p. 3629-37.

122. Dimova, R., *Recent developments in the field of bending rigidity measurements on membranes.* Adv Colloid Interface Sci, 2014. **208**: p. 225-34.

123. Marsh, D., *Elastic curvature constants of lipid monolayers and bilayers.* Chem Phys Lipids, 2006. **144**(2): p. 146-59.

124. Nagle, J.F., *Introductory lecture: basic quantities in model biomembranes.* Faraday Discuss, 2013. **161**: p. 11-29; discussion 113-50.

125. Mell, M., et al., *Bending stiffness of biological membranes: what can be measured by neutron spin echo?* Eur Phys J E Soft Matter, 2013. **36**(7): p. 75.

126. Bouvrais, H., *Bending Rigidities of Lipid Bilayers: Their Determination and Main Inputs in Biophysical Studies.* Advances in Planar Lipid Bilayers and Liposomes, Vol 15, 2012. **15**: p. 1-75.

127. Lindahl, E. and O. Edholm, *Mesoscopic undulations and thickness fluctuations in lipid bilayers from molecular dynamics simulations.* Biophys J, 2000. **79**(1): p. 426-33.

128. Hofsass, C., E. Lindahl, and O. Edholm, *Molecular dynamics simulations of phospholipid bilayers with cholesterol.* Biophys J, 2003. **84**(4): p. 2192-206.

129. Levine, Z.A., et al., *Determination of biomembrane bending moduli in fully atomistic simulations.* J Am Chem Soc, 2014. **136**(39): p. 13582-5.

130. Watson, M.C., et al., *Determining biomembrane bending rigidities from simulations of modest size.* Phys Rev Lett, 2012. **109**(2): p. 028102.

131. Watson, M.C., et al., *Thermal fluctuations in shape, thickness, and molecular orientation in lipid bilayers.* J Chem Phys, 2011. **135**(24): p. 244701.

132. Venable, R.M., F.L. Brown, and R.W. Pastor, *Mechanical properties of lipid bilayers from molecular dynamics simulation.* Chem Phys Lipids, 2015. **192**: p. 60-74.

133. Wang, X. and M. Deserno, *Determining the Lipid Tilt Modulus by Simulating Membrane Buckles.* J Phys Chem B, 2016. **120**(26): p. 6061-73.

134. Hamm, M. and M.M. Kozlov, *Elastic energy of tilt and bending of fluid membranes.* European Physical Journal E, 2000. **3**(4): p. 323-335.

135. Johner, N., D. Harries, and G. Khelashvili, *Curvature and Lipid Packing Modulate the Elastic Properties of Lipid Assemblies: Comparing HII and Lamellar Phases.* J Phys Chem Lett, 2014. **5**(23): p. 4201-6.

136. Khelashvili, G., et al., *Molecular origins of bending rigidity in lipids with isolated and conjugated double bonds: the effect of cholesterol.* Chem Phys Lipids, 2014. **178**: p. 18-26.

137. Khelashvili, G., et al., *Calculating the Bending Modulus for Multicomponent Lipid Membranes in Different Thermodynamic Phases.* J Chem Theory Comput, 2013. **9**(9): p. 3866-3871.

138. Johner, N., D. Harries, and G. Khelashvili, *Erratum to: Implementation of a methodology for determining elastic properties of lipid assemblies from molecular dynamics simulations.* BMC Bioinformatics, 2016. **17**(1): p. 236.

139. Johner, N., D. Harries, and G. Khelashvili, *Implementation of a methodology for determining elastic properties of lipid assemblies from molecular dynamics simulations.* BMC Bioinformatics, 2016. **17**: p. 161.

140. Kessel, A., N. Ben-Tal, and S. May, *Interactions of cholesterol with lipid bilayers: the preferred configuration and fluctuations.* Biophys J, 2001. **81**(2): p. 643-58.

141. Jo, S., et al., *CHARMM-GUI: a web-based graphical user interface for CHARMM.* J Comput Chem, 2008. **29**(11): p. 1859-65.

142. Lee, J., et al., *CHARMM-GUI Input Generator for NAMD, GROMACS, AMBER, OpenMM, and CHARMM/OpenMM Simulations Using the CHARMM36 Additive Force Field.* J Chem Theory Comput, 2016. **12**(1): p. 405-13.

143. Wu, E.L., et al., *CHARMM-GUI Membrane Builder toward realistic biological membrane simulations.* J Comput Chem, 2014. **35**(27): p. 1997-2004.

144. Jo, S., et al., *CHARMM-GUI Membrane Builder for mixed bilayers and its application to yeast membranes.* Biophys J, 2009. **97**(1): p. 50-8.

145. Kucerka, N., M.P. Nieh, and J. Katsaras, *Fluid phase lipid areas and bilayer thicknesses of commonly used phosphatidylcholines as a function of temperature.* Biochim Biophys Acta, 2011. **1808**(11): p. 2761-71.

146. Kucerka, N., S. Tristram-Nagle, and J.F. Nagle, *Structure of fully hydrated fluid phase lipid bilayers with monounsaturated chains.* J Membr Biol, 2005. **208**(3): p. 193-202.

147. Kucerka, N., et al., *Molecular structures of fluid phosphatidylethanolamine bilayers obtained from simulation-to-experiment comparisons and experimental scattering density profiles.* J Phys Chem B, 2015. **119**(5): p. 1947-56.

148. Kucerka, N., et al., *Structure of fully hydrated fluid phase DMPC and DLPC lipid bilayers using X-ray scattering from oriented multilamellar arrays and from unilamellar vesicles.* Biophys J, 2005. **88**(4): p. 2626-37.

149. Kucerka, N., et al., *Lipid bilayer structure determined by the simultaneous analysis of neutron and X-ray scattering data.* Biophys J, 2008. **95**(5): p. 2356-67.

150. Greenwood, A.I., et al., *CRAC motif peptide of the HIV-1 gp41 protein thins SOPC membranes and interacts with cholesterol.* Biochim Biophys Acta, 2008. **1778**(4): p. 1120-30.

151. Kucerka, N., et al., *Areas of monounsaturated diacylphosphatidylcholines.* Biophys J, 2009. **97**(7): p. 1926-32.

152. Pan, J., et al., *Temperature dependence of structure, bending rigidity, and bilayer interactions of dioleoylphosphatidylcholine bilayers.* Biophys J, 2008. **94**(1): p. 117-24.

153. Pan, J., et al., *Structural and mechanical properties of cardiolipin lipid bilayers determined using neutron spin echo, small angle neutron and X-ray scattering, and molecular dynamics simulations.* Soft Matter, 2015. **11**(1): p. 130-8.

154. Pan, J., et al., *Revisiting the bilayer structures of fluid phase phosphatidylglycerol lipids: Accounting for exchangeable hydrogens.* Biochim Biophys Acta, 2014. **1838**(11): p. 2966-9.

155. Phillips, J.C., et al., *Scalable molecular dynamics with NAMD.* J Comput Chem, 2005. **26**(16): p. 1781-802.

156. Klauda, J.B., et al., *Update of the CHARMM all-atom additive force field for lipids: validation on six lipid types.* J Phys Chem B, 2010. **114**(23): p. 7830-43.

157. Towns, J., et al., *XSEDE: Accelerating Scientific Discovery.* Computing in Science & Engineering, 2014. **16**(5): p. 62-74.

158. Niggemann, G., M. Kummrow, and W. Helfrich, *The Bending Rigidity of Phosphatidylcholine Bilayers - Dependences on Experimental-Method, Sample Cell Sealing and Temperature.* Journal De Physique Ii, 1995. **5**(3): p. 413-425.

159. Fernandez-Puente, L., et al., *Temperature and Chain-Length Effects on Bending Elasticity of Phosphatidylcholine Bilayers.* Europhysics Letters, 1994. **28**(3): p. 181-186.

160. Vitkova, V., et al., *Sugars in the aqueous phase change the mechanical properties of lipid mono- and bilayers.* Molecular Crystals and Liquid Crystals, 2006. **449**: p. 95-106.

161. Guler, S.D., et al., *Effects of ether vs. ester linkage on lipid bilayer structure and water permeability.* Chem Phys Lipids, 2009. **160**(1): p. 33-44.

162. Jablin, M.S., K. Akabori, and J.F. Nagle, *Experimental support for tilt-dependent theory of biomembrane mechanics.* Phys Rev Lett, 2014. **113**(24): p. 248102.

163. Nagle, J.F., M.S. Jablin, and S. Tristram-Nagle, *Sugar does not affect the bending and tilt moduli of simple lipid bilayers.* Chem Phys Lipids, 2016. **196**: p. 76-80.

164. May, E.R., A. Narang, and D.I. Kopelevich, *Role of molecular tilt in thermal fluctuations of lipid membranes.* Phys Rev E Stat Nonlin Soft Matter Phys, 2007. **76**(2 Pt 1): p. 021913.

165. Winterhalter, M. and W. Helfrich, *Bending Elasticity of Electrically Charged Bilayers - Coupled Monolayers, Neutral Surfaces, and Balancing Stresses.* Journal of Physical Chemistry, 1992. **96**(1): p. 327-330.

166. May, S., *Curvature elasticity and thermodynamic stability of electrically charged membranes.* Journal of Chemical Physics, 1996. **105**(18): p. 8314-8323.

167. Andelman, D., *Electrostatic properties of membranes: the Poisson-Boltzmann theory*, in *Handbook of biological physics*. 1995, Elsevier. p. 603-642.

168. Mertins, O. and R. Dimova, *Insights on the interactions of chitosan with phospholipid vesicles. Part II: Membrane stiffening and pore formation.* Langmuir, 2013. **29**(47): p. 14552-9.

169. Song, J. and R.E. Waugh, *Bilayer membrane bending stiffness by tether formation from mixed PC-PS lipid vesicles.* J Biomech Eng, 1990. **112**(3): p. 235-40.

170. Meleard, P., et al., *Mechanical properties of model membranes studied from shape transformations of giant vesicles.* Biochimie, 1998. **80**(5-6): p. 401-13.

171. Vitkova, V., et al., *Surface charge effect on the bending elasticity of lipid bilayers.* Comptes Rendus de l'Academie Bulgare des Sciences, 2004. **57**(11): p. 11-25.

172. Semrau, S., et al., *Accurate determination of elastic parameters for multicomponent membranes.* Phys Rev Lett, 2008. **100**(8): p. 088101.

173. Nickels, J.D., et al., *Mechanical Properties of Nanoscopic Lipid Domains.* J Am Chem Soc, 2015. **137**(50): p. 15772-80.

174. Hamm, M. and M.M. Kozlov, *Tilt model of inverted amphiphilic mesophases.* European Physical Journal B, 1998. **6**(4): p. 519-528.

175. Rosetti, C.M., G.G. Montich, and C. Pastorino, *Molecular Insight into the Line Tension of Bilayer Membranes Containing Hybrid Polyunsaturated Lipids.* J Phys Chem B, 2017. **121**(7): p. 1587-1600.

176. Evans, E.A., *Bending elastic modulus of red blood cell membrane derived from buckling instability in micropipet aspiration tests.* Biophys J, 1983. **43**(1): p. 27-30.

177. Evans, E.A., *Structure and deformation properties of red blood cells: concepts and quantitative methods.* Methods Enzymol, 1989. **173**: p. 3-35.

178. Radmacher, M., *Measuring the elastic properties of living cells by the atomic force microscope.* Methods Cell Biol, 2002. **68**: p. 67-90.

179. Seifert, U., *Configurations of fluid membranes and vesicles.* Advances in Physics, 1997. **46**(1): p. 13-137.

180. Svetina, S. and B. Zeks, *Membrane bending energy and shape determination of phospholipid vesicles and red blood cells.* Eur Biophys J, 1989. **17**(2): p. 101-11.

181. Brown, M.F., *Soft Matter in Lipid-Protein Interactions.* Annu Rev Biophys, 2017. **46**: p. 379-410.

182. Evans, E., W. Rawicz, and B.A. Smith, *Back to the future: mechanics and thermodynamics of lipid biomembranes.* Faraday Discuss, 2013. **161**: p. 591-611.

183. Rawicz, W., et al., *Elasticity, strength, and water permeability of bilayers that contain raft microdomain-forming lipids.* Biophys J, 2008. **94**(12): p. 4725-36.

184. Rutkowski, C.A., et al., *The elasticity of synthetic phospholipid vesicles obtained by photon correlation spectroscopy.* Biochemistry, 1991. **30**(23): p. 5688-96.

185. Ertel, A., et al., *Mechanical properties of vesicles. I. Coordinated analysis of osmotic swelling and lysis.* Biophys J, 1993. **64**(2): p. 426-34.

186. Hallett, F.R., et al., *Mechanical properties of vesicles. II. A model for osmotic swelling and lysis.* Biophys J, 1993. **64**(2): p. 435-42.

187. Kinnun, J.J., et al., *Elastic deformation and area per lipid of membranes: Atomistic view from solid-state deuterium NMR spectroscopy.* Biochimica Et Biophysica Acta-Biomembranes, 2015. **1848**(1): p. 246-259.

188. Koenig, B.W., H.H. Strey, and K. Gawrisch, *Membrane lateral compressibility determined by NMR and x-ray diffraction: effect of acyl chain polyunsaturation.* Biophys J, 1997. **73**(4): p. 1954-66.

189. Pan, J., S. Tristram-Nagle, and J.F. Nagle, *Effect of cholesterol on structural and mechanical properties of membranes depends on lipid chain saturation.* Phys Rev E Stat Nonlin Soft Matter Phys, 2009. **80**(2 Pt 1): p. 021931.

190. Helfrich, W., *Elastic Properties of Lipid Bilayers - Theory and Possible Experiments.* Zeitschrift Fur Naturforschung C-a Journal of Biosciences, 1973. **C 28**(11-1): p. 693-703.

191. Feller, S.E. and R.W. Pastor, *Constant surface tension simulations of lipid bilayers: The sensitivity of surface areas and compressibilities.* Journal of Chemical Physics, 1999. **111**(3): p. 1281-1287.

192. Lindahl, E. and O. Edholm, *Mesoscopic undulations and thickness fluctuations in lipid bilayers from molecular dynamics simulations.* Biophysical Journal, 2000. **79**(1): p. 426-433.

193. Edholm, O. and J.F. Nagle, *Areas of molecules in membranes consisting of mixtures.* Biophys J, 2005. **89**(3): p. 1827-32.

194. Lipowsky, R. and E. Sackmann, *Structure and dynamics of membranes*. Handbook of biological physics. 1995, Amsterdam ; New York: Elsevier Science. v. <1A-1B, >.

195. Klauda, J.B., et al., *Improving the CHARMM force field for polyunsaturated fatty acid chains.* J Phys Chem B, 2012. **116**(31): p. 9424-31.

196. Chodera, J.D., *A Simple Method for Automated Equilibration Detection in Molecular Simulations.* J Chem Theory Comput, 2016. **12**(4): p. 1799-805.

197. Guixa-Gonzalez, R., et al., *MEMBPLUGIN: studying membrane complexity in VMD.* Bioinformatics, 2014. **30**(10): p. 1478-80.

198. Giorgino, T., *Computing 1-D atomic densities in macromolecular simulations: The density profile tool for VMD.* Computer Physics Communications, 2014. **185**(1): p. 317-322.

199. Sodt, A.J. and R.W. Pastor, *Bending free energy from simulation: correspondence of planar and inverse hexagonal lipid phases.* Biophys J, 2013. **104**(10): p. 2202-11.

200. Park, S., et al., *How Tolerant are Membrane Simulations with Mismatch in Area per Lipid between Leaflets?* J Chem Theory Comput, 2015. **11**(7): p. 3466-77.

201. Alwarawrah, M., J. Dai, and J. Huang, *A molecular view of the cholesterol condensing effect in DOPC lipid bilayers.* J Phys Chem B, 2010. **114**(22): p. 7516-23.

202. Evans, E. and W. Rawicz, *Entropy-driven tension and bending elasticity in condensed-fluid membranes.* Phys Rev Lett, 1990. **64**(17): p. 2094-2097.

203. Binder, H. and K. Gawrisch, *Effect of unsaturated lipid chains on dimensions, molecular order and hydration of membranes.* Journal of Physical Chemistry B, 2001. **105**(49): p. 12378-12390.

204. Nagle, J.F. and S. Tristram-Nagle, *Structure of lipid bilayers.* Biochim Biophys Acta, 2000. **1469**(3): p. 159-95.

205. Rand, R.P. and V.A. Parsegian, *Hydration Forces between Phospholipid-Bilayers.* Biochimica Et Biophysica Acta, 1989. **988**(3): p. 351-376.

206. Waheed, Q. and O. Edholm, *Undulation contributions to the area compressibility in lipid bilayer simulations.* Biophys J, 2009. **97**(10): p. 2754-60.

207. Chang, R. and J.W. Thoman, *Physical Chemistry for the Chemical Sciences*. 2014, Canada: University Science Books.

208. Stretton, T. *van der Waal's Constants for Real Gases*. Available from: http://www2.ucdsb.on.ca/tiss/stretton/database/van_der_waals_constants.html.

209. Cantor, R.S., *Lipid composition and the lateral pressure profile in bilayers.* Biophys J, 1999. **76**(5): p. 2625-39.

210. Fernandezpuente, L., et al., *Temperature and Chain-Length Effects on Bending Elasticity of Phosphatidylcholine Bilayers.* Europhysics Letters, 1994. **28**(3): p. 181-186.

211. Greenwood, A.I., S. Tristram-Nagle, and J.F. Nagle, *Partial molecular volumes of lipids and cholesterol.* Chem Phys Lipids, 2006. **143**(1-2): p. 1-10.

212. Khelashvili, G., G. Pabst, and D. Harries, *Cholesterol orientation and tilt modulus in DMPC bilayers.* J Phys Chem B, 2010. **114**(22): p. 7524-34.

213. Venable, R.M., et al., *CHARMM all-atom additive force field for sphingomyelin: elucidation of hydrogen bonding and of positive curvature.* Biophys J, 2014. **107**(1): p. 134-45.

214. Heberle, F.A., et al., *Liposome-Based Models for Membrane Rafts Methodology and Applications.* Liposomes, Lipid Bilayers and Model Membranes: From Basic Research to Application, 2014: p. 143-165.

215. Usery, R.D., et al., *Membrane Bending Moduli of Coexisting Liquid Phases Containing Transmembrane Peptide.* Biophys J, 2018. **114**(9): p. 2152-2164.

216. Kuzmin, P.I., et al., *Line tension and interaction energies of membrane rafts calculated from lipid splay and tilt.* Biophys J, 2005. **88**(2): p. 1120-33.

217. Dick, R.A. and V.M. Vogt, *Membrane interaction of retroviral Gag proteins.* Front Microbiol, 2014. **5**: p. 187.

218. Ono, A. and E.O. Freed, *Plasma membrane rafts play a critical role in HIV-1 assembly and release.* Proc Natl Acad Sci U S A, 2001. **98**(24): p. 13925-30.

219. Brugger, B., et al., *The HIV lipidome: a raft with an unusual composition.* Proc Natl Acad Sci U S A, 2006. **103**(8): p. 2641-6.

220. Chan, R., et al., *Retroviruses human immunodeficiency virus and murine leukemia virus are enriched in phosphoinositides.* J Virol, 2008. **82**(22): p. 11228-38.

221. Lorizate, M., et al., *Comparative lipidomics analysis of HIV-1 particles and their producer cell membrane in different cell lines.* Cell Microbiol, 2013. **15**(2): p. 292-304.

222. Krementsov, D.N., et al., *HIV-1 assembly differentially alters dynamics and partitioning of tetraspanins and raft components.* Traffic, 2010. **11**(11): p. 1401-14.

223. Nanda, H., et al., *Electrostatic interactions and binding orientation of HIV-1 matrix studied by neutron reflectivity.* Biophys J, 2010. **99**(8): p. 2516-24.

224. Dick, R.A., et al., *Hydrodynamic and Membrane Binding Properties of Purified Rous Sarcoma Virus Gag Protein.* J Virol, 2015. **89**(20): p. 10371-82.

225. Datta, S.A., et al., *HIV-1 Gag extension: conformational changes require simultaneous interaction with membrane and nucleic acid.* J Mol Biol, 2011. **406**(2): p. 205-14.

226. Machan, R. and M. Hof, *Recent developments in fluorescence correlation spectroscopy for diffusion measurements in planar lipid membranes.* Int J Mol Sci, 2010. **11**(2): p. 427-57.

227. Goksu, E.I. and M.L. Longo, *Ternary lipid bilayers containing cholesterol in a high curvature silica xerogel environment.* Langmuir, 2010. **26**(11): p. 8614-24.

228. Marquardt, D., et al., *On scattered waves and lipid domains: detecting membrane rafts with X-rays and neutrons.* Soft Matter, 2015. **11**(47): p. 9055-72.

229. Pencer, J., et al., *Method of separated form factors for polydisperse vesicles.* Journal of Applied Crystallography, 2006. **39**: p. 293-303.

230. Charlier, L., et al., *Coarse-grained simulations of the HIV-1 matrix protein anchoring: revisiting its assembly on membrane domains.* Biophys J, 2014. **106**(3): p. 577-85.

231. Dick, R.A., et al., *HIV-1 Gag protein can sense the cholesterol and acyl chain environment in model membranes.* Proc Natl Acad Sci U S A, 2012. **109**(46): p. 18761-6.

232. Nezil, F.A. and M. Bloom, *Combined influence of cholesterol and synthetic amphiphillic peptides upon bilayer thickness in model membranes.* Biophys J, 1992. **61**(5): p. 1176-83.

233. Kucerka, N., et al., *The effect of cholesterol on short- and long-chain monounsaturated lipid bilayers as determined by molecular dynamics simulations and X-ray scattering.* Biophys J, 2008. **95**(6): p. 2792-805.

234. McIntosh, T.J., A.D. Magid, and S.A. Simon, *Cholesterol modifies the short-range repulsive interactions between phosphatidylcholine membranes.* Biochemistry, 1989. **28**(1): p. 17-25.

235. Subczynski, W.K., et al., *Hydrophobic barriers of lipid bilayer membranes formed by reduction of water penetration by alkyl chain unsaturation and cholesterol.* Biochemistry, 1994. **33**(24): p. 7670-81.

236. Simon, S.A., T.J. McIntosh, and R. Latorre, *Influence of cholesterol on water penetration into bilayers.* Science, 1982. **216**(4541): p. 65-7.

237. Kingsley, P.B. and G.W. Feigenson, *Synthesis of a Perdeuterated Phospholipid - 1,2-Dimyristoyl-Sn-Glycero-3-Phosphocholine-D72.* Chemistry and Physics of Lipids, 1979. **24**(2): p. 135-147.

238. Wen, Y., et al., *Effects of membrane charge and order on membrane binding of the retroviral structural protein Gag.* J Virol, 2016.

239. Arnold, O., et al., *Mantid-Data analysis and visualization package for neutron scattering and mu SR experiments.* Nuclear Instruments & Methods in Physics Research Section a-Accelerators Spectrometers Detectors and Associated Equipment, 2014. **764**: p. 156-166.

240. Heberle, F.A., V.N.P. Anghel, and J. Katsaras, *Scattering from phase-separated vesicles. I. An analytical form factor for multiple static domains.* Journal of Applied Crystallography, 2015. **48**: p. 1391-1404.

241. Kucerka, N., et al., *Models to analyze small-angle neutron scattering from unilamellar lipid vesicles.* Phys Rev E Stat Nonlin Soft Matter Phys, 2004. **69**(5 Pt 1): p. 051903.

242. McDonnell, J.M., et al., *Solution structure and dynamics of the bioactive retroviral M domain from Rous sarcoma virus.* J Mol Biol, 1998. **279**(4): p. 921-8.

243. Andrec, M., et al., *A large data set comparison of protein structures determined by crystallography and NMR: statistical test for structural differences and the effect of crystal packing.* Proteins, 2007. **69**(3): p. 449-65.

244. Nelle, T. and J. Wills, *A large region within the Rous sarcoma virus matrix protein is dispensable for budding and infectivity.* J Virol, 1996. **70**(4): p. 2269-76.

245. Dick, R.A., et al., *Membrane Binding of the Rous Sarcoma Virus Gag Protein Is Cooperative and Dependent on the Spacer Peptide Assembly Domain.* J Virol, 2016. **90**(5): p. 2473-85.

246. Best, R.B., et al., *Optimization of the additive CHARMM all-atom protein force field targeting improved sampling of the backbone phi, psi and side-chain chi(1) and chi(2) dihedral angles.* J Chem Theory Comput, 2012. **8**(9): p. 3257-3273.

247. Doktorova, M., D. Harries, and G. Khelashvili, *Determination of bending rigidity and tilt modulus of lipid membranes from real-space fluctuation analysis of molecular dynamics simulations.* Phys Chem Chem Phys, 2017.

248. Dalton, A., et al., *Biochemical characterization of rous sarcoma virus MA protein interaction with membranes.* J Virol, 2005. **79**(10): p. 6227-38.

249. Pan, J., et al., *The molecular structure of a phosphatidylserine bilayer determined by scattering and molecular dynamics simulations.* Soft Matter, 2014. **10**(21): p. 3716-25.

250. Kucerka, N., et al., *Influence of cholesterol on the bilayer properties of monounsaturated phosphatidylcholine unilamellar vesicles.* Eur Phys J E Soft Matter, 2007. **23**(3): p. 247-54.

251. Huang, J., et al., *Nonideal mixing of phosphatidylserine and phosphatidylcholine in the fluid lamellar phase.* Biophys J, 1993. **64**(2): p. 413-25.

252. Khelashvili, G. and D. Harries, *Modeling Signaling Processes across Cellular Membranes Using a Mesoscopic Approach.* Annual Reports in Computational Chemistry, Vol 6, 2010. **6**: p. 237-261.

253. Khelashvili, G., H. Weinstein, and D. Harries, *Protein diffusion on charged membranes: A dynamic mean-field model describes time evolution and lipid reorganization.* Biophysical Journal, 2008. **94**(7): p. 2580-2597.

254. Callahan, E. and J. Wills, *Repositioning basic residues in the M domain of the Rous sarcoma virus gag protein.* J Virol, 2000. **74**(23): p. 11222-9.

255. Andelman, D., *Introduction to electrostatics in soft and biological matter.* Soft Condensed Matter Physics in Molecular and Cell Biology, 2006: p. 97-122.

256. Srinivasan, J., et al., *Application of a pairwise generalized Born model to proteins and nucleic acids: inclusion of salt effects.* Theoretical Chemistry Accounts, 1999. **101**(6): p. 426-434.

257. Gohlke, H., C. Kiel, and D.A. Case, *Insights into protein-protein binding by binding free energy calculation and free energy decomposition for the Ras-Raf and Ras-RaIGDS complexes.* Journal of Molecular Biology, 2003. **330**(4): p. 891-913.

258. Zoete, V., M. Meuwly, and M. Karplus, *Study of the insulin dimerization: binding free energy calculations and per-residue free energy decomposition.* Proteins, 2005. **61**(1): p. 79-93.

259. Dalton, A.K., et al., *Electrostatic interactions drive membrane association of the human immunodeficiency virus type 1 Gag MA domain.* J Virol, 2007. **81**(12): p. 6434-45.

260. Murate, M. and T. Kobayashi, *Revisiting transbilayer distribution of lipids in the plasma membrane.* Chem Phys Lipids, 2016. **194**: p. 58-71.

261. Murray, P., et al., *Retroviral matrix domains share electrostatic homology: models for membrane binding function throughout the viral life cycle.* Structure, 2005. **13**(10): p. 1521-31.

262. Barros, M., et al., *Membrane Binding of HIV-1 Matrix Protein: Dependence on Bilayer Composition and Protein Lipidation.* J Virol, 2016. **90**(9): p. 4544-55.

263. Heftberger, P., et al., *In situ determination of structure and fluctuations of coexisting fluid membrane domains.* Biophys J, 2015. **108**(4): p. 854-62.

264. Op den Kamp, J.A.F., *Lipid Asymmetry in Membranes.* Ann. Rev. Biochem., 1979. **48**: p. 47-41.

265. Perillo, V.L., et al., *Transbilayer asymmetry and sphingomyelin composition modulate the preferential membrane partitioning of the nicotinic acetylcholine receptor in Lo domains.* Arch Biochem Biophys, 2016. **591**: p. 76-86.

266. Hussain, N.F., et al., *Bilayer asymmetry influences integrin sequestering in raft-mimicking lipid mixtures.* Biophys J, 2013. **104**(10): p. 2212-21.

267. Lin, Q. and E. London, *The influence of natural lipid asymmetry upon the conformation of a membrane-inserted protein (perfringolysin O).* J Biol Chem, 2014. **289**(9): p. 5467-78.

268. St. Clair, J.R., et al., *Preparation and Physical Properties of Asymmetric Model Membrane Vesicles*, in *The Biophysics of Cell Membranes*, R. Epand and J.M. Ruysschaert, Editors. 2017, Springer: Singapore. p. 1-27.

269. Pautot, S., B.J. Frisken, and D.A. Weitz, *Engineering asymmetric vesicles.* Proc Natl Acad Sci U S A, 2003. **100**(19): p. 10718-21.

270. Redelmeier, T.E., M.J. Hope, and P.R. Cullis, *On the mechanism of transbilayer transport of phosphatidylglycerol in response to transmembrane pH gradients.* Biochemistry, 1990. **29**(12): p. 3046-53.

271. Hope, M.J., et al., *Phospholipid asymmetry in large unilamellar vesicles induced by transmembrane pH gradients.* Biochemistry, 1989. **28**(10): p. 4181-7.

272. Denkins, Y.M. and A.J. Schroit, *Phosphatidylserine decarboxylase: generation of asymmetric vesicles and determination of the transbilayer distribution of fluorescent phosphatidylserine in model membrane systems.* Biochim Biophys Acta, 1986. **862**(2): p. 343-51.

273. Takaoka, R., et al., *Formation of asymmetric vesicles via phospholipase D-mediated Transphosphatidylation.* Biochim Biophys Acta, 2017.

274. Bloj, B. and D.B. Zilversmit, *Asymmetry and transposition rates of phosphatidylcholine in rat erythrocyte ghosts.* Biochemistry, 1976. **15**(6): p. 1277-83.

275. Herrmann, A., A. Zachowski, and P.F. Devaux, *Protein-mediated phospholipid translocation in the endoplasmic reticulum with a low lipid specificity.* Biochemistry, 1990. **29**(8): p. 2023-7.

276. Cheng, H.T. and E. London, *Preparation and properties of asymmetric large unilamellar vesicles: interleaflet coupling in asymmetric vesicles is dependent on temperature but not curvature.* Biophys J, 2011. **100**(11): p. 2671-8.

277. Szejtli, J., *Introduction and General Overview of Cyclodextrin Chemistry.* Chem Rev, 1998. **98**(5): p. 1743-1754.

278. Bozelli, J.C., Jr., Y.H. Hou, and R.M. Epand, *Thermodynamics of Methyl-beta-cyclodextrin-Induced Lipid Vesicle Solubilization: Effect of Lipid Headgroup and Backbone.* Langmuir, 2017.

279. Mui, B.L., et al., *Osmotic properties of large unilamellar vesicles prepared by extrusion.* Biophys J, 1993. **64**(2): p. 443-53.

280. Evans, E., et al., *Dynamic tension spectroscopy and strength of biomembranes.* Biophys J, 2003. **85**(4): p. 2342-50.

281. Homan, R. and H.J. Pownall, *Transbilayer diffusion of phospholipids: dependence on headgroup structure and acyl chain length.* Biochim Biophys Acta, 1988. **938**(2): p. 155-66.

282. Pomorski, T.G. and A.K. Menon, *Lipid somersaults: Uncovering the mechanisms of protein-mediated lipid flipping.* Prog Lipid Res, 2016. **64**: p. 69-84.

283. Son, M. and E. London, *The dependence of lipid asymmetry upon polar headgroup structure.* J Lipid Res, 2013. **54**(12): p. 3385-93.

284. Son, M. and E. London, *The dependence of lipid asymmetry upon phosphatidylcholine acyl chain structure.* J Lipid Res, 2013. **54**(1): p. 223-31.

285. Nakano, M., et al., *Flip-flop of phospholipids in vesicles: kinetic analysis with time-resolved small-angle neutron scattering.* J Phys Chem B, 2009. **113**(19): p. 6745-8.

286. Eicher, B., et al., *Joint small-angle X-ray and neutron scattering data analysis of asymmetric lipid vesicles.* J Appl Crystallogr, 2017. **50**(Pt 2): p. 419-429.

287. Markones, M., et al., *Engineering Asymmetric Lipid Vesicles: Accurate and Convenient Control of the Outer Leaflet Lipid Composition.* Langmuir, 2018. **34**(5): p. 1999-2005.

288. Eicher, B., et al., *Intrinsic Curvature-Mediated Transbilayer Coupling in Asymmetric Lipid Vesicles.* Biophys J, 2017.

289. Cheng, H.T., Megha, and E. London, *Preparation and properties of asymmetric vesicles that mimic cell membranes: effect upon lipid raft formation and transmembrane helix orientation.* J Biol Chem, 2009. **284**(10): p. 6079-92.

290. Lin, Q. and E. London, *Preparation of artificial plasma membrane mimicking vesicles with lipid asymmetry.* PLoS One, 2014. **9**(1): p. e87903.

291. Li, G., et al., *Efficient replacement of plasma membrane outer leaflet phospholipids and sphingolipids in cells with exogenous lipids.* Proc Natl Acad Sci U S A, 2016. **113**(49): p. 14025-14030.

292. Kishimoto, Y. and N.S. Radin, *A Reaction Tube for Methanolysis; Instability of Hydrogen Chloride in Methanol.* J Lipid Res, 1965. **6**: p. 435-6.

293. Kucerka, N., et al., *Curvature effect on the structure of phospholipid bilayers.* Langmuir, 2007. **23**(3): p. 1292-9.

294. Huang, Z. and E. London, *Effect of cyclodextrin and membrane lipid structure upon cyclodextrin-lipid interaction.* Langmuir, 2013. **29**(47): p. 14631-8.

295. Chiantia, S., et al., *Asymmetric GUVs prepared by MbetaCD-mediated lipid exchange: an FCS study.* Biophys J, 2011. **100**(1): p. L1-3.

296. Lin, Q. and E. London, *Ordered raft domains induced by outer leaflet sphingomyelin in cholesterol-rich asymmetric vesicles.* Biophys J, 2015. **108**(9): p. 2212-22.

297. Halbleib, K., et al., *Activation of the Unfolded Protein Response by Lipid Bilayer Stress.* Mol Cell, 2017. **67**(4): p. 673-684 e8.

298. Ingolfsson, H.I., et al., *Phytochemicals perturb membranes and promiscuously alter protein function.* ACS Chem Biol, 2014. **9**(8): p. 1788-98.

299. Vitrac, H., M. Bogdanov, and W. Dowhan, *In vitro reconstitution of lipid-dependent dual topology and postassembly topological switching of a membrane protein.* Proc Natl Acad Sci U S A, 2013. **110**(23): p. 9338-43.

300. Wang, T.Y. and J.R. Silvius, *Cholesterol does not induce segregation of liquid-ordered domains in bilayers modeling the inner leaflet of the plasma membrane.* Biophys J, 2001. **81**(5): p. 2762-73.

301. Marsh, D., *Protein modulation of lipids, and vice-versa, in membranes.* Biochim Biophys Acta, 2008. **1778**(7-8): p. 1545-75.

302. Williamson, J.J. and P.D. Olmsted, *Registered and antiregistered phase separation of mixed amphiphilic bilayers.* Biophys J, 2015. **108**(8): p. 1963-76.

303. Putzel, G.G., et al., *Interleaflet coupling and domain registry in phase-separated lipid bilayers.* Biophys J, 2011. **100**(4): p. 996-1004.

304. Perlmutter, J.D. and J.N. Sachs, *Interleaflet interaction and asymmetry in phase separated lipid bilayers: molecular dynamics simulations.* J Am Chem Soc, 2011. **133**(17): p. 6563-77.

305. Bhide, S.Y., Z. Zhang, and M.L. Berkowitz, *Molecular dynamics simulations of SOPS and sphingomyelin bilayers containing cholesterol.* Biophys J, 2007. **92**(4): p. 1284-95.

306. Gurtovenko, A.A. and I. Vattulainen, *Lipid transmembrane asymmetry and intrinsic membrane potential: two sides of the same coin.* J Am Chem Soc, 2007. **129**(17): p. 5358-9.

307. Gurtovenko, A.A. and I. Vattulainen, *Membrane potential and electrostatics of phospholipid bilayers with asymmetric transmembrane distribution of anionic lipids.* J Phys Chem B, 2008. **112**(15): p. 4629-34.

308. Vacha, R., M.L. Berkowitz, and P. Jungwirth, *Molecular model of a cell plasma membrane with an asymmetric multicomponent composition: water permeation and ion effects.* Biophys J, 2009. **96**(11): p. 4493-501.

309. Polley, A., S. Vemparala, and M. Rao, *Atomistic simulations of a multicomponent asymmetric lipid bilayer.* J Phys Chem B, 2012. **116**(45): p. 13403-10.

310. Koldso, H., et al., *Lipid Clustering Correlates with Membrane Curvature as Revealed by Molecular Simulations of Complex Lipid Bilayers.* Plos Computational Biology, 2014. **10**(10).

311. Wu, E.L., et al., *E. coli Outer Membrane and Interactions with OmpLA*. Biophysical Journal, 2014. **106**(11): p. 2493-2502.

312. Ingolfsson, H.I., et al., *Lipid Organization of the Plasma Membrane.* Journal of the American Chemical Society, 2014. **136**(41): p. 14554-14559.

313. Sharma, S., et al., *A Coarse Grained Model for a Lipid Membrane with Physiological Composition and Leaflet Asymmetry.* Plos One, 2015. **10**(12).

314. Tian, J.H., et al., *Behavior of Bilayer Leaflets in Asymmetric Model Membranes: Atomistic Simulation Studies.* Journal of Physical Chemistry B, 2016. **120**(33): p. 8438-8448.

315. Park, S., et al., *How Tolerant are Membrane Simulations with Mismatch in Area per Lipid between Leaflets?* Journal of Chemical Theory and Computation, 2015. **11**(7): p. 3466-3477.

316. Reddy, A.S., D.T. Warshaviak, and M. Chachisvilis, *Effect of membrane tension on the physical properties of DOPC lipid bilayer membrane.* Biochim Biophys Acta, 2012. **1818**(9): p. 2271-81.

317. Muddana, H.S., et al., *Atomistic simulation of lipid and DiI dynamics in membrane bilayers under tension.* Phys Chem Chem Phys, 2011. **13**(4): p. 1368-78.

318. Doktorova, M., D. Harries, and G. Khelashvili, *Determination of bending rigidity and tilt modulus of lipid membranes from real-space fluctuation analysis of molecular dynamics simulations.* Phys Chem Chem Phys, 2017. **19**(25): p. 16806-16818.

319. Mills, T.T., et al., *Order parameters and areas in fluid-phase oriented lipid membranes using wide angle X-ray scattering.* Biophys J, 2008. **95**(2): p. 669-81.

320. Shearer, J. and S. Khalid, *Communication between the leaflets of asymmetric membranes revealed from coarse-grain molecular dynamics simulations.* Sci Rep, 2018. **8**(1): p. 1805.

321. Martin, S., et al., *Immunologic stimulation of mast cells leads to the reversible exposure of phosphatidylserine in the absence of apoptosis.* Int Arch Allergy Immunol, 2000. **123**(3): p. 249-58.

322. Allender, D.W. and M. Schick, *Phase separation in bilayer lipid membranes: effects on the inner leaf due to coupling to the outer leaf.* Biophys J, 2006. **91**(8): p. 2928-35.

323. Wagner, A.J., S. Loew, and S. May, *Influence of monolayer-monolayer coupling on the phase behavior of a fluid lipid bilayer.* Biophys J, 2007. **93**(12): p. 4268-77.

324. Collins, M.D. and S.L. Keller, *Tuning lipid mixtures to induce or suppress domain formation across leaflets of unsupported asymmetric bilayers.* Proc Natl Acad Sci U S A, 2008. **105**(1): p. 124-8.

325. Garg, S., et al., *Domain registration in raft-mimicking lipid mixtures studied using polymer-tethered lipid bilayers.* Biophys J, 2007. **92**(4): p. 1263-70.

326. Wan, C., V. Kiessling, and L.K. Tamm, *Coupling of cholesterol-rich lipid phases in asymmetric bilayers.* Biochemistry, 2008. **47**(7): p. 2190-8.

327. May, S., *Trans-monolayer coupling of fluid domains in lipid bilayers.* Soft Matter, 2009. **5**(17): p. 3148-3156.

328. Rog, T., et al., *Interdigitation of long-chain sphingomyelin induces coupling of membrane leaflets in a cholesterol dependent manner.* Biochim Biophys Acta, 2016. **1858**(2): p. 281-8.

329. Chiantia, S. and E. London, *Acyl chain length and saturation modulate interleaflet coupling in asymmetric bilayers: effects on dynamics and structural order.* Biophys J, 2012. **103**(11): p. 2311-9.

330. Hubbell, W.L. and H.M. McConnell, *Molecular motion in spin-labeled phospholipids and membranes.* J Am Chem Soc, 1971. **93**(2): p. 314-26.

331. Smith, A.K. and J.H. Freed, *Dynamics and ordering of lipid spin-labels along the coexistence curve of two membrane phases: an ESR study.* Chem Phys Lipids, 2012. **165**(3): p. 348-61.

332. Budil, D.E., et al., *Nonlinear-least-squares analysis of slow-motion EPR spectra in one and two dimensions using a modified Levenberg-Marquardt algorithm.* Journal of Magnetic Resonance Series A, 1996. **120**(2): p. 155-189.

333. Humphrey, W., A. Dalke, and K. Schulten, *VMD: visual molecular dynamics.* J Mol Graph, 1996. **14**(1): p. 33-8, 27-8.

334. Fiorin, G., M.L. Klein, and J. Henin, *Using collective variables to drive molecular dynamics simulations.* Molecular Physics, 2013. **111**(22-23): p. 3345-3362.

335. Capponi, S., et al., *Interleaflet mixing and coupling in liquid-disordered phospholipid bilayers.* Biochim Biophys Acta, 2016. **1858**(2): p. 354-62.

336. Petrache, H.I., S.E. Feller, and J.F. Nagle, *Determination of component volumes of lipid bilayers from simulations.* Biophys J, 1997. **72**(5): p. 2237-42.

337. Funkhouser, C.M., et al., *Effects of interleaflet coupling on the morphologies of multicomponent lipid bilayer membranes.* J Chem Phys, 2013. **138**(2): p. 024909.

338. Kornberg, R.D. and H.M. McConnell, *Inside-outside transitions of phospholipids in vesicle membranes.* Biochemistry, 1971. **10**(7): p. 1111-20.

339. Ackerman, D.G., F.A. Heberle, and G.W. Feigenson, *Limited perturbation of a DPPC bilayer by fluorescent lipid probes: a molecular dynamics study.* J Phys Chem B, 2013. **117**(17): p. 4844-52.

340. Seelig, A. and J. Seelig, *The dynamic structure of fatty acyl chains in a phospholipid bilayer measured by deuterium magnetic resonance.* Biochemistry, 1974. **13**(23): p. 4839-45.

341. Petrache, H.I., S.W. Dodd, and M.F. Brown, *Area per lipid and acyl length distributions in fluid phosphatidylcholines determined by (2)H NMR spectroscopy.* Biophys J, 2000. **79**(6): p. 3172-92.

342. Sonne, J., F.Y. Hansen, and G.H. Peters, *Methodological problems in pressure profile calculations for lipid bilayers.* J Chem Phys, 2005. **122**(12): p. 124903.

343. Swamy, M.J., et al., *Coexisting domains in the plasma membranes of live cells characterized by spin-label ESR spectroscopy.* Biophys J, 2006. **90**(12): p. 4452-65.

344. St. Clair, J.R., et al., *Preparation and Physical Properties of Asymmetric Model Membrane Vesicles*, in *The Biophysics of Cell Membranes. Springer Series in Biophysics*, R. Epand and J.M. Ruysschaert, Editors. 2017, Springer: Singapore.

345. Takaoka, R., et al., *Formation of asymmetric vesicles via phospholipase D-mediated transphosphatidylation.* Biochim Biophys Acta, 2018. **1860**(2): p. 245-249.

346. Contreras, F.X., et al., *Transbilayer (flip-flop) lipid motion and lipid scrambling in membranes.* FEBS Lett, 2010. **584**(9): p. 1779-86.

347. Sperotto, M.M. and A. Ferrarini, *Spontaneous Lipid Flip-Flop in Membranes: A Still Unsettled Picture from Experiments and Simulations*, in *The Biophysics of Cell Membranes. Springer Series in Biophysics*, R. Epand and J.M. Ruysschaert, Editors. 2017, Springer: Singapore.

348. Sebastian, T.T., et al., *Phospholipid flippases: building asymmetric membranes and transport vesicles.* Biochim Biophys Acta, 2012. **1821**(8): p. 1068-77.

349. Aye, I.L., A.T. Singh, and J.A. Keelan, *Transport of lipids by ABC proteins: interactions and implications for cellular toxicity, viability and function.* Chem Biol Interact, 2009. **180**(3): p. 327-39.

350. Fattal, E., et al., *Pore-forming peptides induce rapid phospholipid flip-flop in membranes.* Biochemistry, 1994. **33**(21): p. 6721-31.

351. Tieleman, D.P. and S.J. Marrink, *Lipids out of equilibrium: energetics of desorption and pore mediated flip-flop.* J Am Chem Soc, 2006. **128**(38): p. 12462-7.

352. Ernst, O.P. and A.K. Menon, *Phospholipid scrambling by rhodopsin.* Photochem Photobiol Sci, 2015. **14**(11): p. 1922-31.

353. de Kruijff, B., E.J. van Zoelen, and L.L. van Deenen, *Glycophorin facilitates the transbilayer movement of phosphatidylcholine in vesicles.* Biochim Biophys Acta, 1978. **509**(3): p. 537-42.

354. Tournois, H., et al., *Gramicidin-induced hexagonal HII phase formation in erythrocyte membranes.* Biochemistry, 1987. **26**(21): p. 6613-21.

355. Kol, M.A., et al., *Membrane-spanning peptides induce phospholipid flop: a model for phospholipid translocation across the inner membrane of E. coli.* Biochemistry, 2001. **40**(35): p. 10500-6.

356. Kol, M.A., et al., *Phospholipid flop induced by transmembrane peptides in model membranes is modulated by lipid composition.* Biochemistry, 2003. **42**(1): p. 231-7.

357. Anglin, T.C., K.L. Brown, and J.C. Conboy, *Phospholipid flip-flop modulated by transmembrane peptides WALP and melittin.* J Struct Biol, 2009. **168**(1): p. 37-52.

358. Killian, J.A., *Gramicidin and gramicidin-lipid interactions.* Biochim Biophys Acta, 1992. **1113**(3-4): p. 391-425.

359. Classen, J., et al., *Gramicidin-induced enhancement of transbilayer reorientation of lipids in the erythrocyte membrane.* Biochemistry, 1987. **26**(21): p. 6604-12.

360. Anglin, T.C., J. Liu, and J.C. Conboy, *Facile lipid flip-flop in a phospholipid bilayer induced by gramicidin A measured by sum-frequency vibrational spectroscopy.* Biophys J, 2007. **92**(1): p. L01-3.

361. Marquardt, D., et al., *(1)H NMR Shows Slow Phospholipid Flip-Flop in Gel and Fluid Bilayers.* Langmuir, 2017. **33**(15): p. 3731-3741.

362. Ingolfsson, H.I. and O.S. Andersen, *Screening for small molecules' bilayer-modifying potential using a gramicidin-based fluorescence assay.* Assay Drug Dev Technol, 2010. **8**(4): p. 427-36.

363. Beaven, A.H., et al., *Gramicidin A Channel Formation Induces Local Lipid Redistribution I: Experiment and Simulation.* Biophys J, 2017. **112**(6): p. 1185-1197.

364. Bystrov, V.F. and A.S. Arsenev, *Diversity of the gramicidin A spatial structure: Two-dimensional 1H NMR study in solution.* Tetrahedron, 1988. **44**(3): p. 925-940.

365. Galbraith, T.P. and B.A. Wallace, *Phospholipid chain length alters the equilibrium between pore and channel forms of gramicidin.* Faraday Discuss, 1998(111): p. 159-64; discussion 225-46.

366. Perly, B., et al., *Estimation of the location of natural alpha-tocopherol in lipid bilayers by 13C-NMR spectroscopy.* Biochim Biophys Acta, 1985. **819**(1): p. 131-5.

367. Andersen, O.S., et al., *Single-molecule methods for monitoring changes in bilayer elastic properties.* Methods Mol Biol, 2007. **400**: p. 543-70.

368. Harroun, T.A., et al., *Experimental evidence for hydrophobic matching and membrane-mediated interactions in lipid bilayers containing gramicidin.* Biophys J, 1999. **76**(2): p. 937-45.

369. Mondal, S., et al., *Quantitative modeling of membrane deformations by multihelical membrane proteins: application to G-protein coupled receptors.* Biophys J, 2011. **101**(9): p. 2092-101.

370. Hwang, W.L., et al., *Asymmetric droplet interface bilayers.* J Am Chem Soc, 2008. **130**(18): p. 5878-9.

371. Mobashery, N., C. Nielsen, and O.S. Andersen, *The conformational preference of gramicidin channels is a function of lipid bilayer thickness.* FEBS Lett, 1997. **412**(1): p. 15-20.

372. Lum, K., et al., *Exchange of Gramicidin between Lipid Bilayers: Implications for the Mechanism of Channel Formation.* Biophys J, 2017. **113**(8): p. 1757-1767.

373. Sapay, N., W.F.D. Bennett, and D.P. Tieleman, *Thermodynamics of flip-flop and desorption for a systematic series of phosphatidylcholine lipids.* Soft Matter, 2009. **5**(17): p. 3295-3302.

374. Renooij, W. and L.M. Van Golde, *The transposition of molecular classes of phosphatidylcholine across the rat erythrocyte membrane and their exchange between the red cell membrane and plasma lipoproteins.* Biochim Biophys Acta, 1977. **470**(3): p. 465-74.

375. Killian, J.A., K.N. Burger, and B. de Kruijff, *Phase separation and hexagonal HII phase formation by gramicidins A, B and C in dioleoylphosphatidylcholine model membranes. A study on the role of the tryptophan residues.* Biochim Biophys Acta, 1987. **897**(2): p. 269-84.

376. Goforth, R.L., et al., *Hydrophobic coupling of lipid bilayer energetics to channel function.* J Gen Physiol, 2003. **121**(5): p. 477-93.

377. Rokitskaya, T.I., E.A. Kotova, and Y.N. Antonenko, *Tandem gramicidin channels cross-linked by streptavidin.* J Gen Physiol, 2003. **121**(5): p. 463-76.

378. Gurtovenko, A.A. and I. Vattulainen, *Molecular mechanism for lipid flip-flops.* J Phys Chem B, 2007. **111**(48): p. 13554-9.

379. Mabrey, S. and J.M. Sturtevant, *Investigation of phase transitions of lipids and lipid mixtures by sensitivity differential scanning calorimetry.* Proc Natl Acad Sci U S A, 1976. **73**(11): p. 3862-6.

380. Goh, S.L., *Model systems for studies at the plasma membrane: Investigating lipid phase behavior and protein-mediated membrane remodeling*. 2013, Cornell University: Ithaca, NY.

381. Angelova, M.I. and D.S. Dimitrov, *Liposome Electroformation.* Faraday Discussions, 1986. **81**: p. 303-+.

382. Morales-Penningston, N.F., et al., *GUV preparation and imaging: Minimizing artifacts.* Biochimica Et Biophysica Acta-Biomembranes, 2010. **1798**(7): p. 1324-1332.

383. Buboltz, J.T. and G.W. Feigenson, *A novel strategy for the preparation of liposomes: rapid solvent exchange.* Biochim Biophys Acta, 1999. **1417**(2): p. 232-45.

384. Buboltz, J.T., *Steady-state probe-partitioning fluorescence resonance energy transfer: a simple and robust tool for the study of membrane phase behavior.* Phys Rev E Stat Nonlin Soft Matter Phys, 2007. **76**(2 Pt 1): p. 021903.

385. Henderson, S.J., *Monte Carlo modeling of small-angle scattering data from non-interacting homogeneous and heterogeneous particles in solution.* Biophysical Journal, 1996. **70**(4): p. 1618-1627.

386. Qian, S. and W.T. Heller, *Peptide-induced asymmetric distribution of charged lipids in a vesicle bilayer revealed by small-angle neutron scattering.* J Phys Chem B, 2011. **115**(32): p. 9831-7.

387. Heberle, F.A., et al., *Model-based approaches for the determination of lipid bilayer structure from small-angle neutron and X-ray scattering data.* Eur Biophys J, 2012. **41**(10): p. 875-90.

388. Kingston, R.L., H.M. Baker, and E.N. Baker, *Search designs for protein crystallization based on orthogonal arrays.* Acta Crystallogr D Biol Crystallogr, 1994. **50**(Pt 4): p. 429-40.

389. Otwinowski, Z. and W. Minor, *Processing of X-ray diffraction data collected in oscillation mode.* Macromolecular Crystallography, Pt A, 1997. **276**: p. 307-326.

390. Schneider, T.R. and G.M. Sheldrick, *Substructure solution with SHELXD.* Acta Crystallogr D Biol Crystallogr, 2002. **58**(Pt 10 Pt 2): p. 1772-9.

391. Bricogne, G., et al., *Generation, representation and flow of phase information in structure determination: recent developments in and around SHARP 2.0.* Acta Crystallogr D Biol Crystallogr, 2003. **59**(Pt 11): p. 2023-30.

392. Emsley, P., et al., *Features and development of Coot.* Acta Crystallogr D Biol Crystallogr, 2010. **66**(Pt 4): p. 486-501.

393. Murshudov, G.N., et al., *REFMAC5 for the refinement of macromolecular crystal structures.* Acta Crystallogr D Biol Crystallogr, 2011. **67**(Pt 4): p. 355-67.

394. McCoy, A.J., et al., *Phaser crystallographic software.* J Appl Crystallogr, 2007. **40**(Pt 4): p. 658-674.

395. Touw, W.G., et al., *A series of PDB-related databanks for everyday needs.* Nucleic Acids Res, 2015. **43**(Database issue): p. D364-8.

396. Jorgensen, K., et al., *Phase-Equilibria and Local-Structure in Binary Lipid Bilayers.* Biochimica Et Biophysica Acta, 1993. **1152**(1): p. 135-145.

397. Risbo, J., M.M. Sperotto, and O.G. Mouritsen, *Theory of Phase-Equilibria and Critical Mixing Points in Binary Lipid Bilayers.* Journal of Chemical Physics, 1995. **103**(9): p. 3643-3656.

398. Sugar, I.P., T.E. Thompson, and R.L. Biltonen, *Monte Carlo simulation of two-component bilayers: DMPC/DSPC mixtures.* Biophysical Journal, 1999. **76**(4): p. 2099-2110.

399. Frazier, M.L., et al., *Investigation of domain formation in sphingomyelin/cholesterol/POPC mixtures by fluorescence resonance energy*

transfer and Monte Carlo simulations. Biophysical Journal, 2007. **92**(7): p. 2422-2433.

400. Honerkamp-Smith, A.R., et al., *Line tensions, correlation lengths, and critical exponents in lipid membranes near critical points.* Biophysical Journal, 2008. **95**(1): p. 236-246.

401. Dai, J.A., et al., *Simulation of the l(o)-l(d) Phase Boundary in DSPC/DOPC/Cholesterol Ternary Mixtures Using Pairwise Interactions.* Journal of Physical Chemistry B, 2011. **115**(7): p. 1662-1671.

402. Lis, M., et al., *GPU-Based Massive Parallel Kawasaki Kinetics in the Dynamic Monte Carlo Simulations of Lipid Nanodomains.* Journal of Chemical Theory and Computation, 2012. **8**(11): p. 4758-4765.

403. Meerschaert, R.L. and C.V. Kelly, *Trace membrane additives affect lipid phases with distinct mechanisms: a modified Ising model.* European Biophysics Journal with Biophysics Letters, 2015. **44**(4): p. 227-233.

404. Srinivasan, J., et al., *Continuum solvent studies of the stability of DNA, RNA, and phosphoramidate - DNA helices.* Journal of the American Chemical Society, 1998. **120**(37): p. 9401-9409.

405. Still, W.C., et al., *Semianalytical Treatment of Solvation for Molecular Mechanics and Dynamics.* Journal of the American Chemical Society, 1990. **112**(16): p. 6127-6129.

406. Onufriev, A., D. Bashford, and D.A. Case, *Exploring protein native states and large-scale conformational changes with a modified generalized born model.* Proteins-Structure Function and Bioinformatics, 2004. **55**(2): p. 383-394.

407. Lee, M.S., et al., *New analytic approximation to the standard molecular volume definition and its application to generalized born calculations.* Journal of Computational Chemistry, 2003. **24**(11): p. 1348-1356.

408. Lee, M.S., F.R. Salsbury, and C.L. Brooks, *Novel generalized Born methods.* Journal of Chemical Physics, 2002. **116**(24): p. 10606-10614.

409. Brooks, B.R., et al., *CHARMM: The Biomolecular Simulation Program.* Journal of Computational Chemistry, 2009. **30**(10): p. 1545-1614.

410. Zoete, V. and O. Michielin, *Comparison between computational alanine scanning and per-residue binding free energy decomposition for protein-protein association using MM-GBSA: Application to the TCR-p-MHC complex.* Proteins-Structure Function and Bioinformatics, 2007. **67**(4): p. 1026-1047.

411. Zoete, V., M.B. Irving, and O. Michielin, *MM-GBSA binding free energy decomposition and T cell receptor engineering.* Journal of Molecular Recognition, 2010. **23**(2): p. 142-152.

412. Gaffney, B.J., *The chemistry of spin labels.* Spin Labeling: Theory and Applications, 1976. **L. J. Berliner, ed.**: p. 182-238.

413. Khelashvili, G., et al., *Computational modeling of the N-terminus of the human dopamine transporter and its interaction with PIP2 -containing membranes.* Proteins, 2015. **83**(5): p. 952-69.

414. Khelashvili, G., A. Galli, and H. Weinstein, *Phosphatidylinositol 4,5-biphosphate (PIP(2)) lipids regulate the phosphorylation of syntaxin N-terminus by modulating both its position and local structure.* Biochemistry, 2012. **51**(39): p. 7685-98.

415. Khelashvili, G., D. Harries, and H. Weinstein, *Modeling membrane deformations and lipid demixing upon protein-membrane interaction: the BAR dimer adsorption.* Biophys J, 2009. **97**(6): p. 1626-35.

416. Andelman, D., *Electrostatic properties of membranes: The Poisson-Boltzmann theory.* . Lipowsky, R., Sackmann, E., editors. Amsterdam: Elsevier Science B.V., 1995.

417. Chaikin, P. and T. Lubensky, *Principles of Condensed Matter Physics.* Cambrige University Press, 2000.

418. Baker, N.A., et al., *Electrostatics of nanosystems: application to microtubules and the ribosome.* Proc Natl Acad Sci U S A, 2001. **98**(18): p. 10037-41.

419. Davis, I.W., et al., *MolProbity: all-atom contacts and structure validation for proteins and nucleic acids.* Nucleic Acids Res, 2007. **35**(Web Server issue): p. W375-83.

420. Perkins, S.J., *Protein volumes and hydration effects. The calculations of partial specific volumes, neutron scattering matchpoints and 280-nm absorption coefficients for proteins and glycoproteins from amino acid sequences.* Eur J Biochem, 1986. **157**(1): p. 169-80.

421. Efimova, Y.M., et al., *On the neutron scattering length density of proteins in H(2)O/D(2)O.* Physica B-Condensed Matter, 2004. **350**(1-3): p. E877-E880.

422. Eldho, N.V., et al., *Polyunsaturated docosahexaenoic vs docosapentaenoic acid-differences in lipid matrix properties from the loss of one double bond.* J Am Chem Soc, 2003. **125**(21): p. 6409-21.

423. Curatolo, W., B. Sears, and L.J. Neuringer, *A Calorimetry and Deuterium Nmr-Study of Mixed Model Membranes of 1-Palmitoyl-2-Oleylphosphatidylcholine and Saturated Phosphatidylcholines.* Biochimica Et Biophysica Acta, 1985. **817**(2): p. 261-270.

424. Davis, P.J., K.P. Coolbear, and K.M. Keough, *Differential scanning calorimetric studies of the thermotropic phase behavior of membranes composed of dipalmitoyllecithin and mixed-acid unsaturated lecithins.* Can J Biochem, 1980. **58**(10): p. 851-8.

425. Vandijck, P.W.M., et al., *Miscibility Properties of Binary Phosphatidylcholine Mixtures - Calorimetric Study.* Biochimica Et Biophysica Acta, 1977. **470**(1): p. 58-69.

426. Jaworsky, M. and R. Mendelsohn, *Fourier-transform infrared studies of CaATPase partitioning in phospholipid mixtures of 1,2-dipalmitoylphosphatidylcholine-d62 with 1-palmitoyl-2-oleoylphosphatidylethanolamine and 1-stearoyl-2-oleoylphosphatidylcholine.* Biochemistry, 1985. **24**(14): p. 3422-8.

427. Schmidt, M.L., et al., *Phase equilibria in DOPC/DPPC: Conversion from gel to subgel in two component mixtures.* Journal of Chemical Physics, 2009. **131**(17).

428. Furuya, K. and T. Mitsui, *Phase-Transitions in Bilayer Membranes of Dioleoyl-Phosphatidylcholine-Dipalmitoyl-Phosphatidylcholine.* Journal of the Physical Society of Japan, 1979. **46**(2): p. 611-616.

429. Lentz, B.R., Y. Barenholz, and T.E. Thompson, *Fluorescence Depolarization Studies of Phase-Transitions and Fluidity in Phospholipid Bilayers .1. Single Component Phosphatidylcholine Liposomes.* Biochemistry, 1976. **15**(20): p. 4521-4528.